1-1-2007

Tribological properties of diamond-like carbon and boron carbide coatings against aluminum: Adhesion & friction at different temperatures and environments.

Ying Zhang
University of Windsor

Tribological Properties of Diamond-Like Carbon and Boron Carbide Coatings Against Aluminum: Adhesion & Friction at Different Temperatures and Environments

By: YING ZHANG

A Thesis
Submitted to the Faculty of Graduate Studies
through Engineering Materials
In Partial Fulfillment of the Requirements for
The Degree of Master of Applied Science at the
University of Windsor

Windsor, Ontario, Canada

2007

Your file Votre référence
ISBN: 978-0-494-35051-5
Our file Notre référence
ISBN: 978-0-494-35051-5

ABSTRACT

This thesis investigates the adhesion, friction and wear behaviour of diamond-like carbon (DLC) coatings and boron carbide (B_4C) coatings. Both temperature and environmental stability of these coatings were investigated. Pin-on-disc tests against a 319 Al alloy revealed that tungsten carbide (WC) doped hydrogenated DLC coatings displayed lower coefficient of friction (COF) and wear rates than monolithic nonhydrogenated DLC coatings. WC-DLC coatings with a top layer of DLC (DLC/WC-DLC) withstood higher temperatures than WC-DLC coatings. Aluminum adhesion with the WC-DLC and DLC/WC-DLC coatings was observed at 300 and 350 °C, respectively. B_4C coatings exhibited higher COF and more aluminum adhesion under all test conditions. While testing under the N_2 atmosphere reduced COF values for all the coatings, the humidity level of the test environment exerted various influence on each coating. The mechanisms of adhesion, friction and wear of the tribosystems were discussed based on the Al alloy-coating interactions under specific test conditions.

ACKNOWLEDGEMENTS

I would like to express my sincere gratitude to Dr. A. T. Alpas for his supervision and support throughout my study at the University of Windsor. Dr. E. Konca provided invaluable perspectives to wear tests and Dr. X. Meng-Burany is acknowledged for the FIB characterization of DLC coatings. I am grateful to all my colleagues in the Tribology of Lightweight Materials group for their opinions, support and friendship. In particular, I thank A. Abougharam for his help with many experiments at the GM Global Research & Development Center.

Dr. Y.-T. Cheng, Dr. T. Perry, Dr. J. Dasch as well as Dr. M. Lukitsch of GM are appreciated for their precious discussion. Dr. M. Lukitsch is also acknowledged for his support for surface mechanical characterization.

Mr. J. Barvinek of IonBond Inc. Cambridge ON is greatly appreciated for supplying the samples.

Finally, the financial support from NSERC, General Motors of Canada is greatly appreciated. I also acknowledge the scholarship provided by the University of Windsor (International Graduate Student Scholarship).

TABLE OF CONTENTS

LIST OF ABBREVIATIONS

DLC	Diamond-Like Carbon
H-DLC	Hydrogenated DLC
NH-DLC	Non-Hydrogenated DLC
MWF	Metal Working Fluid
HSS	High Speed Steel
PVD	Physical Vapour Deposition
CVD	Chemical Vapour Deposition
PACVD	Plasma Assisted CVD
PECVD	Plasma Enhanced CVD
PLD	Pulsed Laser Deposition
SEM	Scanning Electron Microscopy
ERDA	Elastic Recoil Detection Analysis
RH	Relative Humidity
R_a	Surface Roughness
R_c	Hardness in Rockwell C Scale
XRD	X-Ray Diffraction
COF	Coefficient of Friction
VHN	Vickers Hardness Number

LIST OF TABLES

LIST OF FIGURES

CHAPTER 1 INTRODUCTION

Many methods have been taken into consideration in order to accomplish the goal of dry machining of aluminum alloys; among them is the development of coatings that can be applied to the tool surfaces in order to reduce aluminum adhesion. Coatings that withstand high temperature and maintain their frictional stability in various environments are required for this purpose. This chapter briefly describes the driving force behind the current research and presents the need to better characterize promising tribological coatings such as B_4C and DLC.

1.1. Driving Force for Dry Machining and Manufacturing

The growing magnitude of environmental issues has prompted the reduction and eventual elimination of metal working fluids (MWF) in the manufacturing industry--an aim reinforced by anticipated government regulations and potential economical benefits. In the United States alone, the National Institute for Occupational Safety and Health (NIOSH) recommends that occupational exposures to cutting fluid aerosols be limited to 0.5 mg/m^3--a marked departure from the current standard value of 5 mg/m^3 [1]. This recommendation stems from the detrimental effects of cutting fluid aerosols suffered by machine shop workers as well as the work environment at large. NIOSH presented solid evidence that workers who are constantly exposed to MWFs have an increased risk of non-malignant respiratory and skin diseases [1]. Consequentially, machining methods

that eliminate the use of MWFs will have a substantial positive impact on the overall quality of the working environment.

Replacing cutting fluids will also potentially bring about secondary economic benefits in addition to direct cost savings, because the process of recycling dry chips does would not require a cleaning operation before their reuse. It has been estimated that the cost of the cutting fluid system's fluid filtration, disposal and maintenance makes up approximately 17% of the overall manufacturing cost [2-4].

1.2. Dry Machining of Aluminum and Associated Problems

North American automotive manufactures are constantly seeking new ways to increase the fuel efficiency of their vehicles by reducing vehicle weight in order to fight their foreign competitors. Substituting steel or cast iron with aluminum alloys provides approximately a 66% reduction in weight due to the lower density of the Al alloys (2.7 vs. 7.8 g/cm^3). For this reason, automotive companies have been interested in this type of component replacement wherever possible. Presently, most engine components and some chassis parts are made out of different aluminum alloys. For example, a 319 Al grade cast aluminum alloy is used to manufacture engine blocks. While reducing the vehicle weight is always a goal, environmentally friendly machining and shaping technologies are also being explored--among them is dry machining.

Dry machining of aluminum alloys presents challenges. In the absence of MWFs, aluminum chips that are formed during the machining process adhere to the tool surfaces.

This type of adhesion has also been also observed in other forming operations such as sheet forming and deep drawing, and causes tool failures which--in turn--leads to poor product surface quality. This adhesion problem is amplified during dry drilling operations when aluminum chips adhere to the surfaces of the drill flutes--clogging them in a very short time and ceasing the process of chip evacuation. The clogged drills do not last long in service. The average number of holes that an uncoated high speed steel (HSS) drill can achieve in the dry drilling of a 319 Al alloy block is less than 50--far from the expectation of 1×10^4 holes set by the industry [5]. The severity of aluminum adhesion to an uncoated HSS drill after the dry drilling of a 319 Al alloy is illustrated in the example of **Figure 1. 1**.

1.3 Substitution of Coatings for Metal Working Fluids to Reduce the Material Adhesion to Tool Surfaces

Heat generation is one of the most important factors to consider in any kind of machining process. The heat produced during machining originates from plastic deformation of the workpiece material and the friction between the tool and the workpiece. A great deal of heat is dispersed by the removal of the workpiece material, and another part is conducted into the deeper regions of both the workpiece and the tool during mechanical contact. The application of a MWF has three main purposes: first, to reduce friction by separating the two rubbing surfaces of the tool and the workpiece (lubrication effect), second, to assist in the removal of chips from the cutting area

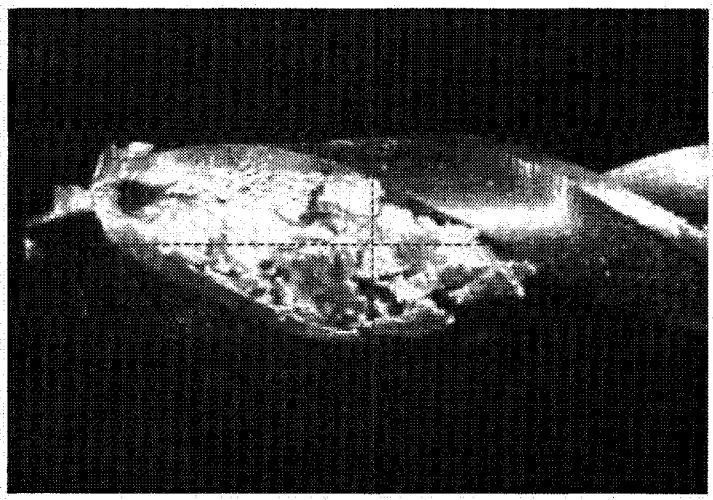

Figure 1. 1 Uncoated HSS drill after dry drilling of 319 Al alloy. Aluminum was severely adhered to drill flutes (courtesy of GM R&D Center). The drill was 6.35 mm diameter, 2-flute, high helix, with 118° point angle. Drilling was done at 61 m/min speed and 0.13 mm/rev. feed.

(flushing effect), and third, to dissipate the heat both by increasing the contact areas and simply flowing away (cooling effect).

The use of a tool coating in place of the traditional MWF intends to achieve the lubrication effect and flushing effect provided by the fluid and many efforts have been undertaken to develop coating materials that fulfil the demands of high hardness, low friction and low tendency of adhesion to workpiece material. Hard coatings deposited by physical vapour deposition (PVD)--specifically TiN, CrN, TB_2, TiCN and TiAlN--usually have some friction-reducing effect, but the COF value during dry sliding against metals remains in the range of 0.3 to 0.8--still too high for dry machining [6-7]. According to previous tribological tests against aluminum, these hard coatings are not as good as DLC coatings in terms of aluminum adhesion mitigating properties [7].

1.4 The Need for Current Study

As explained above, developing a tool coating that does not adhere to aluminum and exhibits a low COF when dry sliding against aluminum is the primary requirement to successfully perform the dry machining of Al alloys. Considering the frictional heat generated during dry machining and the heating requirements of other applications such as aluminum hot forming, an effective coating must have significantly high temperature stability.

While B_4C coatings have been successfully applied to tools for the machining of aluminum alloys, the reported applications were under lubrication [8-9] and as far as the

author is aware, their tribological behaviour against Al alloys has not been studied. Examining the Al adhesion and tribological behaviour of B_4C coatings during dry sliding under different test conditions is necessary in order to investigate its suitability as a tool coating for the dry machining of Al alloys. Such studies might reveal that a specific condition is optimal for the operation of B_4C coatings.

Previous studies have shown that a DLC coating is better than other hard coatings for reducing aluminum adhesion (**Figure 1. 2**) and for lowering the COF when dry sliding against a 319 Al alloy [7]. However, said coating exhibited a COF ~0.3 at 120 °C and was totally removed from the substrate after testing at 300 °C [7]. Such poor thermal stability is undesirable in dry machining, stamping and rolling processes where heat is generated or presented--creating the need for more stable DLC coatings.

Aluminum has also been reported to adhere to nonhydrogenated DLC (NH-DLC) coatings in inert atmospheres such as argon and vacuum, but it exhibits a much lower tendency towards adhesion in ambient air [7]. The testing environment also affects the friction behaviour of DLC coatings. Studies on the ways in which testing environments affect the tribological behaviour of DLC coatings are presented in **Section 2.2.5.**

1.5 Scope and Objectives

The 319 Al alloy was chosen as a counterface material for this work because of its wide application in the automotive industry. Three coating were examined--boron carbide coatings (B_4C), tungsten carbide doped hydrogenated DLC coatings (WC-DLC) and

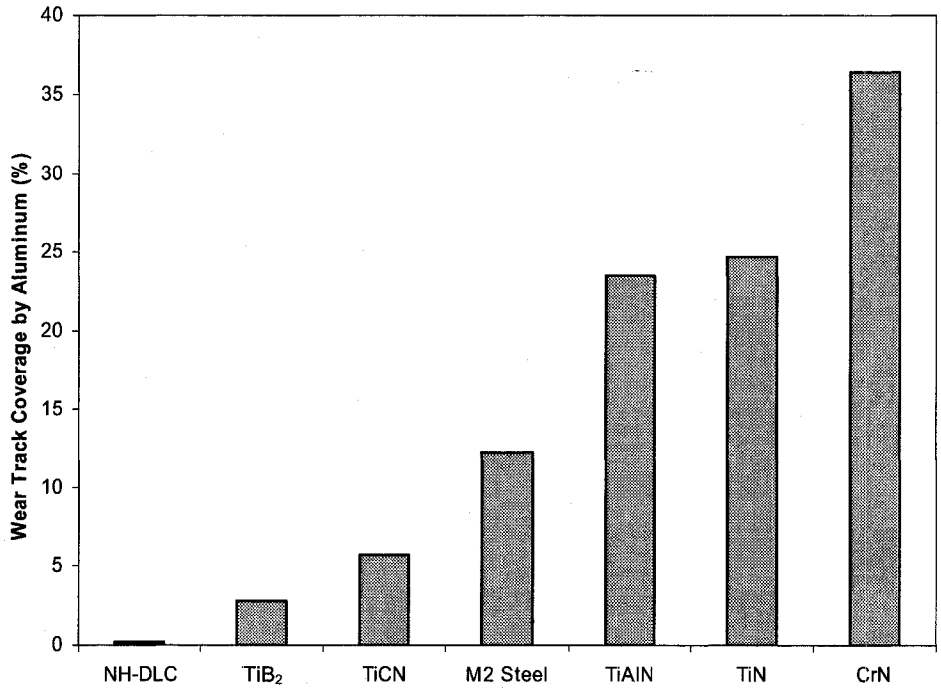

Figure 1. 2 Ranking of various coatings in terms of amount of aluminum adhesion onto the coating 7. 319 Al did not adhere to the NH-DLC coating. The results were measured from wear tracks generated on various coatings after testing at room temperature in ambient air (33-51% RH) at 5 N applied load and 0.12 m/s sliding speed.

tungsten carbide doped hydrogenated DLC coatings with a top DLC layer (DLC/WC-DLC). 52100 steel (AISI) was tested against B_4C coatings for comparison to 319 Al.

Considering both the background and motivation described in the previous sections, the scope and objectives of this work are listed in the following two main groups:

1.5.1 Adhesion of Al to the Coatings

To study the influence of factors such as testing temperature and environment on Al transfer to the coatings, and to rank the coatings according to the amount of Al adhesion they exhibit under various testing conditions.

1.5.2 Tribological Behaviour of DLC Coatings and B_4C Coating against 319 Al

To investigate the tribological behaviour of the DLC coatings and B_4C coatings against Al by studying the effects of testing temperature and environment on said behaviour.

The investigation began by running unlubricated pin-on-disc tests under various test conditions, and then subjecting the tested sample to inspection using methods such as scanning electron microscopy (SEM) and optical surface profilometry in order to analyze the surface changes induced by the tests and, in turn, quantify the material adhesion. The details of the methodology used are presented in **Chapter 3**.

1.6 Thesis Outline

Chapter 2 provides a survey of the open literature on i) the tribological behaviour of B_4C coatings including the controlling factors and ii) the tribological behaviour of DLC coatings including controlling factors. **Chapter 3** describes the experimental methods and procedures used to characterize the test materials used in this work, then gives details regarding the material studied, the pin-on-disc machine, wear test conditions and the procedures that were applied to evaluate the test results.

Chapters 4 and 5 display the results and discuss the pin-on-disc tests that were performed to investigate the transfer of 319 Al alloy to the coatings and the tribological behaviour of the coatings when dry sliding against 319 Al. The effects of both testing temperature and environment are discussed in each chapter. Comparison with previous work on the transfer and adhesion of Al to various coating surfaces and the corresponding tribological behaviour is also presented in these chapters.

Chapter 6 closes this thesis with conclusions and suggestions for future work.

CHAPTER 2 LITERATURE SURVEY

Two different types of coatings, namely boron carbide and diamond-like carbon were studied in this work because of their anticipated beneficial tribological properties when sliding against aluminum. There is little prior work on this topic. However, it is instructive to do a general survey of structures and mechanical properties of these coatings. Investigations on the friction and wear behaviour against mostly steel counterfaces are also reviewed.

Literature on the tribological behaviour of B_4C coatings is scarce compared to the more established application of ceramic boron carbide. The first part of this chapter focuses on boron carbide (B_4C) coatings and their tribological aspects with a brief review of the B_4C structure followed by an introduction to B_4C and its coating form. Then a survey of the published works on the deposition of B_4C coatings and their tribological behaviour is given--finishing with a summary of the papers on the "abrasiveness" of B_4C coatings that describe one of the current major applications of B_4C coatings.

The second part of this chapter gives an account of the three hybridisation states of carbon atoms to introduce DLC coatings, then reviews previous studies that investigate the tribological behaviour of DLC coatings as well as the effects of influencing factors such as coating composition, test temperature and environment--ending with a brief literature summary.

2.1 Review of the Literature on the Tribological Behaviour of the Boron Carbide Coatings

2.1.1 Introduction to Boron Carbide and Boron Carbide (B_4C) Coatings

Boron carbide exists as a stable single phase compound in a large homogeneity range from 8 up to 20 at.% C concentration--as shown in the phase diagram (**Figure 2. 1**) proposed by Elliot [10]. The most stable boron carbide structure is rhombohedral with a stoichiometry of $B_{13}C_2$, $B_{12}C_3$ or B_4C. These rhombohedral structures of boron carbide consist of 12 icosahedral clusters of atoms linked by direct covalent bonds and through 3-atom inter-icosahedral chains along the longest diagonal of the rhombohedron. The boron-rich icosahedral structures reside at the vertices of a rhombohedron as shown in **Figure 2. 2**. The B and C atoms can easily substitute for each other within both the icosahedra and the intericosahedral chains -- the main reason for boron carbide's large homogeneity range [11-13]. The most widely accepted structural model for B_4C with 20 at.% C has $B_{11}C$ icosahedra with C-B-C intericosahedral chains. As the carbon content decreases, the C-B-C chains are replaced with C-B-B chains until they are nearly depleted. Further decreases in the carbon content result in the replacement of $B_{11}C$ icosahedral with B_{12} icosahedral. In the case of the amorphous boron carbide, it is believed that the structure is still based on a random icosahedral network at a carbon content less than 50 at.% [14].

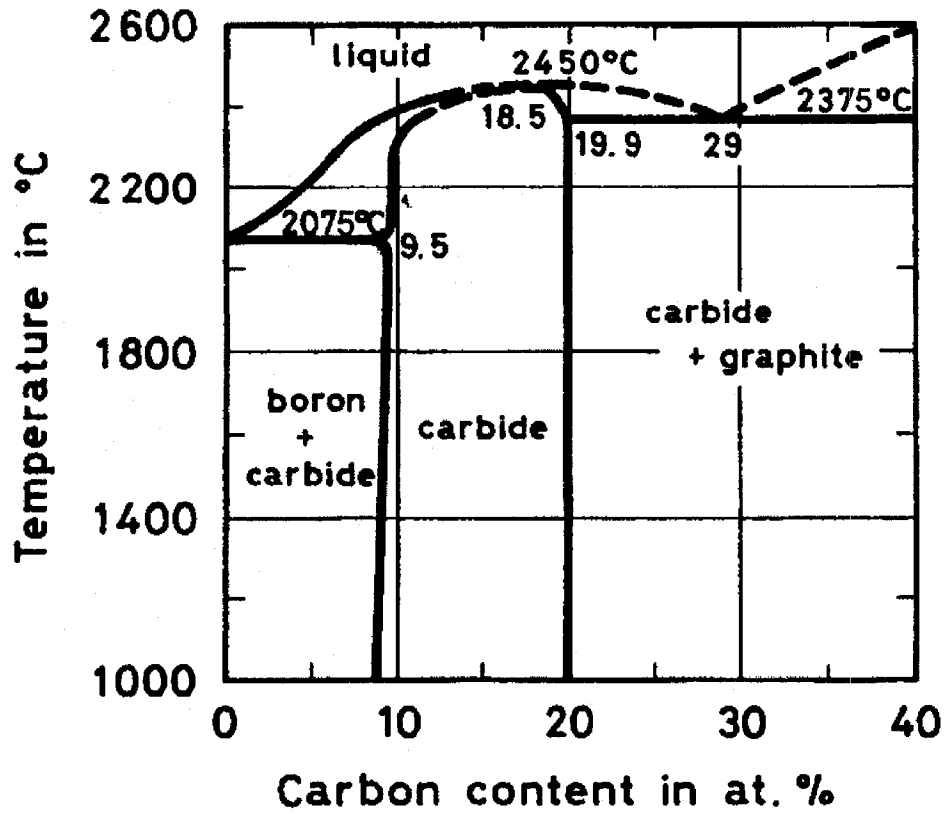

Figure 2. 1 Phase diagram for the B-C system by Elliott 10. The large homogeneity range from 8 up to 20 at.% C where carbides exist is shown.

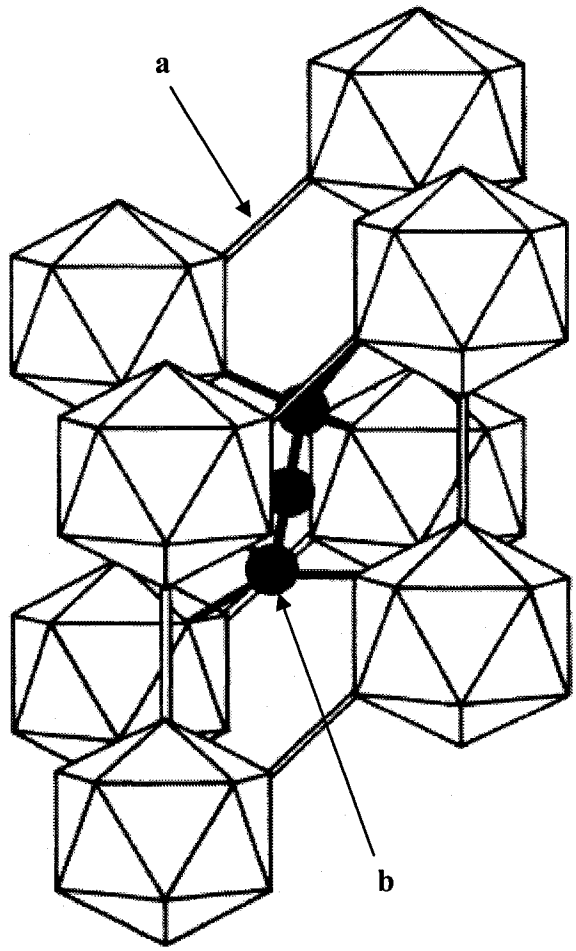

Figure 2. 2 The rhombohedral crystal structure of boron carbides. A twelve-atom boron-rich icosahedron resides at the corners of a rhombohedron. Each icosahedron is bonded to six other icosahedra through direct bonds (**a**). In addition, three-atom intericosahedral chains (**b**) connect icosahedra. Each chain links six different icosahedra since the end atoms of each chain are bonded to three different icosahedra. Atoms are placed at the vertices of the icosahedra and within the three-atom intericosahedral chain [12].

Boron carbide is the third hardest material (VHN 4828) known, surpassed only by diamond (VHN 12000) and cubic boron nitride (6500 VHN). It is characterized by a high melting point (2350 °C), high thermal stability, high elastic modulus (360-460 GPa) and a low density. The mechanical properties of boron carbides, compiled by Sezer and Brand [15], are presented in **Table 2. 1**. Boron carbide has been used in a wide range of industrial applications, from grinding wheels for sharpening cutting tools to super-abrasives in polishing and grinding media, as well as rotor bearings. The intrinsic brittleness however, combined with its highly abrasive nature against metallic parts has limited the extended application of boron carbide.

Since the inception of thin hard coating technologies in the 1970's, a number of hard materials such as TiN, CrN, TiB_2 etc. have been applied as tribological coatings. Among these hard coatings, boron carbide films have received attention. The properties of the coating, however, can vary significantly depending on the deposition method and properties. Generally, boron carbide coatings deposited at room temperature are amorphous and display a low hardness value (as low as 13 GPa) [16], while coatings prepared at high temperatures can reach a hardness value comparable to that of bulk boron carbide (~47 GPa) or higher (i.e. 100 GPa)--due to crystallization [17-20]. The mechanical properties (hardness and elastic modulus) of boron carbide coatings measured by different investigators are summarized in **Table 2. 2**.

Table 2. 1 Properties of boron carbide compiled by Sezer and Brand [15].

Density (g/cm^3)	2.52
Vickers hardness (kg/mm^2)	4828 (20 °C)-2170 (900 °C)
Toughness ($MPa.m^{1/2}$)	2.9-3.7
Elastic modulus (GPa)	360-460
Poisson ratio	0.14-0.18
Shear modulus (GPa)	158-188
Tensile strength (N/mm^2)	155 (980 °C)-162 (1425 °C)

Table 2. 2 Mechanical properties of boron carbide coatings.

Hardness GPa	Elastic modulus GPa	Reference
15-43	Not reported	Yang et al. [16]
20-41	162-283	Eckardt et al. [17]
13-18	120-144	Ahn et al. [18]
15.6-25.6	162-210	Monteiro et al. [19]
19-100	Not reported	Salimijazi et al. [20]
42.5-50.4	300-420	Han et al. [21]

It is interesting to note that the amount of literature published on the tribological properties of B_4C coatings is considerably less than the attention paid to other hard coatings of the C-B-N coating system. However, this relative shortage of knowledge on said properties has not prevented the industrial application of B_4C coatings from enjoying an Edisonian approach. Diamond Black Technology, Inc., (Conover, NC) held the world-wide patent rights for the magnetron sputtering deposition of boron carbide (trademarked as DiamondBLACK^{TM}) and had successfully commercialized its deposition [22-27]. Other manufactures, such as IonBond, also provide customers with B_4C coatings (including the ones studied in this work). Boron carbide coatings are being used in a wide range of applications such as gears, molds, tools and cutting edges. In fact, a 3-10 time improvement in tool life compared to the uncoated tools (as high as 20 times in some situations) could be achieved when DiamondBLACK^{TM} was applied to tools used for the machining of various grades of aluminum alloys (314, 319, 356, 30, 6061, 7075). For example, studies have shown that a tap coated with DiamondBLACK has lasted for 2000 taps, while the same tap coated with TiN lasted only 20 taps when tapping a high silicon aluminum [9]. The application of boron carbide coatings to the cobalt drills used for machining titanium and aluminum alloys, and to the cutting tool used for machining of aluminum alloys can be found in [8]. None of these cases, however, reported the absence of MWF during the machining process.

Section 2.1.2 provide a brief summary of the deposition process of boron carbide coatings for tribological applications, followed by an account of studies on the self-lubricity of boron containing surfaces (**Section 2.1.3**). Work analyzing the abrasiveness of boron carbide coatings (in order to design a finite life run-in coating to improve the fatigue resistance of machine parts) is summarized at the end (**Section 2.1.4**).

2.1.2 Deposition of Boron Carbide Coatings

The two most extensively studied methods for the deposition of B_4C coatings are chemical vapour deposition (CVD) and physical vapour deposition (PVD) by sputtering. During various CVD processes, BCl_3 [28-29] or boranes (e.g. B_2H_6) [30] are used as boron sources and the deposition process is carried out in a reducing (hydrocarbons and H_2) atmosphere at a high temperature (≥ 300 °C). A schematic drawing of the plasma-assisted chemical vapour deposition (PACVD) system used in [29] is shown in **Figure 2. 3**. A wide composition variation similar to that of bulk boron carbide has been observed in the boron carbide coatings prepared using these methods (from $B_{4.7}C$ to $B_{13}C_2$). A review of the CVD of boron carbide that includes a compilation of various B_xC_y phases prepared can be found in [15]. Several factors such as usage of hazardous gas (like BCl_3 and boranes), difficulty in controlling of the coating stoichiometry, and requirements for relatively high deposition temperature have limited the application of CVD processes.

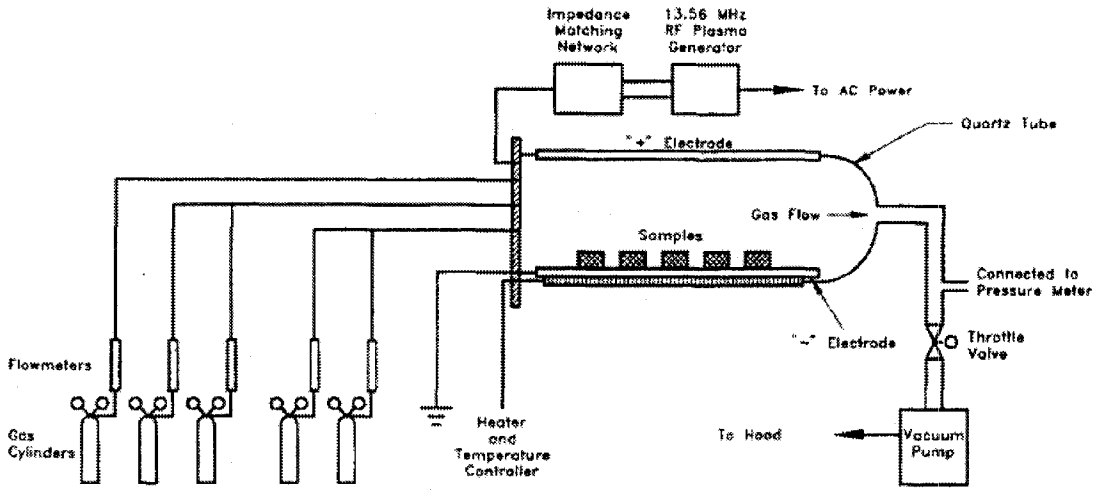

Figure 2. 3 Schematic diagram of the PACVD system used by Tsou et al. [29]

The sputtering deposition of B_4C coatings are conducted at relatively low temperatures--when compared to CVD--using Ar as a sputtering gas. Usage of B_4C targets as source material eliminates the unwanted variation in coating composition. The sputtering deposition of B_4C coatings is studied for the manufacturing of B_4C coatings intended for tribological purposes [17-18].

Eckardt et al. [17] deposited B_4C coatings using d.c. magnetron sputtering deposition with a B_4C target and Ar sputtering gas. Small amounts of acetylene (flow rate between 1 and 8 sccm) were added as a reactive gas and the boron content of the coatings decreased nearly linearly with the acetylene gas flow while carbon content simultaneously increased also nearly linearly. The produced coatings displayed a coefficient of friction that was investigated using a pin-on-disc tester against 100Cr6 balls (4.76 mm in diameter) under a load of 1N and with a sliding speed of 0.04 m/s. The test temperature and relative humidity were kept at 21 °C and 45-50%, respectively. The COF decreased from 0.9 (without C_2H_2) to a lowest value of 0.15 at a C_2H_2 flow rate of 4 sccm. However, this decrease in COF could not be related to any detectable coating structure change. It was also observed that a peak value of 41 GPa for hardness and 283 GPa for elastic modulus occurred at 2 sccm C_2H_2. The authors suggested that hydrogen was embedded in microvoids and defects, causing internal stress that resulted in less ductile material with increased hardness. Continued incorporation of hydrogen into the B_4C coating formed additional hydrogen bondings (i.e. B-H and C-H), resulting in a less rigid structure. The

authors also presented a comparison between modified B_4C and Ti doped DLC coatings deposited in the same chamber. The results showed that they had comparable COF values (0.25 for modified B_4C vs. 0.20 for Ti doped DLC) and wear rates (4.5-7.5 $m^3N^{-1}m^{-1}\times10^{-15}$ for modified B_4C vs. 5-10 for $m^3N^{-1}m^{-1}\times10^{-15}$ Ti doped DLC).

Ahn et al. [18] studied the tribological behaviour of sputtered boron carbide coatings and the influence of processing gas. The B_4C coated coupons were tested against 3 mm diameter steel balls using micro-oscillating tests in ambient air (40-45% RH). A load of 0.3 N, sliding speed of 4.43 mm/s and stroke length of 3 mm were used. The tested coatings were deposited by d.c. magnetron sputtering deposition with a B_4C target and various amounts of methane gas. The hardness, elastic modulus and roughness of the coatings decreased with the increase in CH_4 gas concentration--an observation attributed to the formation of an increasing amount of crystalline phase combined with the reduction of the polymeric C-H bond within the B_4C coating. The sample deposited without CH_4 showed a high and unstable COF (0.4) from the beginning of the test, whereas the COFs were significantly lower and stable for other films due to the introduction of CH_4 (**Figure 2. 4**). The lifetime of the coating was also increased, and the friction coefficient of deposited boron carbide films considerably decreased from ~0.4 to 0.1 for coatings deposited without CH_4 and coatings deposited with 1.2 vol.% CH_4, respectively. An examination of the wear tracks on the sample with 1.2 vol.% CH_4 exhibited material transfer from the steel ball and a low wear rate. The authors concluded

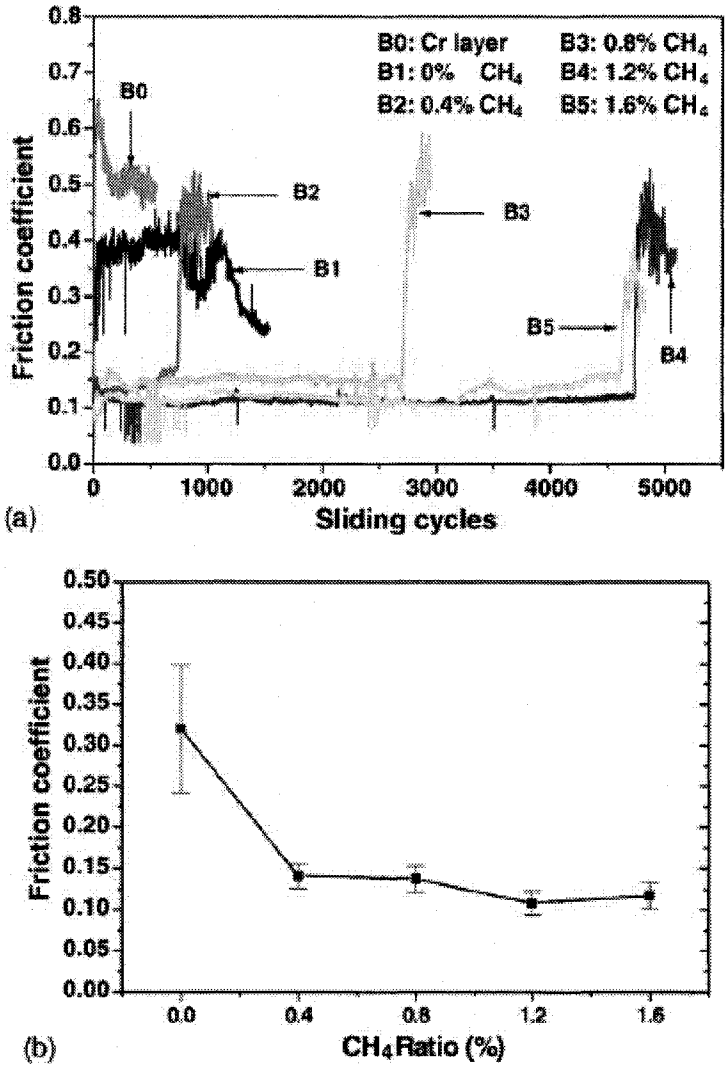

Figure 2. 4 The friction behaviour of B_4C coatings (with various CH_4 ratios in the processing gas) dry sliding against 52100 steel [18]. **a)** Friction coefficient as a function of number of sliding cycles; **b)** Steady state friction coefficient as a function of CH_4 ratio.

that the greater amount of graphite phase in the film deposited with an increasing CH_4 addition might contribute to the lower friction and higher wear resistance of the boron carbide coating.

2.1.3 Self-Lubricity of Boron Carbide Coatings: Effect of Relative Humidity

Erdemir et al. [31-33] conducted extensive studies on boric acid, boron and boron oxide containing surfaces, as well as boron carbide surfaces. They proposed a lubrication mechanism for the boric acid forming surfaces based on the inter-layer slip between the crystal layers of boric acid. Their study has been cited in later work on the tribological behaviour of tribo-systems containing boron carbide [34-36]. The following section introduces the crystal chemistry of boric acid then reviews studies that attribute the tribological behaviour of boron containing systems to the formation of boric acid on the sliding surfaces.

2.1.3.1 Crystal Chemistry of Boric Acid

Despite minor variations in measured atomic position, investigators agree that the unit cell of boric acid ($3H_2O{\cdot}B_2O_3$ or H_3BO_3) is triclinic and made up of boron, oxygen and hydrogen arrayed in layers parallel to the basal plane of a triclinic crystal [31]. The cell parameters and the triclinic crystal structure of boric acid are presented in **Figure 2. 5.**

The volume of the unit cell is 0.263 nm^3, which accommodates four boric acid molecules and the c-axis is inclined to the basal plane at an angle of 101°--causing

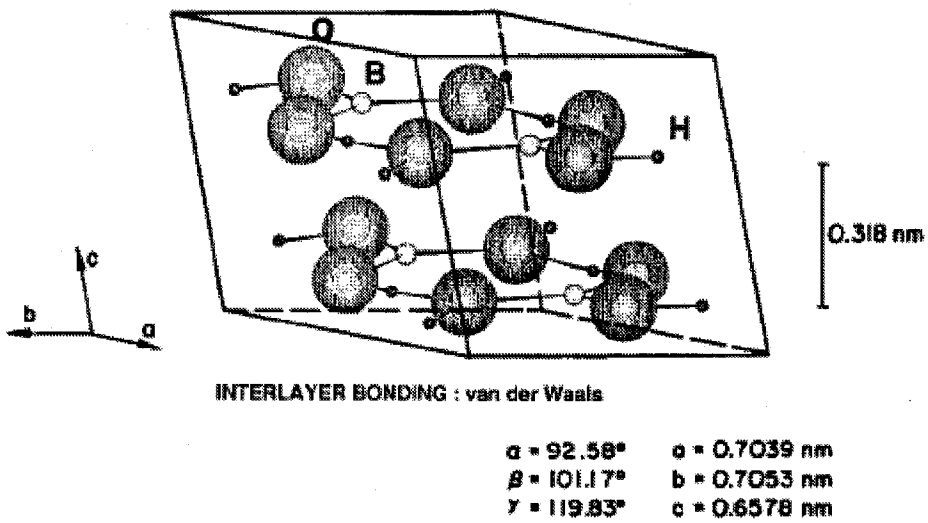

Figure 2. 5 Layered triclinic crystal structure of H_3BO_3 [31].

alternate layers to shift along the c-axis. The layers are 0.318 nm apart, held together by weak van der Waals forces. This layered crystal structure and unique bonding of boric acid resemble those of graphite, leading investigators to hypothesize that boric acid should also be applied as a solid lubricant. Erdemir [31] tested cold pressed boric acid pins against AISI 52100 steel discs and observed a COF of approximately 0.1--proving that boric acid was an effective solid lubricant. SEM results also revealed that the worn pin tips of pressed boric acid exhibited some preferred alignment of its platelike crystallites as a result of the sliding contact.

2.1.3.2 Self-lubrication of Boron Containing Surfaces

The effect of boric acid film formation on the friction behaviour of boron and boron oxide containing surfaces has been studied by Erdemir et al. [32]. The authors deposited boron oxide and boron on AISI M50 steel discs and conducted pin-on-disc tests in ambient air (23 °C, 50% RH) against AISI M50 steel balls under a combination of 1 N applied load and 0.1 m/s sliding speed. For the steel pin/boron oxide coated disc pair, a steady-state COF value of 0.05 was reached. Large colonies of platelike crystallites aligned parallel to the contact surface were revealed by SEM inspection of wear tracks after the tests. The Raman spectra of the platelike crystallites and the near-surface region of the boron oxide coating were found to be similar to that of a boric acid standard. Thus, the authors concluded that boron oxide reacted spontaneously with the water molecules in an open environment at room temperature due to a negative standard heat of reaction

(-45.1 kJ/mol). The reaction produced a thin boric acid film on top of the boron oxide coating. Under sliding contact, the layers of boric acid could align themselves parallel to the direction of relative motion. Once aligned, the layers slid over one another with relative ease, providing low friction. For the steel pin/boron coated disc pair, a steady state COF of 0.07 was measured. The authors [32] suggested that this was due to the reaction of the boron with the oxygen in the air, followed by boric acid formation with water. The same mechanism of boric acid formation was also used to explain the low COF of ~0.05 observed for annealed borided steel surfaces [37-38]. The process formation of boric acid lubricating layer on boron or boron oxide containing surface can be summarized by the following sequential chemical reactions [32][37]:

$$2B + \frac{3}{2}O_2 \rightarrow B_2O_3, \Delta H_{1023} = -1218 \text{ kJ/mol}, \qquad \textbf{Equation 2. 1}$$

$$\frac{1}{2}B_2O_3 + \frac{3}{2}H_2O \rightarrow H_3BO_3, \Delta H_{298} = -45.1 \text{ kJ/mol}. \qquad \textbf{Equation 2. 2}$$

It should be noted that boron carbide is not low friction material on its own merit. It needs boric acid formation. In order to achieve boric acid lubrication, either pre-annealing of the boron carbide coating in air [34][39] or presence of sufficient water vapour within the environment is necessary [35-36]. By annealing in the presence of oxygen, boron oxide is formed by the following chemical reaction:

$$B_4C + O_2 \rightarrow B_2O_3 + C + CO(g)\uparrow + CO_2(g)\uparrow \qquad \textbf{Equation 2. 3}$$

During this reaction, more solid carbon is produced at lower partial pressure of oxygen, while higher partial pressure of oxygen results in the favourable formation of gaseous

products. Once a layer of boron oxide is formed on the surface of boron carbide, the adsorption of water by this layer results in the formation of boric acid following the chemical reaction described above. The oxidation of B_4C is not thermodynamically favourable, however, because it is stable up to 600 °C in the presence of oxygen [39].

Erdemir et al. [39] demonstrated the difference in the friction behaviour of boron carbide and annealed boron carbide (800 °C in air for 1h) by testing them against 440C steel balls. For the steel/boron carbide pair, a COF of 0.7 was observed while the value for the annealed boron carbide/steel pair was 0.04. Raman peaks identical to those observed for the boric acid standard were detected on the surface of the annealed boron carbide, but did not appear on the as-received boron carbide (**Figure 2. 6**). The authors concluded that the low COF of the boron carbide surfaces could be achieved as a direct consequence of the sequential formation of a boron oxide layer on the boron carbide surface during annealing, followed by the formation of a boric acid film during cooling.

Cuong et al. [36] studied the effect of relative humidity on the tribological properties of boron carbide coating against steel. The experiments were conducted on d. c. magnetron sputtering deposited B_4C coatings against 3 mm diameter steel balls using an oscillating tester under a 0.3 N load, 4.43 mm/s sliding speed and a stroke length of 3 mm. Three relative humidity (RH) levels of 5%, 45% and 85% were used. At 5% RH, the COF was ~0.42--decreasing considerably to 0.11 and 0.09 at 45% and 85% RH, respectively (**Figure 2. 7**). At 85% humidity, the coating remained remarkably intact even after

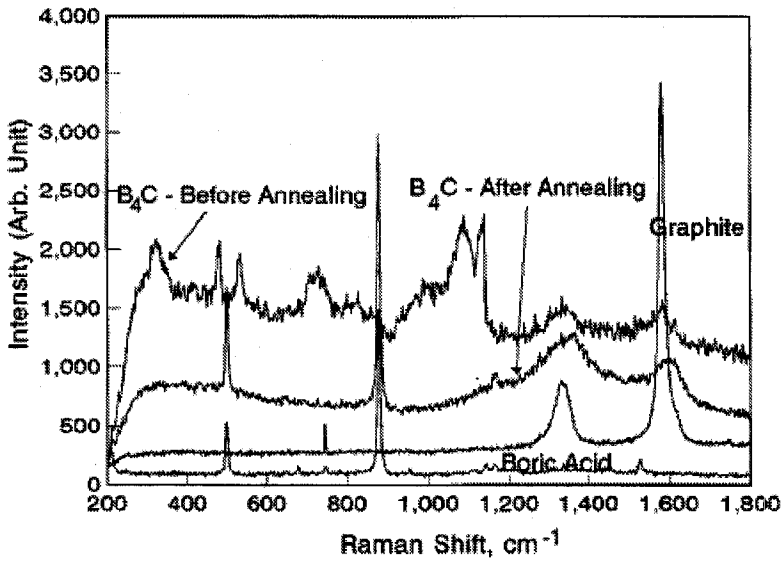

Figure 2. 6 Raman spectra of as-received and annealed B_4C. Raman spectra of H_3BO_3 (boric acid) and graphite standards are also included for comparison [39].

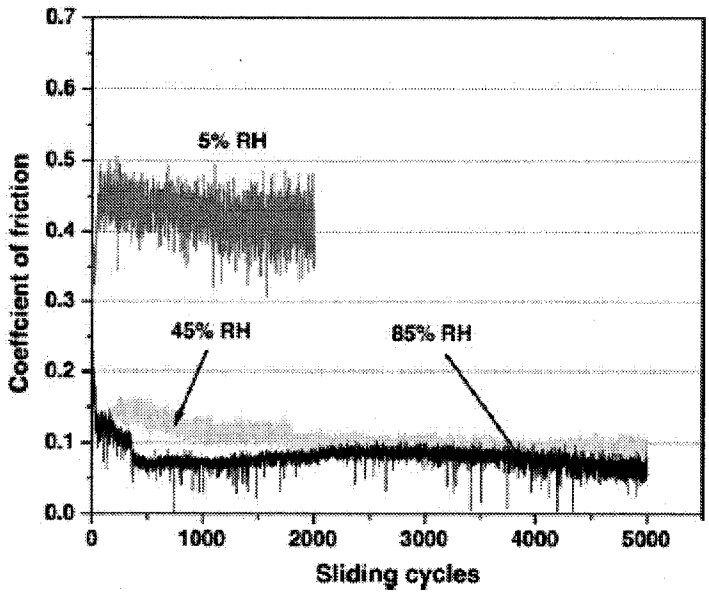

Figure 2. 7 COF curves of B_4C coating sliding against steel balls at different relative humidity levels [36].

10,000 sliding cycles. By contrast, the coating suffered a virtually complete removal at 45% RH after 10000 cycles. At 5% RH, complete coating removal occurred after 5000 cycles. The presence of boron oxide/boric acid and graphitic carbon was detected by X-ray photoelectron spectroscopy (XPS) within the wear track of the boron carbide coating at 45% after 5000 cycles. The authors attributed this low and stable friction characteristic of boron carbide coatings in medium and high humidity environments to the boric acid formation and formation of carbon in the graphite phase at the top layer of the boron carbide coating's wear track.

2.1.4 Study on the Abrasiveness of Boron Carbide Coatings

Erdemir [40] suggested that hard coatings could increase the fatigue resistance of a coated part by polishing mating surfaces during sliding contact. Polishing could remove asperities on the mating surface that would have otherwise caused high local stresses, and eventually contact fatigue failure. Boron carbide increases the contact fatigue life of a coated component because it polishes the counterface. In order to effectively design a "finite life run-in" boron carbide coating which would stop polishing the counterface after a designed period, a series of papers studying the system of 52100 steel sliding against B_4C coated, case carburized low carbon steel coupons have been published in the open literature [41-45]. These papers employed a parameter termed coating abrasiveness--i.e. counterface abrasion rate--to characterize the ability of the coatings to polish their counterface. Thus, in the case of sliding against 52100 steel, the average

coating abrasiveness during n cycles $\overline{A(n)}$ is defined as the total volume of the steel removed, divided by the total distance traveled:

$$\overline{A(n)} = \frac{V}{d} = \frac{V}{2\pi rn} \qquad \textbf{Equation 2. 4}$$

where V is the volume of steel removed, d is the distance traveled and n is the number of cycles. The instantaneous abrasion rate on the nth cycle is defined as A_n.

Accordingly, Harris et al. [41] analyzed the surface topology variations of B_4C coatings. Changes in the surface's statistical properties such as asperity height are monitored for the 52100 steel counterface as the sliding distance increased. They found that the average abrasion rate of the steel balls decreased as the sliding distance increased, and obeyed a power law scaling relationship (**Figure 2. 8**). Because of their linear relationship in a log-log scale, it can be shown that A_n is given by

$$A_n = A_1\left(n^{1+\beta} - (n-1)^{1+\beta}\right) \qquad \textbf{Equation 2. 5}$$

where A_1 is the abrasion rate on the first cycle and β is the slope of the line in **Figure 2. 8.** The roughness of the steel surface decreased as the sliding distance increased after the first cycle. No material transfer was observed between the sliding counterfaces. Three regions of wear were identified--i) run-in, where the ball surface experiences significant

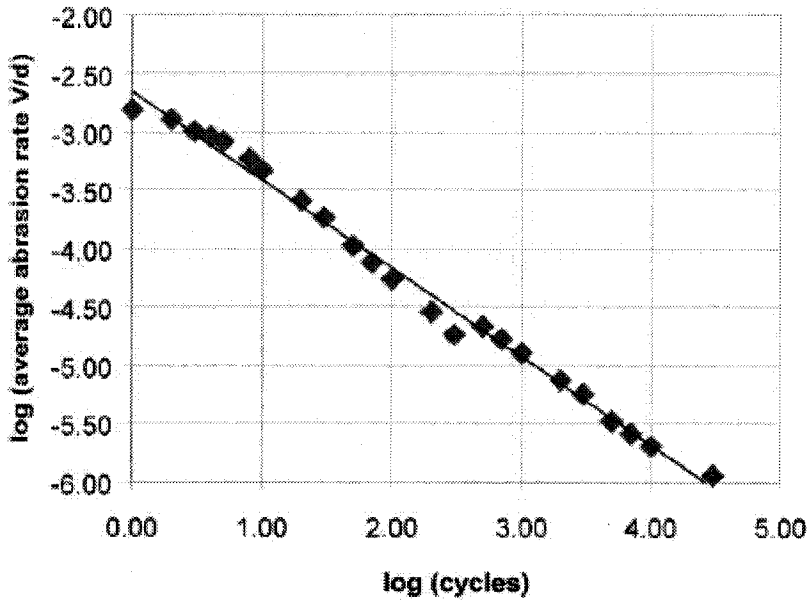

Figure 2. 8 Average abrasive rate vs. number of ball-on-disc cycles for the 52100 steel ball against B_4C coating. The line is a linear least square fit [41].

modification; ii) polishing, where the worn surface becomes stable; and iii) over run-in, where the run-in wear features reappear.

Harris et al. [42] published a follow-up paper that measured the abrasion rate of the 52100 steel under loads ranging from 5 to 1100 g and found that the average abrasion rate at and above 100 g of load showed a simple power law dependence on the number of cycles, but a deviation from this type of dependence was observed at lower loads (**Figure 2. 9**). The loss of the boron carbide's abrasiveness was correlated with a reduction of the asperity sharpness on the boron carbide surface, which eventually became nearly atomically smooth (R_a = 2nm) as shown in **Figure 2. 10**. No transfer of boron carbide coating onto the steel ball was detected during the entire test, while the transfer of iron onto the coating was observed by iron Auger map after 100 cycles--only to disappear after 500 cycles. Boron was detected in an oxidized form within the worn track on the coating after 500 cycles, but not after 100 cycles. The authors proposed that the process was a chemical–mechanical polishing in which the steel is mechanically abraded by the boron carbide, while the boron carbide is chemically polished by the steel.

Other factors that might influence the abrasiveness of B_4C carbide coatings have been studied, such as the load [43], contact conditions [44], coating thickness and roughness, substrate roughness [45]. Borodich et al. [43] proposed a model by solving a Hertzian type contact problem and the results were consistent with experiments conducted under loads of 5, 10, 20, 100, 500 and 1100 g. It was found

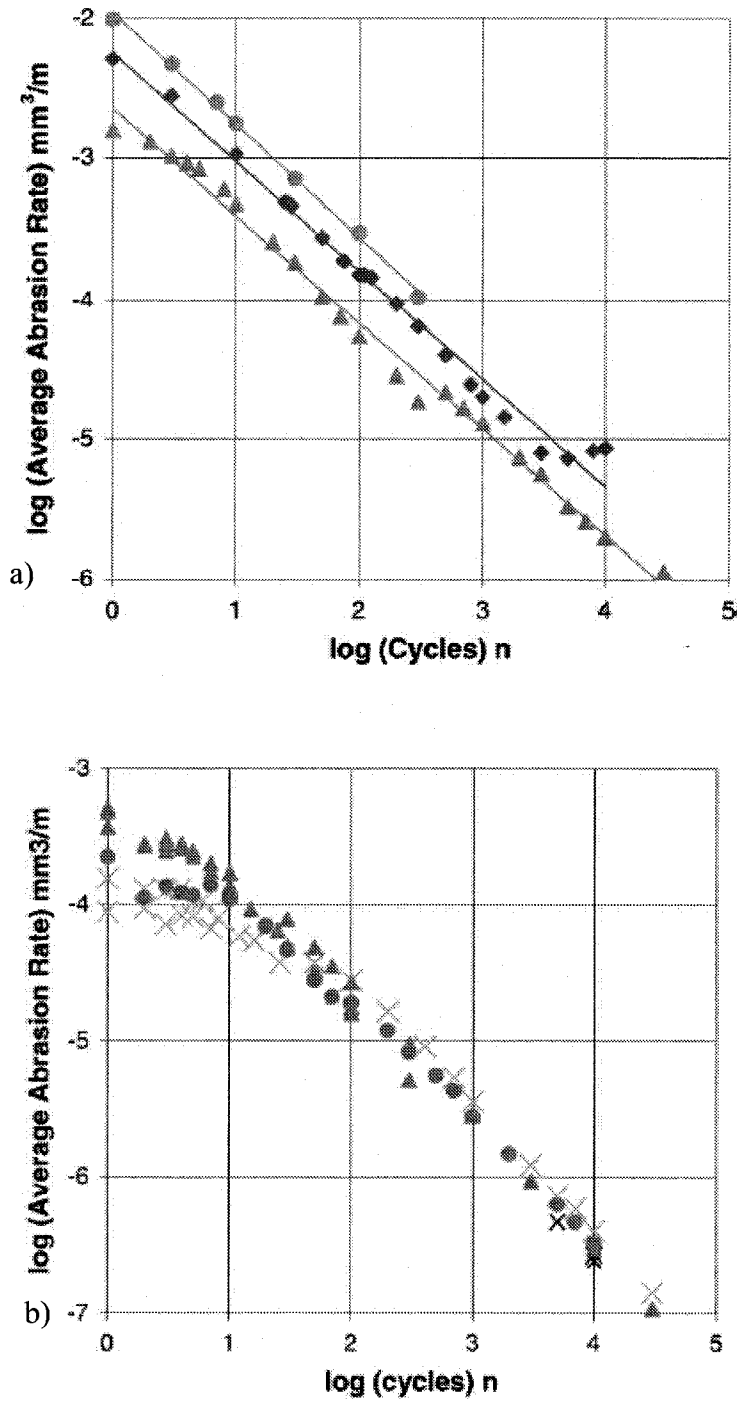

Figure 2. 9 Average abrasion rate as a function of number of cycles for loads of a) 100g (triangles), 500 g (diamonds), 1000 g(circles) and b) 5g (crosses), 10 g (circles), 20 g (triangles) [42].

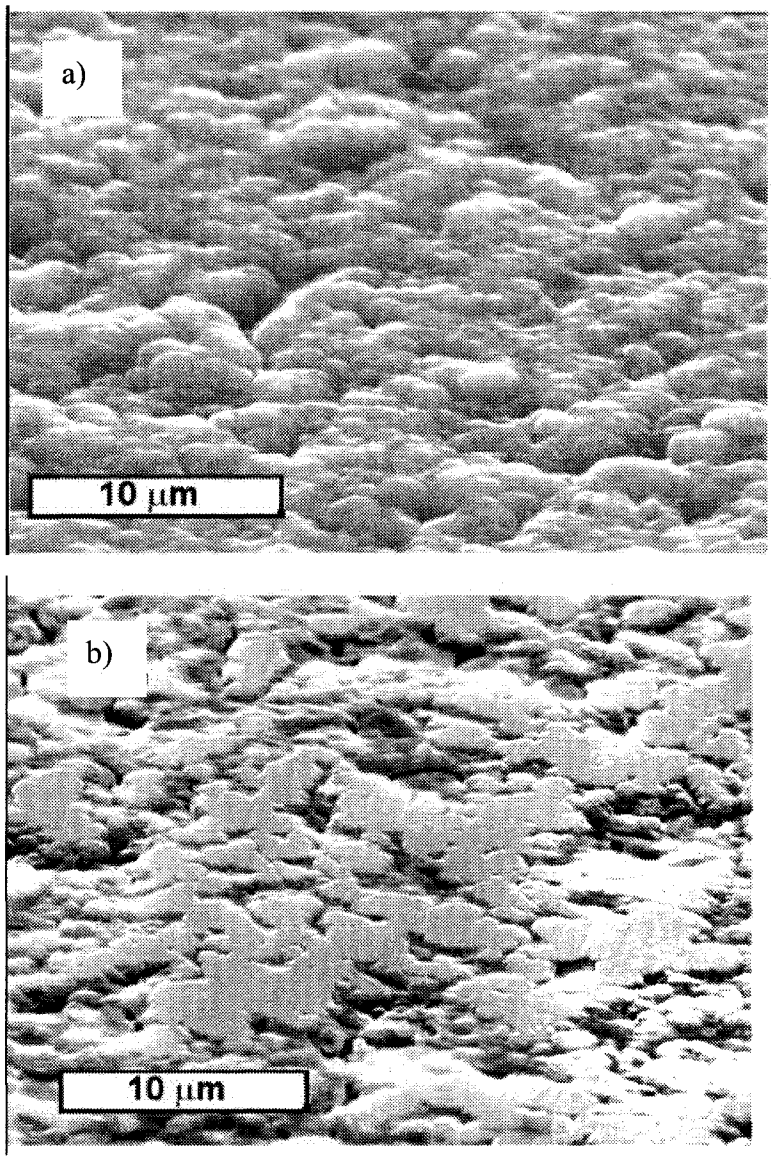

Figure 2. 10 SEM images of the **a)** as deposited B_4C surface and **b)** heavily worn surface after testing at 100 g load for 500 cycles against 52100 steel [42].

experimentally that a higher load only resulted in a higher initial (first cycle) abrasiveness (A_1) but had no effect on the rate at which the coating abrasiveness decreased. Their model predicted that A_1 should approximately scale as $(\text{load})^{2/3}$ and a depencence of $(\text{load})^{0.69}$ was observed in the experiments. The effects of the B_4C coating's contact condition on its abrasiveness were studied by Siniawsi et al. [44] by running experiments using various contact conditions--i.e. ball-on-disc, pin-on-disc and cone-on-disc--at the same load of 10 g. The results revealed that the rate at which the coating abrasiveness decreased was independent of the macro-scale contact conditions. Their study supported the classic Greenwood–Williamson model [46], which states that the number of micro-scale contacts and the total actual area of contact between two surfaces remain constant for a given load. Thus for a constant actual area of contact caused by the same load, the number of B_4C asperities within also remained constant, resulting in the same rate at which coating abrasiveness decreased regardless of macro-scale contact conditions.

Among all the factors studied, coating roughness alone was found by Siniawski et al. [45] to be capable of influencing both the initial abrasiveness of the coating and the rate at which the coating abrasiveness decreased. The average asperity radius of curvature ($\overline{R}$) was calculated for both the smooth coating (r.m.s. 10 nm) and rough coating (r.m.s. 330 nm) and the rougher coating had an initially smaller value of $\overline{R}$, indicating that the asperities were sharper—a fact that corresponded to a larger initial average coating

abrasiveness. The smoother coating, on the other hand, had an initially larger value of $\overline{R}$, indicating that the asperities were blunter--corresponding to a smaller initial average coating abrasiveness. For both coatings, $\overline{R}$ increased as the sliding cycle increased, indicating that the asperities became blunter as the sliding process progressed (**Figure 2.** 11). However, the authors provided no explanation as to why the rate at which the coating abrasiveness decreased was higher for the rough coating than the smooth coating.

A survey of the literature on the tribological behaviour of B_4C coatings thus suggests that the completed work was mostly conducted to obtain a better understanding of the abrasive interaction between a B_4C coating and a steel counterface material. The lubricating mechanism between a boron containing surface and steel has been clarified. However, for the purpose of tool coating development for the dry machining of aluminum alloys, it is essential to investigate the transfer and adhesion behaviour between the B_4C coating and Al alloy as well as the effect of influencing factors such as test temperature and environment on this material pair. No report on the tribological behaviour of the B_4C coating/Al pair has been published to take account of these factors. Thus the current study, which is aimed at understanding the friction and wear of B_4C at elevated temperatures and various environments, is fully justified.

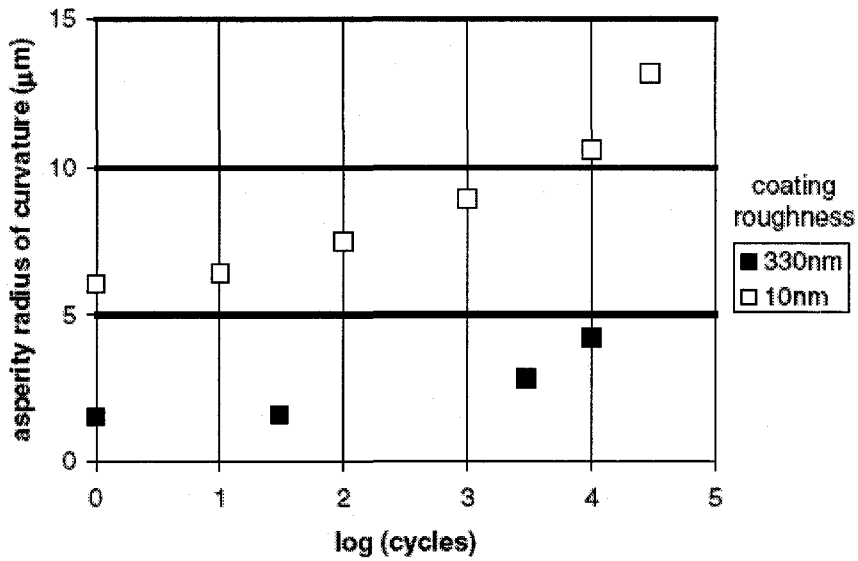

Figure 2. 11 Average asperity radius of curvature for the two coating roughness values as a function of sliding circles. The increasing trend of the curves indicated the coatings became blunter as the sliding cycles increased [45].

2.2 Review of the Literature on the Tribological Behaviour of the Diamond-like Carbon Coatings

2.2.1 Hybridisation States of Carbon

The term Diamond-Like Carbon (DLC) generally refers to a metastable form of amorphous carbon containing a significant fraction of sp^3 bonds mixed with sp^2 bonds. Carbon exists in a great variety of crystalline and disordered structures because of its three hybridisations: sp^3, sp^2 and sp^1 (**Figure 2. 12**) [47]. In the sp^3 configuration, a carbon atom's four valence electrons are each assigned to a tetrahedrally directed sp^3 orbital, which makes a strong σ bond to an adjacent atom. Diamond consists of 100% sp^3 hybridised carbon atoms and its extreme physical properties derive from this type of strong and directional σ bonds. In the three-fold coordinated sp^2 configuration, three of four valence electrons enter triagonally directed sp^2 orbitals, which form σ bonds in a plane. The fourth electron of the sp^2 atom lies in a π orbital, which sits normal to the σ bonding plane. This π orbital forms a weaker bond with a π orbital on one or more neighbouring atoms. As another most common allotrope of carbon, graphite is formed by sp^2 hybridized atoms and inherits its strong intra-layer σ bonding and weak van der Waals bonding between its layers from this bonding structure. These basal planes of graphite can align themselves parallel to the direction of relative motion and slide over one another with relative ease, thus providing low friction and the strong interatomic bonding and packing in each layer is thought to help reduce wear in the presence of water

in the atmosphere [48]. In the sp^1 configuration, two of the four valence electrons enter σ orbitals, each forming a σ bond directed along the ±x-axis, and the other two electrons enter π orbitals in the y and z directions.

2.2.2 Introduction to DLC Coatings

The first hard amorphous carbon coatings were deposited by a carbon ion beam produced in an argon plasma onto room temperature substrates by Aisenberg and Chabot [49]. Following their work, explosive growth has occurred in this field over the past three decades and now the expression "DLC" subsumes a variety of coatings with ranging composition and properties. The structure of these coatings can be interpreted as a random network of covalently bonded carbon in hybridized tetragonal (sp^3) and trigonal (sp^2) local coordination. The compositions of the various forms of amorphous C-H alloys can be displayed on a ternary phase diagram as in **Figure 2. 13** [47]. There are many amorphous carbons with disordered graphitic ordering--namely soot, char, glassy carbon and evaporated amorphous carbon. These are located in the lower left corner of **Figure 2. 13**. The two hydrocarbon polymers--polyethylene ($(CH_2)_n$) and polyacetylene ($(CH)_n$)--define the limits of this triangle in the right corner beyond which interconnecting C-C networks cannot form, and only linear polymer molecules develop. The open literature tends to favour the nomenclature of DLC coatings used by Grill [50]. In this system, the "DLC" term is commonly used to designate the hydrogenated form of

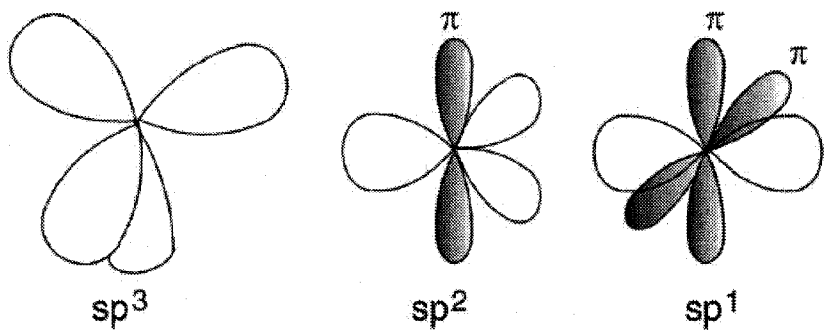

Figure 2. 12 The sp^3, sp^2 and sp^1 bonding of carbon [47].

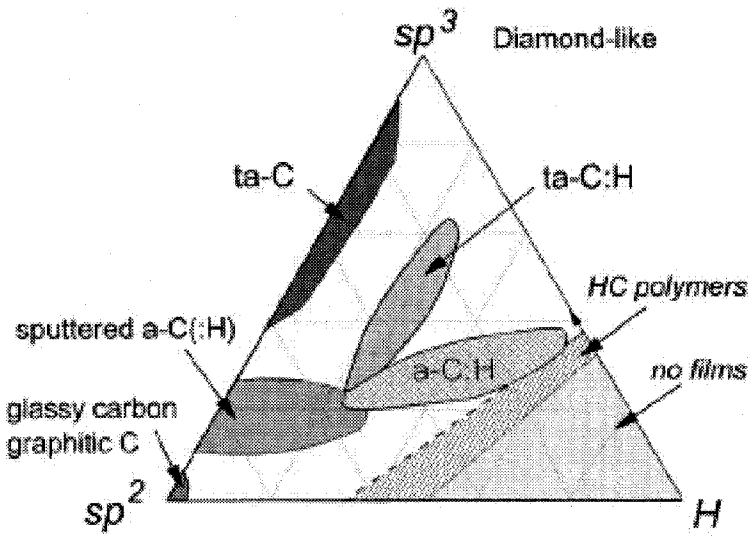

Figure 2. 13 Ternary phase diagram of bonding in amorphous carbon-hydrogen alloys [47].

diamond-like carbon (a-C:H), which contains up to approximately 50 at.% hydrogen with sp^3 fractions smaller than 50%, while the ''ta-C'' (tetrahedral carbon) term is used to designate the non-hydrogenated carbon (a-C), which contains less than 1 at.% hydrogen with sp^3 fractions up to 85% or more. An overlap of these two major sub-categories of diamond-like amorphous carbon--both in hydrogen content and sp^3 fractions--is represented by the term "ta-C:H", although it is seldom used in literature. For simplification, H-DLC is used to denote hydrogenated DLC, and NH-DLC represents non-hydrogenated DLC in this work.

The structure and properties of a DLC coating depend on the deposition technique and the parameters used during deposition. The commonly used techniques to deposit DLC coatings are i) DC/RF magnetron sputtering, which is the most common industrial process for the deposition of DLC [51-55], ii) plasma enhanced chemical vapour deposition (PECVD), which is a popular laboratory method [56-57], iii) ion beam deposition [49], iv) arc ion plating [58] and v) pulsed laser deposition (PLD) [59-60]. These deposition techniques share a common feature--specifically that ions containing carbon are generated and condensed on the substrates to form coatings. The methods used to produce deposition species, and the plasma characteristics do differ significantly. In DC/RF magnetron sputtering, carbon ions are formed during the sputtering of the graphite target by argon ion plasma while the substrate can be either biased or just grounded, which results in a difference in the driving force on the ions towards the

substrate. Hydrocarbon species are produced by the plasma decomposition of hydrocarbon gases (e.g. acetylene) and then accelerated towards a DC-biased substrate in the PECVD processes. Ion beam methods are characterized by ion sources which produce carbon ions from methane while a vacuum arc discharge between a graphite cathode and grounded anode is utilized to generate energetic carbon ions in an arc ion plating process. Pulsed laser deposition vaporizes carbon targets using pulsed excimer lasers to form intense plasmas, which then extends towards the substrate. A comprehensive reference on the deposition techniques is available [61].

Studies report that sp^3/sp^2 ratio in the deposited coatings are in the decreasing order for arc ion plating, pulsed laser deposition, ion beam deposition, plasma-enhanced chemical vapour deposition, and DC/RF magnetron sputtering [62-63]. The common feature of these techniques is that the deposition is energetic--i.e. carbon species strike the substrate with an energy significantly greater than that represented by the substrate temperature. Particles with excessive energies are then subjected to rapid thermal quenching, resulting in amorphous DLC coatings characterized by high hardness, high elastic modulus and high internal stresses.

The mechanical properties mentioned above directly correlate with the fraction of sp^3 C in the coatings. Compilations of the mechanical properties of DLC coatings show that the hardness of H-DLC coatings is in the range 10-30 GPa, with a corresponding elastic modulus 6-10 times higher. The coatings are characterized by internal compressive

stresses in the range 0.5-7 GPa. Due to their higher sp^3 C fraction, the hardness of NH-DLC can reach higher values (in the range of 40-80 GPa), and their elastic modulus can reach values up to 900 GPa--but the residual stress can also reach high values, up to 13 GPa [47][50]. The stresses in DLC coatings can be reduced by either incorporating N, Si, O or metals in the coatings [64-66] or by building multilayered structures with both soft and hard layers [67-68]. Such coating composition and structure modification has resulted in families of DLC coatings known as doped/nanocomposite DLC coatings and multilayer DLC coatings.

DLC coatings are most widely used to exploit the low friction coefficients and high wear resistance of these materials. Many efforts have been made to characterize the tribological behaviour of various types of DLC coatings. The friction and wear characteristics of these coatings depend strongly on both intrinsic factors, such as coating composition and structure (sp^3/sp^2 ratio, hydrogen content, etc.) and external conditions, such as varying test environments (test temperature, humidity level, gaseous species present in the test atmosphere, etc.). The following sections provide a detailed account of previous studies on the tribological behaviour of the various types of DLC coatings and the influencing factors.

2.2.3 Transfer Layer Formation and Friction-induced Graphitization

Summarizing the tribological properties of various DLC coatings is difficult because of the generally poor definition of deposition conditions of a specific coating. The

challenges of structurally characterizing the amorphous materials and the lack of any standardization of tribological characterization are the other major difficulties. In most cases observations suggested that the tribological behaviour of DLC appears to be controlled by a transferred layer formed during the sliding of the surfaces in contact. This layer generally is a mixture of both materials from the coating and its counterface and interacts with the gaseous species within the sliding environments. The easy shearing of this interfacial layer is the most frequently quoted mechanism for the low COF and wear rates of the DLC coatings [69-78].

Ronkainen et al. [69] studied the effect of tribofilm formation on the tribological performance of a H-DLC coating (~26 at.% hydrogen) deposited by RF PECVD from methane on AISI 330 B steel substrates. Pin-on-disk tests were performed at room temperature at RH = 50±5%. The applied load was varied from 5 to 40 N, and the sliding velocities were 0.1-3.0 m/s. The COF of DLC against both steel and alumina was found to decrease with increasing load and speed. This behaviour correlated with the observed formation of a transfer layer on the pin surface, consisting mainly of pin material oxides. Carbon appeared only in the debris found in the front of the contact area and its content increased with increasing load and sliding velocity, producing the low friction coefficients. Evidence of carbon enrichment on the pin surface was also detected, although the amount of carbon was rather low. The carbon formed a low shear strength surface layer on the sliding surface--suggesting that the low coefficient of friction is

caused by a combination of a tribolayer containing stable oxide and a low shear strength carbon layer.

Erdemir et al. [70] studied the tribological behaviour of H-DLC coatings deposited by a methane ion beam on substrates of Ti6A14V. Pin-on-disk experiments showed that the films had low COFs ($\mu < 0.1$). This frictional response was characterized by an initial break-in period followed by an intermediate constant friction stage (COF ~0.05, **Figure 2. 14**). The presence of a carbon transfer layer was observed on the wear scars of the pin surfaces. Transmission electron microscope images and electron diffraction patterns from the transfer layer indicated that it contained a distribution of fine graphite nanoparticles (<5 nm) in a distorted diamond-like structure. Micro-laser Raman spectroscopy showed that the transfer layer had a disordered graphite structure different from the original DLC film. Raman spectra taken from the wear track of the DLC film also revealed evidence for graphitization (**Figure 2. 15**). It has been shown that a typical DLC Raman spectra are composed of two main peaks located at about 1540 cm^{-1} (G band) and about 1360 cm^{-1} (D band) respectively. The G band has been assigned to the graphitic sp^2-bonded carbon and the D band to the disordered graphitic phase and sp^2 sites [47]. As the sp^3/sp^2 ratio decreases in the H-DLC coating, the G band will shift positively accompanied by an increase of the intensity of the D band [79]. **Figure 2. 15** makes it evident that the G peak of the material within the wear track (after 1000 m of sliding at room temperature under

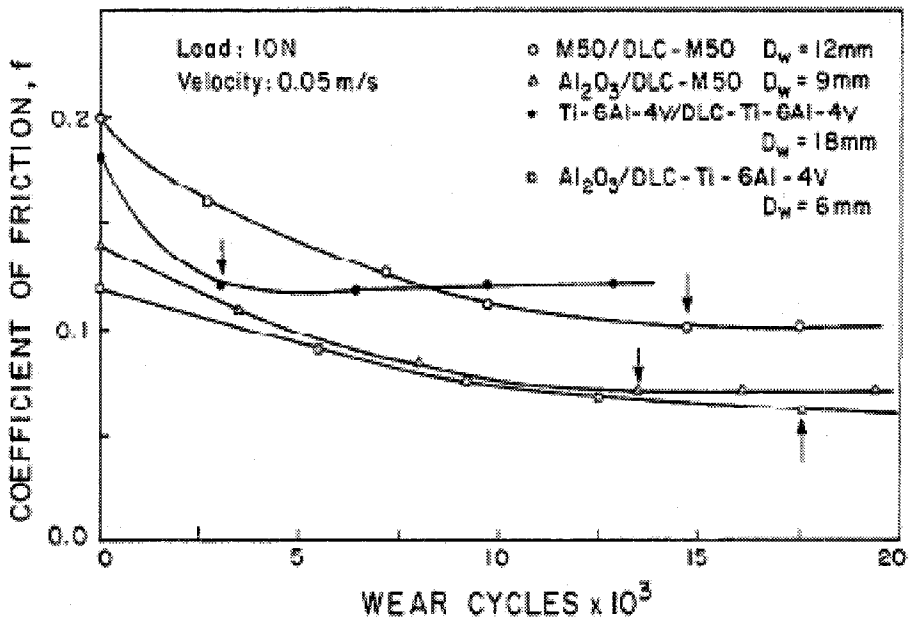

Figure 2. 14 Variation of the coefficient of friction as a function of number of wear cycles. The arrows indicate the end of the break-in stage. (D_w denotes the wear track diameter) [70].

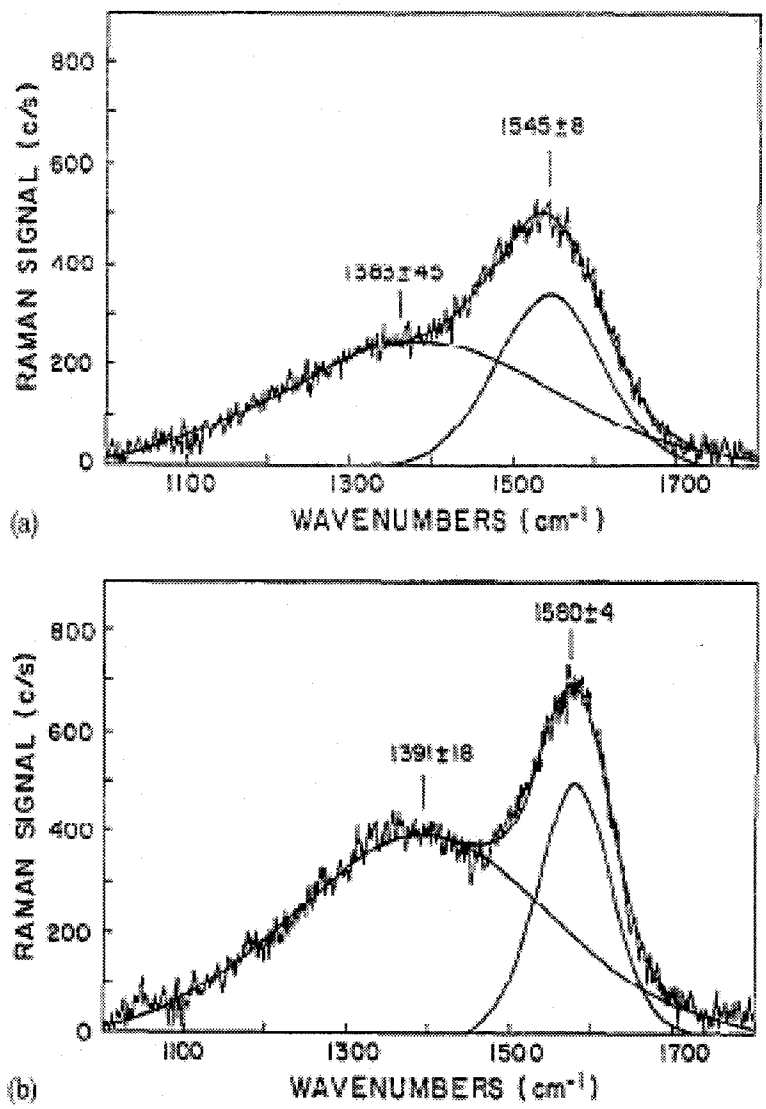

Figure 2. 15 Typical Raman spectra taken from **a)** as-deposited DLC film and **b)** wear track region after testing. (Wear testing conditions: M50/DLC-M50, 10 N load and 1 km sliding distance.) [70]

5N, 0.05 m/s and 30% RH) was shifted to higher frequency and coincided with G peak of graphite (1580 cm^{-1}). There was also a significant increase in the intensity of the low frequency peak due to the contribution from D band graphite. In light of these observations, the intermediate friction stage was mainly attributed to the formation of the transfer layer. During experiments with long durations, a further reduction in friction was observed--a steady- state low friction of 0.02-0.03 and ultra-low wear rate of about 1.6×10^{-9} $mm^3/(Nm)$ (calculated from the cross sectional surface profiles of the wear tracks) were reached. The steady-state low friction was related to the complete transformation of diamond-like to graphite-like carbon by a friction-induced annealing.

Liu and Meletis [73] also presented evidence of the graphitization of DLC coatings during dry sliding. They conducted pin-on-disc tests on H-DLC coatings deposited on Ti-6Al-4V substrates at room temperature by methane ion-beam deposition against Ti-6Al-4V pins in ambient air (about 30% RH). For the as-deposited DLC coating, the debris from the wear track region and the transfer film present on the pin counter surfaces were examined by a transmission electron microscope (TEM). The TEM diffraction pattern of the as-deposited coating revealed an amorphous structure with medium-range sp^3 domains while the debris exhibited a distorted DLC coating structure as well as a graphite structure. Small graphite particles (0.5-1.0 nm) were found to form clusters within the transfer film. The authors attributed this particular cluster formation to friction-related effects of heat and strain. The authors concluded that friction-induced

graphitization occurred during sliding. They suggested that the transformation proceeds with a precursor hydrogen atom release stage and shear deformation that converts the $(111)_{DLC}$ into $(002)_{GRAPHITE}$ planes, facilitating the nucleation of graphite, which is supported by the fact that $(111)_{DLC}$ and $(002)_{GRAPHITE}$ planes have identical atomic arrangements with only a slight difference in atomic spacing (0.257 nm for $(111)_{DLC}$ and 0.246 nm for graphite). The low friction observed was attributed to the low shear strength of the hexagonal graphite planes.

The effects of sliding speed and applied load on the friction and graphitization behaviour of ion beam (methane) deposited H-DLC coatings were studied by Liu et al. [74] by performing pin-on-disc tests against ZrO_2. The sliding speed was varied from 0.06 to 1.6 m/s and the applied load was in the range of 1 to 10 N--resulting in a decreased COF and DLC coated disc wear with the increase in sliding speed and applied load. The steady-state COF was 0.18 at a sliding speed of 0.06 m/s and an applied load of 1N, whereas the COF dropped to 0.05 when the sliding speed and load were increased to 1.6 m/s and 10 N. The authors believed that the combination of low sliding speed and applied load was not enough to promote graphitization--a necessary phenomenon for achieving a low steady-state COF. It was also suggested that a higher sliding speed facilitates the hydrogen release from the DLC structure by increasing the temperature at the contact asperities (flash temperature over 1000 °C were predicted for their system). The applied load was thought to shear and transform the DLC layer into graphite after

hydrogen release.

Scharf and Singer [75] developed an in situ Raman tribometer to study the friction behaviour of amorphous diamond-like nanocomposite (DLC) coatings containing four elements C, H, Si, O deposited by plasma-enhanced chemical vapour deposition. The tests were conducted in a reciprocating configuration at normal loads of 6.4 and 23.9 N against sapphire balls in either dry (~4% RH) or humid (~40% RH) air at room temperature. They observed that a transfer film quickly formed on the sapphire surface and the tribosystem exhibited very low COF values in the range of 0.03-0.05. They identified several processes including thickening, thinning and loss of the transfer films. They correlated observed friction instability to transfer film loss. The in-situ Raman spectra showed that the graphitic peak intensity of the transfer film increased as the sliding process proceeded compared with the as-deposited coating, which was evidence of coating graphitization and transfer film thickening (**Figure 2. 16**).

Sanchez-Lopez et al. [76] studied the structural changes that occurred during the dry sliding of DLC coatings with different hydrogen contents (H/C ratio varied from 0 to 10 in the precursor gases) against uncoated 52100 steel balls under 10 N load with a sliding speed of 0.1 m/s for a distance of 500 m. Examination of the transfer layers on the counterface material by Raman spectroscopy indicated the presence of a disordered graphite-like structure and diamond-like structure for the hydrogenated DLC coatings and the non-hydrogenated coating respectively. The transfer layer, however, was found to be

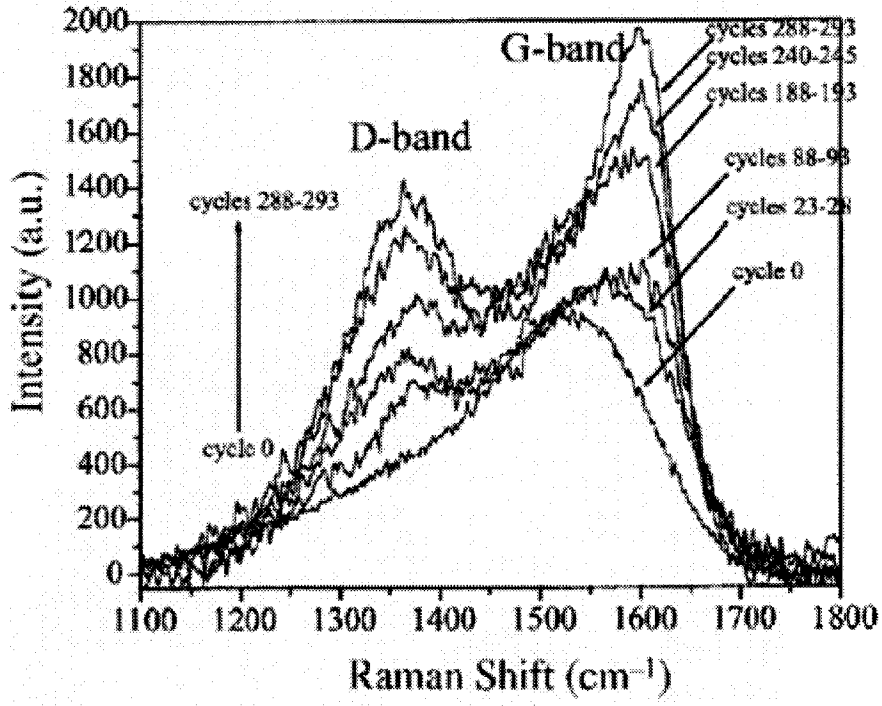

Figure 2. 16 In situ Raman spectra versus sliding cycles for DLN coating at low contact stress (0.7 GPa) in ~40% RH air [75].

amorphous just like the as-deposited coating by TEM and electron diffraction. The authors concluded that these graphitic regions must be smaller than 2 nm since they could not detect any of the typical features of nanocrystalline graphite by TEM and electron diffraction.

Konca et al. [78] tested NH-DLC (1 at.% H) in inert atmospheres (vacuum of 6.65×10^{-4} Pa, argon, helium and nitrogen), ambient air (47% RH) and a 60% He-40% H_2 mixture (referred to as "hydrogen" hereafter in the text) using a pin-on-disc configuration under a constant load of 5N and a sliding speed of 0.12 m/s against a 319 Al alloy. The average COF values of the NH-DLC coating were found to be in the range of 0.56-0.74 and the recorded COF values never went below 0.4 in inert gases. A significant amount of wear of the NH-DLC coating occurred in all the tests conducted in the inert atmospheres. The average COF value dropped to 0.12 when the test was conducted in ambient air. The lowest average value (0.03) for the studied NH-DLC coating was observed when the test was performed in hydrogen environment. The COF curve recorded during sliding in this condition featured a very low and steady COF regime of 0.010-0.016. A carbonaceous transfer layer was observed by SEM after testing in hydrogen, which was correlated to the very low COF exhibited by the coating. Micro-Raman investigation revealed that both the wear track produced in hydrogen and the transferred film on the corresponding pin tip contained carbon that was more graphite-like than the original coating (**Figure 2. 17**). The authors attributed this change

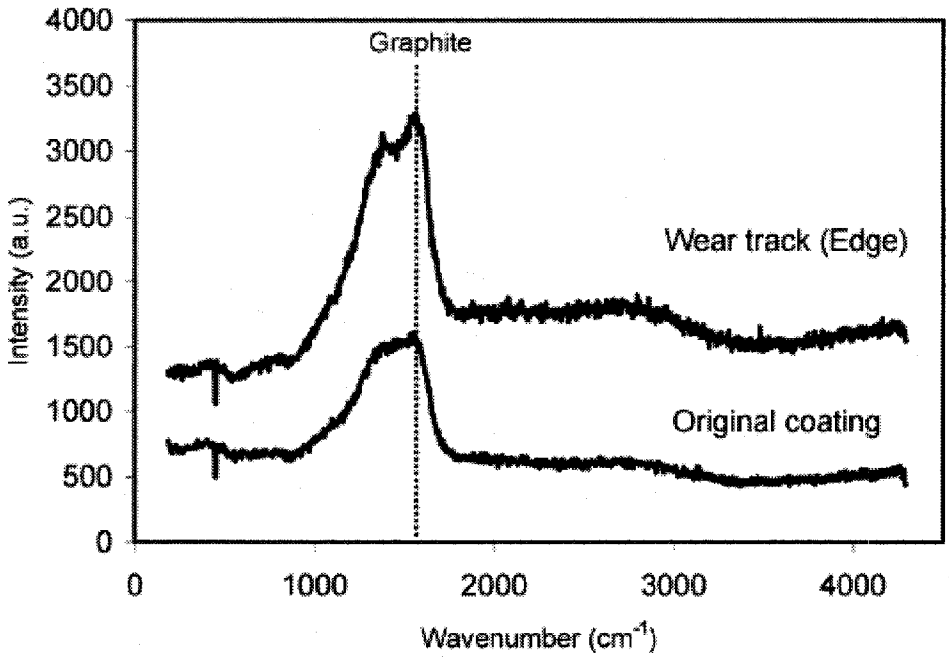

Figure 2. 17 Micro-Raman spectra of the worn and unworn regions of the non-hydrogenated DLC that was run against the 319 Al alloy in hydrogen [78]. The increase in the peak intensity around 1370 and 1550 cm^{-1} was correlated to friction-induced graphitization by the authors.

to the friction-induced graphitization of the coating.

2.2.4 Effect of Hydrogen Content of the DLC Coatings

A compilation of COFs of DLC coatings recorded for room temperature tests has shown that the COF values span a range of 0.007-0.8 in vacuum ($P < 10^{-4}$ Pa), while in ambient air at 20% < RH < 60% they span a range of 0.05-0.7 with ranges between 0.007 and 0.02 in vacuum and between 0.1 and 0.4 in ambient air being most typical [80-86]. The large spread in friction coefficient values is mainly caused by variations in the hydrogen contents of the coatings. Several studies have shown that the presence of a sufficient amount of hydrogen in a DLC coating is the most critical intrinsic factor determining its tribological behaviour in various environmental conditions [81-83]. For example in vacuum, the DLC coatings containing a large amount of hydrogen (~40 at.%) have very low COF values (0.007-0.02) [81][83][85]. On the other hand, the non-hydrogenated DLC coatings (< 5 at.%) exhibit high COF values (0.5-0.8) in vacuum [83][86]. It is generally agreed that the high COF of the non-hydrogenated DLC coatings in vacuum is due to the strong interactions between the "dangling bonds" of surface carbon atoms and the counterface materials [83][85-86]. For the hydrogenated DLC coatings, hydrogen prompts the formation of C-H bonds and hence passivates the dangling carbon bonds on the DLC surfaces, resulting in a low COF in vacuum [83][87-88].

Erdemir [81][87] studied the effects of hydrogen on the tribological properties of diamond-like carbon films by measuring the friction coefficient of DLC coating against itself. PECVD deposited hydrogenated DLC coatings were produced with varying

hydrogen to carbon (H/C) ratios up to 10 by varying the source gases (i.e. C_2H_2, C_2H_4, CH_4 and CH_4+H_2). An arc-PVD method was then employed to deposit non-hydrogenated DLC coatings. The coatings were applied to both AISI-H13 steel disks and M50 steel balls and tested in a ball-on-disc configuration under 10 N (sliding velocities of 0.3-0.5 m/s) in both dry nitrogen and open air. They reported an almost direct relationship between the H/C ratios of the source gases and the friction and wear coefficients of the resultant DLC coatings in nitrogen. The COFs of the coatings grown in source gases with very high H/C ratios (e.g. 10) were very low (0.003), whereas the COFs of the hydrogen-free DLC coatings (with essentially zero H/C ratio) was very high (0.65). The COFs of coatings grown in source gases with intermediate H/C ratios were between 0.003 and 0.65 (**Figure 2. 18**). Experiments also revealed that the frictional properties of these coatings were very sensitive to testing environments. Specifically, when tested in open air, the COF of hydrogen-free DLC dropped to 0.25, whereas that of highly hydrogenated DLC increased to 0.06. The very low friction of the coatings produced with a high H/C ratio of the source gas was attributed to the presence of excessive hydrogen within the coating. It was suggested that hydrogen atoms--either bonded to carbon or in the form of interstitials-- eliminated strong covalent and π–π^* interactions at sliding DLC interfaces and provided shielding of carbon atoms by di-hydration (i.e. two hydrogen atoms bonded to one carbon atom).

Donnet and his colleagues [83][89] showed that hydrogen in the testing environment could help hydrogenated DLC coatings (34 and 40 at.% H) reach very low COFs. The authors investigated the friction behaviour of hydrogenated DLC coatings deposited by PECVD. Tests were performed against 52100 steel pins using a reciprocating sliding

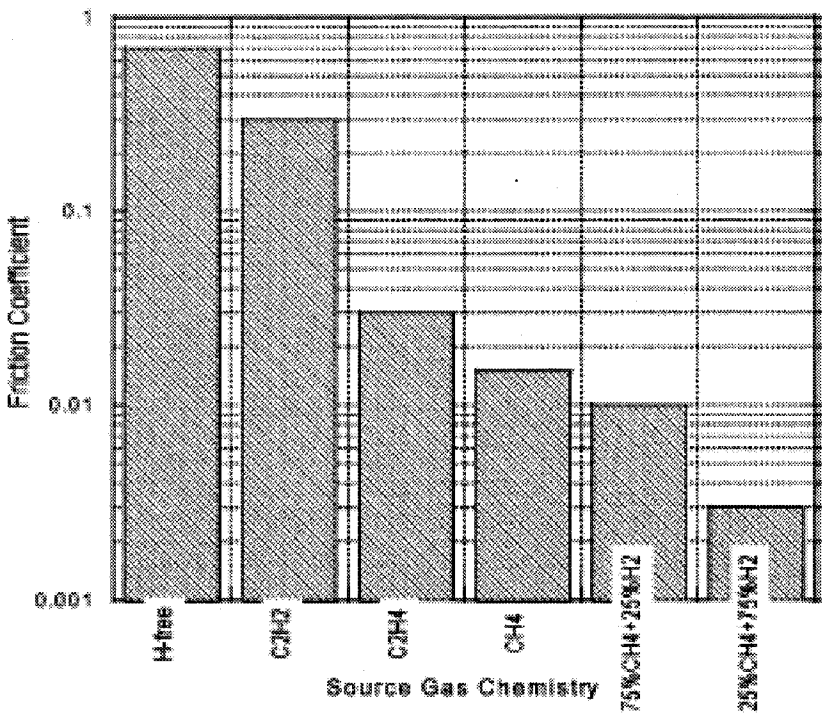

Figure 2. 18 Relationship between friction coefficients of DLC films and hydrogen-to-carbon ratios of various source gases used to deposit the films [81].

machine under vacuum (10^{-9} hPa), hydrogen and argon environments at 25 and 150 °C. In vacuum, the DLC coating with the lower hydrogen content (34 at.%) exhibited a low COF of 0.01 for the first 100 cycles--after which the COF increased to 0.6, whereas the coating with the higher hydrogen content (40 at.%) maintained a low COF of 0.03 throughout the test. When the DLC with lower hydrogen content (34 at.%) was tested under a hydrogen gas pressure of 1000 Pa, the COF did not increase as it did under vacuum--only reaching 0.006 by the end of the test. The friction behaviour at a lower hydrogen pressure of 100 Pa, however, was similar to that observed during the vacuum test as the COF increased to a high value of 0.6 after a short, very low COF period. Repeating the same test at 150 °C resulted in an even lower COF value of 0.002 at the end of the test. The authors concluded that a very low COF could be attained only when there is enough hydrogen (either provided by internal or external sources) at the sliding interface and that the lower COF caused by the elevation of the testing temperature is due to the more profound thermal-assisted diffusion of hydrogen towards the sliding surface.

The presence of hydrogen in a carbon bonding network has also been found to influence the chemical affinity of carbon atoms toward aluminum atoms. Qi and Hector [90] used a first principles methodology based on density function theory to calculate the work of separation (W_{sep}) between Al/clean reconstructed diamond and Al/H-passivated diamond surfaces. The W_{sep} of the former interface was found to be 4.08 J/m^2 and the latter was 0.02 J/m^2. Electronic structure analysis revealed strong covalent bonding

between Al and C, but no bonds exist between Al and the H-passivated diamond surface. The work required for the decohesion of aluminum was computed to be 1.56 J/m^2, less than the W_{sep} between Al/clean reconstructed diamond. Thus under uniform tensile strain, the clean Al/diamond interface fractured within the Al slab at 12 GPa, with two layers of Al transferring to the diamond surface. The Al/H-terminated diamond interface separated at the interface under 0.4 GPa with no adhesive transfer. Such results were in general agreement with their observation that Al adhered to a clean diamond surface, but not to H-passivated diamond.

2.2.5 Effect of Test Environment on the Tribological Behaviour of DLC Coatings

DLC coatings have demonstrated high sensitivity to water vapour in the environment [86][91-92], which depends on hydrogen content of the coatings (as described in the previous section). Under most environmental conditions, hydrogenated DLC coatings show lower COF values than hydrogen-free DLC coatings. Interestingly, high humidity increases the COFs of the hydrogenated DLC coatings while decreasing those of the hydrogen-free DLC coatings. The increase in the hydrogenated DLC's COFs caused by increasing humidity has been ascribed to the progressively strong bonding of hydrocarbons [93] or H atoms [94] at the surface--a phenomenon that causes viscous drag and even the formation of capillary forces between the sliding surfaces. The inhibition of wear-induced graphitization mechanisms by adsorbed water molecules has also been proposed as the cause [95]. The low COF at high humidities seen in non-hydrogenated

DLC coatings has been attributed to the passivation of the dangling carbon π bonds by adsorbed water molecules, as well as the graphitic nature of the transfer layer that results in a tribological behaviour comparable to that of graphite--which is known to require the presence of adsorbable species such as water to provide lubrication [86].

Konca et al. [80] studied the tribological behaviour of non-hydrogenated DLC coatings (2% H) deposited by unbalanced magnetron sputtering deposition in both vacuum (1.07×10^{-2} Pa) and ambient air (52% RH) using pin-on-disc tests against a 319 Al alloy (the same alloy studied in the current work). The tests were conducted under a combination of 4.9 N load and 0.12 m/s sliding speed. The coatings displayed a high COF of 0.52±0.06 and high wear rates (4.05×10^{-4} mm^3/m) in vacuum when compared to ambient air (for which COF = 0.16±0.04, wear rate = 4.05×10^{-4} mm^3/m were obtained). In a specific experiment, the test was started in ambient air and then the test chamber was pumped down later during the course of sliding and the COF decreased from 0.15 to very low values (0.006-0.02) with the decreasing pressure (from 10^5 Pa to 1.07×10^{-2} Pa)--keeping its low value for some period of time. These were the lowest COF values recorded for HN-DLC. Finally, the COF increased to values typically encountered in straight vacuum tests (COF = 0.50-0.80). It was observed that increasing the duration of ambient air running-in increased the duration of the very low COF regime under vacuum. The authors suggested that the causes of the subsequently observed very low COF regime in vacuum were the creation of C–H bonds containing an easy-shear tribolayer on the

contact surface of the pin during the ambient air running-in period. The passivation of the coating surface by the desorption of residual water molecules on the chamber wall (adsorbed during ambient air running-in) during the vacuum test helped to maintain low COF.

Miyoshi [96] studied the tribological behaviour of hydrogenated DLC coatings (44.4 at.% H) deposited by the PACVD method under different power densities. A low COF of 0.1 was observed when testing occurred in nitrogen rather than in air with 40 % RH (COF = 0.2). The DLC coating deposited at 300 W power density was annealed at 700 °C in vacuum and the test was repeated. The resulting behaviour of the annealed coatings resembled that of the non-hydrogenated DLC coatings: the COF in air was initially lower than in nitrogen. The author attributed this observation to the formation of a graphitic top layer on the coating surface during annealing. However, as the test continued the COF in air increased and became equal to the value for the as-deposited coating--suggesting that the friction behaviour of the DLC coatings was dependent on the mechanical and chemical interactions between the sliding pairs and the testing environment.

Andersson et al. [86][92] demonstrated the varying effects of water vapour pressure on the friction behaviour of NH-DLC and H-DLC (39 at.% H) coatings by conducting self-mating tests using a ball-on-flat configuration under a normal force of 1 N and velocities in the range of 0.025 and 0.075 m/s for approximately 100 revolutions. The COF values for the NH-DLC and H-DLC coatings tested in vacuum (5×10^{-6} Pa) were 0.6

and 0.01, respectively. When water vapour was introduced into the test chamber, however, the DLC coatings exhibited opposite COF value trends. Specifically, the COF of the NH-DLC coatings decreased from 0.6 in vacuum to ~0.2 at 3 Pa of water vapour pressure and further to 0.07 at 2000 Pa of water vapour pressure. In contrast, the COF of the H-DLC coatings increased from 0.01 in vacuum to 0.035 at 460 Pa of water vapour pressure and further to 0.08 at 2000 Pa of water vapour pressure. The difference in the friction behaviour of the coatings under the influence of water vapour pressure is summarized in **Figure 2. 19**. The authors suggested that the decreasing COF of the NH-DLC coatings was caused by the passivation of dangling carbon bonds on the coating surface by adsorbed water molecules. The increase in the COF of H-DLC was attributed to the dipole-like interactions between the counterfaces induced by adsorbed water vapour.

DLC coatings are sensitive to the presence of oxidizing species (oxygen, water vapour) during sliding [97]. Donnet et al. [98] studied the respective role of oxygen and water vapour on the tribology of hydrogenated DLC coatings (42 at.% H). Within the pressure range they studied (vacuum to 6000 Pa), oxygen had no significant effect on the COF value (0.01) of the DLC coatings while the testing with water vapour revealed an increase in COF from 0.01 to 0.1 as the water vapour pressure increased from zero to 500 Pa. The authors attributed the change in the COF to the thickness of the carbonaceous

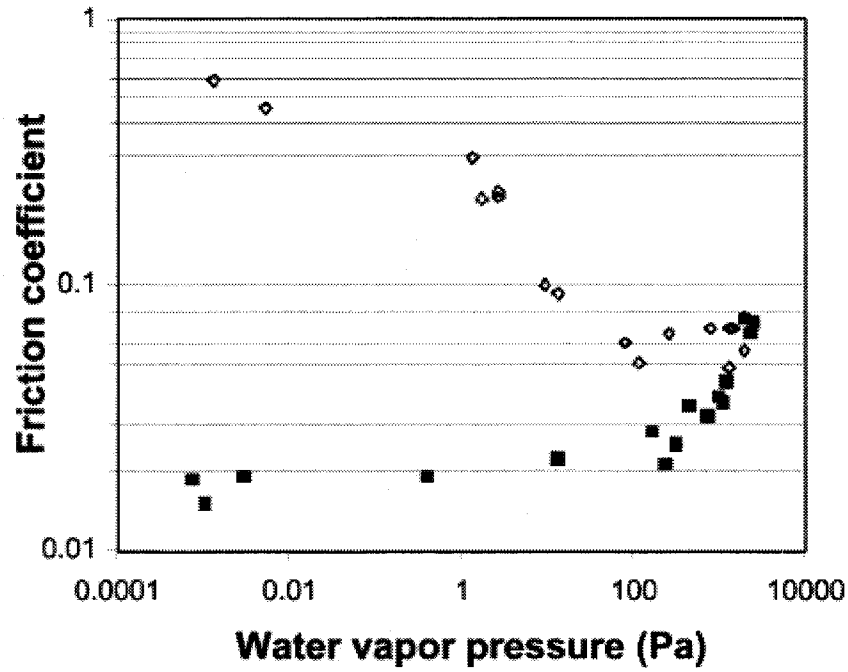

Figure 2. 19 Summary of frictional behaviour of NH-DLC (open diamonds) and H-DLC (full squares) as a function of water vapour pressure [92].

transfer film formed on the counterface material (steel). A considerable amount of transfer film) had formed under vacuum, and this became thinner as the water vapour pressure increased. It follows that water vapour affects the kinetics of the formation of this carbonaceous transfer layer by preventing the accumulation of more transferred material from the original coating.

Kim et al. [84] performed friction measurements on a hydrogenated DLC film in ultra-high vacuum (UHV with a base pressure of $\sim 1\times10^{-11}$ Pa) using self-mating ball-on-flat tests to investigate its intrinsic friction properties without the effects of environmental impurities--a state achieved by rigorously controlling the testing environment. They exposed the coating to systematically varying vapour pressures of H_2O, O_2, and N_2 to understand the nature and extent of the effect that each gas had on the coatings' friction. The results showed that the COFs in the low-pressure regime (from $\sim 1\times10^{-11}$ to 1.33 Pa) were extremely low (~ 0.004) and no notable change was observed for H_2O vapour pressures up to approximately 1.33 Pa. At about 1330 Pa of water vapour pressure, the COF of the coating reached approximately 0.07. The effect of O_2 on the hydrogenated DLC friction showed the same trend. At 19950 Pa--the oxygen vapour pressure in ambient air--COF was about 0.03. However, a much higher O_2 pressure was needed to induce a similar increase in friction compared to that induced by water vapour. Sufficiently pure nitrogen gas has virtually no effect on the COF even at atmospheric pressure. It was noted that the H_2O and O_2 effect on the friction increase observed in this

study was reversible: the friction coefficient returned to the ultralow value when the excess H_2O or O_2 in the chamber was pumped out. This implied that the nature of the interaction between H_2O or O_2 molecules and the DLC surface consisted of physical adsorption, rather than a chemical reaction that permanently affected the surface chemistry. The difference in the strength of the influence induced by H_2O and O_2 was explained by the authors as that water layers possessed greater cohesive energy than the O_2 layers, due to greater dipole interactions that resulted in a stronger physical barrier.

Qi et al. [99] conducted the first principles investigation of the adhesion and friction between NH-DLC coatings and aluminum by using density function theory (DFT) calculations. The experimental part of this work was done by performing pin-on-disc tests in ambient and dry air (40% RH and 0% RH), N_2 and H_2-He mixture (40 vol.% H_2 - 60 vol.% He) environments using the experimental setup in [77]. Modelling work simulated the adsorption of the H_2, N_2 and H_2O at the diamond (111) surface (C surface simulating sp^3 bonds of DLC) in an effort to understand whether or not surface passivation would occur due to chemical reaction, then the work of separation at the interface between Al and the reacted C surfaces (Al/C interface) as well as that between the same reacted C surfaces (C/C interface) was calculated. The comparison of experimental and modelling data is summarized in **eobserved 2. 3**. It is obvious that the observed experimental results could be successfully explained by the strength of interactions between varying surface bonding structures induced by different test environments. Specifically, the highest

System	Al/DLC in H_2	Al/DLC in N_2	Al/DLC in air (40% RH)
Adhesive transfer	DLC transfer to Al	Al transfer to DLC	DLC transfer to Al
Coefficient of friction	0.015	0.72	0.12
Adsorption energy (eV/molecule)	4.66	0.66	1.80
Dissociation status	Atomic H	No dissociation	Atomic OH
Reacted DLC surface	H terminated carbon surface	Carbon surface with dangling bonds	OH terminated carbon surface
Initial contact interface	Al/H–C(111)	Al/C(111)	Al/OH–C(111)
W_{sep} (J/m^2)	0.02	4.5	0.2
Interfacial separation (Å)	3.21	1.86	3.25
Final interface	H–C(111)/H–C(111)	Al/C(111)	OH–C(111)/OH–C(111)
W_{sep} (J/m^2)	0.008	4.5	0.02
Interfacial separation (Å)	3.02	1.86	3.12

Table 2.3 Comparison of experimental and modeling data for the Al/NH-DLC coating pair tested in H_2, N_2 and air with 40% RH [99].

COF observed in N_2 could be attributed to the highest work of separation between Al/C (111) while the intermediate and lowest frictions obtained in air (40% RH) and in H_2 were due to the surface passivation by C-OH bonds and C-H bonds, respectively--which resulted in a lower work of separation.

2.2.6 Thermal Stability and the Effect of Temperature on the Tribological Behaviour of DLC Coatings

Hydrogenated and non-hydrogenated DLC are metastable materials with structures that will convert towards graphite-like carbon by either thermal activation or irradiation with energetic photons or particles. Heating hydrogenated DLC coatings results in the loss of hydrogen and CH_x species, starting at about 400 °C or lower, depending on the deposition conditions and the dopant contained in the coatings [73][100-102]. This prompts changes in the compositions and properties of the material--limiting the use of DLC in applications where elevated temperature is present. The lack of thermal stability is generally attributed to the loss of hydrogen, resulting in a collapse of the structure into a mostly sp^2-bonded network for H-DLC coatings. It has been reported that thermal activation can also induce changes in ta-C (NH-DLC) coatings--causing the conversion of sp^3 carbon bonds to sp^2 bonds [103]. This work suggests that the onset of structural relaxation began at temperatures as low as 100 °C with near full relaxation observed at 600 °C.

Modifications of the DLC coatings such as doping [104-105] or bias grading [106], i.e. varying the deposition power during manufacturing, have been carried out in order to increase the thermal stability, but the resulting coatings did not exhibit significant improvement when compared to pure DLC coatings [73][100-102]. Moreover, these studies have been conducted on thermally annealed DLC coatings by structural characterizations such as SEM, TEM and Raman spectrometry or mechanical property characterization. The reported maximum stable temperatures are obtained without the presence of tribological loading (e.g. sliding) during the tests.

Vanhusel et al. [107] studied the wear behaviour of H-DLC coatings (containing 35 at.% H measured by elastic recoil detection analysis (ERDA)) that were produced by PACVD in ambient air. Wear experiments were conducted up to a maximum temperature of 300 °C and the investigation was conducted by running low-amplitude oscillatory ball-on-flat tests using corundum (Al_2O_3) as the counterface. They observed a decrease in COF value when the test temperature was increased beyond 100 °C--from 0.13 at room temperature to 0.07 at 300 °C--and the wear scars became larger and deeper. The same tests were performed on annealed samples (300 °C for 16 h) and similar results were recorded. They proposed that the dehydrogenation and/or structural change from sp^3- to sp^2- bonded carbon of a very thin top layer of the coating were the reason for the decrease in COF and the increase in wear rate at elevated temperatures.

Bermond et al. [108] performed elevated temperature pin-on-disc tests on DLC coated 100C6-steel (equivalent to AISI 52100) couples at elevated temperatures up to 400 °C. The DLC coatings studied had a multilayer structure containing silicon deposited by combined PVD and PACVD processes, which resulted in an estimated hydrogen content of 10 at.%. At room temperature and up to 200 °C, the COF values did not exceed 0.3 and the maximum wear track depth did not exceed 2 μm. A transfer layer of graphite and graphite–silica was found to act as a solid lubricant and reduced both friction and wear. At 400 °C, wear was catastrophic with a depth of 15 μm on a 4 μm coating. They concluded that the failure of the DLC coating was due to the softening of the substrates and suggested that the DLC-coated 100C6-steel discs not be used at temperatures higher than 200 °C.

Konca et al. [109] studied the tribological behaviour of NH-DLC coatings at elevated temperatures against 319 Al alloy at 25, 120, 300 and 400 °C in air using a high-temperature tribometer. Three kinds of coatings containing 1.28 at.% hydrogen--namely 80-V DLC (H=10.0 GPa, E=142 GPa), 60-V DLC (H=7.8 GPa, E=99 GPa) and Teer Coatings Graphit-iC^{TM} (H=12.0 GPa, E=175 GPa)--were deposited by unbalanced magnetron sputtering deposition, then studied under an applied load of 4.9 N and a sliding speed of 0.12 m/s. All three coatings exhibited a trend of increasing COF values and wear rates as the testing temperature was elevated. For example, the steady state COF and wear rate for the 80-V coating were 0.17 and 1.25×10^{-6} mm^3/m at 25 °C,

respectively. At 120 °C, the values increased to a COF of 0.30 and a wear rate of $3.08\times10^{-5}mm^3/m$. The COF of the 80-V coating was 0.55 and the wear rate was $3.36\times10^{-4}mm^3/m$ at 300 °C, in addition to observed coating removal from the substrate, and Al adhesion. For the 60-V DLC, coating penetration was observed at 120 °C. Al adhesion onto the Graphit-iC™ occurred at 400 °C. The authors suggested that the degradation of the coating's wear resistance was due to i) inefficiency of the DLC coating surfaces' passivation mechanism by water vapour and ii) loss of the coating's room temperature stability at elevated temperatures.

Krumpiel et al. [110] tested three different DLC coatings (NH-DLC, H-DLC and titanium doped H-DLC) against M2 steel balls at elevated temperatures (up to 450 °C) and in vacuum (10^{-3} Pa). The DLC coatings showed low wear rates ($<2.7\times10^{-7}$ mm^3 $N^{-1}m^{-1}$) at room temperature in ambient air. The NH-DLC failed within 10 m (with a rapid increase of the friction coefficient from 0.35 to 0.6). Ti doped H-DLC and H-DLC failed within a 100 m sliding distance where a slow increase of the friction coefficient from 0.3 to 0.55 was observed. The authors also noted a severe decrease in hardness to less than 50 HV for all coatings after heating them to 450 °C in ambient air--a result related to the lack of hydrogen content in the carbon network as well as drastic oxidation of the coating.

Ni et al. [111] studied the friction, wear and tendency towards aluminum adherence for both unbalanced magnetron sputtering deposited hydrogenated (14 at.% H) and

non-hydrogenated DLC coatings at room and elevated temperatures by testing them against 319 aluminum pins. At room temperature (40% relative humidity, 25 °C), the friction coefficient of the NH-DLC was 0.1, and that of the H-DLC decreased from 0.22 to 0.13 after a running-in period. The H-DLC maintained its low friction coefficient of about 0.18 at 240 °C, but the COF of the NH-DLC increased dramatically to about 0.65--approximately the same value as the friction coefficient of the A319 aluminum alloy against itself. Aluminum transfer to the NH-DLC coating at 240 °C was confirmed by SEM and EDS results. The wear coefficient of the NH-DLC was approximately 40 times higher than that of the H-DLC at 240 °C. The authors concluded that graphitization was responsible for the accelerated wear.

High temperature tests on DLC have also been conducted using a more application-oriented setup. Reisel et al. [112] used a compression-spin test configuration that simulated the forming processes with rotating tools and a high compression load (an axial force of 5000 N) to study the behaviour of DLC under high mechanical and thermal loads. H-DLC and silicon doped DLC (Si-DLC)--both deposited by PE-CVD--were tested in the experiments. Other low wear friction coatings as well as industrial lubricants (graphite, molybdenum disulfide and hexagonal boron nitride) were tested to provide a comparison. A hardened steel (62 HRC) was used as the substrate, and the coated, respectively, pre-lubricated punch was pressed with an axial force of 5000 N into the sleeve, which was heated up to the contact temperature of the modelled forming process.

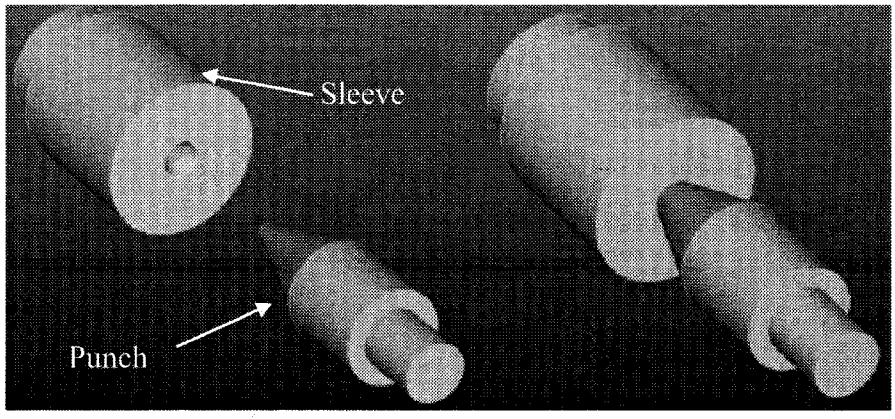

Figure 2. 20 Schematic of the compression-spin test used by Reisel et al. [112]. This experimental setup was adapted by the authors to simulate the forming processes with rotating tools and high compression load.

They reported that at test temperatures of 500 and 700 °C, DLC showed the best performance of all tested coatings and lubricants for a punch rotating speed of approximately 100 mm/min for the longest sliding distance and without failing. Si-DLCseemed only suitable at high temperatures for the given load conditions of the compression-spin test because it presented a similar behaviour like an unlubricated punch between room temperature and 500 °C.

2.2.7 Effect of Doping and Alloying

From a technological point of view, a DLC coating capable of providing a low, predictable and stable COF across a wide range of relative humidities is important to many applications. As stated above, DLC in its pure (monolithic) form cannot comply with such a demand. Non-metallic additive atoms such as Si and F and metal have been incorporated into DLC coatings [113-114] to reduce the moisture sensitivity of hydrogenated DLC coatings. By systematically controlling the content of various dopants in DLC coatings, Gilmore and Hauert [113] explored the possibilities for optimising and tailoring the humidity sensitivity of the tribological properties of DLC coatings. Three alloying elements, Si (up to 35.5 at.%), F (up to 18.6 at.%) and Ti (up to 20 at.%) were added to H-DLC coatings. The friction and wear properties for the resulting coatings were studied by sliding against 100Cr6 steel balls and aluminum pins in a relative humidity range between 5 and 85% --recorded and summarized in **Table 2. 4**. It is notable that through the addition of a few percent of Si (approx. 4 at.% in the case of a

Dopant	Dopant content (at.%)	100Cr6 steel counterface				Alumina counterface			
		$\mu_{5\%}$	$\mu_{65\%}$	$\mu_{85\%}$	Wear rate ($mm^3N^{-1}m^{-1}\times10^{-7}$)	$\mu_{5\%}$	$\mu_{65\%}$	$\mu_{85\%}$	Wear rate ($mm^3N^{-1}m^{-1}\times10^{-7}$)
None	0.0	0.10	0.16	0.20	1.1	0.051	0.14	0.14	1.2
None	0.0	0.046	0.059	0.13	1.3	0.025	0.061	0.082	1.0
None	0.0	0.066	0.083	0.16	1.7	0.034	0.082	0.097	1.3
None	0.0	0.054	0.14	0.16	0.94	0.026	0.078	0.089	1.3
None	0.0	0.073	0.079	0.092	2.1	0.038	0.082	0.077	1.7
Si	1.6	0.057	0.11	0.097	3.9	0.060	0.099	0.10	4.3
Si	1.6	0.086	0.073	0.085	4.3	0.057	0.092	0.095	3.1
Si	2.7	0.073	0.089	0.11	5.6	0.062	0.078	0.088	4.3
Si	3.9	0.080	0.059	0.063	7.7	0.049	0.056	0.073	5.1
Si	3.9	0.082	0.066	0.079	8.0	0.046	0.080	0.11	5.8
Si	4.4	0.066	0.063	0.081	6.5	0.046	0.066	0.078	6.0
Si	5.7	Failed	0.054	Failed	Failed	0.045	0.064	0.088	5.3
Si	5.7	0.094	0.064	0.070	7.5	0.082	0.070	0.088	6.5
Si	22.1	0.60	0.052	0.049	23	0.61	0.063	0.056	25
Si	35.5	0.55	0.07	Failed	Failed	0.61	0.059	Failed	Failed
Si	35.5	0.59	Failed	Failed	Failed	0.52	Failed	Failed	Failed
F	1.2	0.11	0.13	0.16	1.6	0.043	0.10	0.11	1.8
F	2.6	0.22	0.16	0.15	0.89	0.11	0.12	0.11	2.4
F	3.5	0.76	0.23	0.17	0.77	0.093	0.14	0.098	1.6
F	18.6	0.85	0.51	0.43	1.1	0.18	0.27	0.23	1.3
Ti	0.0	0.069	0.12	0.14	3.0	0.041	0.078	0.10	2.0
Ti	0.0	0.057	0.14	–	2.9	0.050	0.090	0.12	2.4
Ti	0.0	0.11	0.12	0.14	1.3	0.055	0.092	0.11	2.0
Ti	5.8	0.055	0.13	0.13	1.2	0.052	0.11	0.098	1.7
Ti	7.9	0.062	0.10	0.12	1.3	0.040	0.091	0.098	1.2
Ti	14	0.065	0.11	0.12	1.7	0.032	0.095	0.11	2.2
Ti	20	0.040	0.11	0.11	2.6	Failed	Failed	Failed	Failed

Table 2. 4 Average friction coefficient and total wear values for the various coating/counterface combinations studied by Gilmore and Hauert [113]. The effect of different dopants and dopant concentrations on the humidity sensitivity of the coatings are reflected.

steel counterface and approx. 6 at.% in the case of an aluminum counterface), it was possible to render the DLC practically insensitive to changes in ambient humidity. Its COF was essentially stabilized at approximately 0.075 against steel as well as aluminum over the relative humidity range of 5–85%. With the addition of approximately 2-3 at.% F, the COF of F-DLC could be stabilised at approximately 0.15 against steel and 0.11 against aluminum for the relative humidity range of 5–85% [113]. The addition of Ti appears to be ineffective for controlling the tribological humidity sensitivity of DLC. In the case of Si alloyed DLC, the improvement in moisture sensitivity comes at a price--namely a decrease in wear resistance (almost 20-fold increase in wear rate with 20% Si addition). On the other hand, the addition of F or Ti did not diminish the wear resistance and even slightly improved it for concentrations up to 10 at.%. It is interesting to mention that by adding higher concentrations (above approx. 10 at.% in the case of Si and above approx. 3 at.% in the case of F) it was possible to obtain inverted moisture sensitivity (decreased COF with increasing humidity level) when rubbing against both steel or aluminum in the case of Si-DLC, and against steel only for F-DLC (**Table 2. 4**).

Generally, metal doped DLC (Me-DLC) coatings with low metal content (atomic ratios of Me/C up to approx. 0.3) have lower compressive stress than pure DLC (< 1GPa [115-116]). These properties make metal doping a promising method for the improvement of DLC coatings, and studies on Me-DLC have focused more on the synthesis and characterization of the coatings than on exploring their tribological

mechanisms [51][117-119]. A brief account of the tribological studies on tungsten-containing DLC coatings is presented in this section, due to its relevancy to the current work.

Strondl et al. [120] studied the tribological properties of tungsten-containing H-DLC coatings deposited by magnetron sputtering deposition under different plasma densities applied during deposition by testing the coatings against alumina balls under 0.010 m/s for 15000 revolutions (testing load was not specified by the authors). The COF for all the samples deposited under different plasma densities was a uniform 0.1-0.2, while the wear resistance of the coating was measured with a Calo tester operating with an aluminum suspension. A slight decrease occurred--from 6.4×10^{-15} $m^3N^{-1}m^{-1}$ for the coating deposited under the lowest plasma density, to 4.5×10^{-15} $m^3N^{-1}m^{-1}$ for the sample deposited under the highest plasma density.

Hieke et al. [121] compared the mechanical and tribological properties of two types of tungsten-containing H-DLC coatings (W-H-DLC) against an H-DLC coating reference. The tungsten containing DLC coatings studied by the authors are the same types of coatings studied in this work. The first type of W-H-DLC was deposited by a PVD process (denoted as WC-DLC). The second type of sample was produced by applying an H-DLC top layer by r.f. PACVD on the W-H-DLC coating of the first type (denoted as DLC/WC-DLC). The thickness of the top layer on the DLC/WC-DLC coating and the reference H-DLC coating were both 1.5±0.1 μm. The COF values of the coatings were

measured by pin-on-disc tests against 100Cr6 steel balls under 3N load and 30 rpm rotation speed in ambient air (19 °C, 50% RH), and the wear rates were measured by ball cratering method. It was observed that the wear rate of both the reference H-DLC and the DLC/WC-DLC coating was 0.7 $\times 10^{-15}$ $m^3N^{-1}m^{-1}$ with a six fold increase to 4.2×10^{-15} $m^3N^{-1}m^{-1}$ observed for the WC-DLC coating. However, the COF values of the three types of coatings were similar--specifically 0.2±0.06. Nanoindentation measurements revealed that the hardness of the WC-DLC coating was 11 GPa while the values for H-DLC and DLC/WC-DLC were 22 and 21 GPa, respectively.

As observed in [121], tungsten containing DLC provided desirable tribological properties under ambient condition. Hence, given the fact that doping may increase temperature and environment stability, it is important to characterize the friction and wear of WC-DLC and DLC/WC-DLC under these conditions. This is one of the main objectives of the work undertaken in this thesis.

2.3 Survey Summary of the Literature

The structure and properties of two important carbon based coatings, namely B_4C and DLC have been surveyed in this chapter. The present literature survey on the tribological behaviour of B_4C coatings revealed the following:

1. Boron carbide coatings vary in structure and composition due to the large B-C homogeneity range.

2. Magnetron sputtering deposition produces boron carbide coatings with a B/C ratio of nearly 4, and their tribological properties can be tailored through the addition of reactive gas.

3. The self-lubricity of boron-containing surfaces is caused by the sequential formation on the boron-containing surface of boron oxide, and then boric acid.

4. A finite life run-in coating, which wears out after a certain specific period of sliding, can be achieved by utilizing the high abrasiveness of boron carbide coatings to increase the fatigue resistance of the coated parts.

5. The most widely used counterface materials for the study of the tribological behaviour of B_4C coatings were different types of steel (52100, 440C). No report on B_4C against aluminum has been presented, signifying a need for the present work in order to investigate the transfer and adhesion of an Al alloy onto a B_4C coating as well as to analyze the tribological behaviour of a B_4C coating dry sliding against an aluminum alloy for the purpose of tool coating development.

The literature on the tribological behaviour of the DLC coatings was more extensive and the survey provided the following information:

1. DLC is a metastable form of amorphous carbon containing a significant fraction of sp^3 bonds mixed with sp^2 bonds. The mechanical properties of

DLC coatings directly correlate with the fraction of sp^3 hybridised carbon in the coatings.

2. The friction and wear behaviour of DLC coatings depends strongly on the formation of an easy-to-shear, carbonaceous material at the sliding interface and the interaction of the carbon containing material with the gaseous species present in the test environment.

3. Sufficient hydrogen content (40 at.%) within the DLC coating (H-DLC) leads to very low COF and wear rates in inert environments while the introduction of oxygen and especially water vapour adversely affects their tribological behaviour.

4. DLC coatings with low hydrogen content (< 2 at.%, NH-DLC) show high COF and high wear rates in an inert environment. The presence of appropriate reactive gaseous species in the test environment is necessary for them to exhibit low COF and wear rates. They have about the same friction and wear under ambient conditions as H-DLC coatings.

5. Increasing the test temperature increases the wear rate of DLC coatings regardless of their hydrogen content and structure.

6. There is a temperature limit above which the DLC coatings graphitize and oxidize significantly. This temperature depends on the structure and composition of the coating.

7. Doped DLC coatings have mostly been studied for their deposition and characterization rather than to discover their tribological properties under different temperature and environment conditions. Limited work suggest that they extend the temperature and environment stability of DLCs.

8. The most used counterfaces for the study of the tribological behaviour of DLC were different steels (52100, 440 C, M52 etc.), ceramic-based materials or their coated versions.

9. Sliding against aluminum, while well reported, has not been extensively studied. It is essential to explore the tribological behaviour of WC doped DLC coatings dry sliding on an Al alloy in order to fulfill the objectives of the current work. Particularly, the effect of WC addition needs to be studied.

CHAPTER 3 EXPERIMENTAL PROCEDURES

This chapter describes the experimental methods and analysis techniques that have been used to characterize the materials tested in this work. The pin and substrate materials used in the wear tests are introduced in terms of their preparation and structure. Boron carbide (B_4C) coatings and two types of DLC coatings are studied in this work--namely WC-DLC and DLC/WC-DLC--and their preparation, mechanical properties and structural and surface characteristics are presented. Finally, the tools and procedures used for the evaluation of the test results, including the calculation of coating wear rates and the quantification of material adhered to a coating sample, are explained.

3.1 Characterization of Test Materials

3.1.1 Thickness Measurements of Coating Using Radical Sectioning Method

Ball cratering is a conventional method used to measure the thickness of coatings. In this technique, the coated surface is subjected to wear by rotating a sphere (with a diameter of R) pressed against it (**Figure 3. 1** a)). An abrasive suspension, usually diamond, is fed into the contact region between the sphere and the coating surface to induce three-body abrasive wear of the coated sample. This process results in the formation of a wear crater on the coated sample. For example, the crater on the DLC/WC-DLC sample is shown in **Figure 3. 1 b)**. By measuring the inner diameter (d)

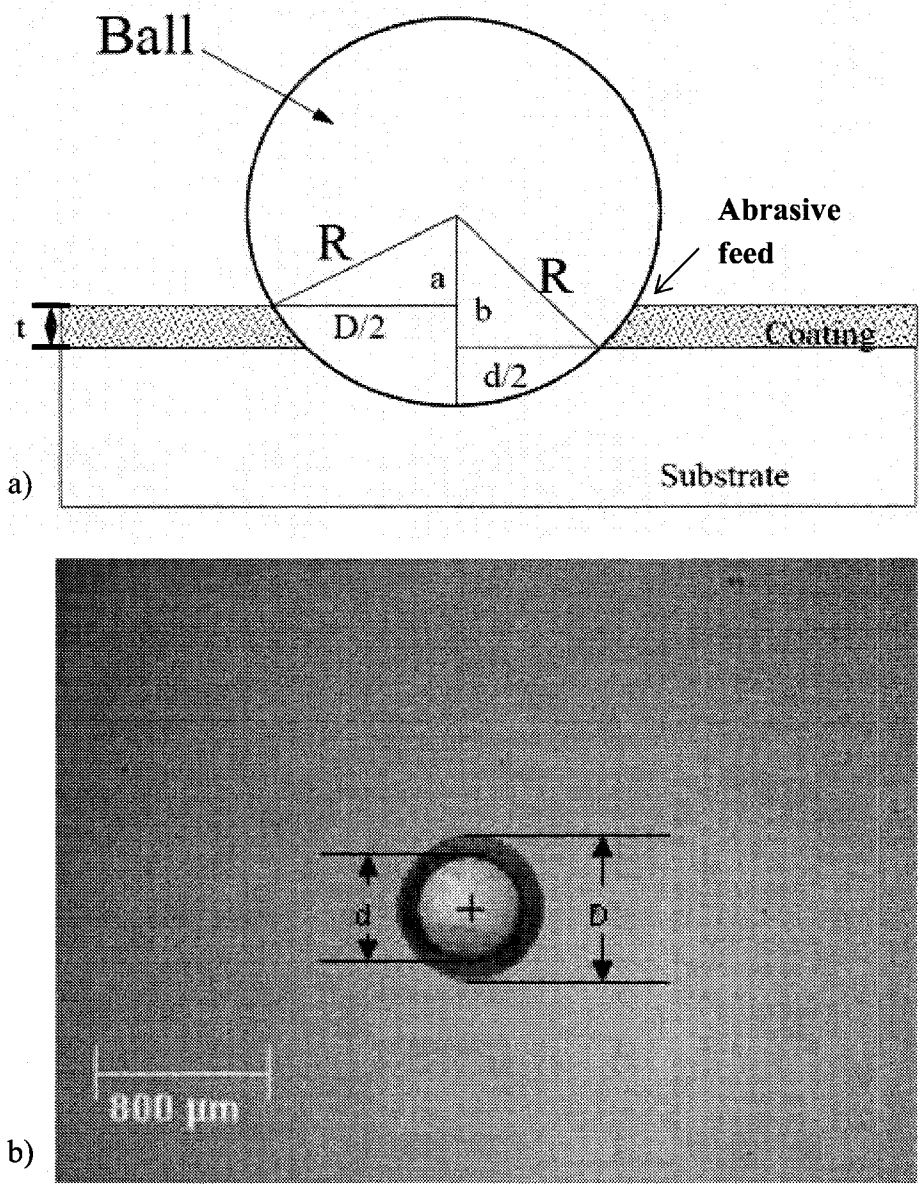

Figure 3. 1 a) Side view of the radical sectioning configuration. A hard ball is pressed against the coated sample and abrasive suspension is fed to the contact region to remove material by three-body abrasive wear.**b)** Top view of the resulting worn crater of the DLC/WC-DLC coating. The diameters of the inner and outer circles (d and D) are measured to calculate the coating thickness (t) using **Equation 3.1.**

and outer diameter (D) of the circles, the thickness of the coating (t) can be calculated from the geometry of the wear scar using the following equation,

$$t = \left[\sqrt{R^2 - \left(\frac{D}{2}\right)^2} - \sqrt{R^2 - \left(\frac{d}{2}\right)^2}\right] \qquad \textbf{Equation 3. 1}$$

In this study, the CSM CALOTEST® machine--located at General Motors Global Research and Development Center in Warren, Michigan, USA (referred as GM R&D Center hereafter in the text)--was used to measure the thickness of the coatings tested. The CSM CALOTEST® used hardened steel balls with 25.4 mm diameters to create the craters in this work. In **Figure 3. 1 b)**, D = 668 μm, d = 492 μm which, according to **Equation 3.1**, makes t = 2.006 μm. Mean values of the thicknesses of the coatings were determined by averaging three measurements.

3.1.2 Mechanical Property Measurement Tools

3.1.2.1 Rockwell Hardness Measurements

A Rockwell Macromet® (Model 1800-5100T) hardness tester at the University of Windsor was used to measure the Rockwell C hardness (HRC, R_c) of the M2 tool steel substrates. The Rockwell C test uses a conical diamond indenter (0.2 mm tip radius) with a major load of 150 kg. An average of eight measurements was taken to obtain the reported value.

3.1.2.2 Vickers Micro Hardness Measurements

A Buehler Micromet II® (Model 1600-9000) hardness tester at the University of Windsor was used to measure the Vickers microhardness values (HV) of the pin material as well as the coatings using a square-base diamond pyramid indenter (136 ° tip angle). The indentation load applied to measure the pin material was 100 g. All pre-set loads between 5 g and 1000 g (inclusive) of the tester were applied.

3.1.2.3 Nanoindentation of Coatings

To investigate a broad range of hardness responses for the coatings--specifically at very low loads--nano-indentation of the coatings was performed. An MTS Nano indenter XP located at GM R&D was employed to measure the hardness. In addition, elastic moduli were also determined. In this technique, a small diamond tip (Berkovich indenter) is progressively forced into the coating to a certain depth (h_{max}) or until a preset load (F_{max}) is reached. The entire loading and unloading process is recorded as a load-displacement curve. As an example, the indentation load-displacement curve for the B_4C coating is shown in **Figure 3. 2**. The hardness and elastic modulus values of a sample are extracted from its indentation load-displacement curve using the analysis methods developed by Oliver and Pharr [122]. This analysis requires knowledge of the area function of the indent, i.e. the expression of the contact area (A) of the indent in terms of the distance from its tip (h). The area of a perfect Berkovich indent is $A = 24.5h^2$. The indentation of a sample of known hardness and elastic modulus (most commonly

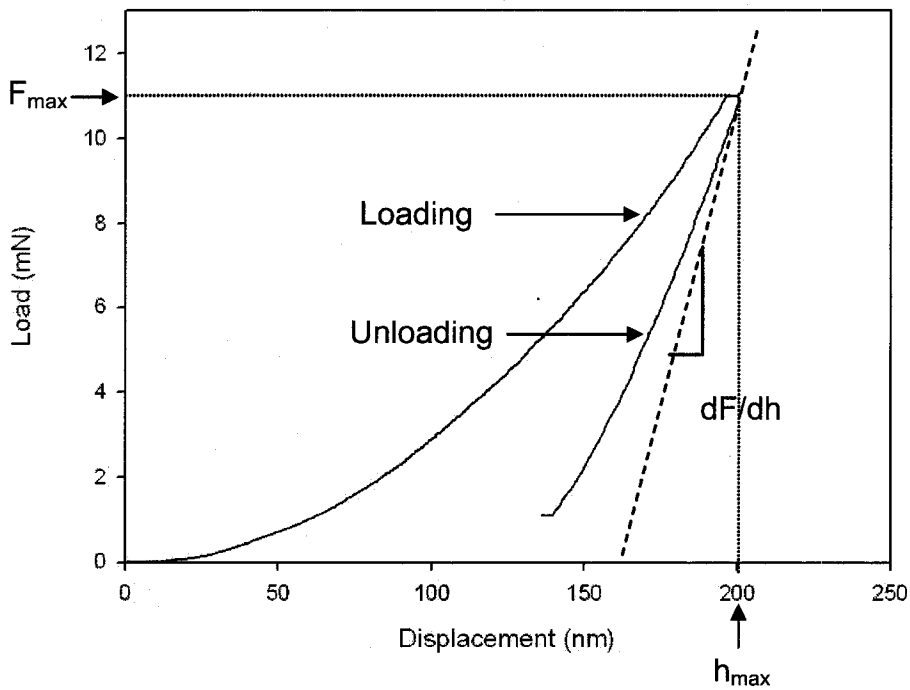

Figure 3. 2 The indentation load-displacement curve for the as-received B_4C coating.

fused silica) is used to calibrate the instrument. The hardness H of the sample can simply be calculated from the ratio of the maximum applied load F_{max} to the contact area of the indent:

$$H = \frac{F_{\max}}{A} \qquad \textbf{Equation 3. 2}$$

To calculate the elastic modulus of the sample, the slope of the initial part of the unloading curve is calculated:

$$\frac{dF}{dh} = \beta\left(\frac{2}{\sqrt{\pi}}\right)E^*\sqrt{A} \qquad \textbf{Equation 3. 3}$$

where E^* is called the combined modulus. The elastic modulus of the sample (E_s) is then calculated using the following equation:

$$\frac{1}{E^*} = \frac{\left(1-v_i^2\right)}{E_i} + \frac{\left(1-v_s^2\right)}{E_s} \qquad \textbf{Equation 3. 4}$$

where E_i and v_i are the elastic modulus and the Poisson's ratio of the indenter and v_s is the Poisson's ratio of the sample. During the nanoindentation measurements of the coatings, the maximum depth of indentation (h_{max}) was kept at less than 10% of the total coating thickness in order to minimize the substrate effect. Each nanohardness value reported in the current work is averaged from at least ten measurements.

To cover a broader range of hardness responses for the coatings, the results of the Vickers hardness tests were converted into metric units (GPa) and plotted together with the nanoindentation results. The combination of the two test scales enables the hardness response of the coatings be examined comprehensively--at both the coating response dominated region and substrate response dominated region. The results are presented in **Section 3.2.2.**

3.1.3 Structural Characterization Methods

3.1.3.1 Sample Preparation by Cryogenic Fracture Method

Cryogenic fracture method was used to create a cross sectional view of the B_4C coating in order to investigate the coating's microstructure. The coated steel disc was cut from the uncoated side using an electrical discharge machine (wire EDM) to create a narrow groove (0.6 mm width) as shown in **Figure 3. 3**. A layer of 0.5 mm thickness of material was left uncut. The sample with the groove was then submerged into liquid nitrogen (T = -196 °C) and fractured by driving a chisel into the groove.

3.1.3.2 Sample Preparation by Focused Ion Beam

A state of the art focused ion beam apparatus located at the University of Michigan Ann Arbor, (Michigan, USA) was applied as a micromachining tool to create a cross-section of the DLC/WC-DLC coating and image it to clarify the coating layer structure. In this focused ion beam micro-machining process, a beam of gallium was accelerated to an energy of typically 30 keV, and then focused on the sample by

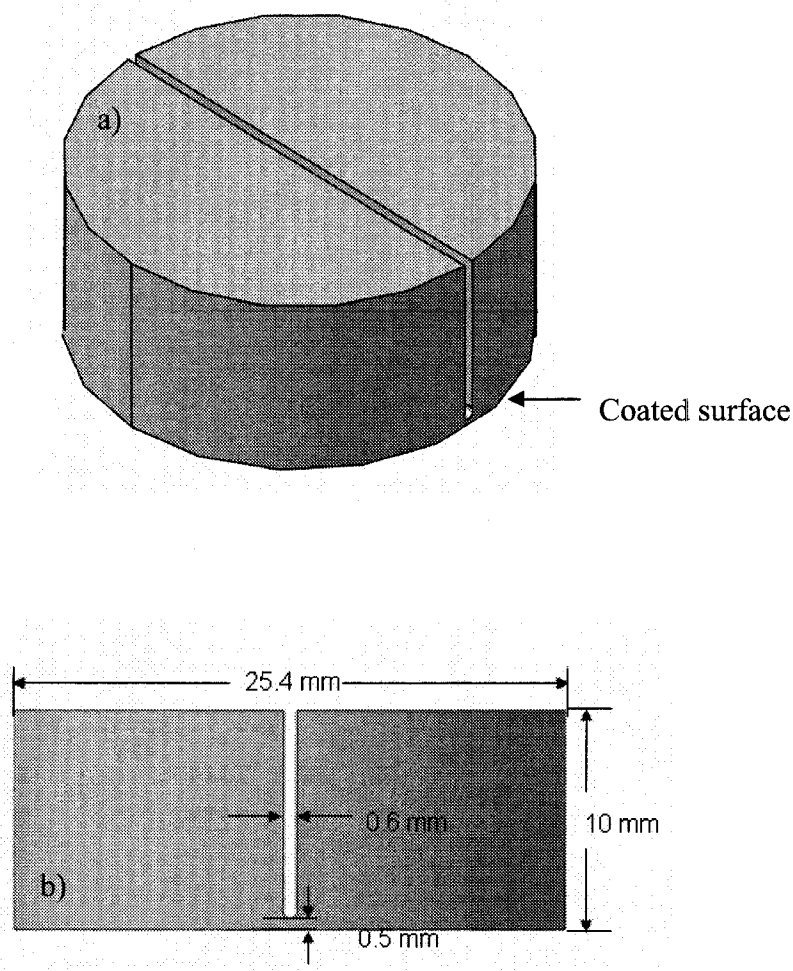

Figure 3. 3 Schematic drawing of the cutting scheme for cryogenic sample creation: **a)** Isometric view; **b)** Right view.

electrostatic lenses. When the high-energy gallium ions struck the sample, they removed the sample atoms from the surface by sputtering. Controlling the location of the ion beam allowed for the formation of trenches to be cut into the coatings, revealing the cross-sectional structure of interest. The ion beam was then used to image the cross-sectional structure.

3.1.3.3 X-ray Diffraction

A Siemens D5000 diffractometer using a Cu Kα (λ = 1.5406 nm) source tube at the GM R&D Center was used for the X-ray diffraction studies. Sample data was collected over a two-theta range, from 10-100 degrees for the studied materials.

3.1.3.4 Raman Spectroscopy

Raman spectroscopy is a technique that uses light to obtain structural information of materials utilizing the Raman effect. It is a standard, non-destructive technique for the characterization of carbon-based materials 79. When a beam of light impinges on a carbon substance, most of the photons are elastically scattered without an energy shift. However, a small portion of the photons exite the molecules in the sample and are then scattered inelasticaly. Briefly, the Raman effect is the shift in the energy of the inelastically scattered light from the incident light by the various vibration modes of the inspected substance. Such shifts in energy can be related to the different atomic arrangements induced by the complex bonding structures of carbon [123].

The Raman spectrum is a plot of the intensity of the scattered light against the energy

difference between the elastically and inelastically scattered light. For amorphous carbon, the Raman spectra are characterized by a peak centered around 1300-1380 cm^{-1} (D band) and a peak centered around 1520-1580 cm^{-1} (G band). The D band is correlated to the breathing mode of sp^2 sites only in carbon chains and the G band is derived from the stretch vibration of any pair of sp^2 sites. The unususal fact is that G and D bands of varying intensity, position and width dominate the spectra of DLC coatings even when no widespread graphitic structure is present [124]. The thorough interpretation of Raman is a well studied topic and beyond the scope of this work. Thus a general guideline is applied to extract structural information from the spectra obtained: the G band frequency increases with decreasing sp^3/sp^2 ratio and the D band intensity decreases with increasing sp^3/sp^2 ratio [79][124].

The Raman spectra of the DLC coatings tested in this work were obtained using the spectrometer at the GM R&D Center. The Raman spectra were collected by a Dilor microprobe system fitted with a 10X objective. Approximately 25 mW of YAG laser light (532 nm) was focused onto the samples, and at least two 60-second exposures were signal-averaged for each spectrum.

3.1.4 Surface Profilometry

A Wyko NT 1100 optical surface profilometer at the University of Windsor was used to characterize the surface topographies of the samples before and after the tests--including measurements of sample surface roughness and profile acquisition of the

wear tracks.

3.1.5 Elastic Recoil Detection

Elastic recoil detection (ERD) is a method used specifically to detect hydrogen in surface layers of up to approximately 1 μm thickness. This technique is non-destructive, absolute, fast and independent of the host matrix and its chemical bonding structure [125].

In ERD, a beam of $^{4}He^{+}$ ions are accelerated to 1-2 MeV and directed at the sample surface in a glancing angle geometry. The hydrogen atoms are knocked out of the sample, and form recoiled hydrogen ions. The concentration of hydrogen is then extracted from an analysis of the energy spectrum of the detected hydrogen ions.

In the current work, the hydrogen content measurement of the DLC coatings were conducted at Michigan Ion Beam Laboratory for Surface Modification and Analysis located at the University of Michigan Ann Arbor (Michigan, USA).

3.2 Description of the Coatings and the Substrate Material

3.2.1 M2 Steel Substrates

An annealed M2 tool steel bar, 2.54 cm in diameter, was machined to provide the substrates. The nominal composition (wt.%) of M2 steel (AISI type M-2) is shown in **Table 3. 1.** The M2 steel bar was first cut into 1 cm thick discs. The discs were then subjected to a heat treatment procedure that consisted of austenizing at 1200 °C for 3-4 minutes followed by air cooling to 25 °C and then tempering at 560 °C for 120 minutes.

Table 3. 1 Nominal chemical composition (wt.% of the M2 steel substrates

% C	% Cr	% V	% W	% Mo	% Mn	% Si	% Fe
0.83	4.0	2.0	6.0	5.0	0.27	0.35	Balance

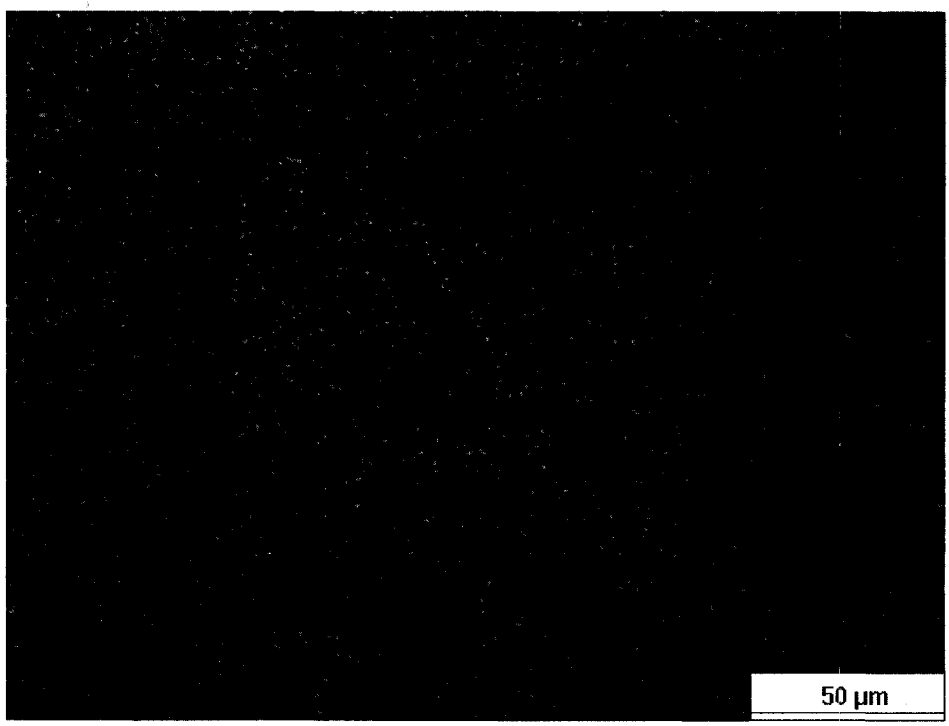

Figure 3. 4 Optical microstructure of M2 steel. The small particles are various carbides.

The purpose of the heat treatment was to increase the hardness of the substrates to provide better support to the coatings.

Coarse grinding of the hardened M2 steel discs was conducted by a grinding machine to remove the burr marks from previous cutting, followed by fine grinding in running water using SiC emery papers (120, 240, 400 and 600 grit). Water-based diamond suspensions of 3 and 1 μm were used to polish the disc surfaces. The final hardness of the M2 steel discs was 63±2 R_c. The final surface roughness of the polished M2 steel discs as measured by the optical surface profilometer was 9.5 ± 4.1 nm (R_a). The optical image of the microstructure of the M2 steel after polishing is shown **Figure 3. 4**. The polished discs were sent to Ionbond© Toronto (1315 Industrial Road, Unit 10 CA-Cambridge, Ontario N3H 4W3) for the deposition of coating samples.

3.2.2 Hardness Response of the Coatings over Varying Contact Severity

Hardness is one of the longest used and most widely accepted parameters cited to characterize the contact response of tribological materials. The relationship between hardness and the material's wear rate is straightforward. Many different testing scales have been developed to better describe the hardness response of a particular material. Among these are Rockwell scales and the Vickers microhardness scale. A thorough treatment of the issues of hardness testing can be found in [126].

The hardness response of a coated system is more complex than that of bulk materials. The measured hardness of a coating on its substrate is strictly a "composite"

value consisting of both contributions from the coating and from the substrate beneath it. On contact scales that are less than the coating's thickness, the coating dominates the coating response while the substrate response dominates much more severe scales. The typical hardness response with respect to varying contact scales for a system consisting of a hard coating and a soft substrate is shown in **Figure 3. 5**. Modelling work combined with experimental studies has been conducted in order to measure and explain the composite behaviour of coated systems for the purpose of better understanding and controlling their wear properties [127-130].

In the current study, a unitless parameter, relative indentation depth (*RID*), as proposed by Korsunsky et al. [127] is chosen to represent the contact severity during hardness measurements. *RID* is defined as the ratio of the maximum indentation depth (h_{max}) to the coating thickness (t),

$$RID = h_{\max} / t \qquad \textbf{Equation 3. 5}$$

The hardness responses of the three types of coatings studied were plotted against RID (**Figure 3. 6**). The first two points presented for each coating were measured by nanoidentation and proved significantly higher than those measured using a Vickers hardness tester. The best exclusion of substrate contribution was obtained at 200 nm indentation depth (approx. 10% coating thickness), thus the corresponding values were

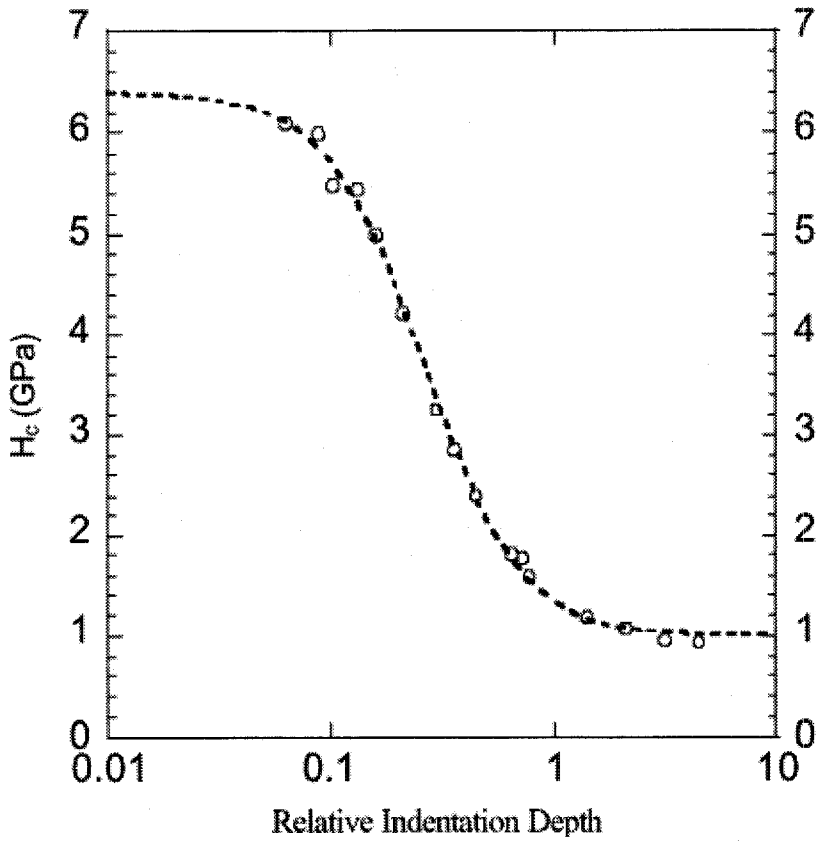

Figure 3. 5 Measured hardness plotted against relative indentation depth (the ratio of maximum indentation depth to the coating thickness) for a set of micro-macro indentation results for a 20-μm-thick nickel coating on copper substrate 130.

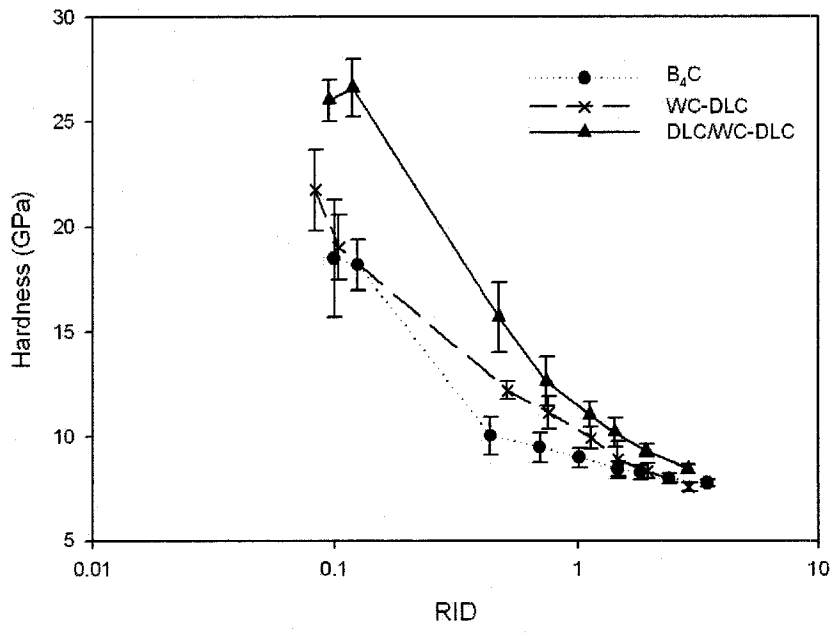

Figure 3. 6 The hardness of the studied coatings plotted against the relative indentation depth (RID). RID is defined as the ratio of the maximum indentation depth during a measurement to the coating thickness, which is indicative of severity of mechanical contact between the indenter and the coating. The lines were added to guide the eye only.

reported as "coating hardness." As the indenter penetrated deeper into the coated system, a drastic drop in the hardness value was observed for all the coatings, converging at ~7.76 GPa--approximately equivalent to the M2 substrate hardness (63±2 R_c). However, no abrupt decrease in the measured hardness was observed for the coatings tested, which indicated that catastrophic coating failure by delamination and coating removal did not occur even when the coatings were penetrated by the indenter (*RID* > 1). This is indicative of good coating adhesion to the substrate.

3.2.3 Boron Carbide Coating

Boron carbide (B_4C) coatings were provided by Ionbond© Toronto. The commercial designation of said B_4C coating is TriboCote® 50. The coating was deposited by the planar magnetron sputtering of a B_4C target using Ar as the sputtering gas [131] on polished M2 steel discs as described in **Section 3.2.1**. The thickness of the B_4C coating was measured to be 2.0 ± 0.2 μm. The hardness and elastic modulus values of the B_4C coating were measured as 18.5±1.3 GPa and 273.2±10.8 GPa, respectively. The surface roughness (R_a) of the B_4C coating was measured as 10.8 ±1.2 nm.

The XRD pattern of the coated sample (**Figure 3. 7**) exhibited strong peaks from the M2 substrate. The B_4C phase was observed, but only slightly above the background at 2θ values of 23, 34 and 36 degrees. This was indicative of a partially crystallized coating structure. The SEM image of the B_4C coating cross-section created by cryogenic fracture method was interpreted as exhibiting both a "glassy" amorphous region and a

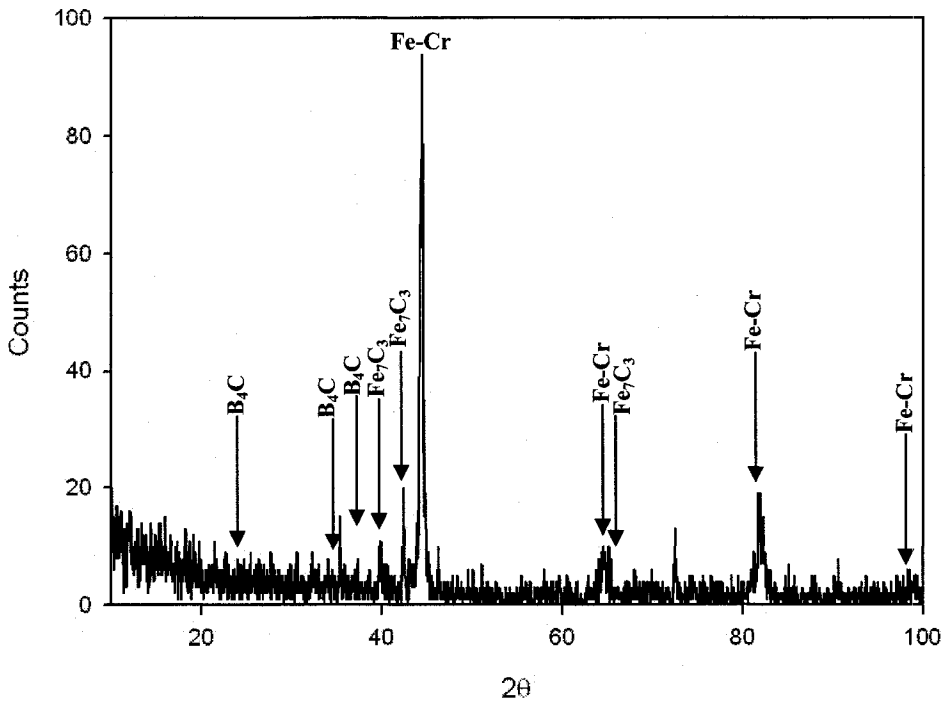

Figure 3. 7 XRD pattern of the B_4C coating.

"crystallized" columnar region (**Figure 3. 8**). The B_4C coating, in turn, was defined as a partially crystallized coating.

3.2.4 Diamond-like Carbon Coatings

3.2.4.1 WC-DLC Coatings

Tungsten doped hydrogenated diamond-like coatings (WC-DLC) were deposited on hardened M2 steel discs (63±2 R_c) by Ionbond© Toronto using the reactive planar magnetron sputtering deposition of tungsten carbide targets with Ar and a hydrocarbon reactive gas [131]. The commercial designation of said coating is TriboCote® 40.

The thickness of the WC-DLC coating was measured to be 2.4±0.008 μm. At an indentation depth of 200 nm, the hardness and elastic modulus values of the WC-DLC coating were measured as 21.8±1.9 GPa and 167.2±9.7 GPa, respectively. The surface roughness (R_a) of the WC-DLC coating was measured as 11.1±1.9 nm while their hydrogen content was measured to be 25 at.%.

The Raman spectrum of the as-deposited WC-DLC coating (**Figure 3. 9**) exhibited a well defined peak around 1526 cm^{-1}, indicating the coating had a considerable ratio of sp^3 bonded carbon.

The XRD pattern of the as-deposited WC-DLC coating (**Figure 3. 10**) did not exhibit any sharp peaks, but a diffuse peak around 38° indicated that the coating had an amorphous structure. Combined with information disclosed by [131], the WC-DLC coating was defined as a coating consisting of tungsten carbide particles embedded in an

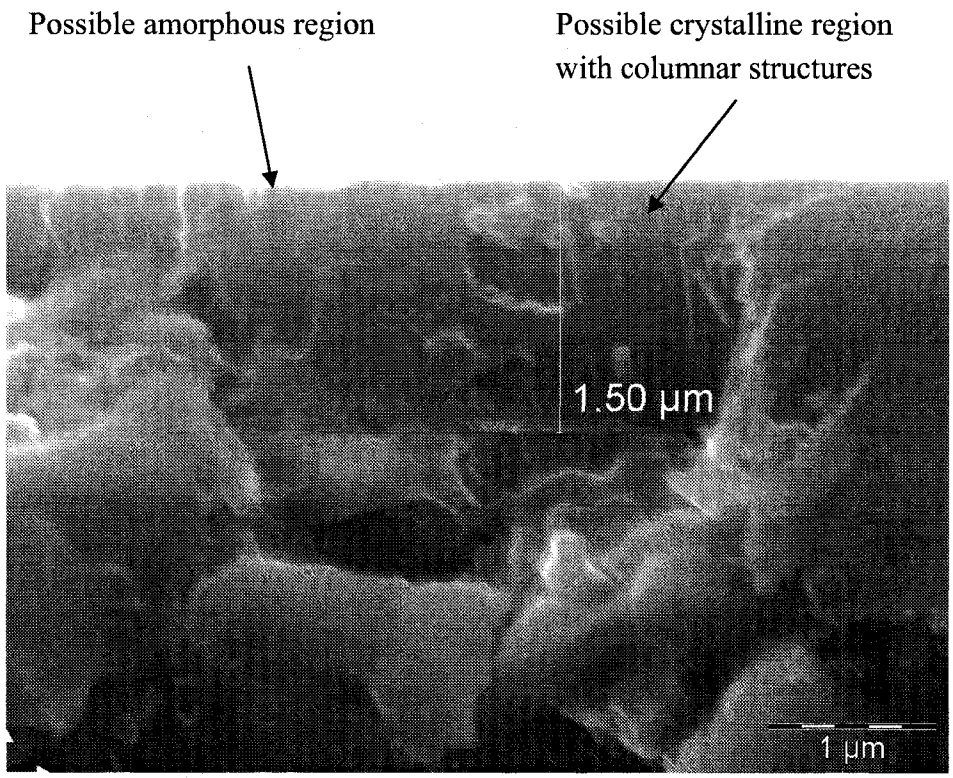

Figure 3. 8 Cross section of the B_4C coating.

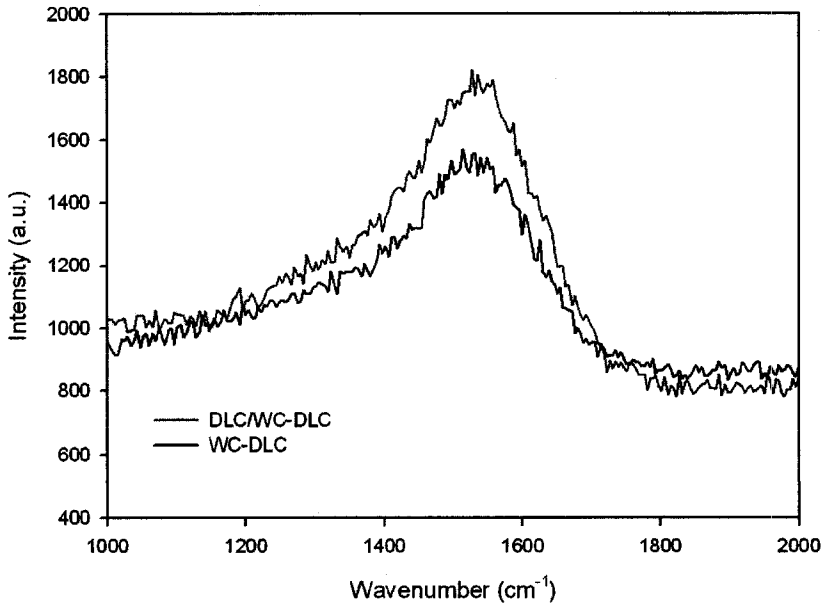

Figure 3. 9 The Raman spectra of the as-deposited WC-DLC coating and DLC/WC-DLC coating.

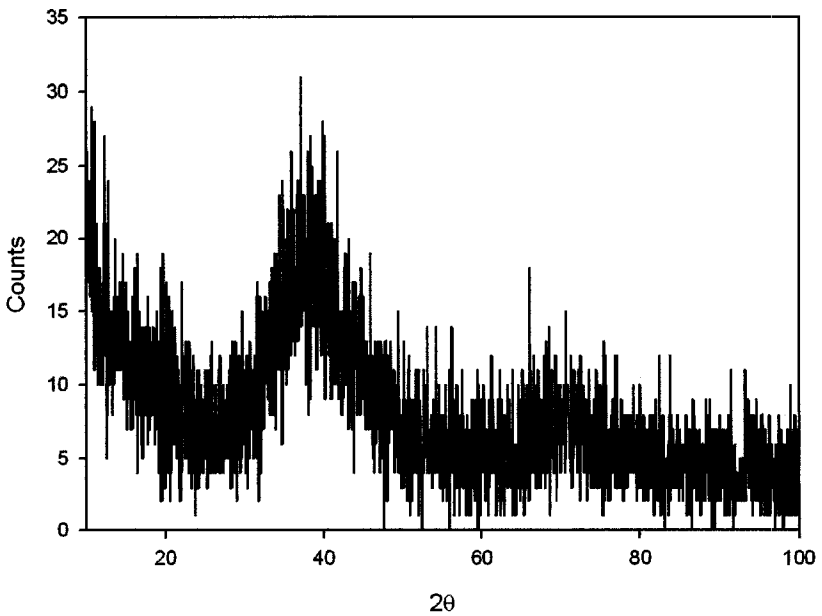

Figure 3. 10 XRD pattern of the WC-DLC coating. The broad peak spans 30-50° is indicative of an amorphous structure.

amorphous hydrogenated carbon matrix. The schematic drawing of the WC-DLC coating structure is presented in **Figure 3. 11**.

3.2.4.2 DLC/WC-DLC Coating

The second type of DLC coating was designated as DLC/WC-DLC, which was a multilayered coating provided by Ionbond© Toronto, commercially designated as TriboCote® 40/41. It was prepared by depositing a layer of WC-DLC coating using the same procedure as the WC-DLC coating, followed by the application of a top DLC layer using plasma assisted chemical vapour deposition [131]. The layered structure of the DLC/WC-DLC coating is confirmed by both plane view SEM image and FIB cross-section image (**Figure 3. 12**) The EDS spectrum obtained from the entire imaging area as shown in **Figure 3. 13.** Tungsten was detected, which was probably in the form of WC particles.

The thickness of the DLC/WC-DLC coating was measured to be 2.1±0.2 μm. At an indentation depth of 200 nm, the hardness and elastic modulus values of the DLC/WC-DLC coating were measured as 26.0±1.0 GPa and 220.4±6.8 GPa, respectively. The surface roughness (R_a) of WC-DLC coating was measured as 8.9±1.3 nm while the hydrogen content of DLC/WC-DLC coatings was measured to be 24 at.%.

The Raman spectrum of the as-deposited DLC/WC-DLC coating (**Figure 3. 9**) exhibited a well defined peak around 1530 cm^{-1}, indicating that the top DLC layer had a amorphous carbon structure with considerable ratio of sp^3 bonded carbon. The schematic

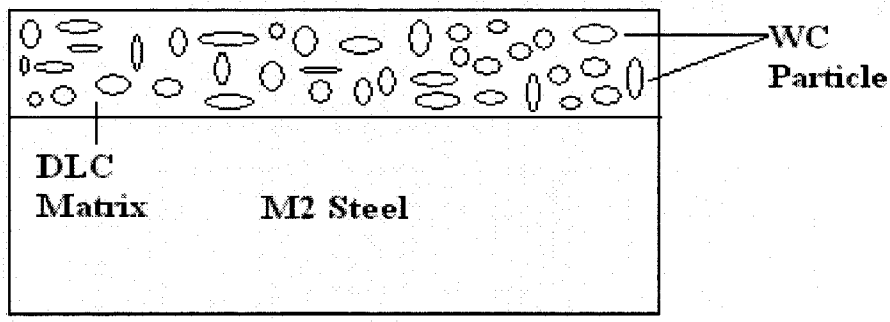

Figure 3. 11 Schematic drawing of WC-DLC coating structure (not to scale).

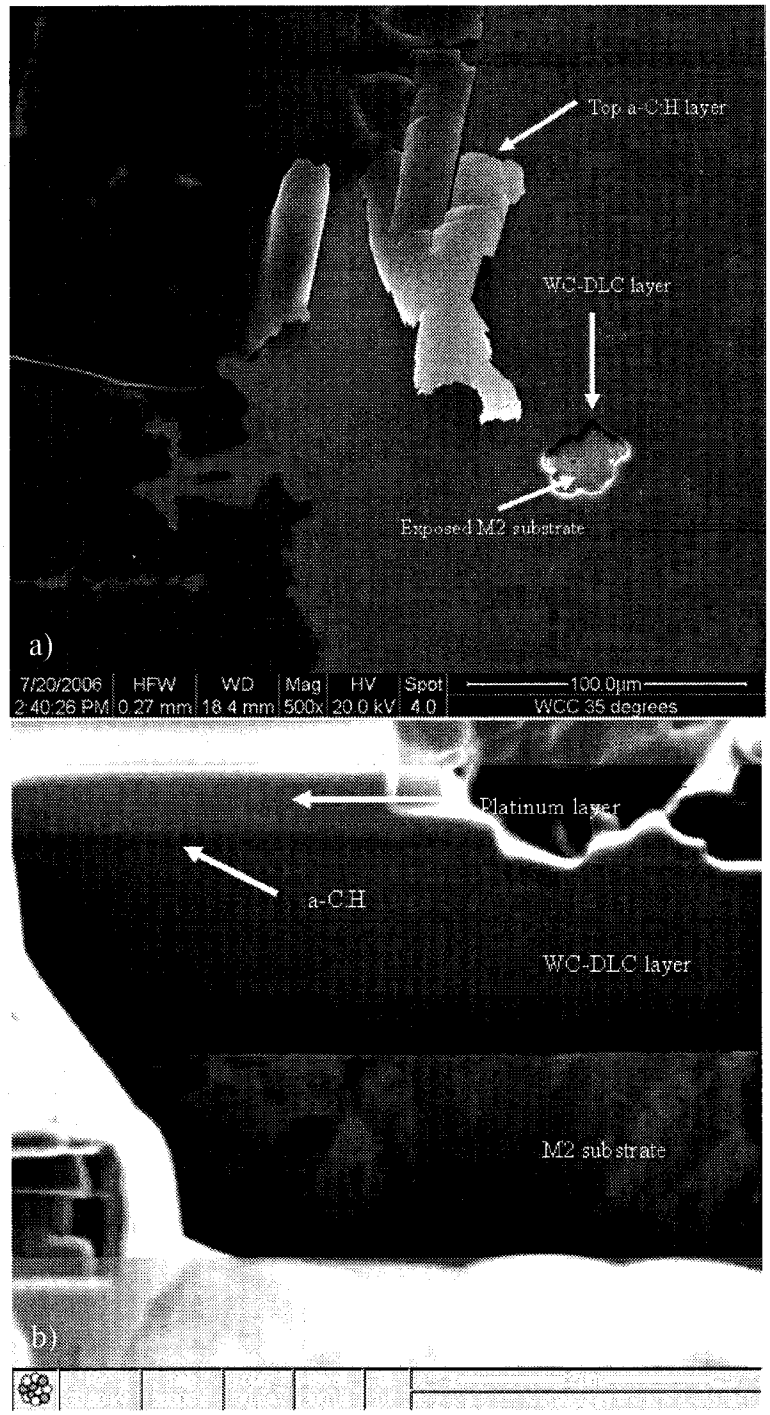

Figure 3. 12 a) Plane view SEM image demonstrating the layered structure of DLC-WC-DLC coating (in this deliberately selected view, the coating's top layer (H-DLC) was delaminated during deposition) **b)** FIB cross-section (courtesy of Dr. Meng-Burany) of the DLC/WC-DLC coating. A platinum protective layer was deposited on top of the coating before the ion milling process. A layered structure of the DLC/WC-DLC coating can be recognized.

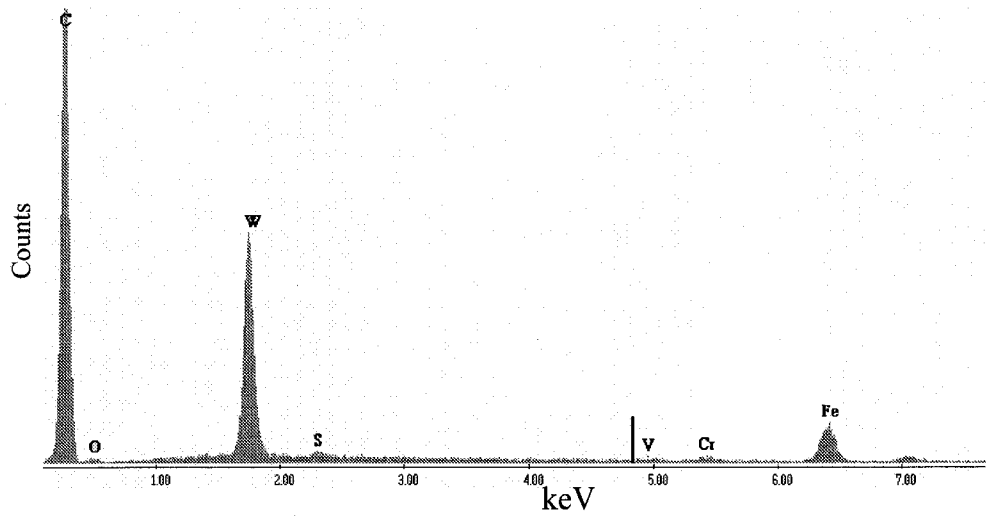

Figure 3. 13 EDS spectrum obtained from the whole area shown in **Figure 3. 12 a)**, which presents the evidence of tungsten content in the coating (within WC-DLC layer).

drawing of the DLC/WC-DLC coating structure is presented in **Figure 3. 14**. The properties of the three studied coatings were summarized in **Table 3. 2**.

3.3 Description of 319 Al Alloy Counterface

The tribological behaviour of the coatings was investigated against an Al 319 alloy because it is widely used throughout the automotive industry to manufacture components such as engine blocks. 319 Al alloy pins of 15 mm in length were made out of a cast alloy brick. One end of the pin was machined into a hemisphere of 3 mm in diameter. The machined pins were then heat treated in air to T5 condition (200 °C for 8 hours). The nominal composition of the 319 Al alloy is given in **Table 3. 3.** The optical microstructures of the 319 Al pins are shown in **Figure 3. 15**. The average hardness of the 319 Al pins was 96.2±11.7 HV_{100}.

3.4 Description of 52100 Steel Counterface

The friction behaviour of B_4C coatings was studied against SAE/AISI 52100 bearing steel (referred to 52100 steel hereafter in the text) because it is the most widely used counterface material for studying the tribological behaviours of B_4C coatings [36][41-45]. The composition (wt%) of the 52100 steel is as follows: 0.98 to 1.1% C, 0.25 to 0.45% Mn, 0.15 to 0.35% Si, 1.3 to 1.6% Cr, and Fe to the balance. 52100 balls, 3 mm in diameter, were provided by National Precision Ball Group of Mechatronics, Inc. (WA, USA). The hardness of the ball was reported to be 700 HV_{25} by Chen et al. [132].

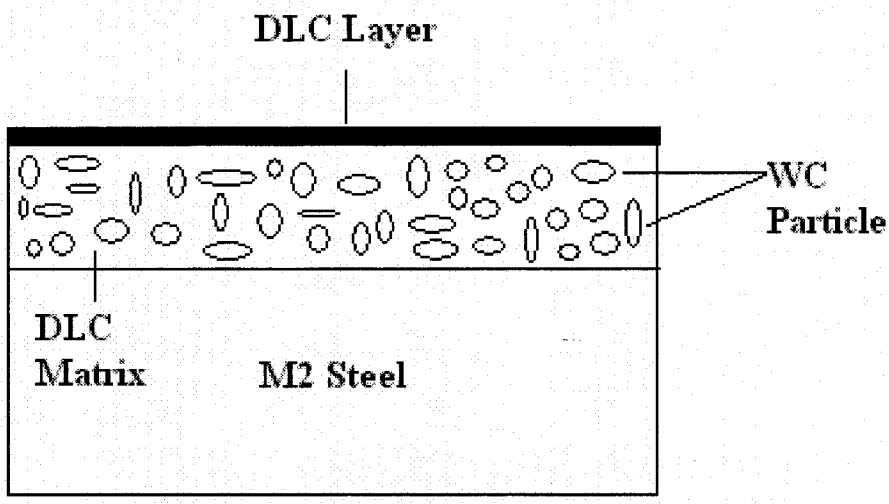

Figure 3. 14 Schematic drawing of DLC/WC-DLC coating structure.

Table 3. 2 Coating properties

Sample	Thickness (μm)	Hardness (GPa)	Elastic Modulus (GPa)	R_a (nm)
B_4C	2.0±0.2	18.5±1.3	273.2±10.8	10.8±1.2
WC-DLC	2.4±0.008	21.8±1.9	167.2±9.7	11.1±1.9
DLC/WC-DLC	2.1±0.2	26.0±1.0	220.4±6.8	8.9±1.3

Table 3. 3 Nominal chemical composition (wt%) of the 319 Al alloy

% S	% Cu	% Fe	% Mg	% Zn	% Mn	% Ni	% Ti	% Al
6	3.5	0.26	0.08	0.01	<0.01	<0.01	0.08	Balance

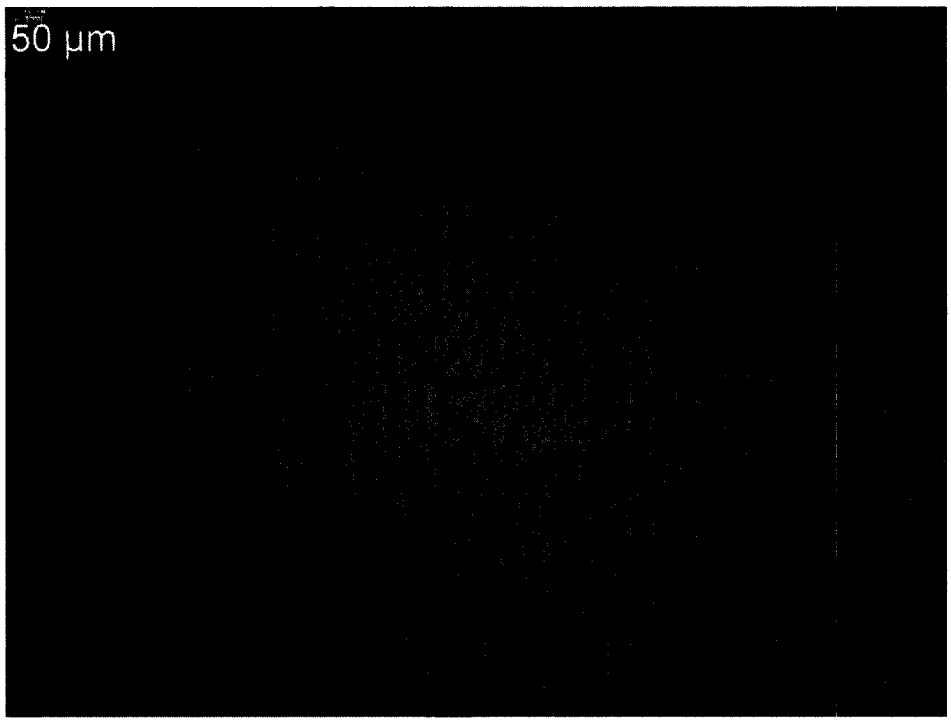

Figure 3. 15 The optical image of the micro structure of the 319 Al pin material.

3.5 Pin-on-disc Tribometer

A high temperature tribometer (CSM, Switzerland) at the University of Windsor was used for the pin-on-disc tests under varying test conditions (**Figure 3. 16**). The tribometer is connected to a computer that controls the sliding speed using the number of revolutions per minute of the driving motor. The test duration can be set by the total number of revolutions, sliding distance or time elapsed. A computer controlled heating module underneath the sample holder heats the sample for the elevated temperature tests (capable of heating to up to 800 °C).

A standard test routine is established and followed for each test. First the pin and coated disc are cleaned in an ultrasonic hexane bath and installed in corresponding holders attached to the tribometer. Then, the diameter of the sliding track is adjusted by turning the knob which moves the friction arm horizontally. The friction arm is built with a position sensing capacity so that the sliding track diameter can be displayed on the computer. Both the friction arm and disc holder are levelled horizontally using a pocket level (Starrett® EDP 50570) for precise loading. The test load is applied on top of the pin holder. All test information (load applied, sliding speed, test duration, test temperature, file identification) are keyed into the computer program and the test is started. A typical screen shot of the test configuration step is shown in **Figure 3. 17**. The friction force is measured by a built-in strain gauge from the very small deflections of the friction arm.

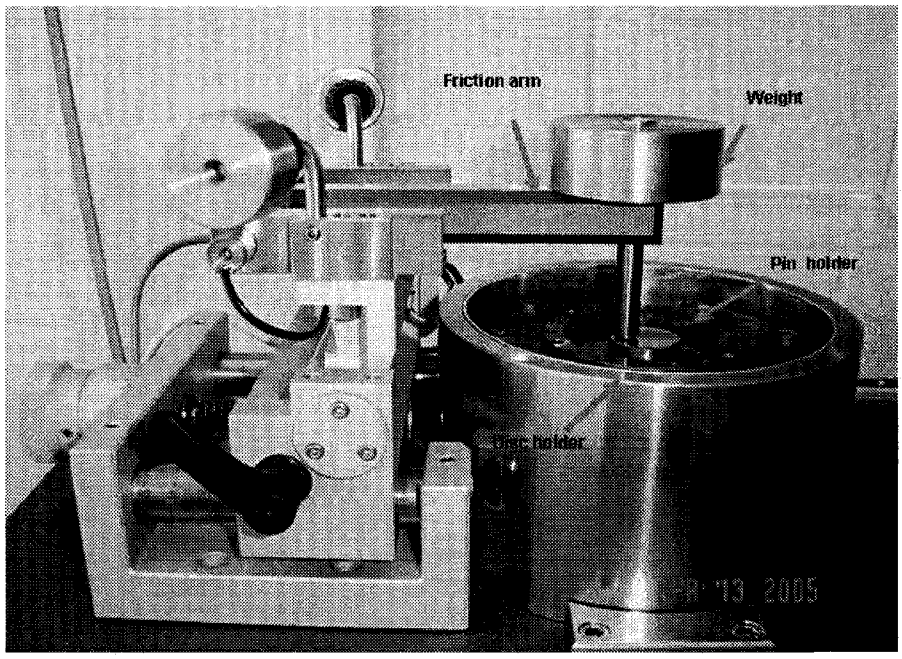

Figure 3. 16 The high temperature tribometer (CSM, Switzerlanf) at the University of Windsor.

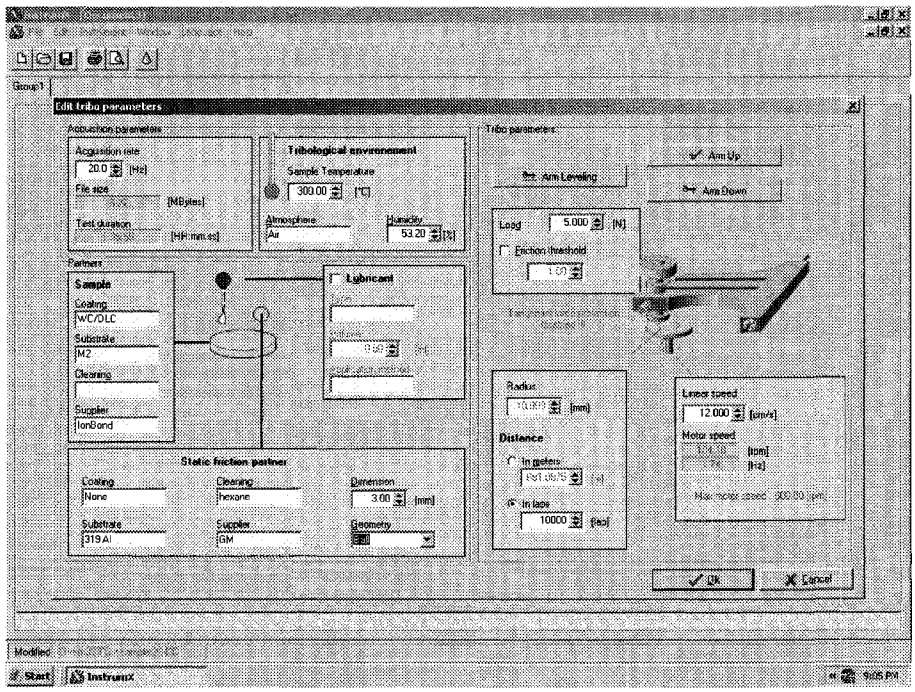

Figure 3. 17 A typical screen of the pin-on-disc test setup procedure.

3.6 Test Conditions

3.6.1 Loading Conditions

All pin-on-disc tests used a constant combination of a load of 5 N and a linear sliding speed of 0.12 m/s. The total number of revolutions used in a particular test depended on the purpose of that test. Typically, a total of 10^3 revolutions was used when the main focus of the test was to observe the general trend of the coefficient of friction curve and observe the adhesion and material transfer phenomenon. A total of 10^4 revolutions were chosen when the aim was to cause a measurable amount of coating wear in that particular test condition.

3.6.2 Control of Test Temperature

To study the tribological behaviour of the coatings at elevated temperatures, the value of the desired test temperature was first keyed into the controlling program. The computer-controlled heating module underneath the sample holder was then activated to heat the sample. The test was started once the preset temperature was reached. The elevated test temperatures (120, 300 and 350 °C) were maintained at a set value by the tribometer.

3.6.3 Control of Test Atmosphere

The actual relative humidity in the lab was 14±5% (referred to as 14% RH thereafter in the text) in autumn and winter and 51±6% (referred to as 51% RH thereafter in the text) in summer--as determined using a handheld hydrometer. The two humidity levels chosen

by this work are 51% and 14% in order to study the effect of relative humidity on the tribological behaviour of the coatings. A nitrogen flow at the rate of 1 litre/s was introduced into the test chamber through a pipe to create a nitrogen atmosphere. The test chamber was sealed by a transparent acrylic glass cover lined with foam during the N_2 test.

The COF curves reported in this work are chosen from at least two tests under each condition as a representative, while all the COF curves recorded are presented in **Appendix A** of this thesis.

3.7 Evaluation Tools and Procedures

3.7.1 Optical and Scanning Electron Microscopy, Energy Dispersive Spectroscopy

Optical microscopy of the samples was performed using the Zeiss Axiovert 25 CF inverted microscope at the University of Windsor. A scanning electron microscope (SEM, JEOL JSM-5800LV) and an SEM equipped with an energy dispersive spectroscope (EDS) were used to characterize the pin and disc surfaces.

3.7.2 Quantification of the Amount of Adhesion

The surface profiles of the wear tracks were obtained using the Wyko NT 1100 optical surface profilometer described in **Section 3.1.4**. At least eight pictures were taken from each wear track at different locations (**Figure 3. 18**). The following methodology was used to analyze the surface profile in order to evaluate the amount of material that adhered to the coatings (**Sections 3.6.2.1** and **3.6.2.2**).

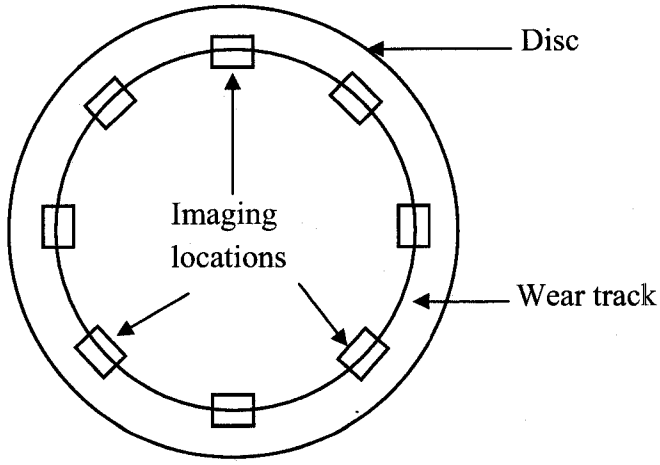

Figure 3. 18 Schematic drawing of the locations where surface profile pictures were taken.

3.7.2.1 Area Fraction of the Wear Track Covered by Adhered Material

A standard routine has been developed and followed in this work in an attempt to measure the area fraction of the wear track covered by adhered material. The procedure for doing this is outlined below.

1) Acquisition of the surface profile at the locations indicated in **Figure 3. 18.** A typical surface profile of the wear track taken from one of the locations indicated for the B_4C coating tested at 120 °C is shown in **Figure 3. 19**. The red particles shown in **Figure 3. 19 a)** are adhered aluminum after the test. The width of the wear track was measured. The area of the wear track (A_t) was calculated by multiplying the measured track width by the length of the profiling area. This approximation is justified by the fact that the length of each profiling area was ~ 1 mm, while the radius of the wear track was typically 9 to 11mm. The area of the whole imaging area (A) was also calculated using the same method to determine the area fraction (A_1) of the image covered by the wear track,

$$A_1 = \frac{A_t}{A} \quad . \qquad \textbf{Equation 3. 6}$$

2) Conversion of the surface profile into gray scale image. By converting the color mode, the contrast caused by the height difference between the adhered material and worn track in a surface profile image was enhanced for more precise analysis by an image analysis program (Buehler Omnipotent) to determine the percentage of the area covered

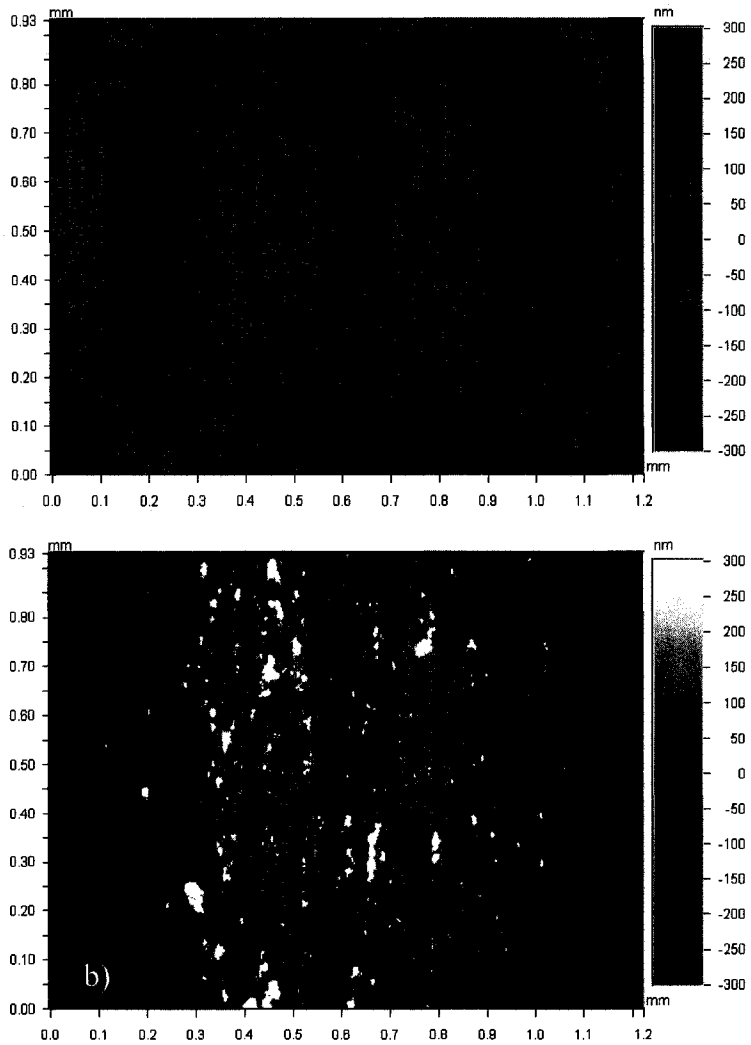

Figure 3. 19 Typical surface profile of the wear track on B_4C coating after tested at 120 °C against 319 Al. **a)** Spectral colour representation of the profile; the red areas are adhered Al. **b)** A gray scale version of **a)**, which was processed by image analysing software to measure the amount of Al adhesion.

by adhered aluminum (A_2) (**Figure 3. 19 b)**),

$$A_2 = \frac{A_{Al}}{A} \qquad \textbf{Equation 3. 7}$$

where A_{Al} is the area covered by adhered aluminum and A is the area covered by the image. The result was then divided by the area fraction covered by the wear track to determine the wear area fraction covered by adhered material, A_{cover}:

$$A_{cover} = \frac{A_2}{A_1} = \frac{A_{Al}/A}{A_t/A} = \frac{A_{Al}}{A_t} \qquad \textbf{Equation 3. 8}$$

3.7.2.2 Thickness of the Adhered Material

Bearing ratio curves were adapted in the current study to provide an estimation of the thickness of adhered material. Basically, bearing curves represent how much material will "bear" an incoming plane at a certain depth in a 3-D space. However, a 2-D diagram is used below to explain these concepts. **Figure 3. 20** shows a two-dimensional surface profile of an evaluation length L. The profile is bounded by a line labelled 0%--which is even with the highest peak--and a line labelled 100%, which is even with the lowest valley. A line at a depth p below the highest peak is also shown. The bearing length (L_b) is defined as the sum of the profile lengths where the line at depth p intercepts the surface,

$$L_b = \sum_{i=1}^{n} b_i$$ **Equation 3. 9**

As a three-dimensional extension of this concept, if a plane were to intercept the profile surface at this depth p, individual areas would be created as $A_1, A_2, A_3, \ldots, A_n$. The sum of these areas would make up the bearing area A_b,

$$A_b = \sum_{i=1}^{n} A_i$$ **Equation 3. 10**

Thus the bearing area ratio t_p, is defined as the ratio of the bearing area to the total evaluation area (A),

$$t_p = \frac{A_b}{A}.$$ **Equation 3. 11**

The bearing ratio curve is simply a graphical presentation of the t_p parameter in relation to the surface level. **Figure 3. 21** shows the average bearing ratio curves of the unworn B_4C coating and the B_4C coating tested at 120 °C. The highest peak--as bounded by 0% bearing ratio--increased significantly due to material adhesion. It should be noted that a large portion of the curves are flat, indicating the mean "flat" surface of the coating. This feature of the curves enables the truncation (marked by the dashed rectangle) of the curve to emphasize only the height increase caused by the adhesion. The curves reported in this work are the truncated form as shown in **Figure 3. 21 b)**.

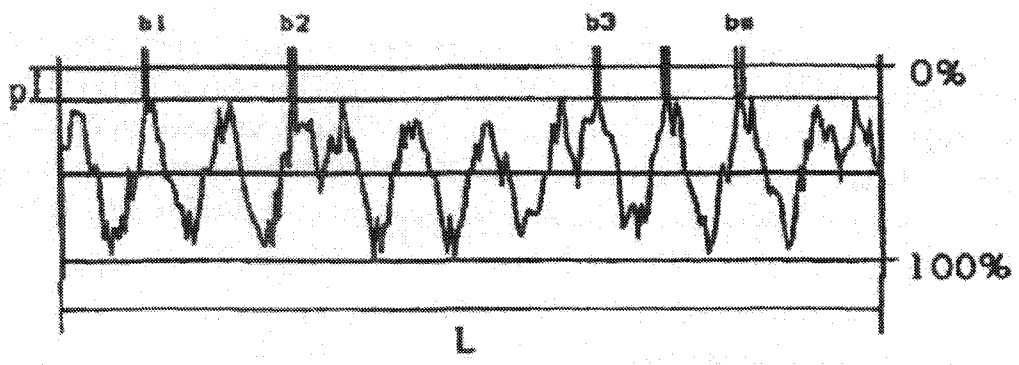

Figure 3. 20 A two dimensional surface profile of an evaluation length L. The bearing length is defined as the sum of the profile lengths (b_1, b_2, b_3,..., b_n) where the line at depth p intercepts the sampled profile.

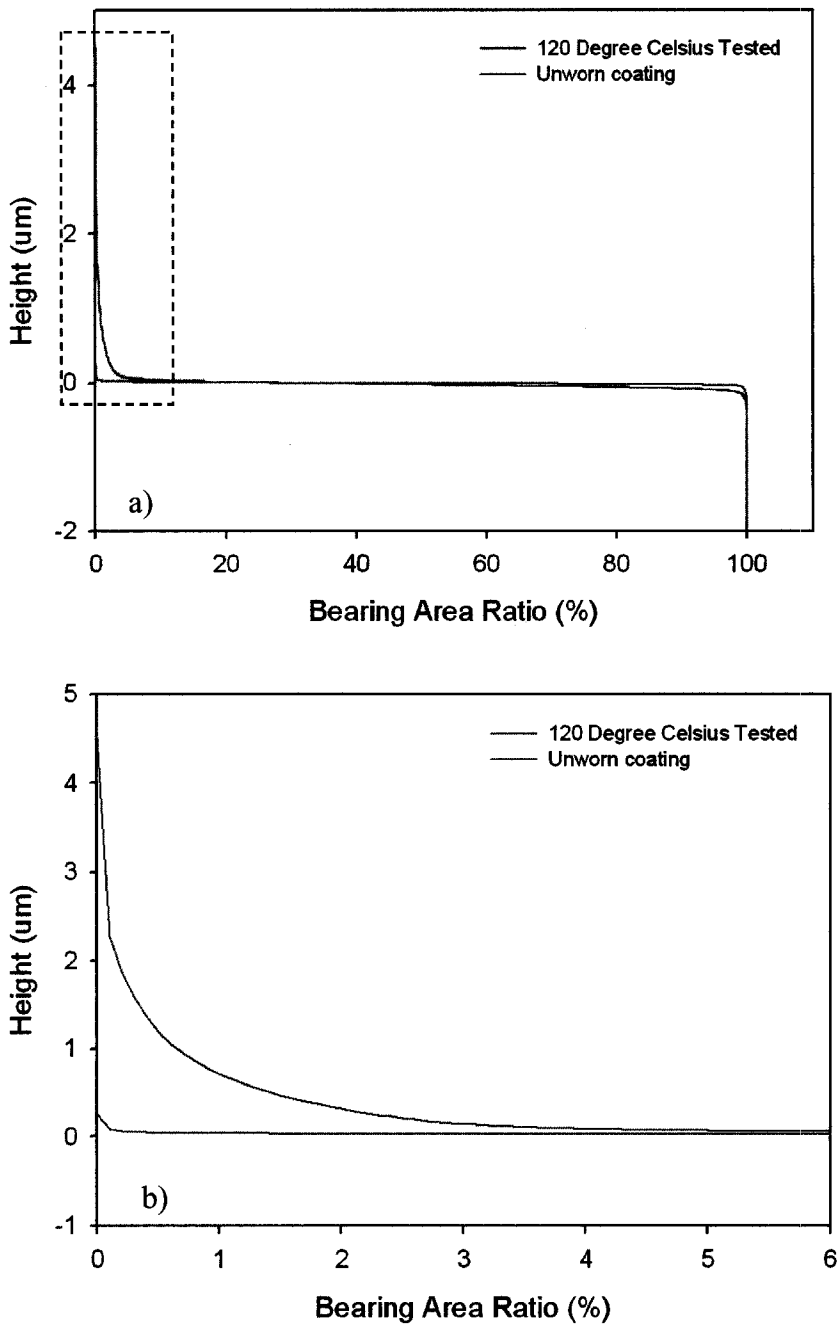

Figure 3. 21 a) Bearing ratio curves of the unworn B_4C coating and B_4C coating tested at 120 °C; **b)** Truncation of **a)** as indicated by the dashed rectangle. The purpose of this truncation is to emphasize the height increase caused by material adhesion.

3.7.3 Measurement of Wear Rates

The wear rate (W) of a sample is expressed as mm^3/m, i.e. the volume loss of material per unit sliding length. For a circular track, the volume of the material removed (V_w) can be calculated by multiplying the average cross-sectional area (A_{cross}) of the wear track with the perimeter of the circle ($2\pi R$) passing through the center of the wear track. Thus

$$V_w = 2\pi R A_{cross} \qquad \textbf{Equation 3. 12}$$

The average A_{cross} is found by measuring the A_{cross} of the wear track at twelve different locations using the optical surface profilometer. As an example, the surface and cross-sectional profiles of a region of the wear track on the WC-DLC coating tested against 319 Al at 120 °C are shown in **Figure 3. 22**. The wear rate can be expressed as

$$W = \frac{V_w}{L}, \text{ and} \qquad \textbf{Equation 3. 13}$$

$$L = 2\pi R N \qquad \textbf{Equation 3. 14}$$

where L is the sliding distance and N is the number of revolutions slid respectively. Thus,

$$W = \frac{2\pi R A_{cross}}{2\pi R N} \qquad \textbf{Equation 3. 15}$$

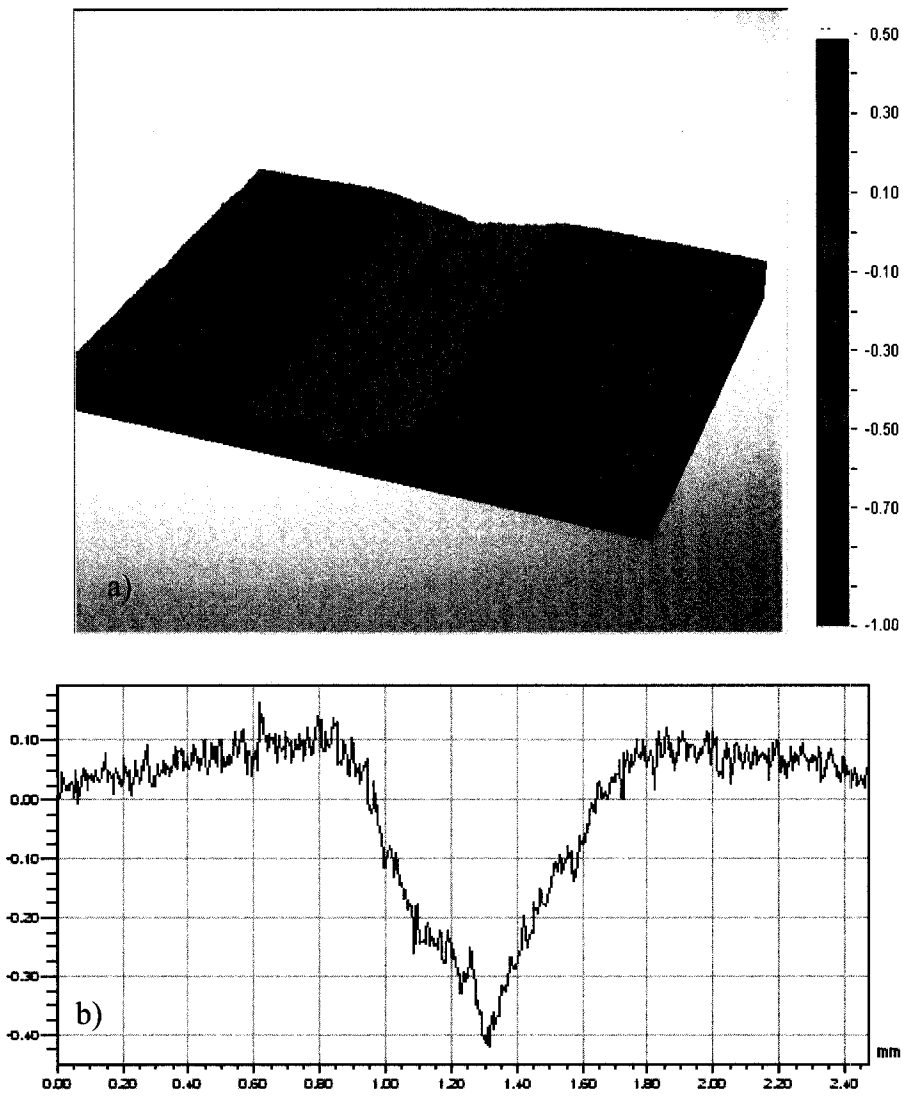

Figure 3. 22 a) The surface and **b)** the cross-sectional profiles of a region of the wear track on the WC-DLC coating tested against 319 Al at 120°C.

Cancellation of the $2\pi R$ term results in

$$W = \frac{A_{cross}}{N}$$ **Equation 3. 16**

The average results were plotted against test temperature and presented in **Sections 5.1** and **5.2**.

CHAPTER 4 TRIBOLOGICAL BEHAVIOUR OF B_4C COATINGS AGAINST 319 AL ALLOY

While B_4C coatings are successfully used on tools for the machining of aluminum alloys [8-9] and on automotive gear boxes [133] to improve fatigue resistance, their tribology against Al is not known. This chapter reports on the tribological behaviour of B_4C coatings deposited on M2 steel substrates subjected to dry sliding against a 319 Al alloy. These experiments aim to evaluate whether or not B_4C is suitable as a tool coating material for the dry machining of Al alloys by determining their COF and their tendency to adhere to aluminum. The effects of test temperature and working atmosphere on the amount of aluminum adhesion and friction were studied in particular, and the morphology of the wear tracks was examined using SEM. Optical surface profilometry was also employed in order to quantify the amount of Al transfer and the severity of wear damage. Another goal of this study was to compare the aluminum adhesion mitigating performance of B_4C coatings against Al with that of other industrial coatings. 52100 steel balls were also used as counterfaces against B_4C coatings. The friction behaviour of 319 Al and 52100 steel against B_4C coatings at different test temperatures was compared.

4.1 Pin-on-disc Tests in Ambient Air against 319 Al

At 25°C (51% RH) B_4C coatings tested against 319 Al were characterized by COF values fluctuating between 0.4 and 0.7 (**Figure 4. 1**), and a pronounced squeak accompanied the entire testing period. SEM observation showed that there were chunks of adhered material distributed inside the worn track after 10^4 revolutions of testing (**Figure 4. 2 a)** and **b)**) and the coating was removed as shown in a back scattered SEM image (**Figure 4. 2 c)**) and the EDS spectrum of the exposed substrate (**Figure 4. 2 d)**). The EDS results revealed that the adhered material was oxidized aluminum that had been transferred from the pin tip onto the coating surface (**Figure 4. 2 e)**). The wear debris produced after the test was confirmed to be oxidized Al exhibiting two main morphology types: larger plate-wedge like chips and smaller rounded particles (**Figure 4. 3**). Some of the plate-wedge like chips seemed to be agglomeration of small round particles. An examination of the worn pin tip after testing in ambient air for 10^4 revolutions showed that there were loosely attached chips at the exit side of the pin tip (**Figure 4. 4 a)**). EDS composition analysis was conducted on the worn pin tip at different locations, and only a negligible amount of carbon could be detected beyond the expected aluminum oxide. The wear rate of the pin was calculated to be $9.73\times10^{-4}mm^3/m$--data achieved by measuring the size of the wear scar on the pin tip and following the wear rate definition in **Section 3.7.3**. Because the coating was removed from the substrate, efforts to measure the wear rate of the coating were practically rendered meaningless. Thus, another test with the

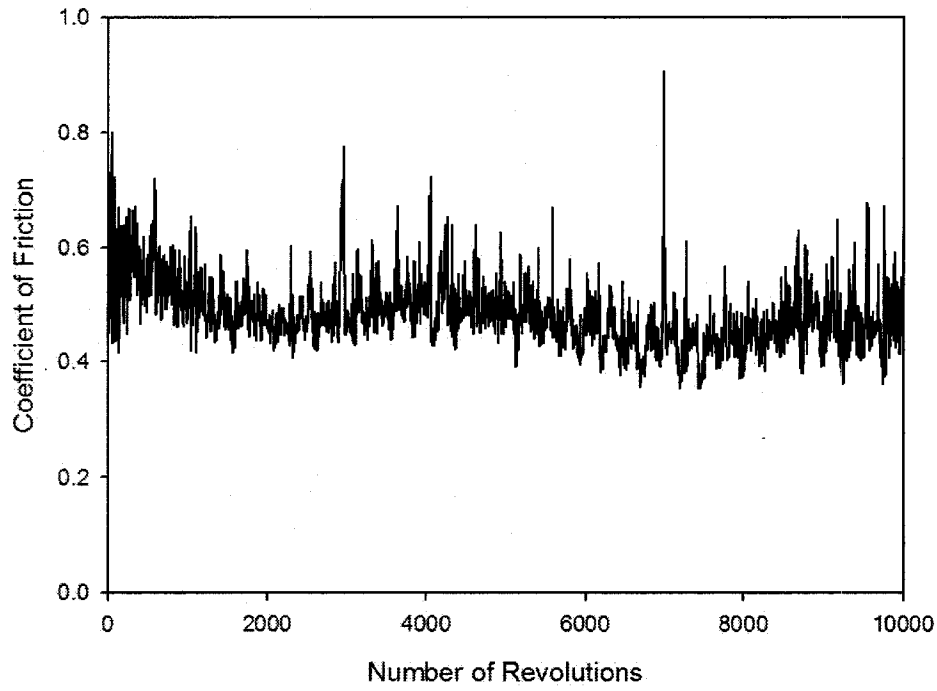

Figure 4. 1 COF curve of the B_4C coatings against 319 Al as a function of number of revolutions tested at room temperature (25 °C) in ambient air (51% RH) for 10^4 revolutions.

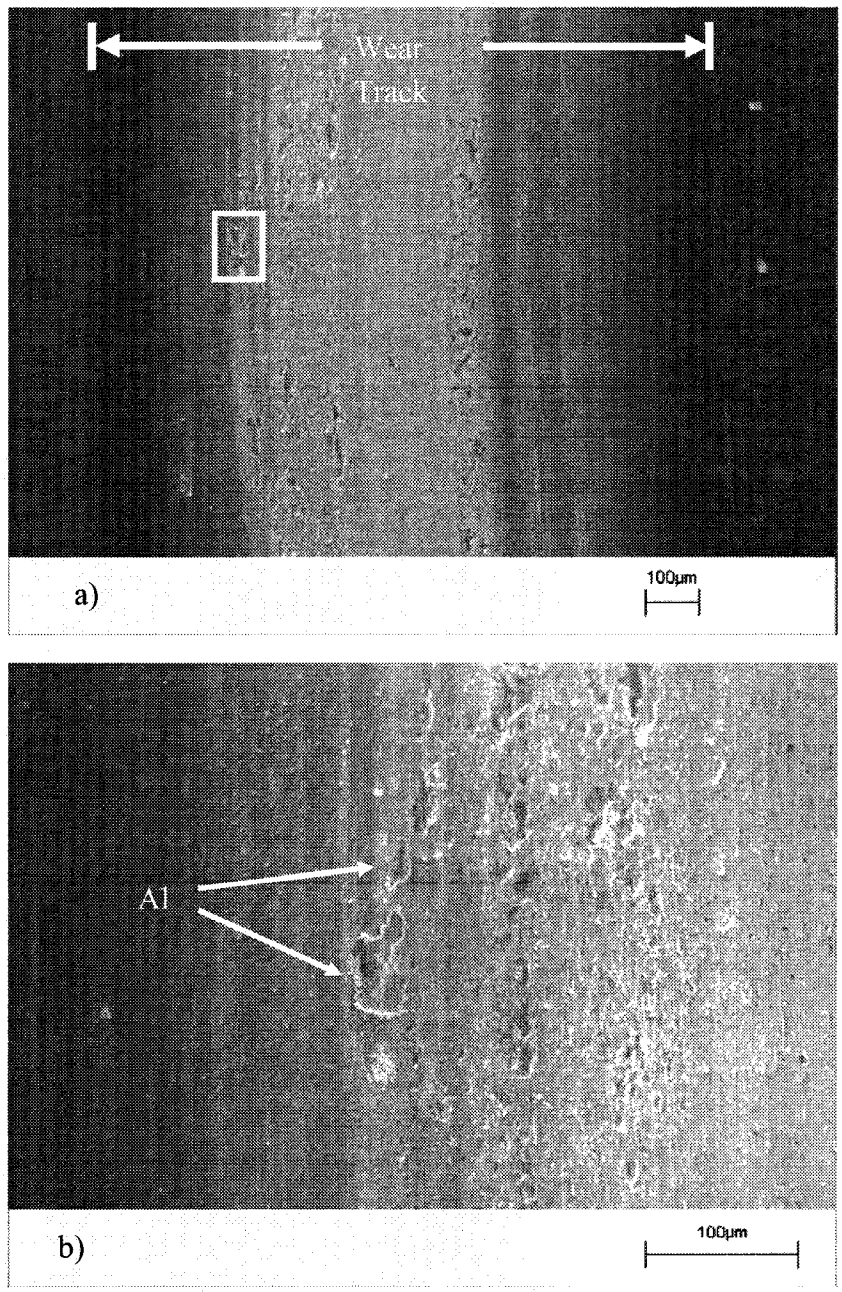

Figure 4.2 a) Secondary electron SEM image of a region of the wear track of the B_4C coating tested against 319 Al in ambient air (51% RH) for 10^4 revolutions; **b)** An enlargement of the framed region in **a)**, showing adhered Al pieces.

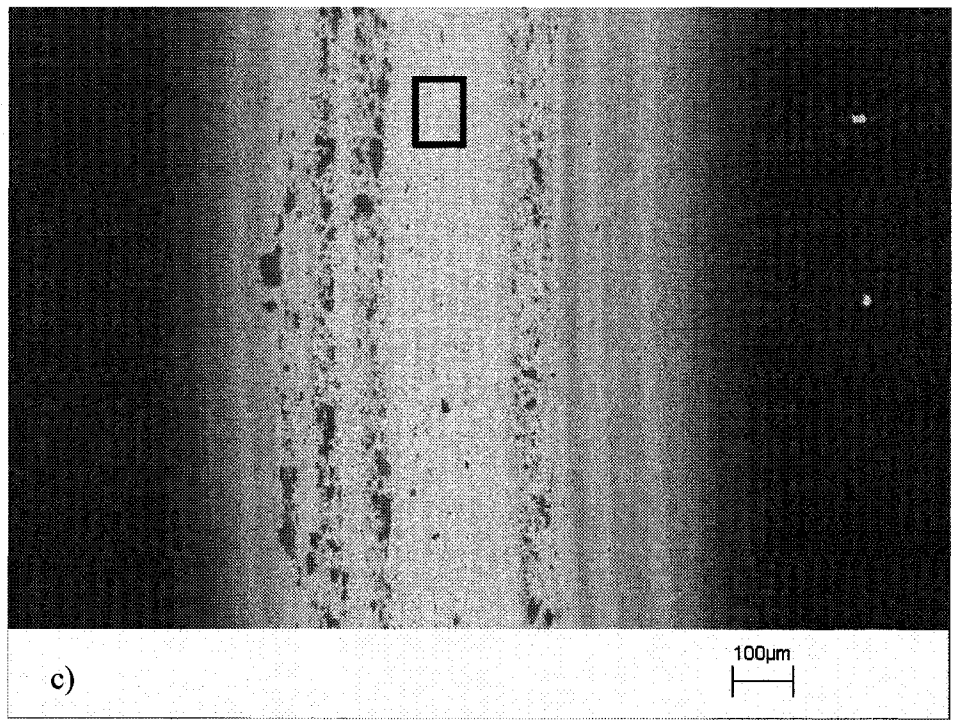

Figure 4.2 c) Backscattered SEM image of the same region in **a)**, showing that B_4C coating was removed

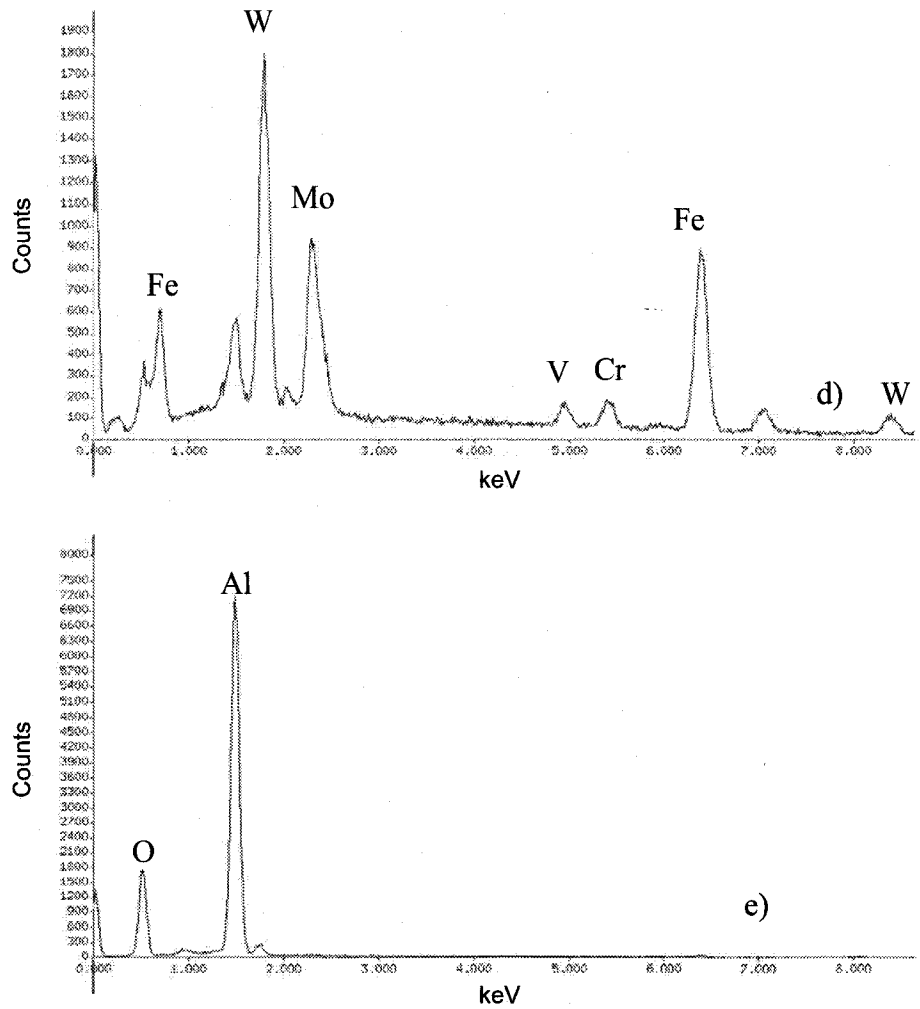

Figure 4. 2 d) EDS spectrum of the area indicated by the frame in c), which shows the elements in the substrate material; **e)** EDS spectrum of the adhered material as marked by the frame in **a)**, which is oxidized aluminum.

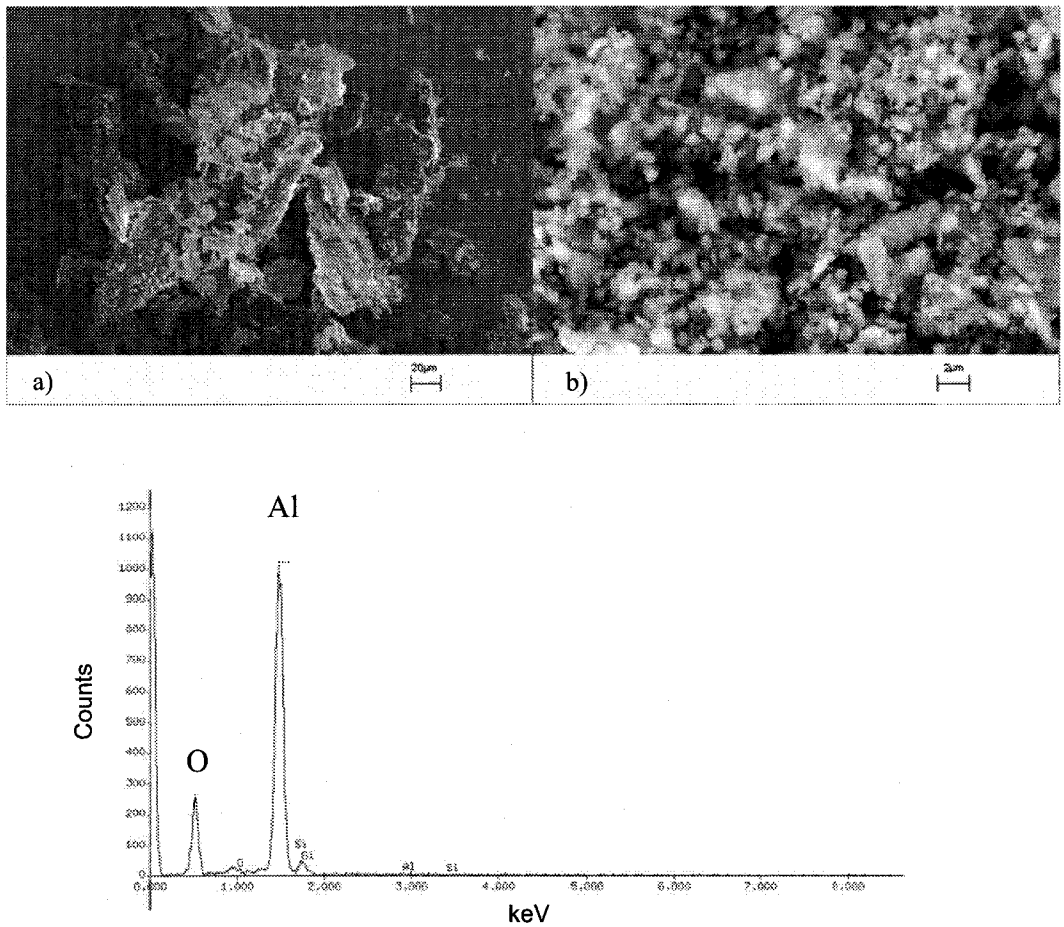

Figure 4. 3 Wear debris collected after tested against 319 Al in ambient air (51% RH) for 10^4 revolutions. Two kinds of morphology were observed (plate-wedge like **(a)** and small round particles **(b)**). The EDS **(c)** spectrum of the debris showed that they consisted of oxidized aluminum.

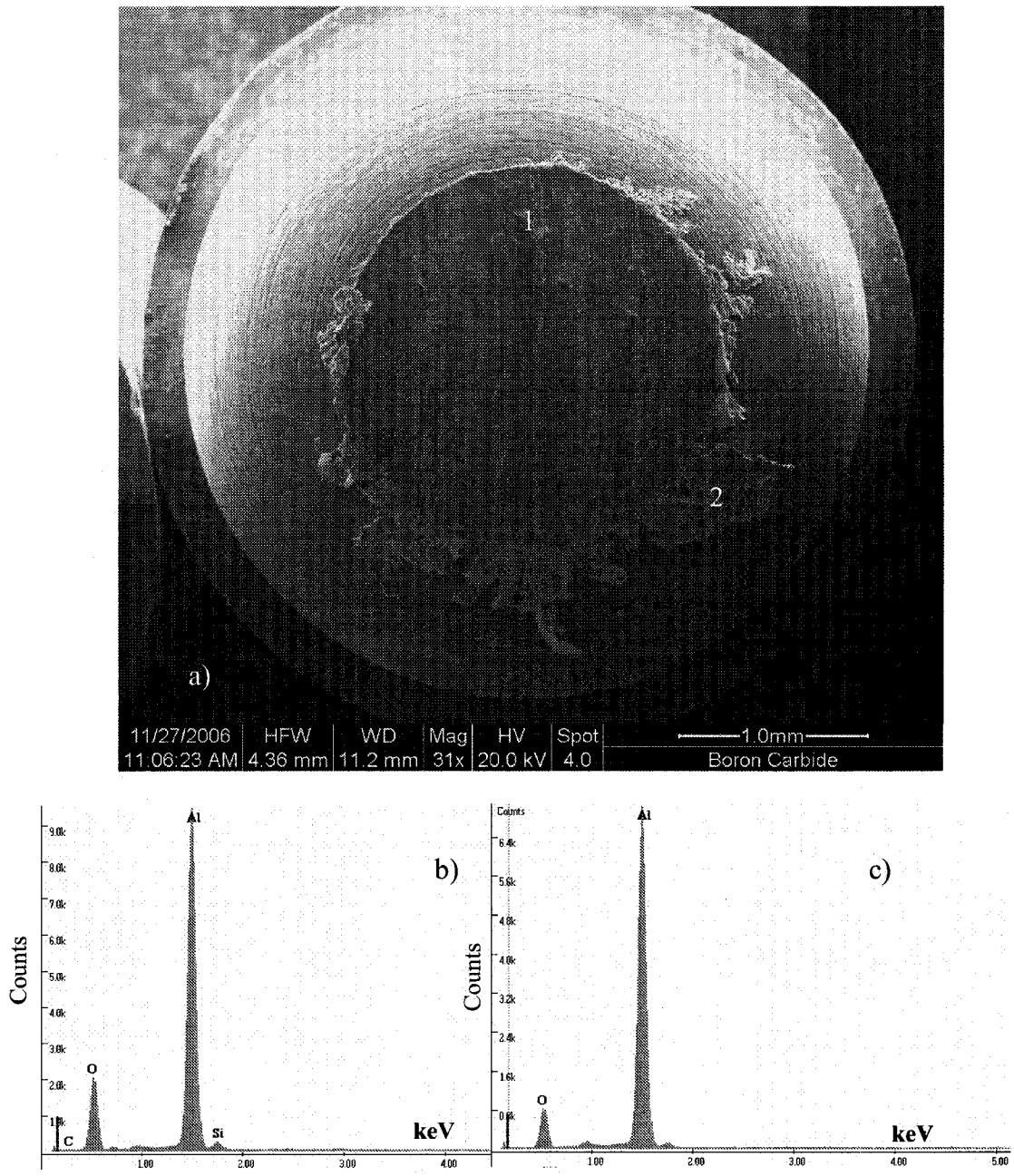

Figure 4. 4 a) Secondary electron SEM image of a 319 Al pin tip tested in ambient air (51% RH) for 10^4 revolutions. Extruded aluminum chips can be observed at the exiting side of the worn region. EDS spectra of regions labelled as 1 (**b)**) and 2 (**c)**) are also presented.

same conditions was conducted and then stopped at 10^3 revolutions to study the transfer and adhesion of aluminum. **Figure 4. 5** shows that aluminum transfer to the coating occurred even after 1000 revolutions. The corresponding COF curve recorded is shown in **Figure 4. 6 a)**. The area fraction of the wear track covered by transferred aluminum was measured to be 0.84±0.40% and the wear rate of the B_4C coating was 4.2×10^{-5} mm^3/m.

4.2 Pin-on-disc Tests at Elevated Temperatures against 319 Al

To investigate the effect of temperature on the material adhesion and friction behaviour of B_4C coatings, the B_4C coatings were also tested against 319 Al at 120 and 300 °C. The COF curves recorded during the course of sliding contact between the 319 Al pins and B_4C samples are presented in **Figure 4. 6 a)**. When tests at elevated temperatures were conducted, the pin-on-disc machine made a disturbing noise throughout the test, so the test duration was limited to 10^3 revolutions in order to protect the equipment. At 120°C, the COF curve exhibited the same trend it displayed at room temperature--fluctuating between 0.4 and 0.7. The variation of the COF curve was enlarged from 0.3 to 0.8 at 300°C, and as the test temperature was increased, the COF curve of the coating seemed to fluctuate around a slightly lower mean value. In an attempt to quantify this observation, the mean COF values were calculated for three different temperatures. The average COF values were 0.48±0.06, 0.44±0.06 and 0.44±0.09 at 25, 120 and 300 °C, respectively (**Figure 4. 6 b)**). SEM images (**Figure 4. 7**

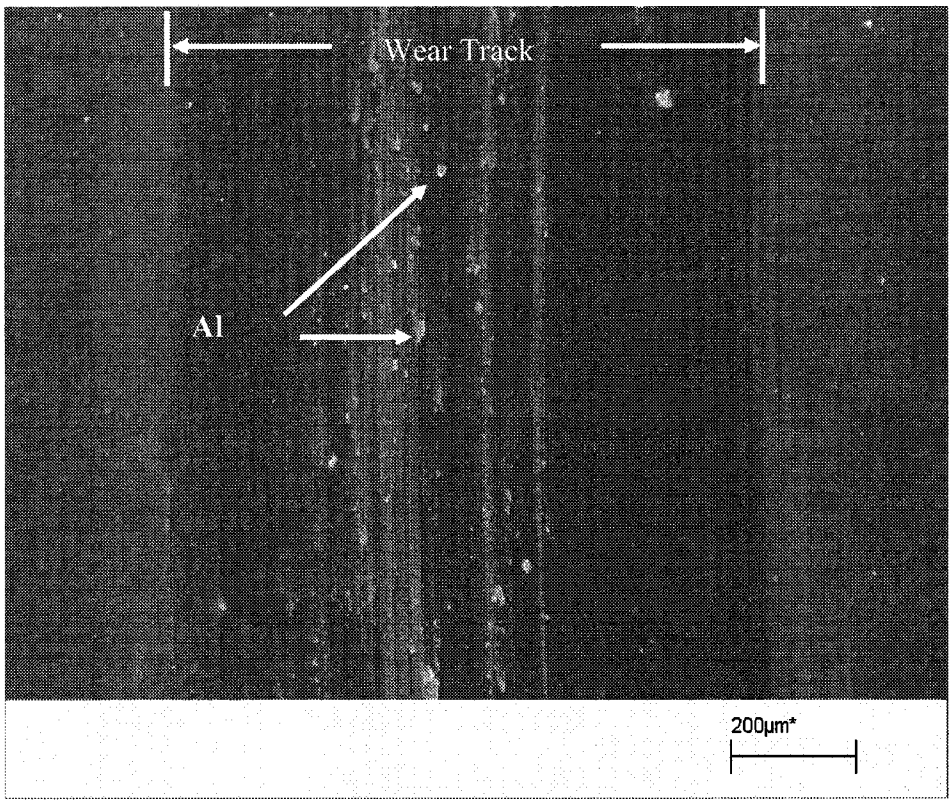

Figure 4. 5 Secondary electron SEM image of a region of the wear track of the B_4C coating tested against 319 Al at room temperature (51% RH) for 10^3 revolutions.

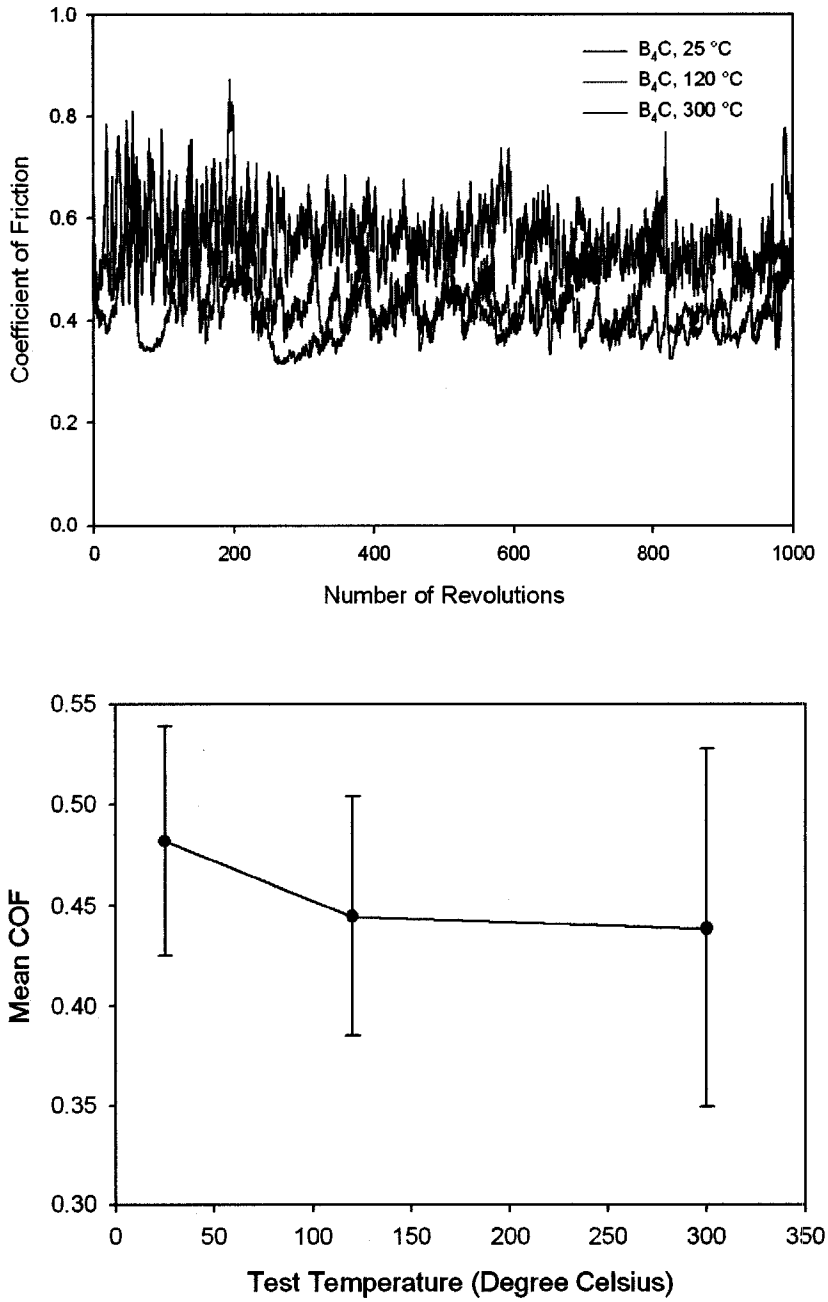

Figure 4. 6 a) COF curves of the B_4C coatings against 319 Al as a function of number of revolutions at different temperatures; **b)** Mean COF values calculated from the curves shown in a) for different test temperatures.

and **Figure 4. 8**) showed that as the test temperature was increased, the amount of transferred aluminum also drastically increased. The adhered aluminum appeared in the form of small, discrete flakes on the wear tracks tested at 25 °C after 10^3 revolutions (**Figure 4. 5**). At 120 °C, an increase in the size of adhered aluminum platelets could be readily observed, characterized by a change in the shape from flakes to patches. The patches grew considerably at 300 °C and overlapping of adhered aluminum patches occurred as shown in **Figure 4. 8**. This growth from small aluminum islands at 25 °C into chunks of overlapping aluminum slabs at 300 °C was also confirmed by 3-D profile images of the wear tracks (**Figure 4. 9**). The wear track area fraction covered by adhered aluminum was measured to be 3.9±1.4% at 120 °C and 16.3±1.7% at 300 °C (**Figure 4. 10**). The bearing ratio curves of the same area reveal that the thickness of adhered aluminum increased in tandem with the test temperature (**Figure 4. 11**).

In an attempt to elucidate the frictional behaviour of B_4C coatings tested at elevated temperatures, the mechanical properties of the coatings were measured after testing the samples at 300 °C using nano-indentation. The hardness and elastic modulus of the sample tested at 300 °C were 16.0±1.1 GPa and 257.3±15.4 GPa, respectively--a 7 % decrease in both the coating hardness and elastic modulus when compared to those of the as-deposited coatings (**Figure 4. 12**). The coating was annealed in an Ar atmosphere at 300 °C for 90 min and investigated by SEM and EDS line scans across the coating-substrate interface in order to investigate the possible change in coating

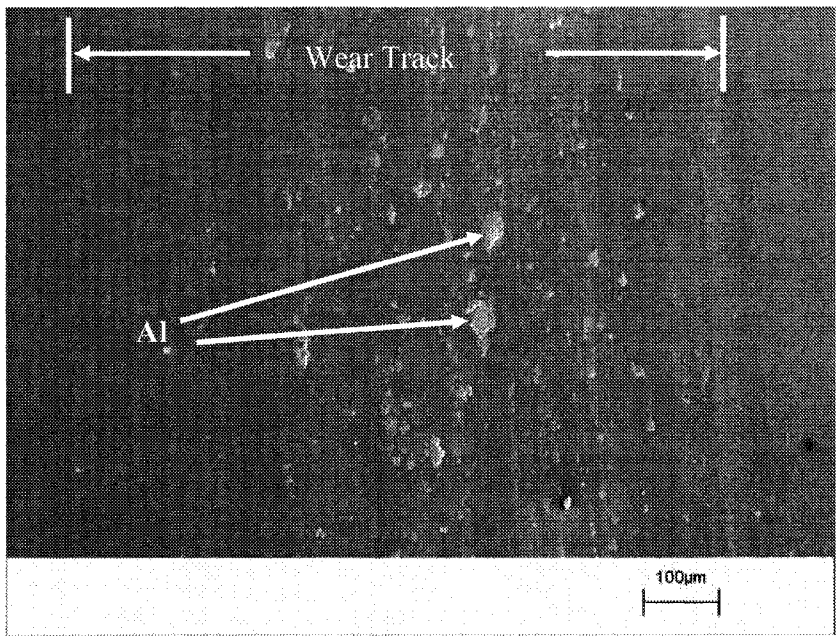

Figure 4. 7 Secondary electron SEM image of a region of the wear track of the B_4C coating tested against 319 Al at 120 °C for 10^3 revolutions.

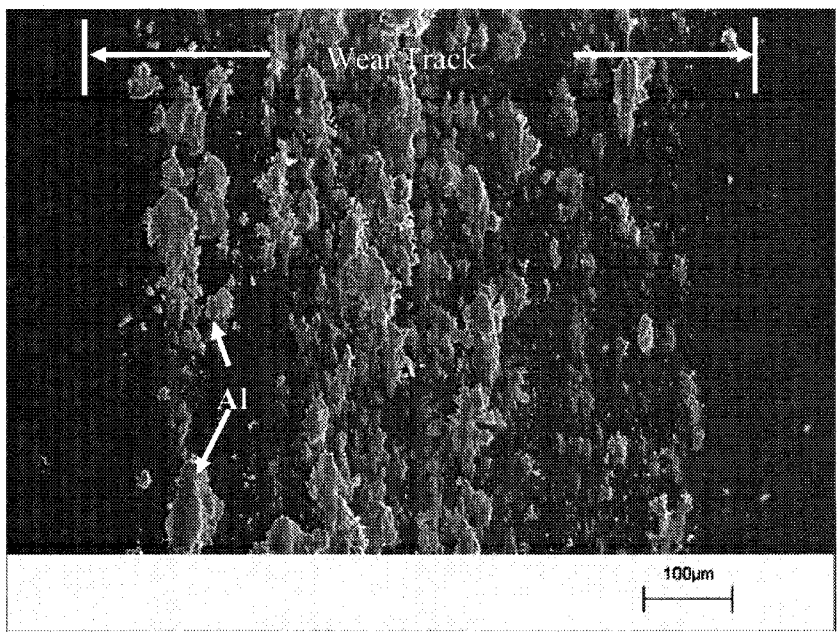

Figure 4. 8 Secondary electron SEM image of a region of the wear track of the B_4C coating tested against 319 Al at 300 °C for 10^3 revolutions.

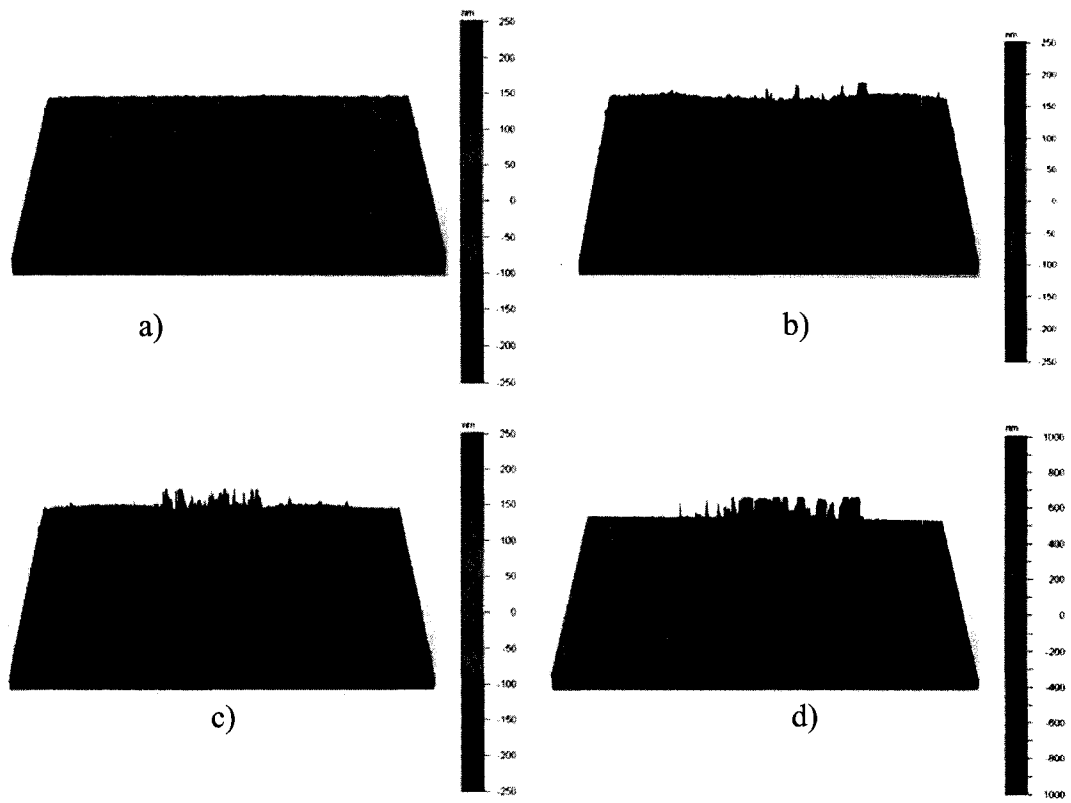

Figure 4. 9 3-D surface profile images of B_4C coatings: **a)** Unworn coating; **b)** Tested at 25 °C; **c)** Tested at 120 °C; **d)** Tested at 300 °C.

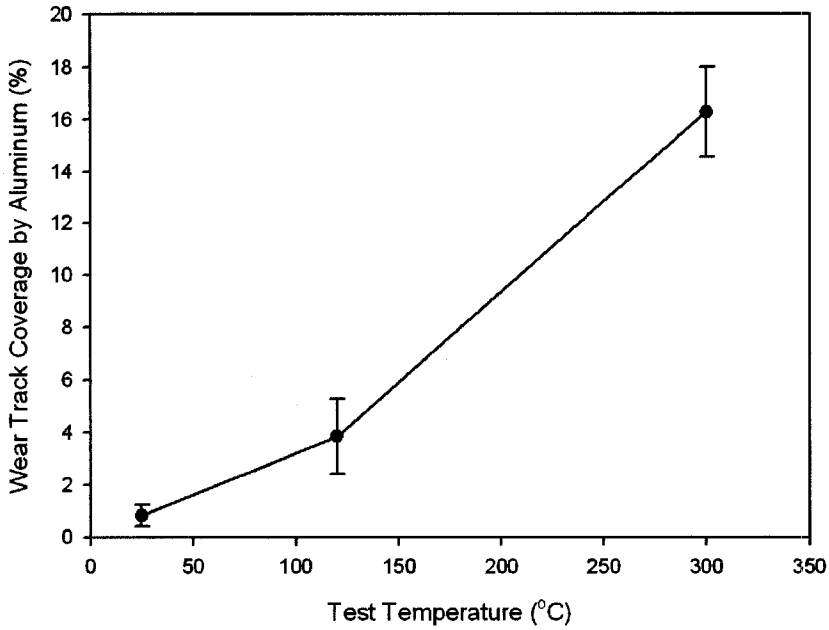

Figure 4. 10 Effect of test temperature on the percentage of the wear tracks on B_4C coatings covered by aluminum. The test performed at 25 °C was under 51% RH.

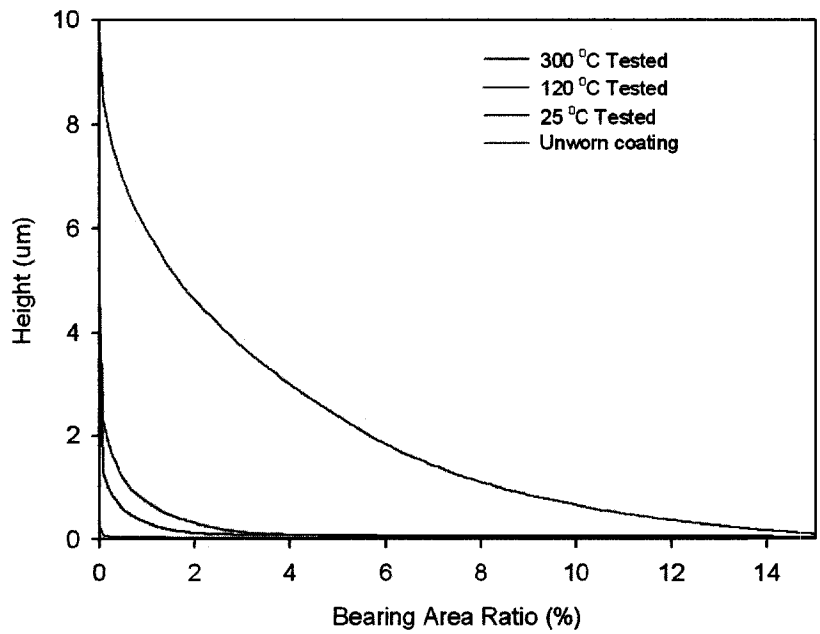

Figure 4. 11 The bearing ratio curves of the sampling region used to measure the amount of aluminum coverage at different test temperatures. The test performed at 25 °C was under 51% RH.

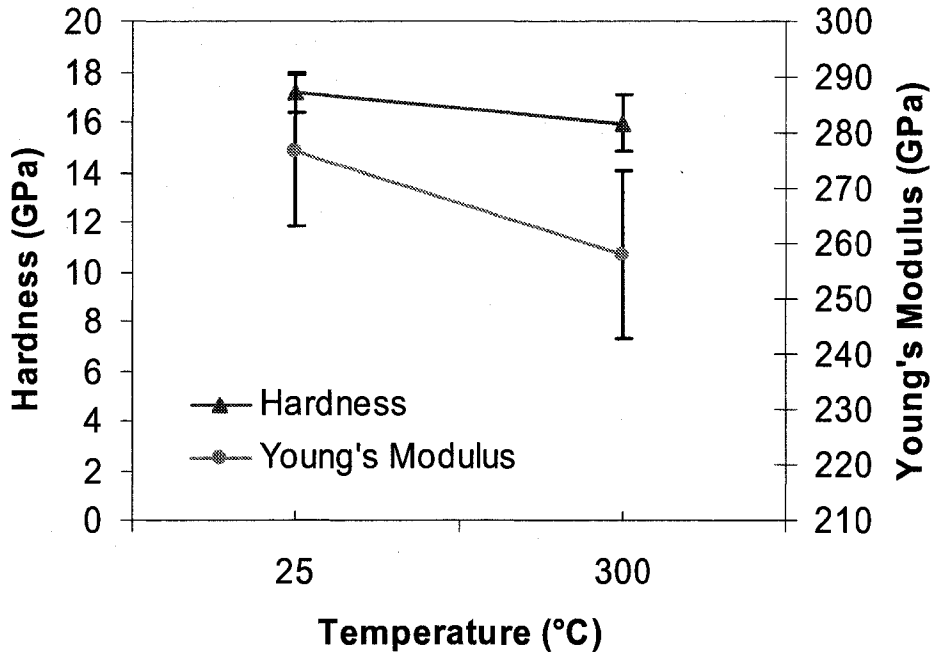

Figure 4. 12 Hardness and elastic modulus plotted as a function of test temperature.

composition and structure. A columnar structure with well defined column boundaries was observed for the annealled B_4C sample (**Figure 4. 13**). The EDS line scan results (**Figure 4. 14 b)**) displayed that the boundary between the coating and substrate was less sharp after annealing--a detail indicated by a smoother change in the carbon counts over the coating-substrate boundary when compared to that of the as-received coating (**Figure 4. 14 a)**).

4.3 Pin-on-disc Tests Against 52100 Steel

The friction behaviour of B_4C coatings dry sliding against 52100 steel at different test temperatures was studied for comparison with that of 319 Al against B_4C coatings.

The COF values of 52100 steel against B_4C coating varied between 0.7 and 0.9 when tested at room temperature at 51% RH. At 120 °C, the COF values fluctuated between 1.2 and 0.8. When tested at 300 °C, the COF curve fluctuated between 0.7 and 1.1 at the beginning of the testing course and stabilized (relatively) at approximately 1.0 (**Figure 4. 15 a)**). The average COF values were 0.80±0.05, 1.03±0.09 and 0.94±0.10 at 25, 120 and 300 °C, respectively (**Figure 4. 15 b)**). A comparison between the average COF values of B_4C coatings tested against 319 Al and 52100 steel is presented in **Figure 4. 16**. The friction of 52100 steel against B_4C coatings was conspicuously higher than that of 319 Al against B_4C coatings, which never surpassed 0.5.

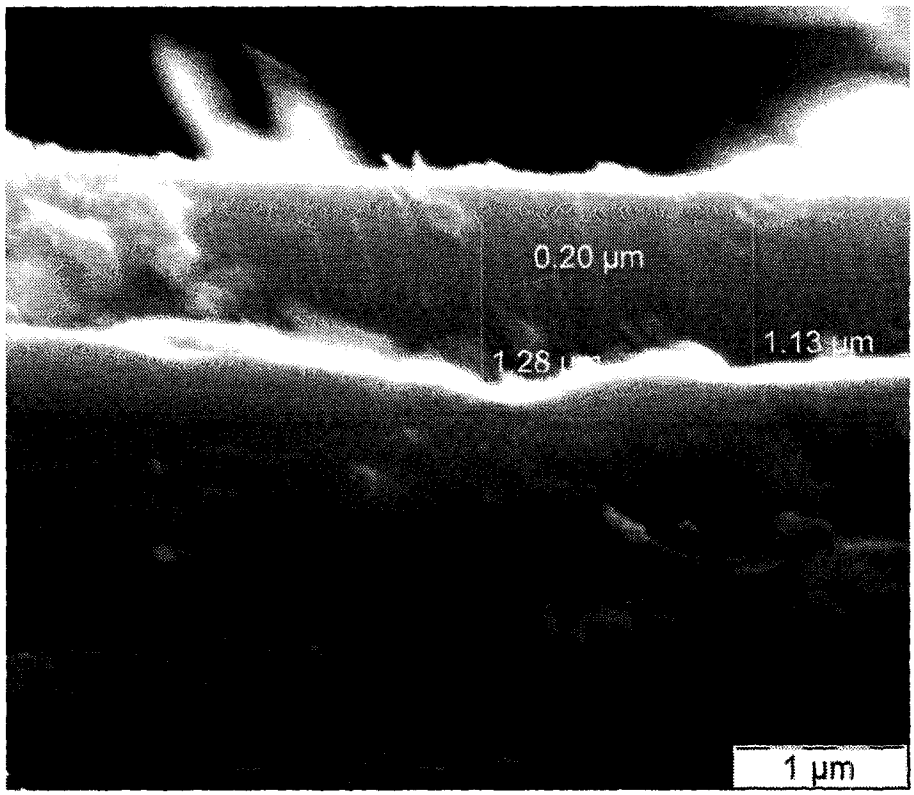

Figure 4. 13 SEM cross-sectional image of the B_4C coating after annealing at 300 °C for 90 min. A columnar structure was revealed.

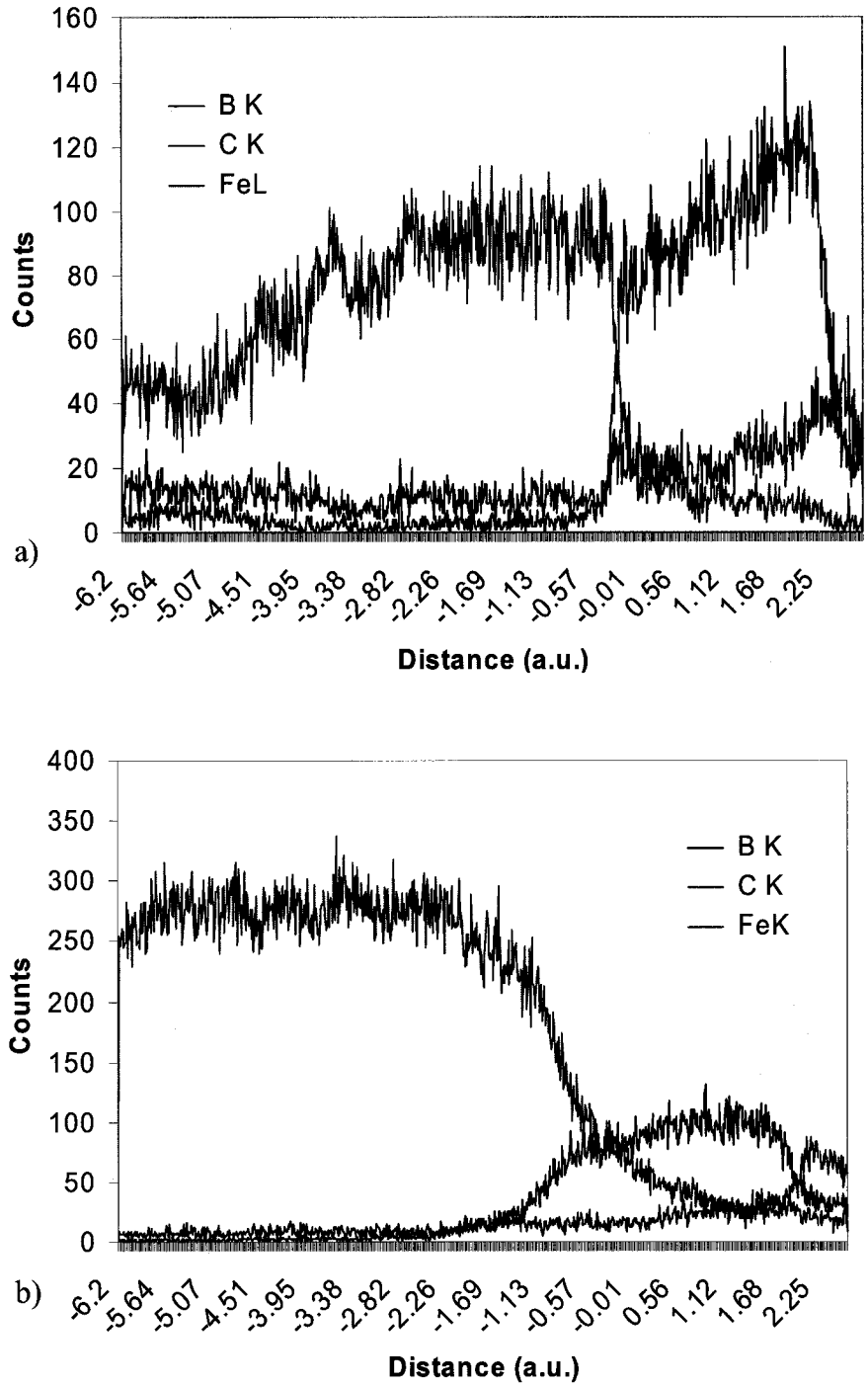

Figure 4. 14 EDS line scan of **a)** as-received and **b)** annealed boron carbide coating. The scan was conducted over the coating-substrate interface. In both figures, zero position denotes the interface and the coating located at the positive direction of the Distance axis.

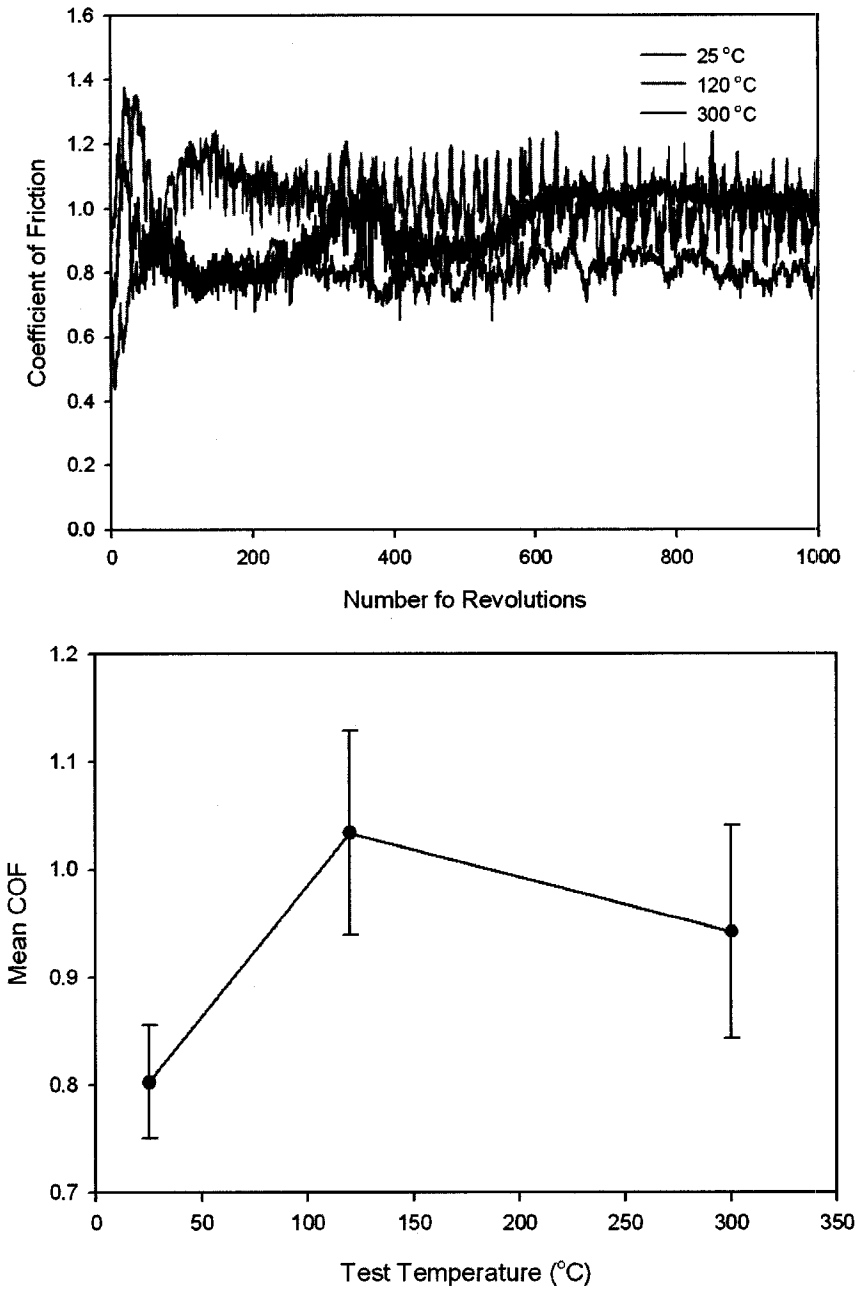

Figure 4. 15 a) COF curves of the B_4C coatings against 52100 steel as a function of number of revolutions at different temperatures; **b)** Mean COF values calculated from the curves shown in a) for different test temperatures.

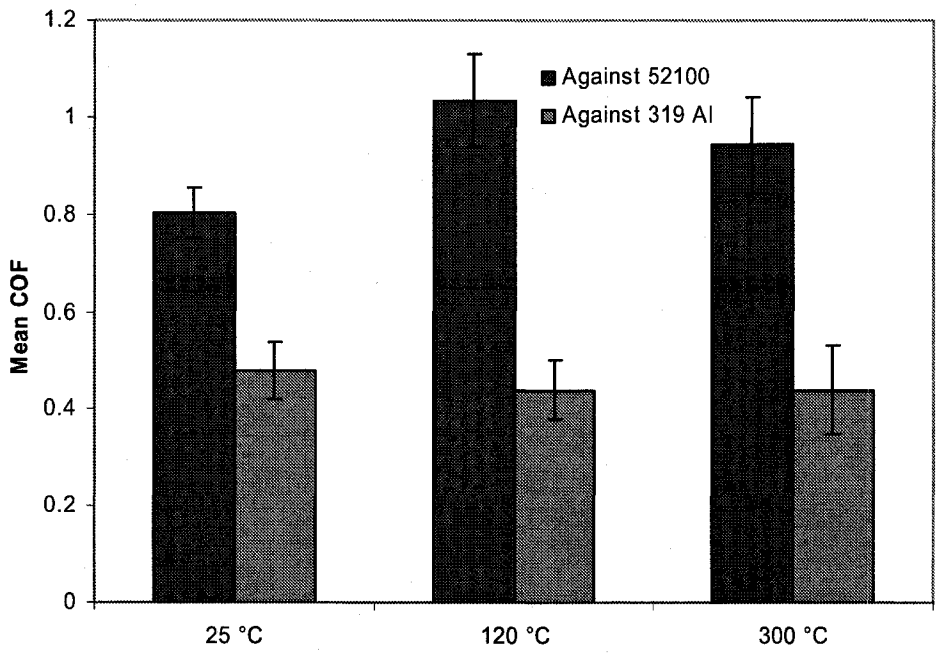

Figure 4. 16 Comparison of mean COF values of B_4C coatings sliding against 319 Al and 52100 steel at different test temperatures.

4.4 Pin-on-disc Tests in Varied Environments against 319 Al

The COF curve became more stable when tested at a lower relative humidity of 14 % compared to that tested at 51% RH with a mean COF value of 0.45±0.04 was observed at the end of the testing period. The fluctuations of the curve were effectively reduced to between 0.4 and 0.5, but the COF curves for the test conducted at 14.4% RH displayed a gradually increasing trend (**Figure 4. 17**). Aluminum adhesion was observed on the wear tracks after testing at 14% RH for 10^3 revolutions (**Figure 4. 18**). 0.49±0.07% of the wear track area was covered by aluminum transferred from the pin.

The most favourable friction behaviour of a B_4C coating dry sliding against 319 Al was recorded when the coating was tested in nitrogen. A steady state COF of 0.36 was attained throughout the test (**Figure 4. 17**), and the SEM image of the wear track after the test in N_2 showed adhered aluminum with a more uniform shape and spatial distribution (**Figure 4. 19**). The fraction of the wear track covered by transferred aluminum was measured at 1.8±0.5%. The 3-D surface profile images of the wear tracks on the samples tested in different atmospheres, the plot of wear track fraction covered by adhered aluminum against test atmosphere and the corresponding bearing ratio curves of the sampling regions are presented in **Figure 4. 20**, **Figure 4. 21** and **Figure 4. 22** respectively.

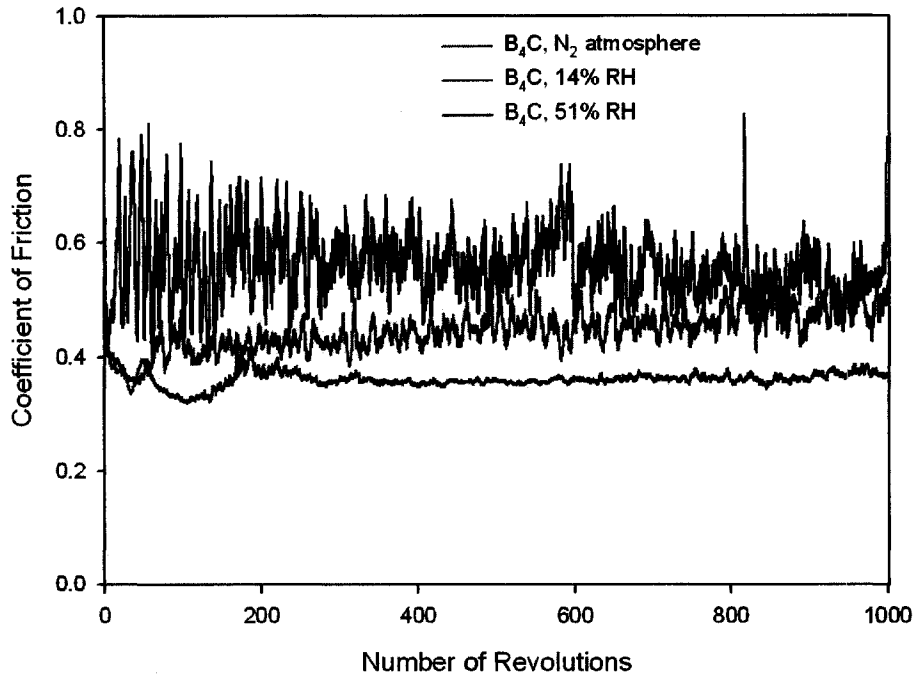

Figure 4. 17 COF curves of the B_4C coatings against 319 Al as a function of number of revolutions in different test atmospheres.

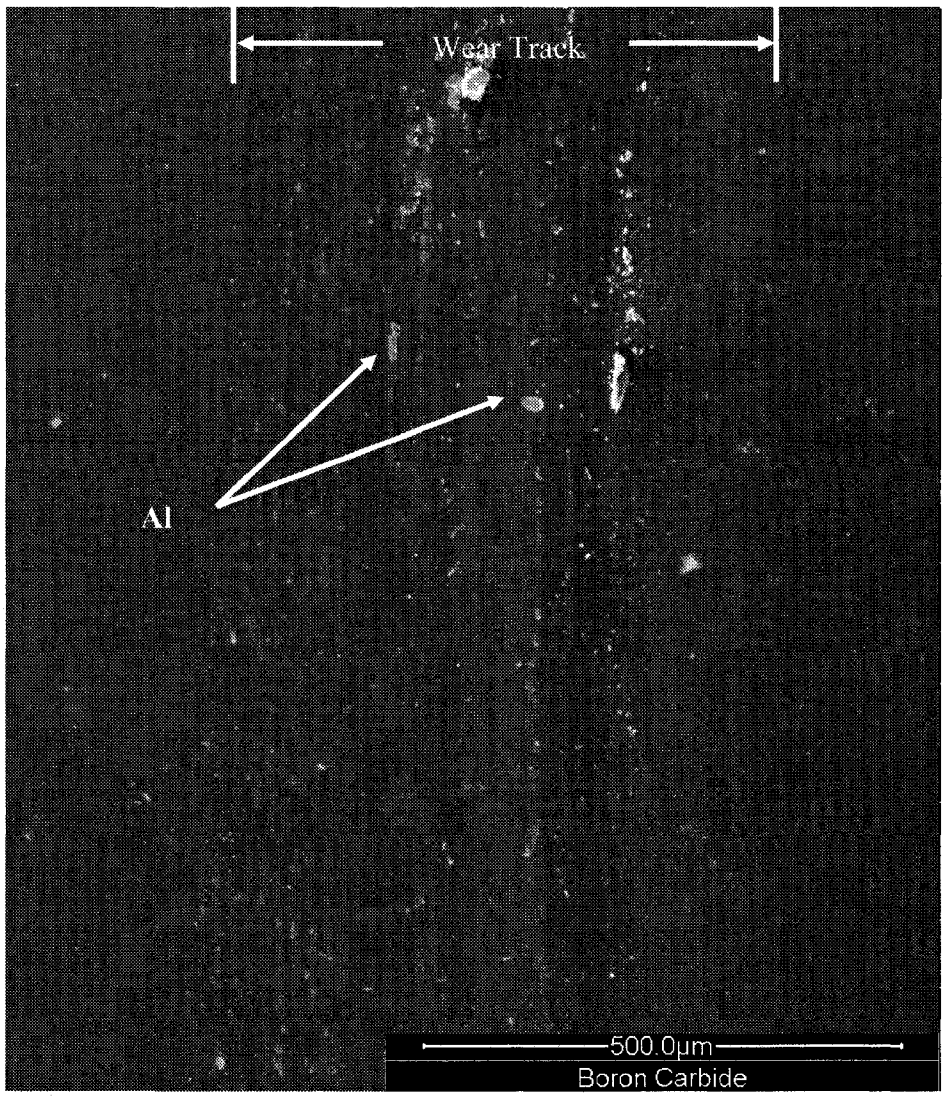

Figure 4. 18 SEM image of a region of the wear track of the B_4C coating tested against 319 Al at 14.4% RH for 10^3 revolutions.

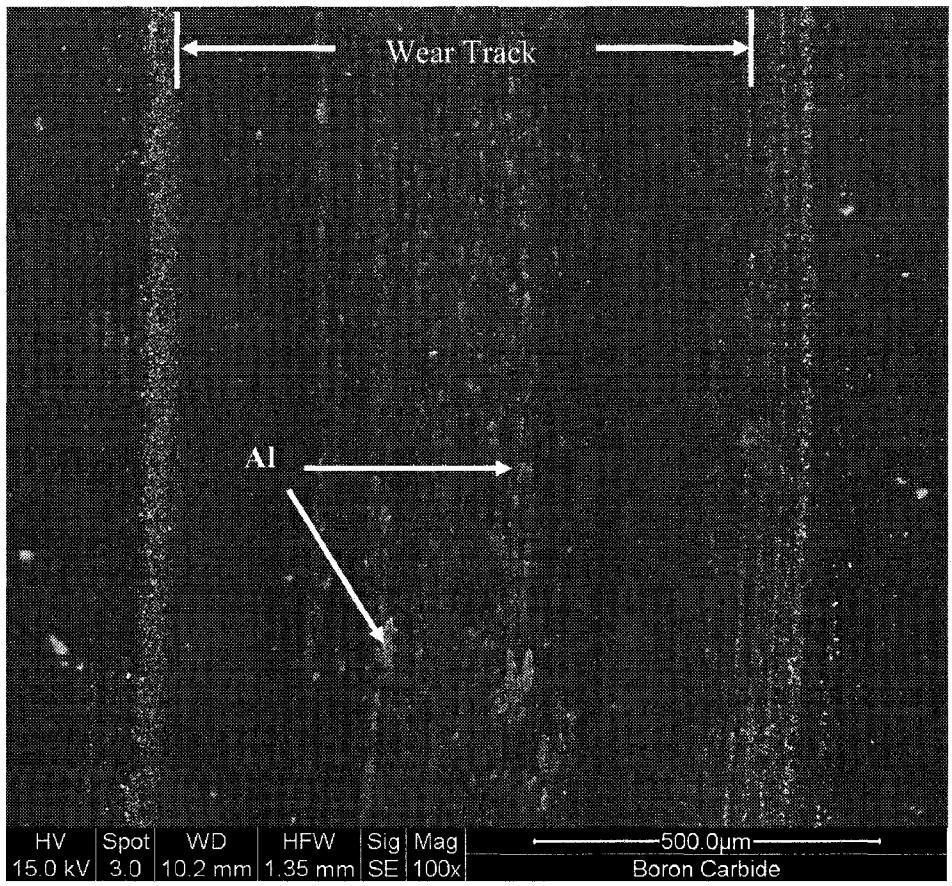

Figure 4. 19 SEM image of a region of the wear track of the B4C coating tested against 319 Al in N_2 for 10^3 revolutions.

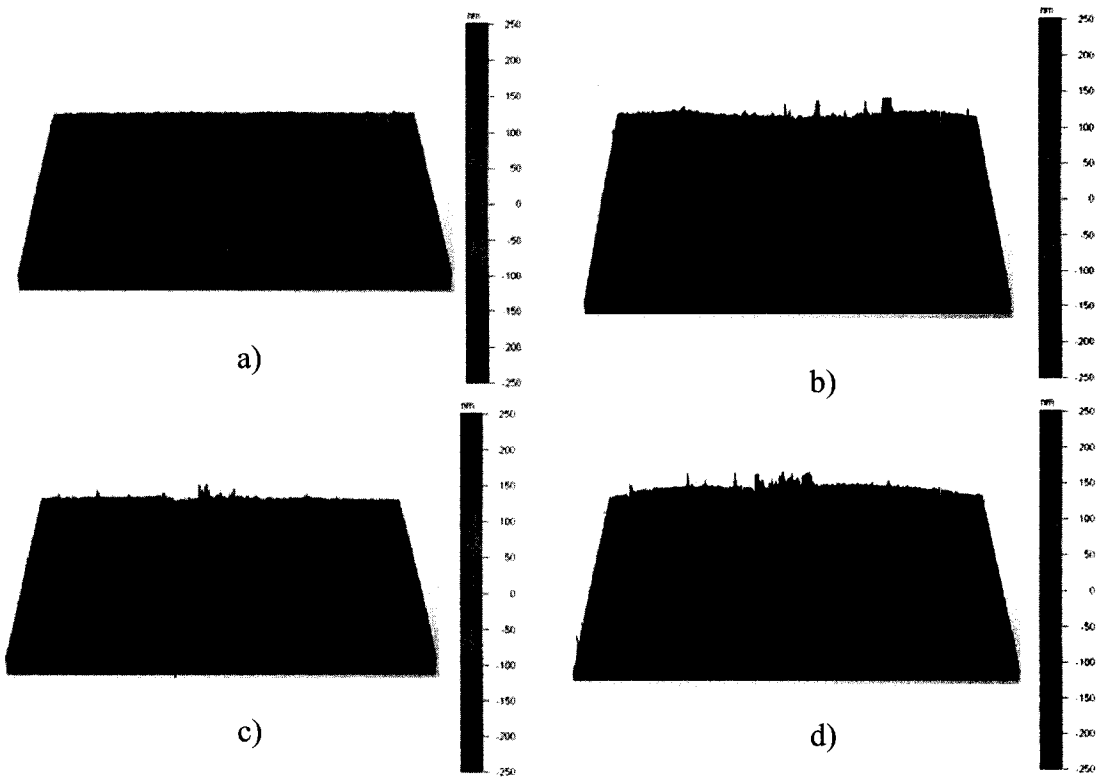

Figure 4. 20 3-D surface profile images of B_4C coatings: **a)** Unworn coating; **b)** Tested at 51% RH; **c)** Tested at 14.4% RH; **d)** Tested in nitrogen.

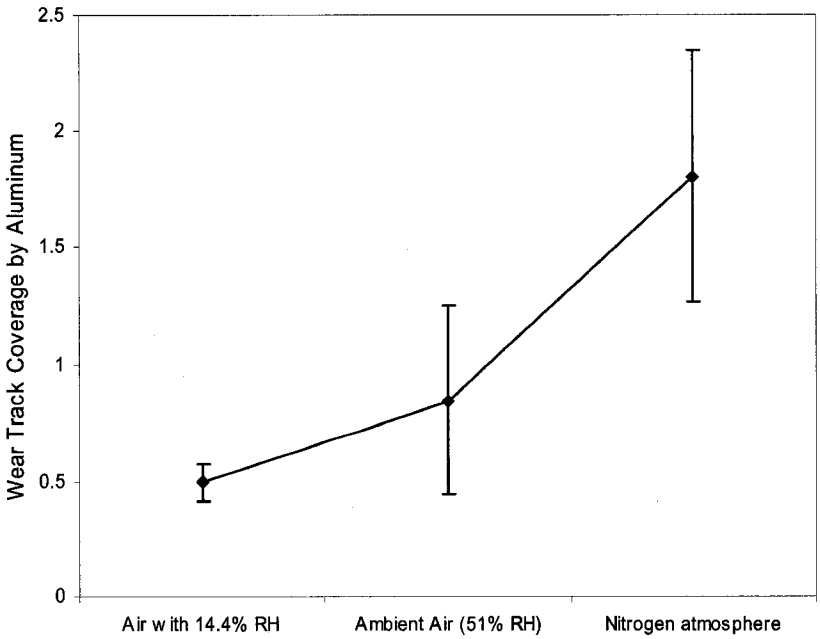

Figure 4. 21 The percentage of the wear tracks on B_4C coatings covered by aluminum as a function of different test environments.

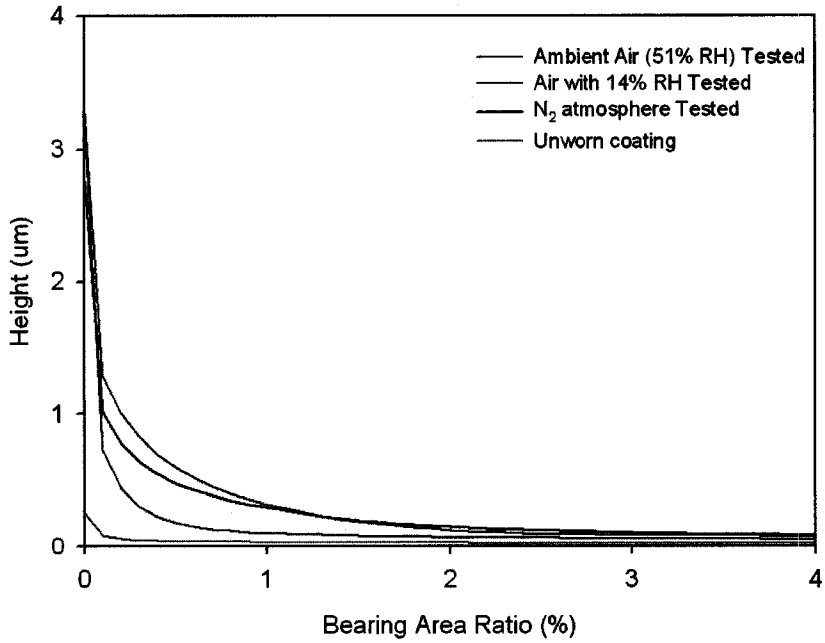

Figure 4. 22 The bearing ratio curves of the sampling region used to measure the amount of aluminum coverage in different test environments.

4.5 Discussion

4.5.1 B_4C Coating Wear Mechanism (against 319 Al) and Al Adhesion onto B_4C at Room Temperature

In previous studies, the COFs of B_4C coatings were reported to be in the range of 0.1-0.9 [17-18][134] at room temperature. However, those studies were conducted by dry sliding steel (usually 52100 steel) against B_4C coatings, and no transfer and adhesion of steel onto B_4C coating was reported at the end of the tests. The wear mechanism of steel sliding against a B_4C coating at room temperature was proposed as an abrasion and chemical-mechanical polishing process. Steel was abraded during this process due to the highly abrasive nature of B_4C coatings while boron carbide reacts chemically with oxygen and water according to **Equation. 2.3** and **Equation 2.2** under load from steel, forming softer material that can then be removed from the surface [36][42].

The author is unaware of any work in the literature that reports on the dry sliding behaviour of a B_4C-Al pair. In the current study, the wear mechanism between the aluminum pin and B_4C coating at room temperature is proposed to be an adhesion-delamination three body abrasion process. When the two surfaces were brought into contact, high local pressure between contact asperities resulted in plastic deformation of the Al asperities and adhesion and consequently the formation of junctions. This process can be thought to be analogous to forcing a B_4C indenter into an aluminum surface on an asperity-asperity scale. During sliding, the contact junctions were destroyed

and reformed repeatedly, resulting in the transfer and adhesion of Al alloy onto the B_4C surface as well as causing the ploughing of B_4C asperities through the weaker Al alloy [135]. The significance of the interaction between contact junctions and repetitive plastic deformation of the near surface Al alloy is discussed in the following text.

Generally, the separation of a contact junction might occur in either of the materials that are coming into contact. According to the current observation, the disengagement of a junction is more likely located within the Al asperities. On an atomic level, this might be due to the low cohesive energy of Al atom layers compared to the work needed to separate an Al/B_4C interlayer (work of separation, W_{sep}). The cohesive energy of Al has been calculated and compared with the calculated work of separation between Al/ceramic layers using a first principles simulation. The results successfully explained the adhesion and transfer behaviour of Al/various ceramic material pairs such as Al/WC, Al/Al_2O_3, Al/CrN and Al/TiN [136-139]. However, no data on the Al/B_4C interface is available--perhaps due to the complexity of the B_4C structure. For the studied Al/B_4C pair, the initial transferred aluminum platelets grew in size, forming "islands" of aluminum on the B_4C coating as the sliding process continued.

The cyclic sliding contact resulted in material loss of the pin through delamination. A hydrostatic pressure field was superimposed during sliding wear on the Al material layers adjacent to the contact surface in addition to the shear stress applied [140]. The plastic shear deformation of the Al on a macrolevel in the subsurface region might have been

induced by the cyclic loading. Such plastic deformation accumulated with repeated loading until the hydrostatic pressure under the contact zone was surpassed by the shear strain, forming cracks below the contact surface in the vicinity of pre-existing voids and second phase particles. Detached metallic flakes could have formed as a result of crack propagation parallel to the surface. A similar observation has been reported by Zhang and Alpas on an aluminum-7% silicon alloy [141]. These detached flakes were probably harder than the original bulk 319 Al alloy due to work hardening caused by plastic deformation or even grain refinement on a nanocrystalline level. The hardened flakes were then extruded from the pin tip at the exit side of the wear zone in the form of plate-wedge like chips, evidenced by Region 2 as marked on **Figure 4. 4**. Some of the freshly detached chips were caught between the sliding surfaces--initiating a three-body abrasion mechanism while others were pushed out of the contact region in the form of loose debris. The chips that remained in the contact region were subjected to sequential mechanical grinding in which the hard Si phase within 319 Al, oxidized aluminum phase and hardened Al grains all served as polishing particles against the B_4C coating. The final products of this abrasion-grinding process were the small, rounded debris particles. Some of the small particles might have been pressed together and left the contact region as a new flake. The whole process continued until the coating was completely worn and Al adhered to the M2 substrate as reported in [7].

The above speculation on aluminum hardening is supported by the observations of Meng-Burany and Alpas [142] on the same 319 Al pin tip after sliding against a NH-DLC surface under a 5 N load at a sliding speed of 0.12 m/s where aluminum transfer and adhesion onto the NH-DLC coating was detected by the authors. Both the transferred Al and Al located at the contact surface of the worn pin were characterized by a refined nanocrystaline structure with an average grain size under 100 nm. A 75% increase in hardness was noted for the worn pin tip.

Al adhered to the currently studied B_4C coating. However, it should be noted that the B_4C coating still managed to reduce the amount of Al adhesion to approximately 30% of the Ti_2B coating, which exhibited the least Al adhesion among other industrial coatings (**Figure 4. 23**).

4.5.2 Effect of Test Temperature on the Tribology and Material Transfer of 319 Al-B_4C Coating System

The measured mechanical properties of B_4C coatings underwent a 7% decrease in both elastic modulus and hardness (**Figure 4. 12**) as the test temperature was increased from 25 °C to 300 °C. Such deterioration is attributed to the possible segregation of the free carbon within the coating towards the coating surface. Generally, disordered carbon phase with graphitic characteristics coexists with the B_4C phase in both bulk boron carbide ceramics and deposited coatings [12][19][20][145]. In its as-deposited state, the free carbon phase was believed to be distributed among the partially crystalline structure

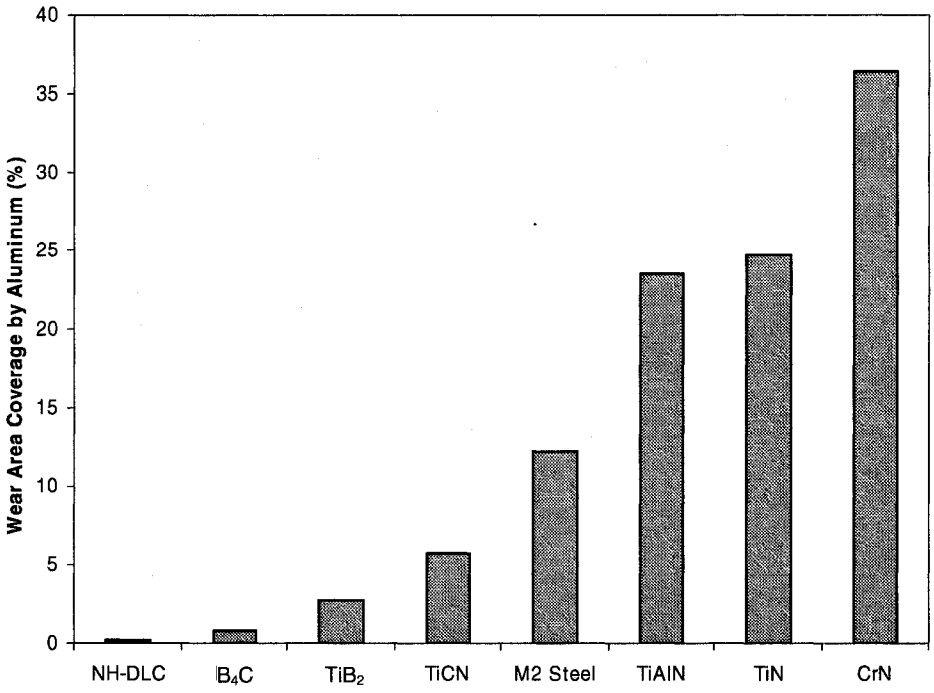

Figure 4. 23 Ranking of the coatings according to amount of aluminum adhesion. The results on materials other than B_4C are from [7].

of the B_4C phase, blurring the boundaries between B_4C columns and lending the coating a "glassy" appearance (**Figure 3. 8**). After the coating was annealed at 300 °C, the free carbon phase gained enhanced mobility due to the high energy nature of grain boundaries and segregated towards the surface. This migration of carbon was the probable reason for more diffused carbon concentration over the coating-substrate interface after annealing (**Figure 4. 14 b)**). The more defined columnar structure shown in **Figure 4. 13** could be the result of "thermal etching" caused by free carbon movement. Consequentially, the coating grows weaker as a result of sapped bonding between the B_4C columns. Thermal softening and oxidation of the Al alloy at an elevated temperature rather than the softening of the coating, however, were the main causes for the decrease in the mean COF (**Figure 4. 6 b)**) as the test temperature was elevated--since the softened coating was still much harder than the 319 Al pin.

At elevated temperatures, the asperities on the B_4C coating retained a large part of their hardness while the contact surface of the Al 319 pin was considerably softened. As the sliding load was applied, the softened Al asperities were more easily deformed and removed from the pin surface by the B_4C asperities. Once transferred to the coating, these aluminum islands acted as growing points for future Al accumulation until big chunks of transferred material were formed on the B_4C coating. As indicated in **Figure 4. 10**, about 3.9% and 16.7% of the wear track area was occupied by adhered aluminum at 120 °C and 300 °C, respectively. These adhered aluminum islands were also in contact with the pin.

The friction force (F) could be treated as the real area of contact between surfaces (A_r) times the overall shear strength (τ) of the contact junctions,

$$F = A_r \tau \qquad \textbf{Equation 4. 1}$$

It followed that the low shear strength of the contacting Al asperities could cause a reduction in friction force. It was also expected that the real area of contact would increase as a result of the Al softening, but the effect was not large enough to overcome the decrease in shearing strength for the Al asperities in contact. The final result was a slight decrease in COF value.

On the other hand, aluminum oxidizes more readily at high temperatures (ΔG° = -1582.3 kJ/mole at 300K [143]). The quick-forming oxide layer prevented further adhesion of Al to itself, which might lead to a higher COF or even seizure of the sliding surfaces. The oxide layer also facilitated the relative sliding of the counterfaces by providing easy shearing contact junctions.

4.5.3 Comparison of the Friction Behaviour of the 319 Al – B_4C Pair and 52100 Steel – B_4C pair

The current observed COF value of ~0.8 for 52100 steel dry sliding against B_4C coatings in ambient air (23.5 C, 51% RH) is consistent with those reported for the same material pair. Since the normal load was the same--5 N for both 319 Al and 52100 steel--it follows that the difference in their COF values was caused by the frictional force

that occurred during sliding contact. According to **Equation 4.1**, the higher COF value for 52100 steel in ambient air can be explained by its significantly higher shear strength than 319 Al.

When the 52100 steel balls were tested at elevated temperatures, however, an opposite trend was observed for the average COF value. While the 319 Al exhibited a slight decrease in the average COF value, those for 52100 steel against the B_4C coating exhibited an obvious increasing trend when testing at 120 °C. The observed increase might be attributed to the formation of a hard, patchy oxide layer on the steel ball surface that affected the contact conditions at the real area of contact. A more detailed characterization of the wear track and the worn ball surface is needed before any conclusion can be made.

4.5.4 Effect of Test Environment on the Friction and Material Transfer of 319 Al-B_4C Coating System

The study showed that the COF curve of a B_4C coating dry sliding against 319 Al exhibited a lower mean value and variation when tested in air at a lower humidity level **Figure 4. 17**.

While a few papers have discussed the effect of relative humidity on the tribological behaviour of B_4C based materials, the reported trend directly opposes the present observation [34-36][134]. They attributed such behaviour to the lubrication effect of boric acid film formed between the sliding surfaces, but such a mechanism is not

applicable to the present experimental setup because the counterface materials they used against the B_4C based materials were sapphire [34], ceramic B_4C [35] and steel [36][134]--none of which are soft and adhesive the way Al alloy is. After the transfer and adhesion of aluminum onto the B_4C coating surface occurred, the pin material came in sliding contact against B_4C coatings that were partially covered by oxidized Al, suggesting that the tribochemical conditions required to form boric acid were unlikely to be fulfilled. The present study indicates that an increase of COF with respect to an increasing relative humidity level is attributed to grit sharpening caused by moisture-assisted grit microfracture as proposed by Larsen-Basse and Sokoloski [144]. Since B_4C has a low fracture toughness (2.9-3.7 MPa $m^{1/2}$ [145]), this increase in asperity microfracture tends to occur with increasing humidity. Such a process supplies fresh abrasives while the sharpened B_4C surface provides more sites to interact with the relatively soft Al, causing deeper cuts on the Al pin surface. Due to an increased real area of contact, inferior tribological behaviour was observed at higher relative humidity levels--characterized by a higher and more fluctuating COF curve. This argument is indirectly supported by the results reported in Siniawski et al. [134] which showed a constant lower value of average asperity radius (sharper and more abrasive asperities) of curvature value for B_4C coatings at high RH level than at low RH level. At lower humidity levels, the asperities are less sharp--decreasing the abrasion of the soft

aluminum and resulting in a lower COF. The reason why the best tribological behaviour was observed when testing was done in nitrogen is still unknown at this stage.

The test conducted in nitrogen--compared to testing in low humidity--resulted in a larger area of aluminum adhesion (**Figure 4. 21**) and a thicker adhered aluminum layer (**Figure 4. 22**). Compared to tests conducted at 51% RH, the adhered Al after testing in N_2 is larger in area fraction (**Figure 4. 21**) but possibly thinner (**Figure 4. 22**). There seemed to be no simple relationship between the COF values and the morphology of the adhered aluminum. No report on the tribological behaviour of B_4C coatings against Al alloys in a N_2 atmosphere have been found by the author.

4.6 Summary and Remarks

The effect of test temperature and atmosphere on the tribological behaviour of a B_4C coating dry sliding against 319 Al was studied using pin-on-disc tests. Both temperature and atmosphere were identified as significant factors. The findings of the current work are as follows:

1. Compared to other industrial coatings [7], the B_4C coating has a slightly lower tendency to adhere to 319 Al in ambient air under 51% RH.

2. Increasing the test temperature from 25 °C (51% RH) to 300 °C results in a slightly lower COF value (8% lower) while the amount of aluminum adhesion is increased (1800% higher). Such behaviour is attributed to the thermal softening and oxidation of the aluminum.

3. Water vapour has been found unfavourable for reducing the COF--possibly because of grit sharpening of the B_4C coating that results in a higher COF value and more aluminum adhesion.

4. Tests run in N_2 effectively reduced and stabilized the COF value of the tested material pair, resulting in a steady state COF value of 0.36.

5. B_4C coatings are not entirely suitable for tool coatings in the dry machining of aluminum alloys with the current structure and composition, due to adhesion problems and high friction when compared to the DLC coatings presented later in this work.

6. The COF values of 52100 steel dry sliding against a B_4C coating are considerably higher than those tested against 319 Al under the same test conditions, namely in ambient air and at elevated temperatures. The higher strength of 52100 steel compared with 319 Al is proposed to be the reason.

CHAPTER 5 TRIBOLOGICAL BEHAVIOUR OF DLC COATINGS AGAINST 319 AL ALLOY

The previous chapter illustrated why B_4C coatings are not the most promising coating for application to tools for the dry machining of Al. While they did reduce aluminum adhesion when compared to other industrial coatings at room temperature, they did not completely prevent aluminum adhesion--not to mention the fact that the COF value exhibited during dry sliding against 319 Al was slightly high even when tested in N_2.

Studies have shown that aluminum has a lower tendency toward adhesion to NH-DLC coatings when compared to other industrial coatings such as TiN, TiB_2 and TiAlN in ambient air test conditions [7]. Previous work has demonstrated that the tribological behaviour of DLC coatings deteriorates at elevated temperatures--a breakdown that features unstable COF curves, high friction and high wear rates [107-111]. These facts make it necessary to improve the performance of the DLC coatings at elevated temperatures in order to meet the need for better tool coatings.

In an attempt to effectively comprehend the tribological behaviour of the DLC coatings in cutting tool applications, WC-DLC and DLC/WC-DLC coatings were tested against 319 Al, and the structures and properties of these coatings are presented in **Section 3.2**. In summary, the WC-DLC coating is a H-DLC coating (25 at.% H) with WC

particles embedded in its amorphous matrix. DLC/WC-DLC (24 at% H) is a multilayered coating consisting of an H-DLC top layer (approx. 0.1 μm) and a (hydrogenated) WC-DLC layer underneath. The coatings were tested in air at room temperature (14% RH and 51% RH). The effect of the temperature on the tested material was investigated at 120, 300 and 350 °C. The worn pin tip tested against the DLC coatings and the corresponding wear tracks were characterized to understand possible wear mechanism of the tested coatings. The observed results are discussed in terms of interaction between the DLC coating surface and the gaseous species in the environment, the material transfer to counterfaces and the graphitization of the coatings.

5.1 Pin-on-disc Tests in Ambient Air at 51% RH

Both WC-DLC and DLC/WC-DLC coatings exhibited low and stable COFs during testing in ambient air at 51% RH (**Figure 5. 1**) as compared to previously tested B_4C coatings.

The WC-DLC coatings displayed low COF values and wear rates when tested against 319 Al in ambient laboratory air at 51% RH. The COF was initially 0.3, but quickly decreased as the test proceeded. After approximately 600 revolutions (41.5 m of sliding) a steady-state COF value of ~0.14 was attained and maintained throughout the rest of the test. The WC-DLC showed an average wear rate of 1.75×10^{-6} mm^3/m. **Figure 5. 2 a)** illustrates a region of the wear track on the WC-DLC coating tested against 319 Al in ambient air with 51% RH for 10^4 revolutions. The coating remained on the

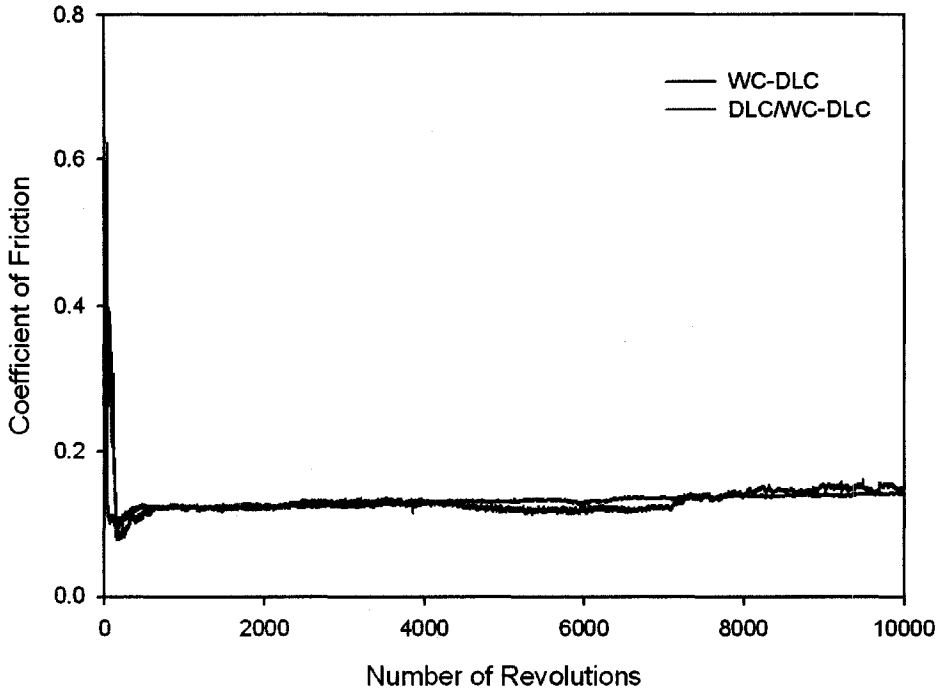

Figure 5. 1 COF curves for the WC-DLC and DLC/WC-DLC coatings tested in ambient air at 51% RH.

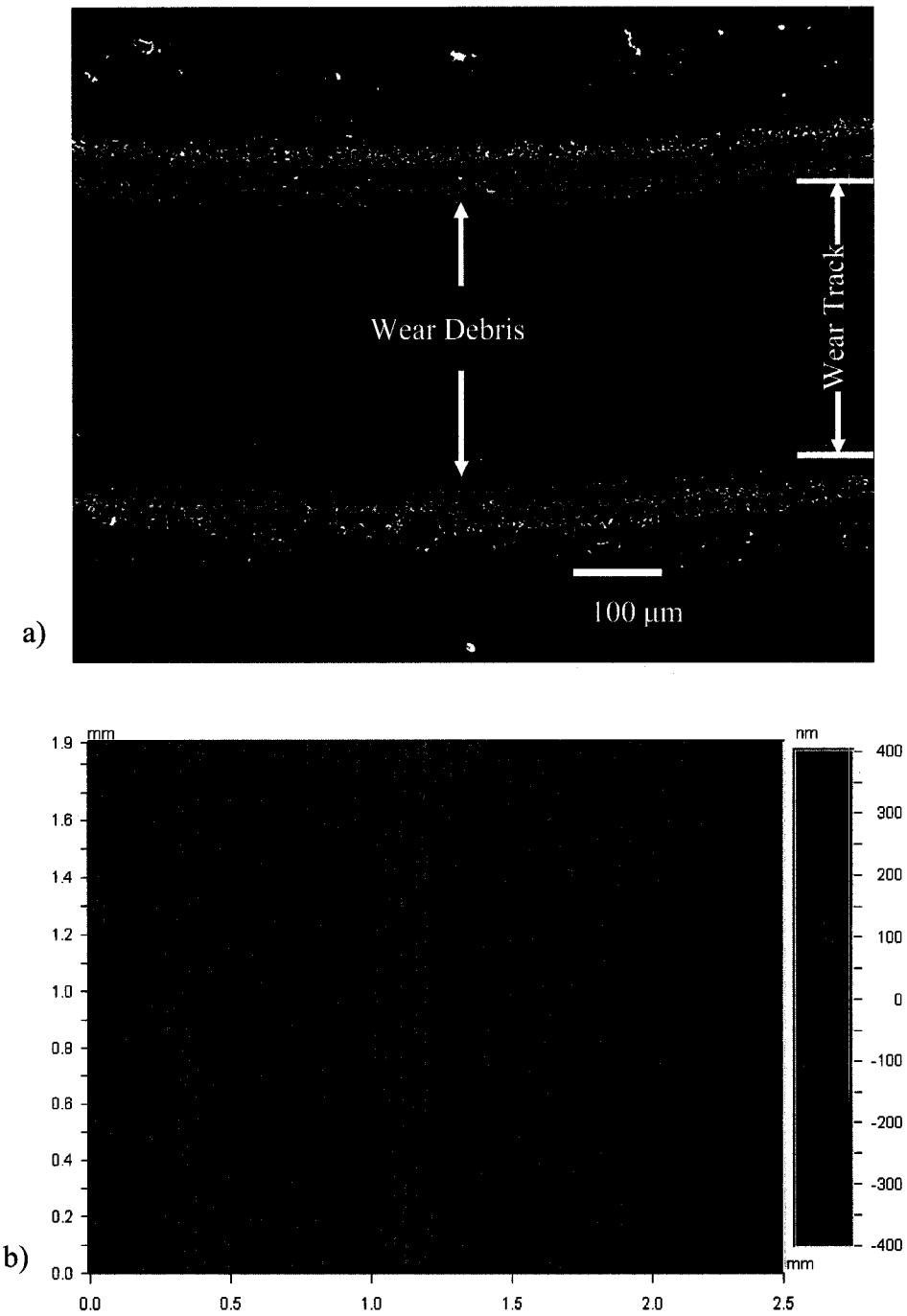

Figure 5. 2 a) The secondary SEM image of the wear track on the WC-DLC coating against 319 Al after 10^4 revolutions of test at room temperature and 51% RH. No Al adhesion is observed on the worn surface. The coating remained on the substrate; **b)** 3-D surface profile image of the same wear track.

substrate after the test, and no transfer of aluminum to the wear track could be detected. The wear track had a smooth, polished appearance with accumulated debris along both sides. A layer of transferred material was observed on the 319 Al pin tip after the test **(Figure 5. 3 a)**--a mixture of mainly aluminum oxide and a small amount of carbonaceous material **(Figure 5. 3 b)**).

The DLC/WC-DLC coatings exhibited low COF values and wear rates that were similar to those recorded for WC-DLC coatings when tested against a 319 Al in ambient laboratory air at 51% RH. The COF was initially 0.17, but decreased as the test proceeded. After approximately 600 revolutions (41.5 m of sliding) a steady-state COF value of ~0.13 was attained and sustained throughout the rest of the test. DLC/WC-DLC coatings exhibited low average wear rate (3.72×10^{-7} mm^3/m). **Figure 5. 4** shows a region of the wear track on the DLC/WC-DLC coating tested against 319 Al in ambient air with 51% RH for 10^4 revolutions. The features of the wear track were similar to those observed on WC-DLC coatings while the corresponding worn pin tip (**Figure 5. 5 a)** and **b)**) was characterized by a layer of similar transferred material.

5.2 Pin-on-disc Tests at Elevated Temperatures

To investigate the effect of temperature on DLC coatings, both WC-DLC and DLC/WC-DLC coating were tested against a 319 Al at 120 °C and 300 °C--or until the the coating failed to reach a steady-state COF value. The sliding of each sample was continued for 10^3 revolutions.

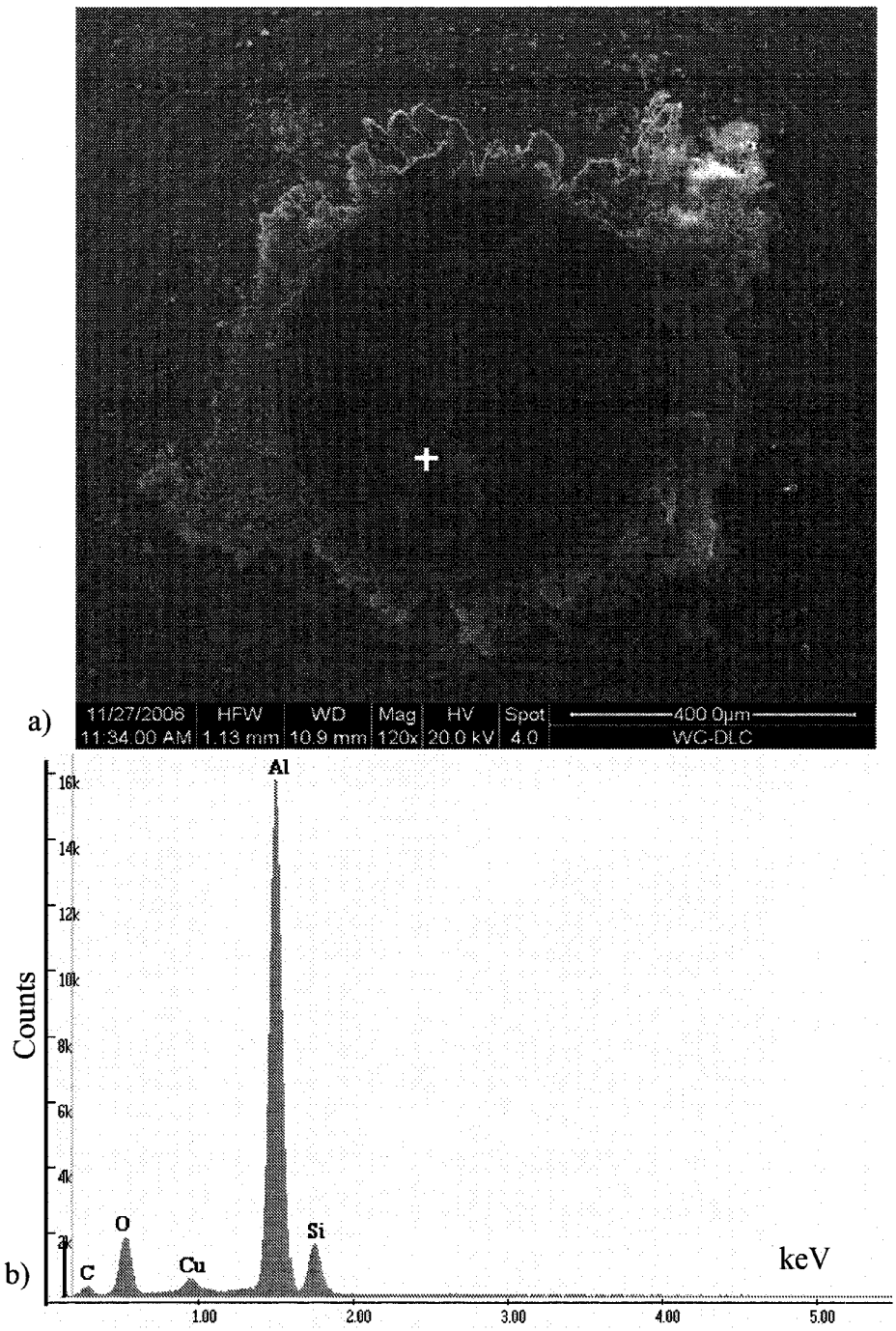

Figure 5. 3 a) SEM image of the 319 Al pin tip after test at room temperature under 51% RH for 10^4 revolutions against WC-DLC coating. A layer of transferred material was observed; **b)** EDS spectrum of the location indicated in **a)**, which shows that the transferred layer consisted of mainly oxidized Al alloy and a small amount of carbon.

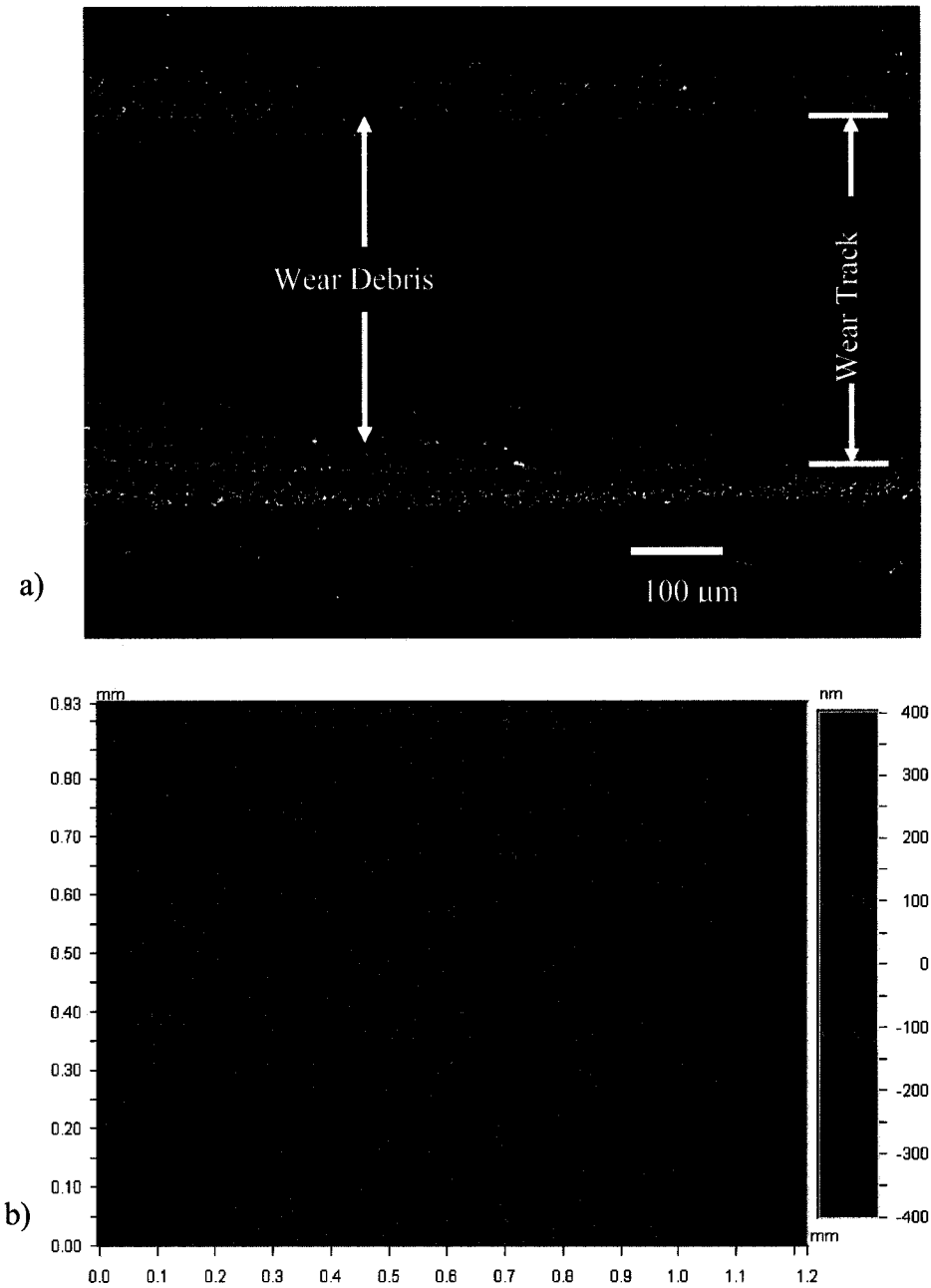

Figure 5. 4 a) The secondary SEM image of the wear track on the DLC/WC-DLC coating against 319 Al after 10^4 revolutions of test at room temperature and 51% RH. No Al adhesion is observed on the worn surface. The coating remained on the substrate; **b)** 3-D surface profile image of the same wear track.

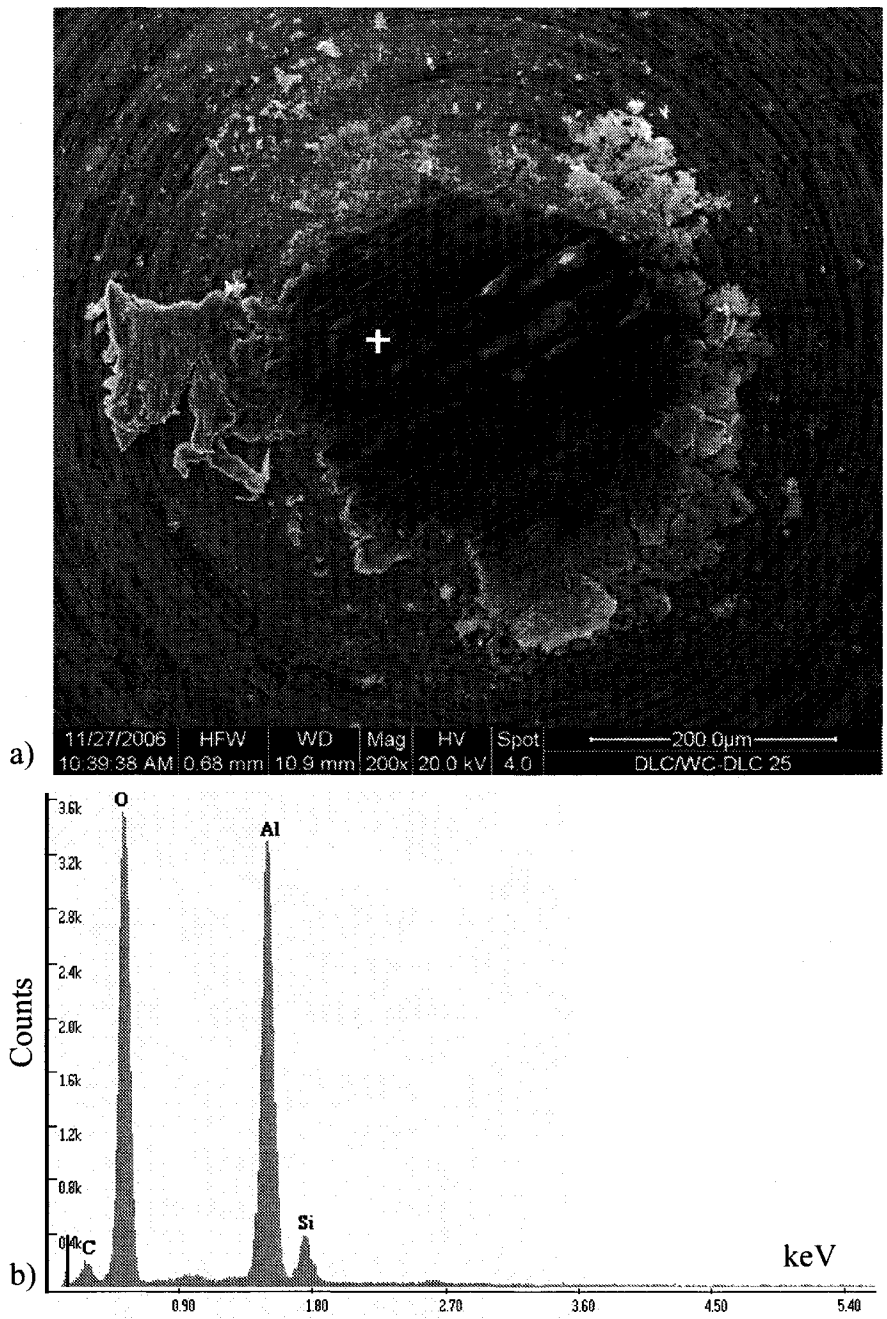

Figure 5. 5 a) SEM image of the 319 Al pin tip after test at room temperature under 51% RH for 10^4 revolutions against DLC/WC-DLC coating. A layer of transferred material was observed; **b)** EDS spectrum of the location indicated in **a)**, which shows that the transferred layer consisted of mainly oxidized Al alloy and a small amount of carbon.

The COF curves representing the WC-DLC coatings sliding against 319 Al pins at 25, 120 and 300 °C are presented in **Figure 5. 6**. The COF curves recorded at 120 °C were characterized by an initial running-in period where the COF values were high (0.6), followed by a rapid decrease to a steady-state value of 0.09 after approximately 100 revolutions—lower than the room temperature steady-state COF of 0.14. However, the wear rate of the WC-DLC coating increased from 1.75 $\times 10^{-6}$ mm^3/m at 25 °C to 2.29 $\times 10^{-5}$ mm^3/m at 120 °C (1200% increase) while the COF curve obtained at 300 °C did not reach a steady-state value--fluctuating between 0.24 and 0.6 throughout the test. The wear rate of the WC-DLC coating tested at 300 °C was measured as 1.20×10^{-4} mm^3/m.

An examination of the wear tracks created by elevated temperature testing revealed clean wear tracks after testing at 120 °C, and the formation of a strip of lighter contrast region in the middle of the wear tracks on the sample tested at 300°C (**Figure 5.** a)). The back scattered electron SEM image of the same region revealed that the difference between the atomic weight of the coating material and the adhered material was small since the contrast between the two was rather low (**Figure 5. 7 b)**). The EDS spectrum of the adhered spot (**Figure 5. 7 c)**) shows that the adhered material was actually a mixture of both materials from the coating and the pin, since carbon, aluminum and oxygen peaks were detected. The wear track was much deeper than that after testing at 25 °C (**Figure 5. 7 d)**. The Raman spectrum of the wear track (**Figure 5. 8)** exhibited a slight shift of the peak located at ~1526 cm^{-1} to ~1535 cm^{-1} compared to the as-received.

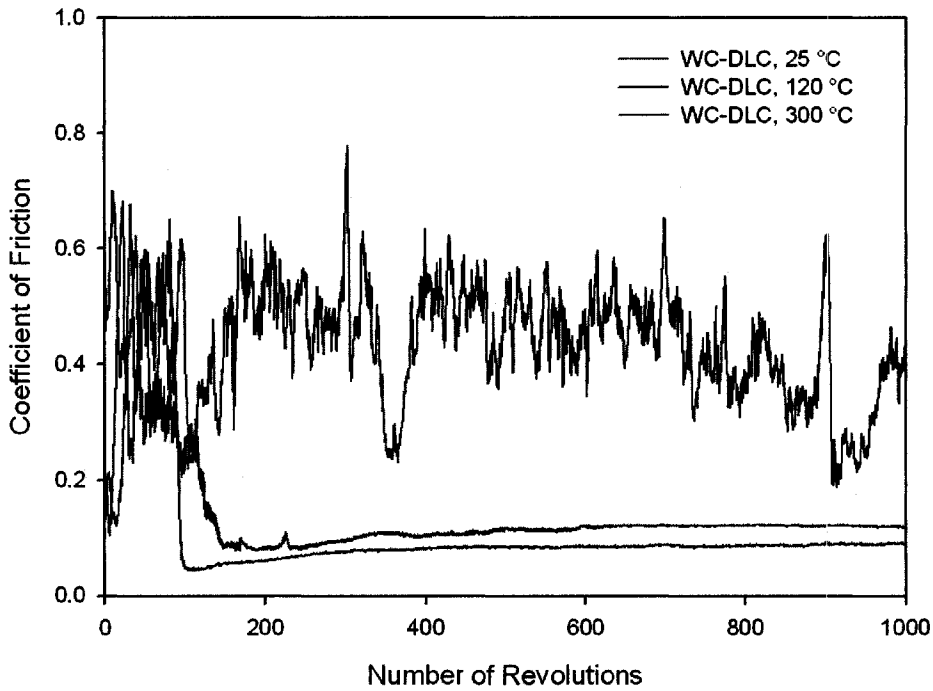

Figure 5. 6 COF curves of the WC-DLC coatings against 319 Al as a function of number of revolutions at different temperatures.

a)

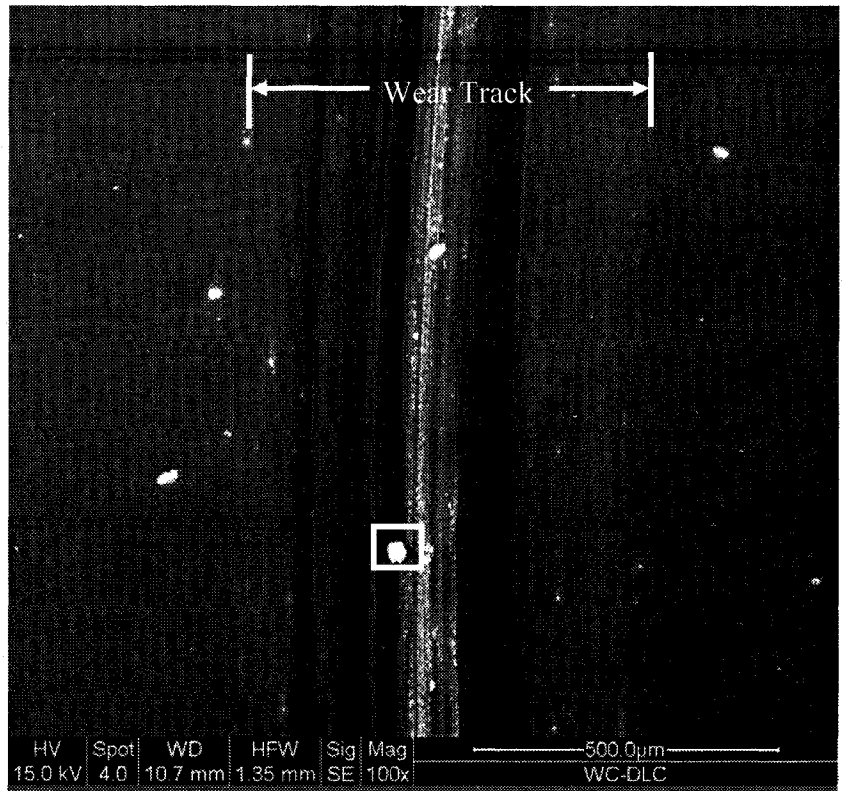

b)

Figure 5. 7 a) The secondary electron SEM image of a section of the wear track of the WC-DLC coating tested at 300 °C; **b)** The back scattered electron SEM image of the same region;

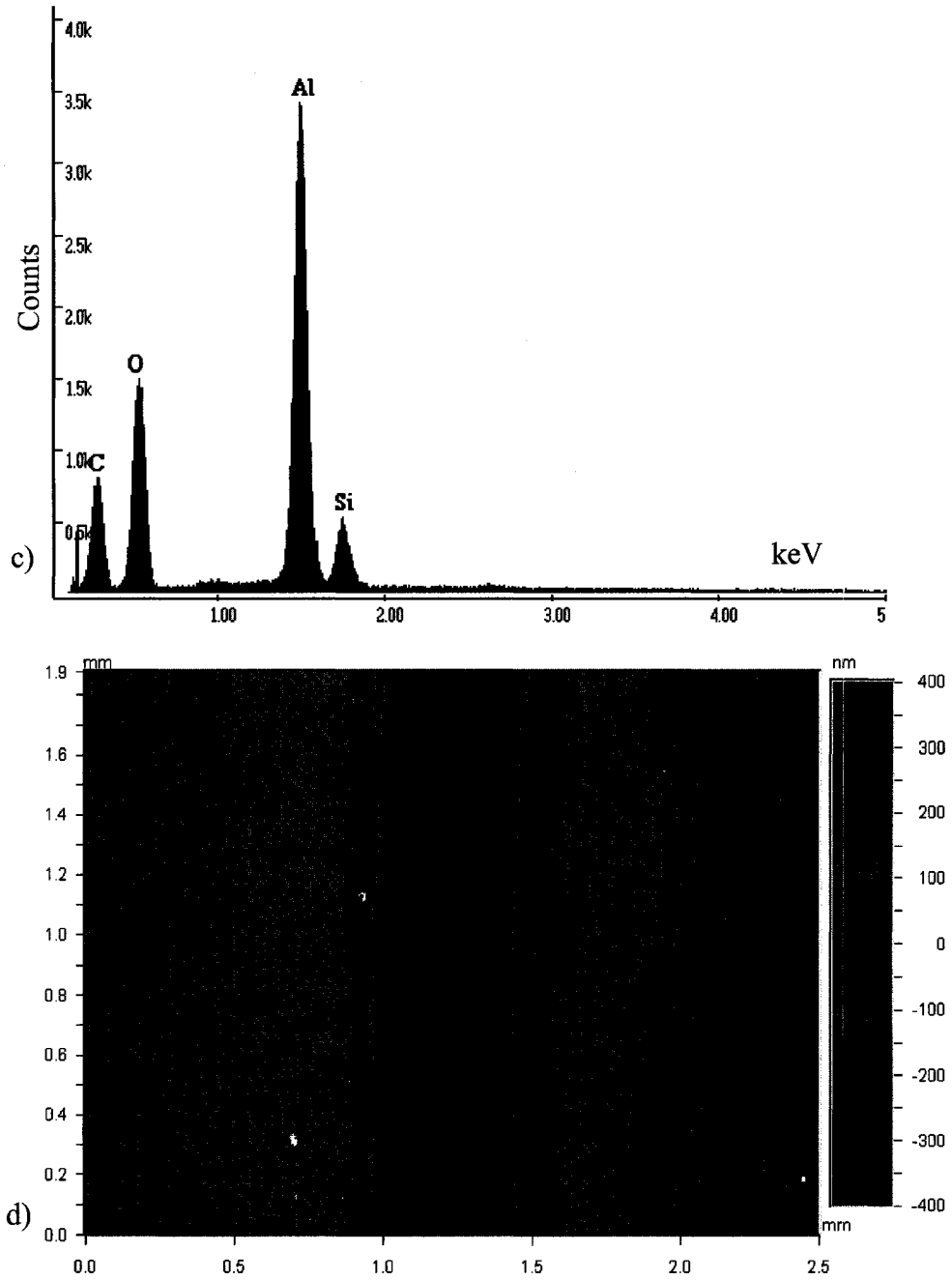

Figure 5. 7 c) The EDS spectrum of the light spot indicated in **a); d)** 3-D surface profile image of the same wear track.

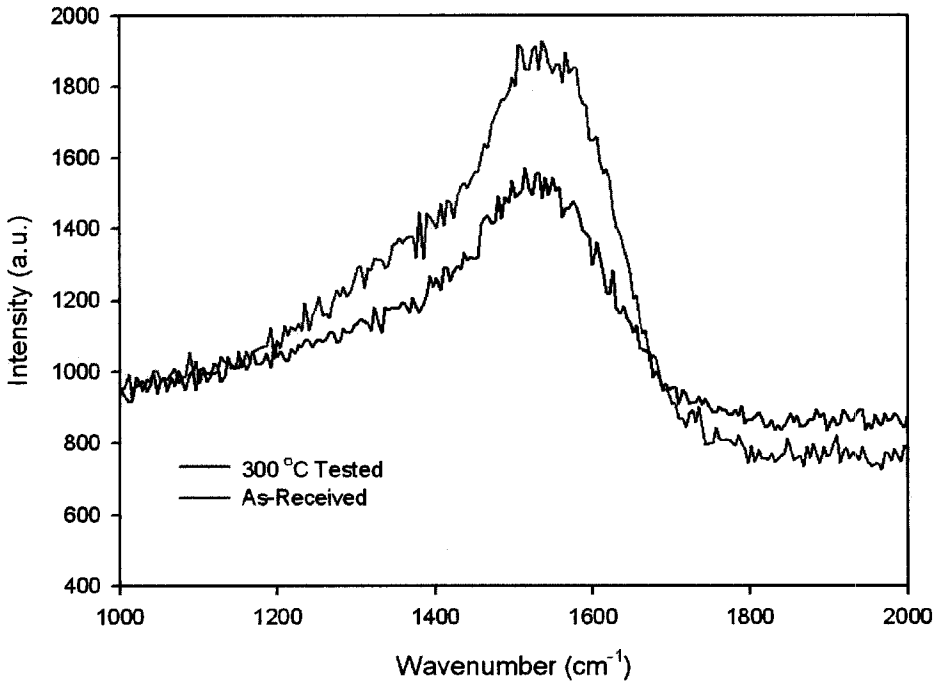

Figure 5. 8 The Raman spectra of the as received WC-DLC coating and the region within the wear track on the WC-DLC coating after tested at 300 °C.

The COF curves of the DLC/WC-DLC coatings sliding against 319 Al pins at 25, 120 and 300 °C are presented in **Figure 5. 9**. At 120°C the COF value was initially as high as 0.70-- dropping to a low steady-state value of 0.08 after only ~100 revolutions. The wear rate of the DLC/WC-DLC coating increased from 3.72×10^{-7} mm^3/m at 25 °C to 6.69×10^{-5} mm^3/m at 120 °C. At 300°C the fluctuations on the COF curve became more significant than those at lower temperatures and it took ~300 revolutions to reach the onset of steady state COF regime, which featured a steady state value of 0.10. Since the DLC/WC-DLC coating was able to reach a steady state COF value at 300 °C, the test temperature was increased to 350 °C. At 350 °C, the coating failed to attain a steady state friction even after 10^3 revolutions. The average COF was calculated as 0.52±0.07. The wear rate of the DLC/WC-DLC coating was 9.30×10^{-5} mm^3/m at 350 °C, which was lower than that of the WC-DLC coating at 300 °C (1.20×10^{-4} mm^3/m). The wear rates of DLC based coatings as a function of test temperature are presented in **Figure 5. 10**.

At temperatures up to 300°C, the 319 Al transfer onto the DLC/WC-DLC coatings was undetectable by SEM observation. For these coatings, a noticeable amount of material transfer onto the worn surface was detected at 350°C in the form of a continuous strip in the middle of the wear track (**Figure 5. 11 a)**). The wear track on the DLC/WC-DLC coating after testing at 350 °C shared the similar composition characteristics to that of the WC-DLC coating after testing at 300 °C-- as demonstrated by back scattered SEM image and EDS spectrum (**Figure 5. 11 b)** and **c)**). The

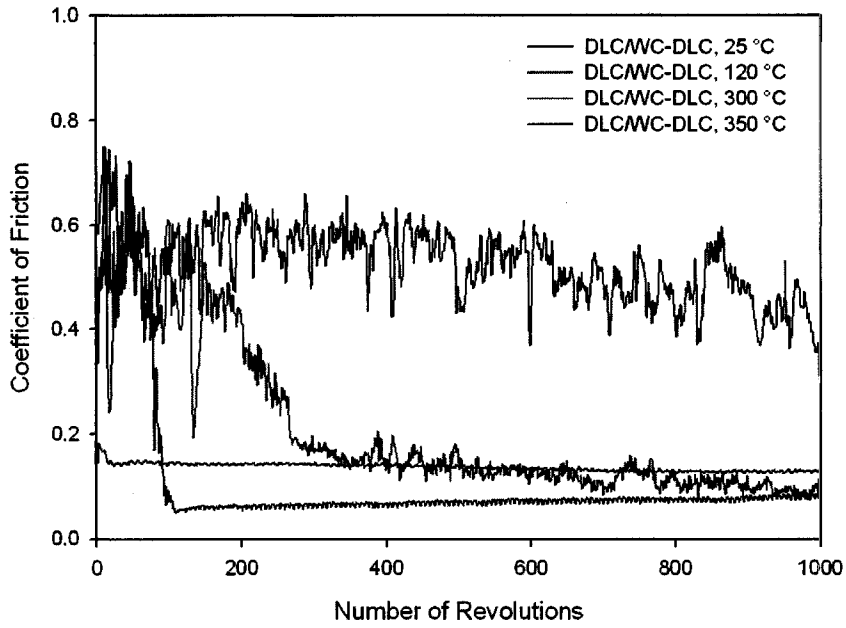

Figure 5. 9 COF curves of the DLC/WC-DLC coatings against 319 Al as a function of number of revolutions at different temperatures.

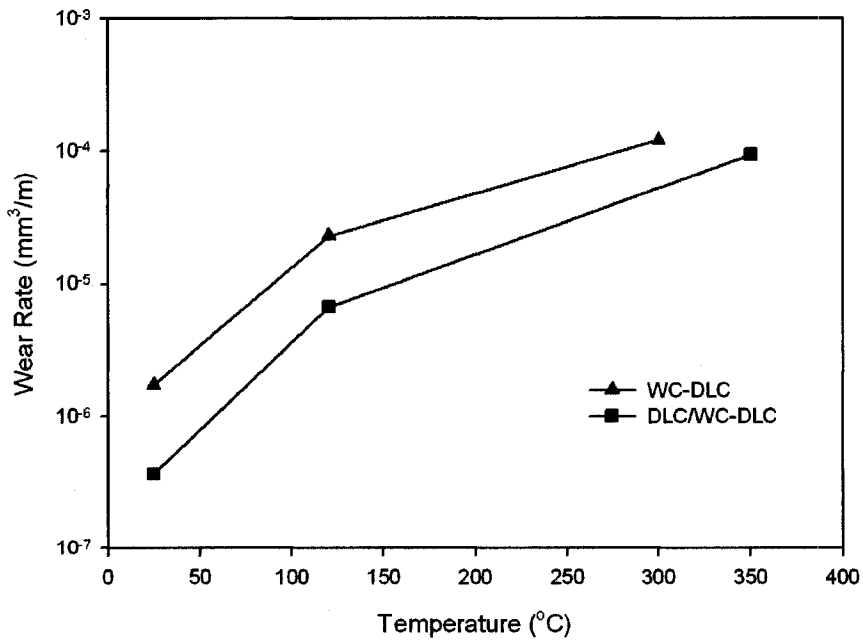

Figure 5. 10 The wear rates of DLC based coatings as a function of test temperature.

a)

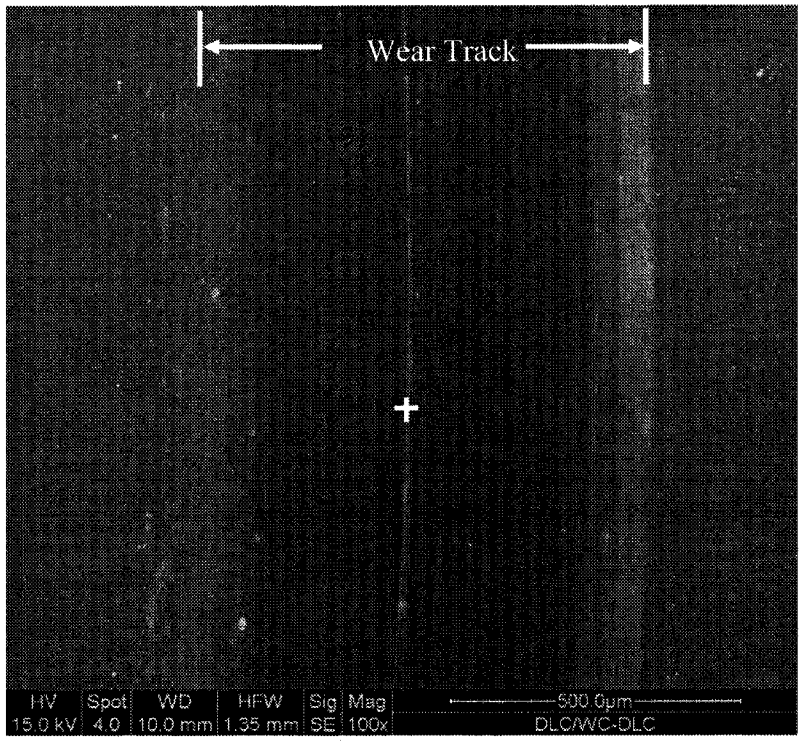

b)

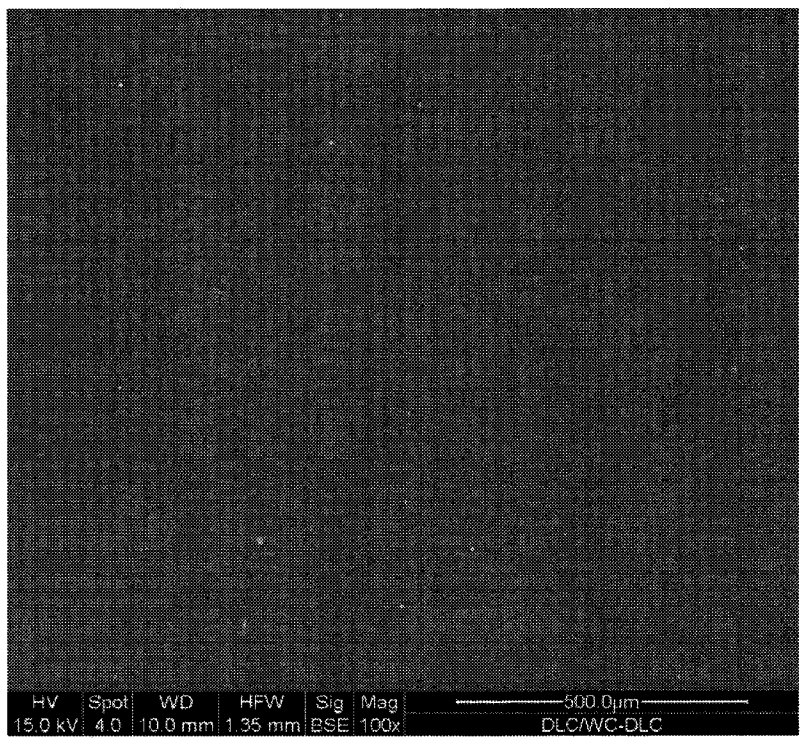

Figure 5. 11 a) The secondary electron SEM image of a section of the wear track of the DLC/WC-DLC coating tested at 350 °C; **b)** The back scattered electron SEM image of the same region.

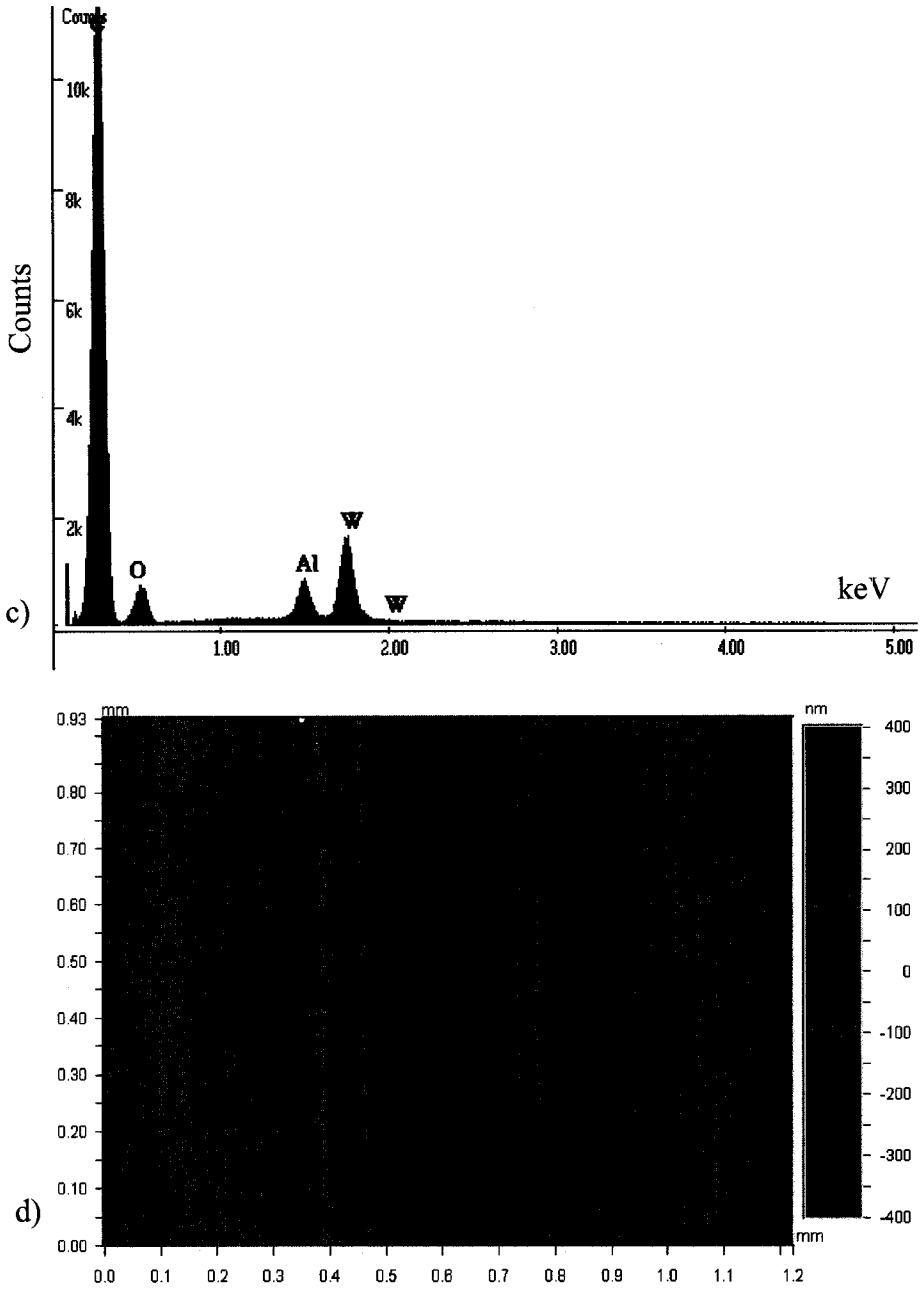

Figure 5. 11 c) The EDS spectrum of the location indicated in a); **d)** 3-D surface profile of the same wear track.

observation of a much deeper wear track than that after testing at 25 °C was consistent with the profound increase in the coating wear rate (**Figure 5. 11 d)**)..

A transferred film was found on the pin tip after testing against a DLC/WC-DLC coating for 10^3 revolutions at 350 °C (**Figure 5. 12 a)**). Compared to the transferred films formed on the pin tips at room temperature (**Figure 5. 3 a)** and **Figure 5. 5 a)**), it had a loose appearance and its carbon content was considerably higher (**Figure 5. 12 b)**). The higher amount of transferred material was also consistent with the deeper wear track observed (**Figure 5. d)**) compared to that produced after testing at 25 °C. The Raman spectrum of the wear track after being tested at 350 °C exhibited a slight shift of the peak located at 1530 cm^{-1} to 1541 cm^{-1} compared to the spectrum of the as-received coating (**Figure 5. 13**). The significance of Raman spectra readings for both WC-DLC and DLC WC-DLC coatings is discussed in **Section 5.5.3.**

5.3 Hardness and Elastic Modulus of Tested Samples

As **Section 2.2.6** explained, the tribological behaviour of DLC coatings tends to deteriorate as the test temperature is elevated, characterized by an increase in COF values and/or wear rates. The same trend was observed in the current study. In an attempt to correlate the variation in the tribological behaviour with possible mechanical properties variation, room temperature nanoindentation tests were also performed on the samples tested at elevated temperatures. Some of the load-displacement curves recorded during the measurement are shown in **Figure 5. 14** The results are plotted as a function of test

a)

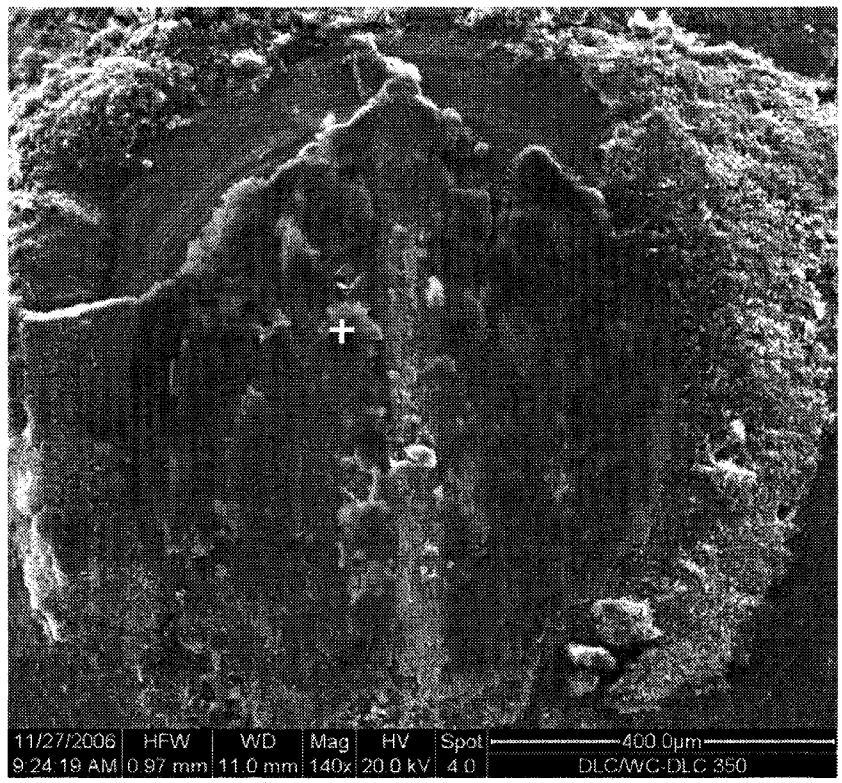

b)

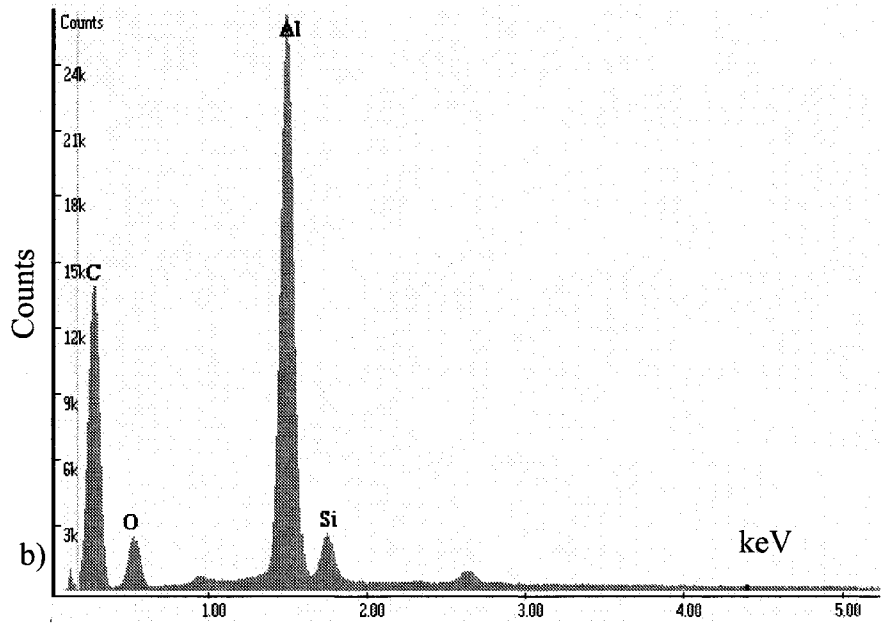

Figure 5. 12 a) SEM image of the 319 Al pin tip after test at 350 °C for 10^3 revolutions against DLC/WC-DLC coating. A layer of transferred material was observed; **b)** EDS spectrum of the location indicated in a), which features a strong carbon peak.

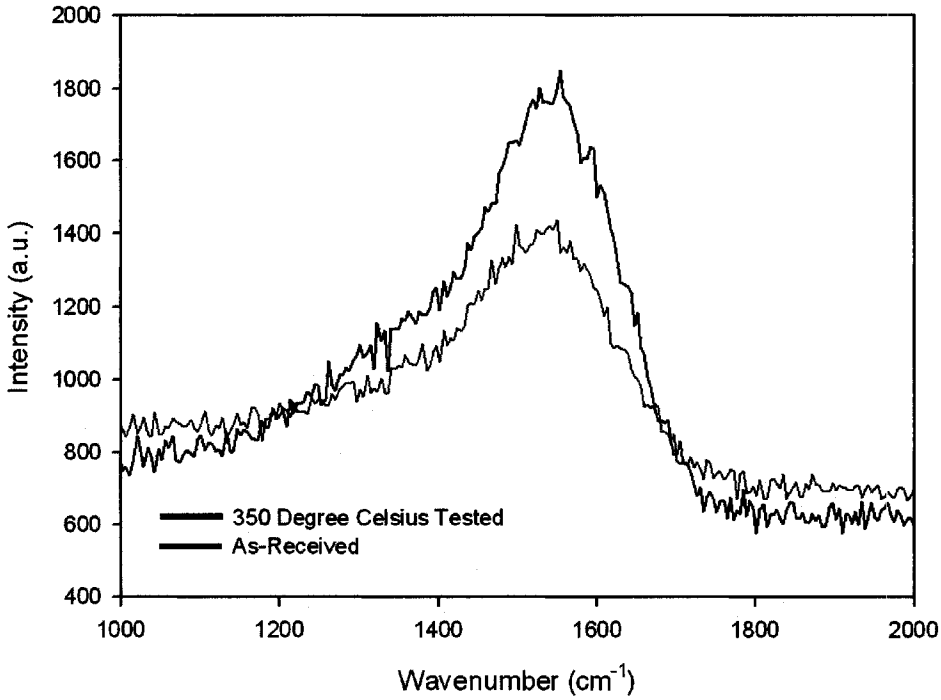

Figure 5. 13 The Raman spectra of the as received DLC/WC-DLC coating and the wear track on the DLC/WC-DLC coating after tested at 350 ° C.

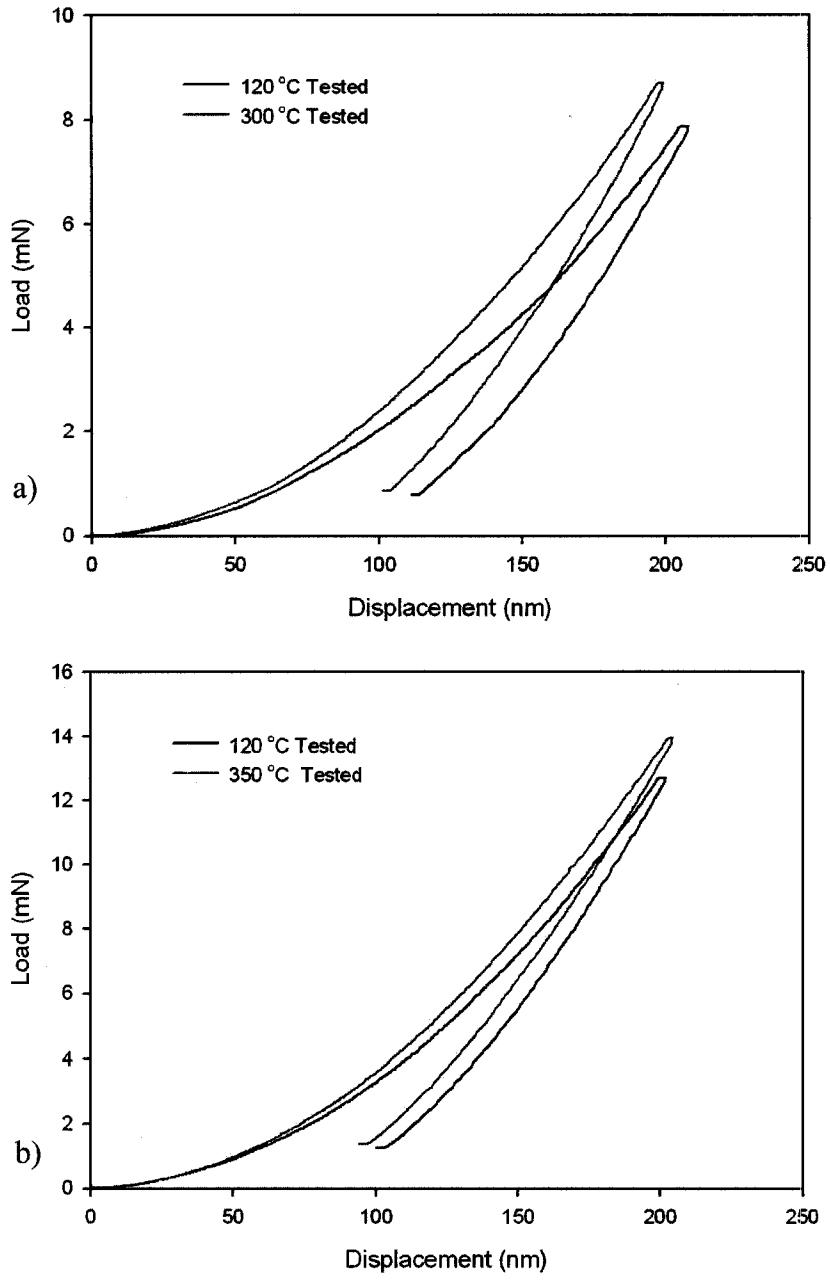

Figure 5. 14 Load-displacement curves recorded during Nanoindentation tests of **a)** WC-DLC and **b)** DLC/WC-DLC coatings after testing at elevated temperatures

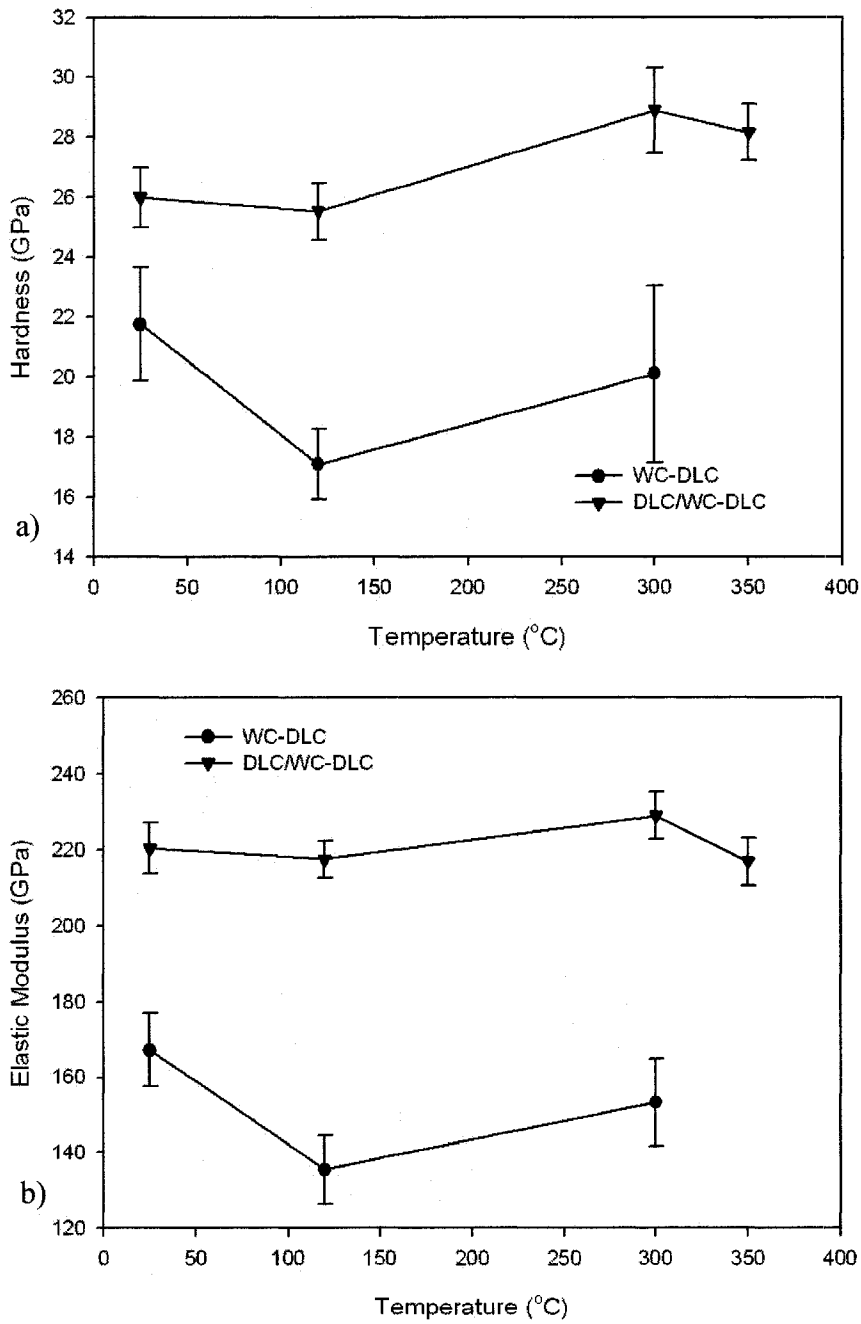

Figure 5. 15 The **a)** Hardness and **b)** Elastic modulus of the WC-DLC coatings and DLC/WC-DLC coatings as a function of test temperature.

temperature as presented in **Figure 5. 15**.

The hardness of the WC-DLC coatings decreased from 21.8±1.9 GPa at 25 °C (as-received coating) to 17.1±1.2 GPa at 120 °C, but increased to 20.1±2.9 GPa after the test was performed at 300 °C. On the other hand, the hardness of DLC/WC-DLC coatings also decreased slightly after testing at 120 °C and then increased after being tested at 300 °C. The hardness was 26.0±1.0, 25.5±0.9, and 28.9±1.4 GPa for the as-received coating and the coatings tested at 120 °C and 300 °C, respectively. After testing at 350°C, the hardness of the coating was 28.1±0.9 GPa--higher than that measured for the as-received coating. The elastic modulus values of both coatings followed the trend of hardness values for each coating.

5.4 Pin-on-disc Tests in Low Humidity (14% RH) and Nitrogen Environments

At room temperature, the DLC based coatings showed steady state COF values after running-in periods of various lengths, regardless of the test environment in which the test was performed. When tested in air under a low humidity of 14% RH, the COF curve of the WC-DLC coating did not display a recognizable shift when compared to the curve recorded under 51% RH (**Figure 5. 16**). The DLC/WC-DLC coating, however, exhibited a drop in the steady state COF value from 0.12 at 51% RH to 0.09 (**Figure 5. 17**). Under a nitrogen atmosphere, the COF values of both DLC based coatings decreased to approximately half of the values recorded in ambient air under ~51% RH--0.06 for WC-DLC coatings and 0.05 for DLC/WC-DLC coatings.

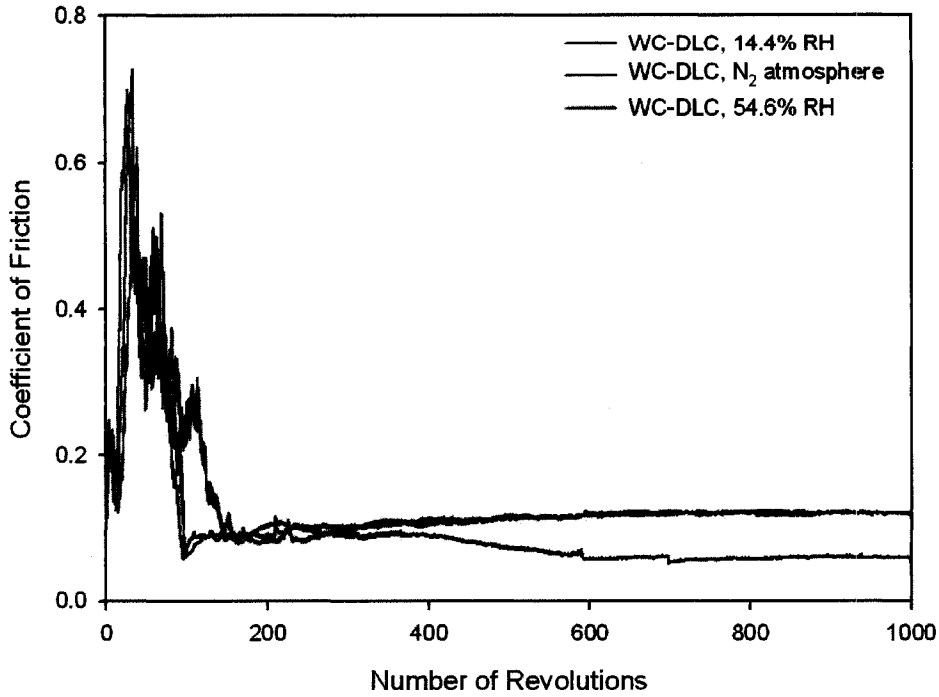

Figure 5. 16 COF curves of the WC-DLC coatings against 319 Al as a function of number of revolutions at different test atmospheres.

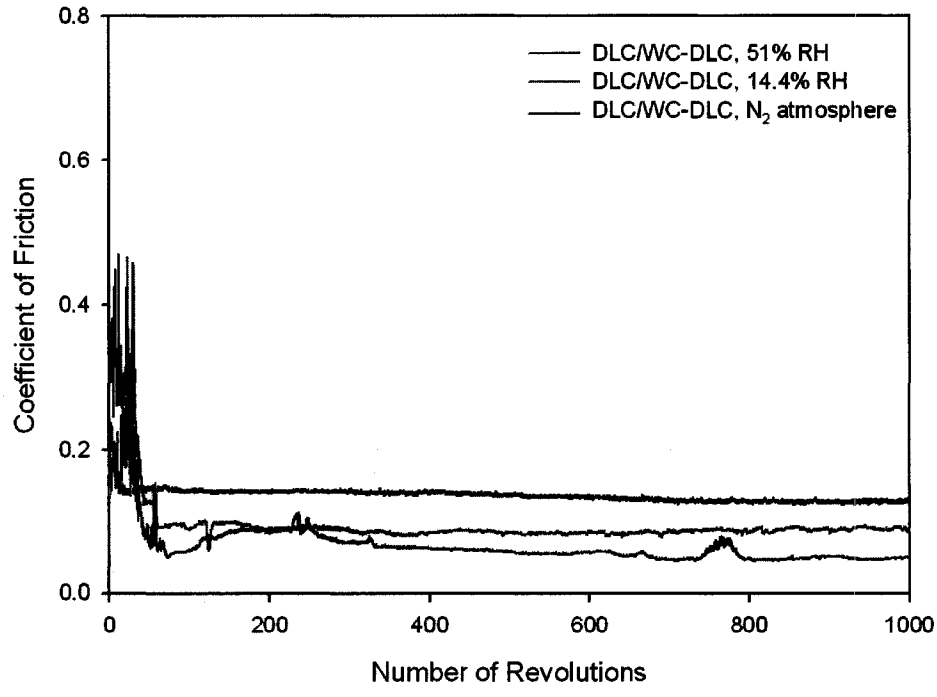

Figure 5. 17 COF curves of the DLC/WC-DLC coatings against 319 Al as a function of number of revolutions in different test atmospheres.

The wear tracks on both coatings that were tested at room temperature in different atmospheres showed no trace of adhered material (**Figure 5. 18** and **Figure 5. 19**).

5.5 Discussion

This section discusses the observed adhesion phenomenon and tribological behaviour of a 319 Al alloy dry sliding against WC containing H-DLC coatings--in accordance to the coating composition and structure. A comparison of the results to those from 319 Al against a B_4C coating and the relevant literature is also presented.

5.5.1 Transfer of 319 Al onto DLC Coatings

At room temperature, NH-DLC, H-DLC and the WC containing H-DLC coatings studied in this work exhibited no adhesion of 319 Al, unlike the B_4C coatings studied, which suffered 0.84% area coverage of the wear track. **Figure 5. 20** illustrates the ranking of various coatings according to the amount of Al that adhered to the wear tracks in ambient air (40-51% RH, 25 °C). All three of the coatings tested in this study are clearly superior industrial candidates for the dry machining of Al.

The aluminum adhesion mitigating property of studied DLC coatings are attributed to the hydrogen content within the coatings. For the WC-DLC and DCL/WC-DLC coatings, the dangling carbon bonds on surfaces are terminated with hydrogen atoms due to their ~ 24 at% carbon content--leading to a weakened interaction between the DLC coating and the aluminum pin material that acts as a shielding effect induced by the hydrogen atoms--prompting the anti aluminum adhesion of the hydrogenated DLC

a)

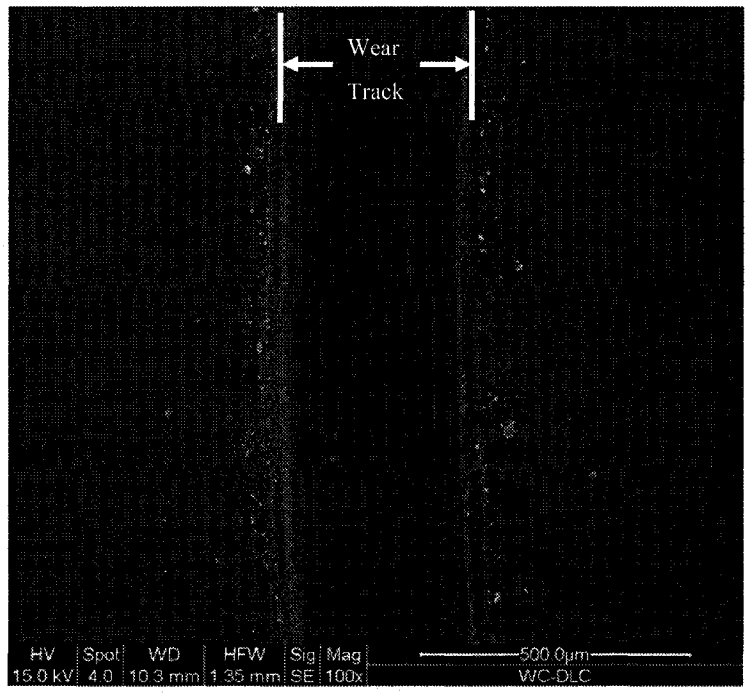

b)

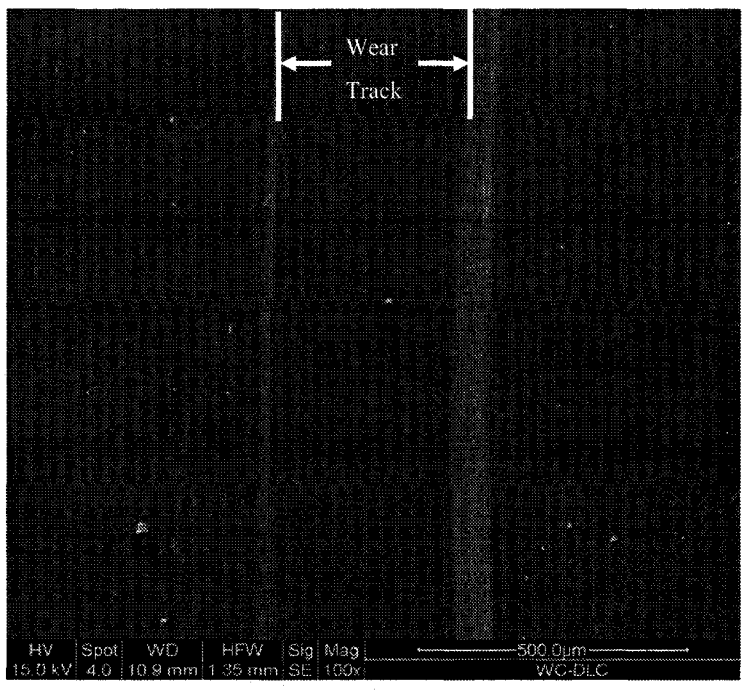

Figure 5. 18 Section of the wear track on the WC-DLC coating after tested against 319 Al **a)** in air with 14% RH and **b)** in N_2. The wear tracks were free of adhered materials.

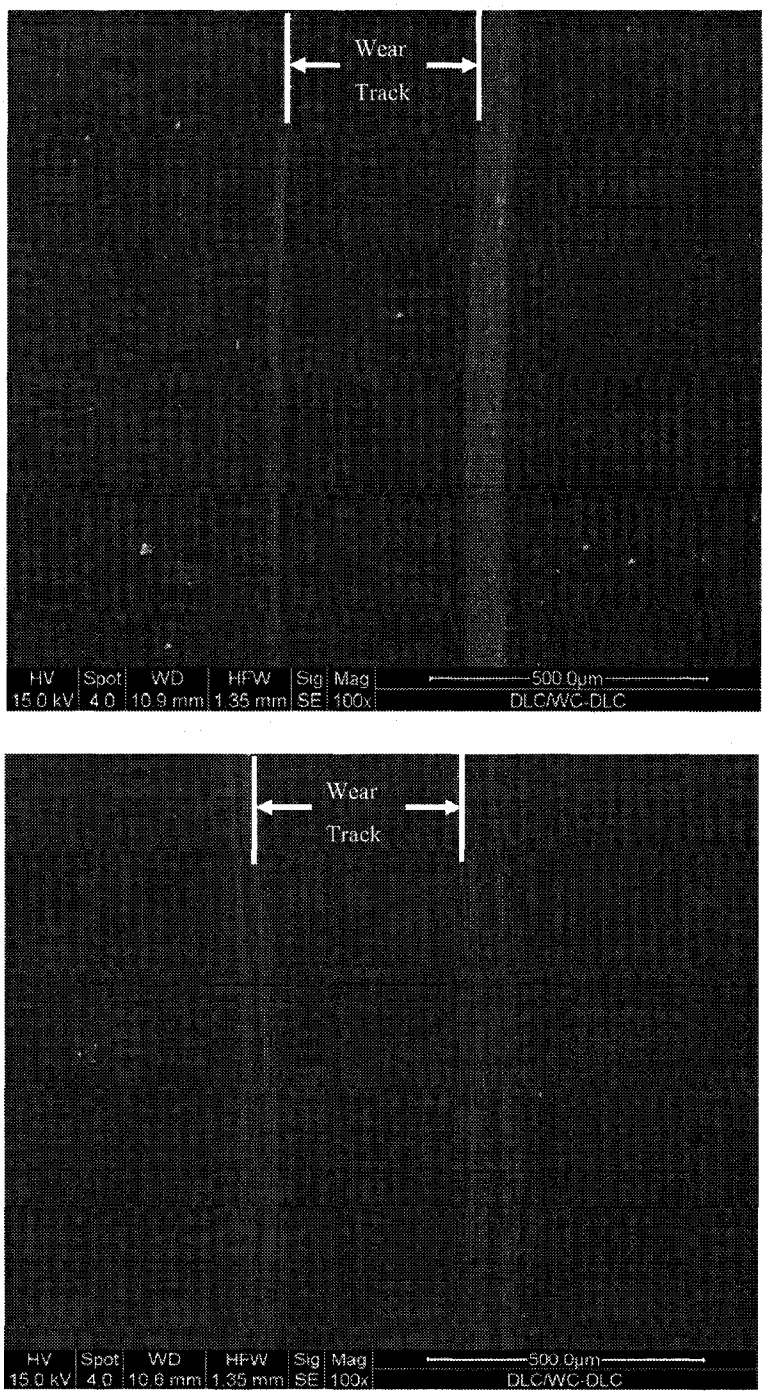

Figure 5. 19 Section of the wear track on the DLC/WC-DLC coating after tested against 319 Al a) in air with 14% RH and b) in N_2. The wear tracks were free of adhered materials.

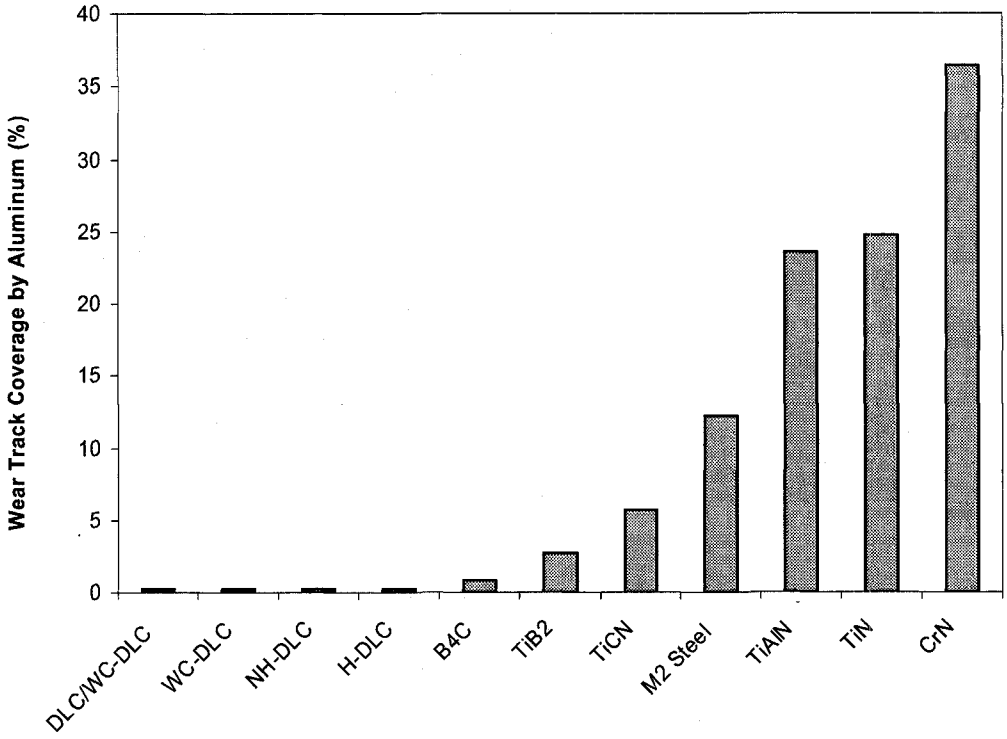

Figure 5. 20 Ranking of various coatings according to the amount of Al adhesion onto the wear tracks in ambient air. The result for H-DLC is from [111] and the rest of the results are adapted from [7] for purpose of comparison.

coatings. The first principles quantum mechanics calculations done by Qi et al. [90] support this opinion by showing that the work of separation is higher between Al/clean diamond (4.08 J/m^2) than Al/H-passivated surface (0.02 J/m^2). The decohesion work within Al atomic layers is calculated to be 1.56 J/m^2, so as long as the hydrogen passivation of the DLC surface is in effect, Al will not adhere to H-DLC coatings.

The current work shows that material containing Al only slightly adheres to hydrogenated DLC coatings at the maximum tested temperatures (300 °C for WC-DLC coating and 350 °C for DLC/WC-DLC coating. This observation implies that the shielding effect provided by the H atoms is sustainable even at elevated temperatures up to 300 °C. However, the ability of NH-DLC coatings to prevent Al adhesion stops when the test temperature is increased. It has been reported that aluminum adheres onto NH-DLC coatings at elevated temperatures as low as 240 °C [111].

5.5.2 Effect of Transfer Layer Formation: Wear Mechanisms DLC Coatings against 319 Al in Ambient Air (51% RH)

Current studied DLC based coatings exhibited low COF and wear rates when tested against 319 Al in ambient laboratory air under 51 % RH. When testing was complete, a well defined layer of transferred material consisting of oxidized aluminum and carbonaceous material (**Figure 5. 3** and **Figure 5. 5**) was observed on the pin tips that had come into sliding contact with the coatings. Such observations are consistent with the

well documented formation of carbonaceous transfer layers on the counterface slid against various DLC coatings in previous studies [69][71-76].

In its as-received state, a DLC coating is unlikely to be worn by a counterface material softer than itself (~20 GPa for DLC coatings vs. ~0.94 GPa for Al 319). Thus, the present work proposes a tribochemical process in which 1) the frictional-heat-induced structural transformation of the topmost surface of the DLC coatings and 2) the chemical reaction of the pin material with oxygen, function synergistically. When the surfaces of the DLC coatings and Al pins were brought into sliding contact, frictional heat was generated between the contact asperities--resulting in a flash temperature increase that rose much higher than room temperature. In order to estimate the temperature rise caused by frictional heating, the method developed by Kong and Ashby [146] was applied to calculate the flash temperature of 319 Al running against WC-DLC and DLC/WC-DLC coatings at the same conditions as the experiments presented in **Section 5.1**. The detailed calculation procedure is described in Appendix 2. The estimated flash temperature at the contact asperities was 165 °C for WC-DLC coating and 84 °C for DLC-WC-DLC coatings--neither of which were high enough to initiate the H release from the bulk coating [73][100].

The above estimation is, however, far from accurate due to the fact that a vigorous treatment of the equivalent length of heat diffusion, the thermal conductivity of the coatings and the partition of the heat between the coatings and their substrates is absent.

It is highly possible that the flash heating of the coating was localized into "hot spots"--resulting in the hydrogen release from the DLC coating only at the contact asperities. It is believed that hydrogen within an amorphous carbon network that contains both sp^3 and sp^2 bonded carbon atoms stabilizes the tetrahetrally coordinated carbon atoms--promoting the cross-linking strength of the coating's relatively sp^2 rich domains [73][147-148]. Further shearing of this weakened, hydrogen-depleted DLC provided the energy needed to overcome the energy barrier so that the coating was converted into a more stable graphitic structure according to the wear-induced graphitization mechanism proposed by Liu and Meletis [73]. A very thin top layer of graphitic material was thus formed by the repetitive contacts between the pin and the coating.

On the pin side, aluminum oxidized readily in the presence of oxygen (ΔG° = -1582.3 kJ/mole at 300K [143]) so that a layer of relatively hard, oxidized (14.71 GPa for alumina) pin material formed quickly in ambient air. This hardened pin surface picked up the top most layer of graphitic material on the DLC coatings as the sliding proceeded, as displayed in **Figure 5. 21**. The oxide layer on the Al 319 surface, however, tended to crack, delaminate and break into loose debris so that the oxide layer sustained a dynamic equilibrium thickness. Some of the debris was caught between the sliding contact region--initiating a three-body abrasion of the graphitized coating's top surface while the hardness of the underneath DLC coatings prevented the abrasive particles from ploughing too deeply into the coating.

a)

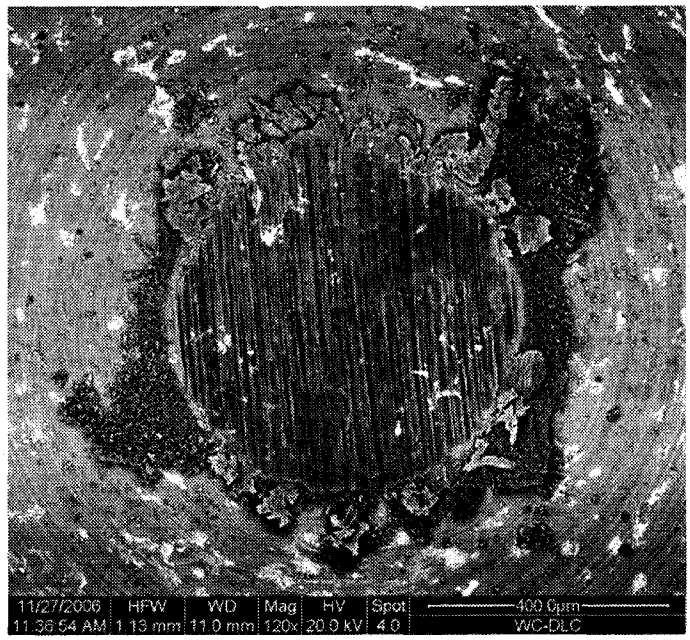

b)

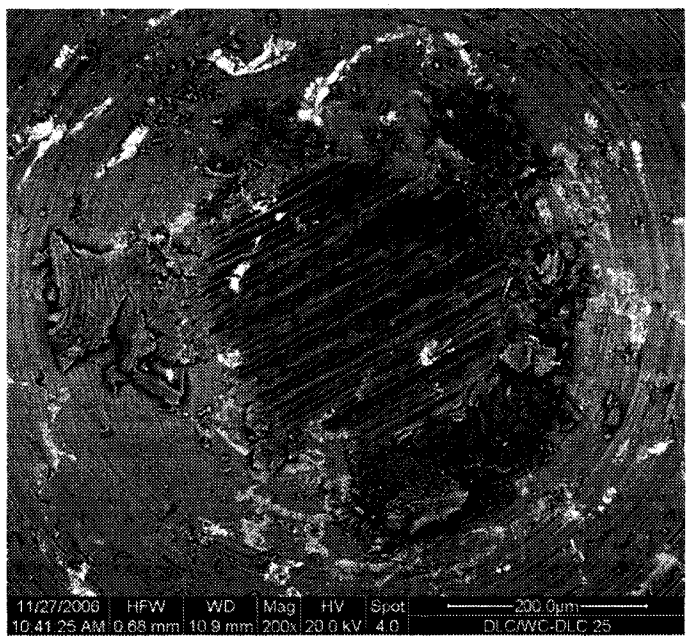

Figure 5. 21 Back scattered SEM images of the 319 Al pin tips tested against a) WC-DLC and b) DLC/WC-DLC coatings at room temperature under 51% RH for 10^4 revolutions. The dark material in both pictures is presumably graphitic carbon formed by friction induced graphitization of the coatings.

The end result of the processes described above is that the actual sliding contact occurred between an oxidized aluminum layer topped with graphitic material and a thin layer of graphitic material located on the coating surface. Under the lubrication of adsorbed water molecules within the test atmosphere, this easy shear graphitic layer acted as a solid lubricant, resulting in low and steady COF values and low wear rates. The pins were also protected from excessive wear by the formation of these layers.

The process explained above did not occur during the sliding of B_4C against 319 Al, so the wear of both the pin and coating materials increased continuously until the coating was totally removed from the substrate and the pin was severely flattened after 10^4 revolutions. The fact that studied DLC coatings remained on the substrate after testing for 10^4 revolutions implies better wear resistance than the B_4C coating against the dry sliding of 319 Al alloy

5.5.3 Effect of Test Temperature on the Tribological Behaviour of DLC Coatings

In this work, the lowest steady state COF values for both WC-DLC and DLC/WC-DLC coatings were recorded at 120 °C. As the testing temperature was increased further, the fluctuation of the COF curve became more conspicuous and no steady state friction behaviour occurred at 300 °C for the WC-DLC coating, or at 350 °C for the DLC/WC-DLC coating. Both the WC-DLC and DLC/WC-DLC coatings exhibited higher wear rates as the test temperature is elevated. The findings of the present work are consistent with previous studies on hydrogenated DLC coatings that observed a

decrease in COF from the room temperature values when testing temperatures entered the range of 100-200 °C. This situation was followed by an abrupt change to high and unsteady friction (failure of the DLC coatings) while monotonically increasing wear rates by elevating the temperature [107][111][149-150]. A comparison of the COF values and wear rates exhibited during dry sliding against 319 Al by H-DLC [111], NH-DLC [109] and the three coatings studied in this work as functions of test temperature is presented in **Figure 5. 22** and **Figure 5. 23**. It is noted that DLC/WC-DLC coating succeeded to attain a low COF value at 300 °C, which is a significant improvement of the friction behaviour of DLC coatings sliding against 319 Al alloys. The studied tungsten containing DLC coatings also exhibited higher wear resistance than monolithic NH-DLC coatings at temperatures higher than 25 °C. However, the wear rates of the WC containing H-DLC coating were approximately one order of magnitude higher than that of H-DLC coating at the highest test temperature. The lowest wear rate exhibited by DLC/WC-DLC coating at 25 °C (51% RH) and lower wear rates than coatings except Ni's H-DLC imply the benefit of multilayering.

Of particular note, this work revealed evidence of coating graphitization. The Raman spectra of the studied DLC coatings after being tested at 300 (WC-DLC) and 350 °C (DLC/WC-DLC) only showed a slight shift of the peak towards higher wavenumber compared to the spectrum of the as-received coating sample (**Figure 5. 8** and **Figure 5. 13**). This could be indicative of the transformation of the carbon bonding structure into a

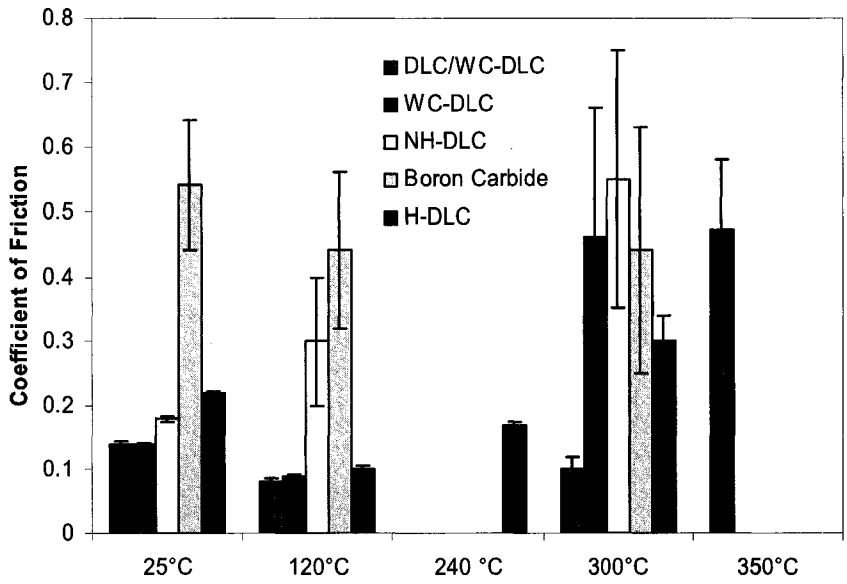

Figure 5. 22 Comparison of COF values of various coatings during dry sliding against a 319 Al alloy at different test temperatures. The results on H-DLC and NH-DLC are from [111] and [109] respectively. The superimposed standard deviation bars reflect the fluctuation of the COF curves.

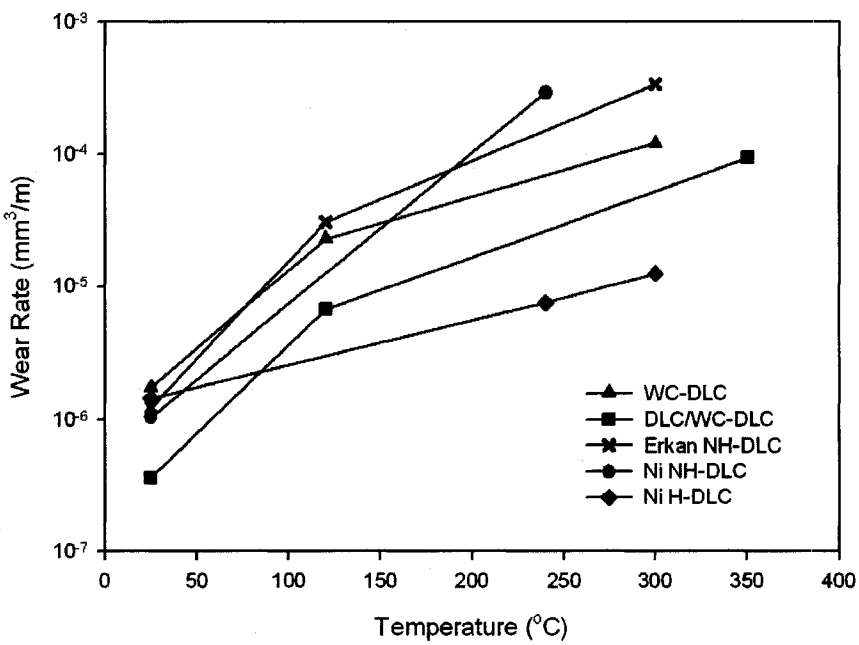

Figure 5. 23 Wear rates of DLC coatings as a function of test temperature. The results on H-DLC and NH-DLC are from [111] and [109] respectively.

more graphitic nature, since the peak located at 1580 cm^{-1} is characteristic of sp^2 bonded carbon atoms [47]. The graphitization of the coating is also implied by the transferred film that was fluffy and loose in appearance found on the 319 Al pin tip after testing at350 °C, exhibiting a high carbon content that was presumably graphitic (**Figure 5. 12 b)**).

Figure 5. 15 illustrates how the mechanical properties of the DLC coatings did not deteriorate significantly even after being tested at 300 and 350 °C. Thus the observed increase in the wear rates of the DLC coatings is attributed to increased graphitization of only the top layer of the DLC coatings at elevated temperatures. This graphitic top layer was more readily removed, exposing a nascent DLC surface which was then subjected to the same process. The higher wear rate of the WC-DLC coating compared to the DLC/WC-DLC coating is considered to be a possible result of its lower hardness combined with the more severe degradation of the coating's mechanical properties.

Possible reasons for the relatively high and unstable COF values exhibited by the DLC coatings at temperatures above 120 °C are:

a. Lack of lubrication between the sliding surfaces. As a metastable material, DLC coatings tend to transform into stable graphite after an energy barrier is overcome. At elevated temperatures, such graphitization processes occur at a higher rate, generating more graphitic carbon between the contact surfaces. However, it is well known that an adsorbed layer of water molecules is required

in order to sustain the graphite's low friction and adsorbed species tend to evaporate from a surface as the temperature is increased. At 120 °C, there was enough adsorbed water between the sliding surfaces to provide a lubrication effect to a higher amount of graphitic material than at 25 °C, so the lowest steady-state COF values were observed. As the test temperature further increased, the amount of water adsorption on the sliding surfaces further decreased and the ease at which the lamella graphitic layers of carbon slide over each other is destroyed--resulting in high and unstable friction around 0.4-0.5, which is close to the value for dry sliding between clean graphite layers [151].

b. Interaction between the pin material and the WC particles. As the surrounding hydrogenated DLC coating was worn by the graphitization process mentioned above, the Al pin could have come into contact with the WC particles embedded in the coating. The minimum work of separation between Al/WC has been calculated to be 3.14 J/m^2 [139]--higher than the cohesive energy of aluminum [90]. The contact between the Al pin and the WC particles would probably prompt the transfer and adhesion of aluminum onto the coating surface. The WC content in the DLC coatings is presumed to be low so that adhesion of materials containing aluminum only occurs on a small scale.

The presence of the top H-DLC layer on the DLC/WC-DLC coating provided an extra barrier layer so that the first proposed explanation becomes the principle one for the

unsteady friction observed before the top H-DLC layer was removed. Once the top H-DLC layer was removed, the pins were more likely to interact with the WC particles according to the second proposed process. For the WC-DLC coating, the interaction between the Al pin and the WC particles after the removal of graphitic carbon became the cause for the variation of the COF curve. The current observations also imply that the hydrogen shielding of carbon atoms provided by the top H-DLC layer could be effective up to 300°C.

5.5.4 Effect of Test Environment on the Tribological Behaviour of DLC Coatings

Variations in the testing environment's relative humidity level exert different influences on the friction behaviour of WC-DLC and DLC/WC-DLC coatings. For WC-DLC coatings, the steady state COF remained practically the same while an increase in the COF value with increasing humidity value was observed for the DLC/WC-DLC coating (**Figure 5. 16** and **Figure 5. 17**). Testing in a nitrogen atmosphere reduced the COF values of both coatings to nearly half of the value obtained at 51% RH.

The observation for the DLC/WC-DLC coatings is typical of the results exhibited by non-doped H-DLC coatings. It is generally accepted that hydrogenated DLC coatings exhibit higher COF values in the presence of water vapour and/or oxygen [84-86][95]. Water and/or oxygen molecules in the environment can be adsorbed onto the coating surface, resulting in a stronger interaction between the coating and the sliding counterface.

Under high relative humidity (~50%), adsorbed water is more likely to form multiple layers, which could result in viscous drag and capillary forces. Current findings on DLC/WC-DLC coatings have verified this mechanism.

The possible reduction of the WC-DLC coating's moisture sensitivity is considered a result of WC incorporation into the amorphous H-DLC coating. Similar results on Ti doped H-DLC coatings have been reported by Gilmore and Hauert [113]. While the mechanism for this phenomenon is unclear at this stage, doping with WC does not eliminate the effect of oxygen adsorption on the friction behaviour of the hydrogenated DLC matrix because the COF of the WC-DLC coating decreased to ~0.06 when the oxygen pressure was reduced by the introduction of an N_2 atmosphere.

5.6 Summary and Remarks

The effects of test temperature and atmosphere on the tribological behaviour of DLC coatings dry sliding against 319 Al were studied using pin-on-disc tests to investigate said coatings' suitability for the dry machining of aluminum alloys. Both temperature and atmosphere were shown to be significant factors in the tribological behaviour of DLC coatings. The findings of the current work are:

1. No transfer and adhesion of pin material were observed under all test conditions except at the maximum tested temperatures for DLC coatings. It is suggested that passivation of the carbon atoms by hydrogen is responsible for this result.

2. Both the WC-DLC and DLC/WC-DLC coatings displayed low and steady COF values around 0.12 and low wear rates in the range of 10^{-6} – 10^{-7} mm^3/m at room temperature in ambient air. This observation is attributed to the formation of a carbonaceous transfer layer on the counterface.

3. DLC/WC-DLC coatings exhibited a lower COF than WC-DLC coatings at elevated temperatures. DLC/WC-DLC coatings presented a steady state COF value of 0.10 at 300 °C whereas the WC-DLC coating failed to reach steady state COF at the same temperature.

4. At 120 °C the steady state COF values for the DLC/WC-DLC (0.08) and WC-DLC (0.09) coatings were lower than the corresponding values at 25 °C (0.12 and 0.14, respectively) at 51% RH.

5. The wear rate of the DLC/WC-DLC coatings was lower at 350 °C (9.30×10^{-5} mm^3/m) than that of WC-DLC coatings at 300°C (1.20×10^{-4} mm^3/m).

6. The fact that coating wear rates increased with elevated temperatures is attributed to the graphitization of the top most layer of the coating for DLC/WC-DLC coatings, while the softening of the coating might also be a contributing factor for the WC-DLC coatings.

7. At room temperature, WC-DLC coatings exhibited the lowest steady state COF values (0.06) in an N_2 atmosphere. WC-DLC showed less sensitivity to atmospheric humidity than DLC/WC-DLC.

CHAPTER 6 CONCLUSIONS

The tribological behaviour of B_4C and DLC (DLC/WC-DLC and WC-DLC) coatings during dry sliding contact with a 319 Al alloy has been investigated under various test conditions in order to probe their suitability as tool coatings used for the dry machining of aluminum alloys. The main conclusions and industrial significance of this study can be summarized as follows:

6.1 Coating Structure

1) The B_4C coating is a partially crystallized coating.

2) The WC-DLC coating is an H- DLC coating containing WC dopants.

3) The DLC/WC-DLC coating is a multilayer coating that combines one layer of WC-DLC coating and one top layer of H-DLC coating.

6.2 Transfer of 319 Al to Various Coating Surfaces

1) In ambient air (51% RH), no Al transfer occurred to the DLC coatings tested in the current work, while Al transfer was observed for the B_4C coatings. However, compared to other industrial coatings, the B_4C coating still managed to reduce the amount of Al adhesion to only 31% of the TiB_2 coating, which exhibited the least Al adhesion among other industrial coatings.

2) Al transferred to B_4C coatings at low humidity (14.4% RH) and in N_2, but not to the H-DLC coatings.

3) The amount of Al transfer increased dramatically at elevated temperatures for the B_4C coatings--namely a 1900% increase was observed at 300 °C compared to 25 °C. For the studied DLC coatings, a small amount of Al transfer occurred only at the maximum temperatures tested (300 °C for the WC-DLC coating and 350 °C for the DLC/WC-DLC coating). Compared to NH-DLC, the Al adhesion mitigating property of tungsten containing H-DLC is superior.

4) A possible explanation for the Al transfer to the B_4C coating surface is that the work of separation between the Al/B_4C interface is higher than the decohesion energy of an Al/Al interface. The excellent Al adhesion mitigating property of the DLC coatings is due to the hydrogen passivation of dangling carbon bonds on the surface.

6.3 COF of the B_4C Coatings

6.3.1 Against 319 Al

1) The mean COF value of B_4C against an Al 319 alloy is 0.48±0.06 at room temperature under 51% RH. The coating was removed from the substrate after 10^4 revolutions of sliding contact. An adhesion-delamination-three body abrasion mechanism involving delaminated, possibly hardened and oxidized Al micro chips from the pin tip is proposed by the author.

2) The mean COF of 319 Al sliding against a B_4C coating decreases slightly (1%) as the test temperature is elevated--perhaps due to the thermal softening of Al and the

self-welding prevention provided by the enhanced formation of oxidized Al at high temperatures (especially at 300 °C).

3) B_4C exhibited a larger fluctuation in COF values at a higher relative humidity level--possibly stemming from the further roughening of the contact surface due to micro-fracturing of the asperities with the presence of more water vapour.

4) The lowest COF--a steady-state value of 0.36--was observed for B_4C coatings when tested in N_2.

6.3.2 Against 52100 Steel

1) The mean COF value of 52100 steel dry sliding against a B_4C coating at room temperature under 51% RH is much higher than that of 319 Al against a B_4C coating (0.80±0.05 vs. 0.48±0.06). This difference is attributed to 52100 steel's higher strength.

2) The mean COF value increased as the test temperature was elevated for the 52100 steel-B_4C coating material pair.

6.4 Tribological Behaviour of the DLC Coatings

1) Both WC-DLC and DLC/WC-DLC coatings displayed low COF values--approximately 0.12--and low wear rates at room temperature. These observations are attributed to the formation of a carbonaceous transfer layer on top of the 319 Al pin, as well as the hydrogen passivation of the DLC coating surfaces.

2) Higher wear rates were observed for both DLC coatings when tested at elevated temperatures--explained by intensified surface graphitization and the sequential, more ready removal of the resulting low-strength graphitic top layer.

3) The steady state COF value was lower when tested at 120 °C, compared to tests run at room temperature (51% RH). Enhanced graphitization of the top most surface of the coatings and lubrication from the surrounding water vapour might be the cause of these results.

4) DLC/WC-DLC coatings exhibited a steady state COF value of 0.10 at 300 °C, whereas the WC-DLC coatings failed to reach steady state COF at the same temperature. The wear rate of the DLC/WC-DLC coatings was lower at 350 °C (9.30×10^{-5} mm^3/m) than that of the WC-DLC coatings at 300°C (1.20×10^{-4} mm^3/m). The presence of a top H-DLC layer is believed to be responsible for the superior high temperature behaviour of DLC/WC-DLC coating.

5) The WC-DLC and DLC/WC-DLC coatings failed to attain a steady state COF at 300 °C and 350 °C, respectively. Such failure could be explained by i) desorption of water from the sliding interfaces at elevated temperatures, leading to insufficient lubrication of the graphitic sliding interface; and/or ii) a stronger interaction between the Al pin tip and the WC particles.

6) The thermal stability of the studied coatings is improved when they are doped by W, compared to non-doped DLC coatings.

7) Doping by WC may reduce the moisture sensitivity of WC-DLC coatings. DLC/WC-DLC is sensitive to the presence of water vapour due to its H-DLC top layer.

6) Testing in N_2 reduced the COF values of both coatings to a very low value of ~0.06. This suggests that N_2 might reduce the amount of oxygen and water molecule adsorption onto the coating surface, resulting in weaker interaction between the coating and the 319 Al pin.

6.5 Industrial Significance of Conclusions: Practical Conclusion

1) The B_4C coating is not totally suitable for the purpose of dry machining Al alloys because its COF value--high compared to that of DLC coatings--and its inability to prevent Al adhesion even at room temperature makes it not as good a choice.

2) WC containing H-DLC coatings are more promising candidates as tool coatings for the dry machining of Al alloys thanks to their low COF values when tested up to 300 °C and the low wear rates exhibited at room temperature.

3) The observation that N_2 gas in the test atmosphere could effectively reduce the COF values of all the tested coatings suggests that the best approach would be "N_2 lubrication"--using nitrogen gas instead of MWF to achieve successful dry machining.

6.6 Suggestions for Future Work

For B_4C coating systems:

1. TEM investigation of the coating structure will provide deeper insight into the relative amount of amorphous and crystalline phase within the coating. The presence

of deposition defects such as graphitic phase between the columnar structures will also be revealed.

2. Al-B_4C coating interface study using TEM to discover structure changes in adhered Al, such as grain refinement. This investigation will provide information on whether the adhesion of Al is caused by chemical bonding or just mechanical interaction.
3. Calculation of the energy required to separate Al/B_4C interface will help us understand the adhesion on an atomic level.
4. Annealing the B_4C coating at a high temperature (600 °C, for example) in air and then testing it against 319 Al in different humidity levels will explain if the tribological properties of B_4C coatings might be improved by introducing a thin boric oxide top layer.
5. Further investigation of the 52100 steel-B_4C coating material pair following the routing used in this work and items 1 to 4 mentioned above.

For the DLC based coatings:

1. The DLC coatings remained effective at providing a low COF in ambient air for 10^4 revolutions. Future studies will extend the duration of the tests to determine how long this desirable property lasts. Testing would continue until penetration of the DLC coatings to provide an estimation of coating life.

2. A detailed TEM investigation of the coating structure will provide a better understanding of the doped WC particles--including determining the amount of WC doped and whether the particles are well crystallized.
3. Anneal the DLC coatings at different temperatures and then conduct the TEM characterization described above. Understanding the structural change of the WC dopants will be essential for a comprehensive explanation of the tribological behaviour of DLC coatings at elevated temperatures.
4. The good tribological behaviour of DLC coatings are attributed to the formation of a carbonaceous transfer layer on the counterface, but in real application (such as drilling), the coating comes into contact with nascent counterface material instead of passing through one point repeatedly. The design of a new test configuration that represents such contact better will simulate a real application. Sliding tests that result in a spiral track would be an excellent choice for this purpose.
5. Further investigation of the transfer layer on the counterface is recommended--including the determination of the shear strength of this layer to better support the low friction mechanism it induces. Detailed structural information on the carbon content in this layer will provide a fuller understanding of the transfer layer formation mechanism.
6. Conduct drilling tests using drills coated with DLC coatings. What if the applied shear stress is increased by at least one order of magnitude? In real drilling, the thrust

force applied is far higher than 5 N. A detailed characterization of the drill after the tests will reveal the operation mechanism of the DLC coating in a real application.

APPENDICES

A 1 Friction of Coefficient Curves

All the COF curves recorded in the current work are presented in this section. All the tests were conducted under 5 N load and 0.12 m/s sliding speed.

A 1.1 319 Al dry sliding against B_4C coatings.

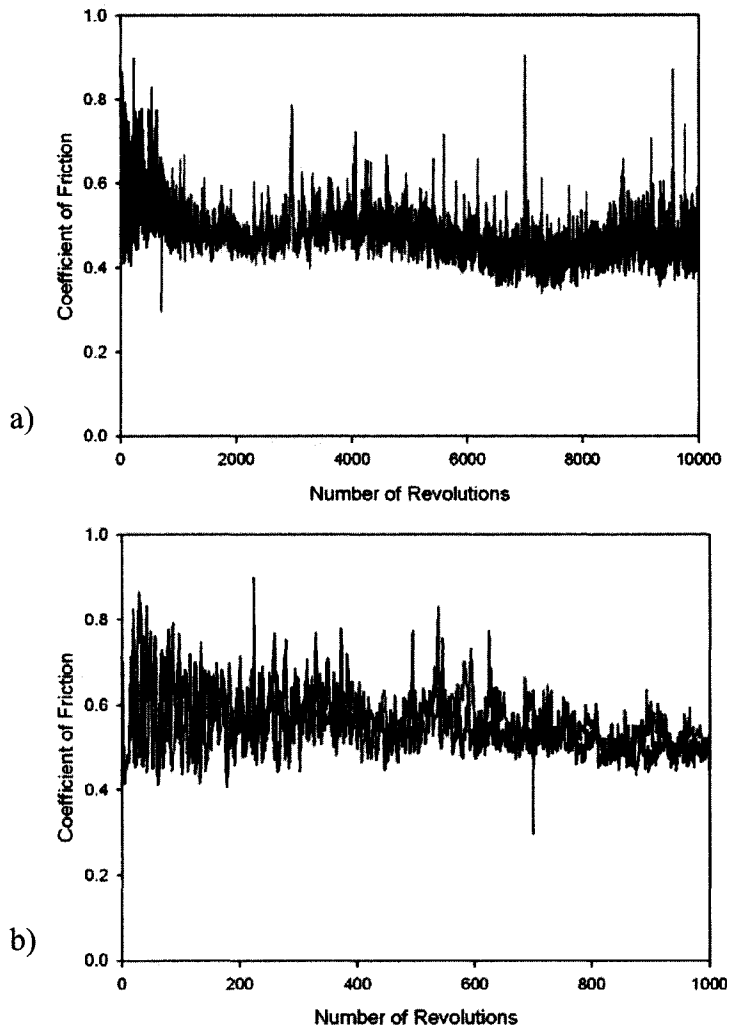

Figure A 1. 1 The COF curves between the B_4C coating and a 319 Al alloy during sliding in ambient laboratory air (25 °C, 51% RH). **a)** up to 10000 cycles of sliding; **b)** First 1000 cycles shown in **a)**.

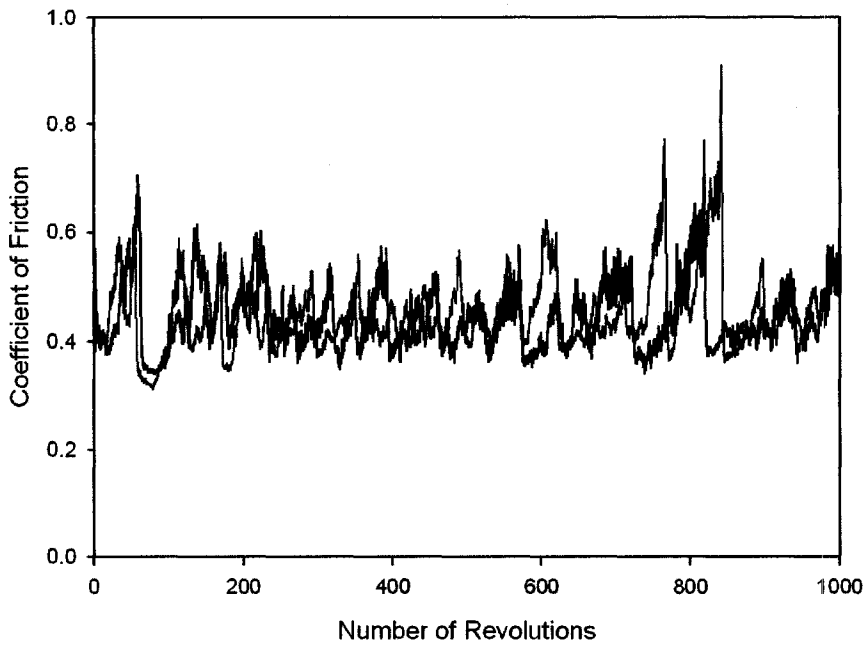

Figure A 1. 2 The COF curves between the B_4C coating and a 319 Al alloy during sliding at 120 °C

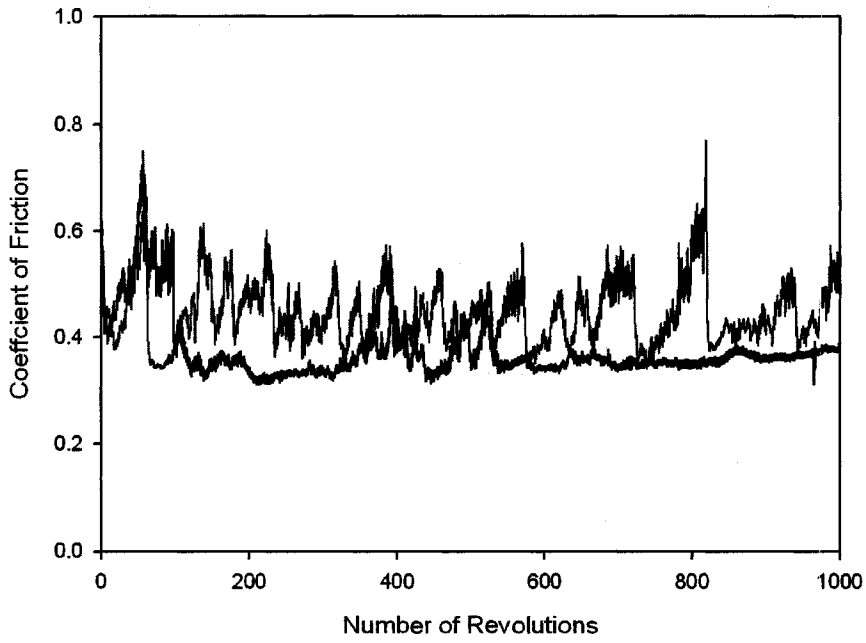

Figure A 1. 3 The COF curves between the B_4C coating and a 319 Al alloy during sliding at 300 °C

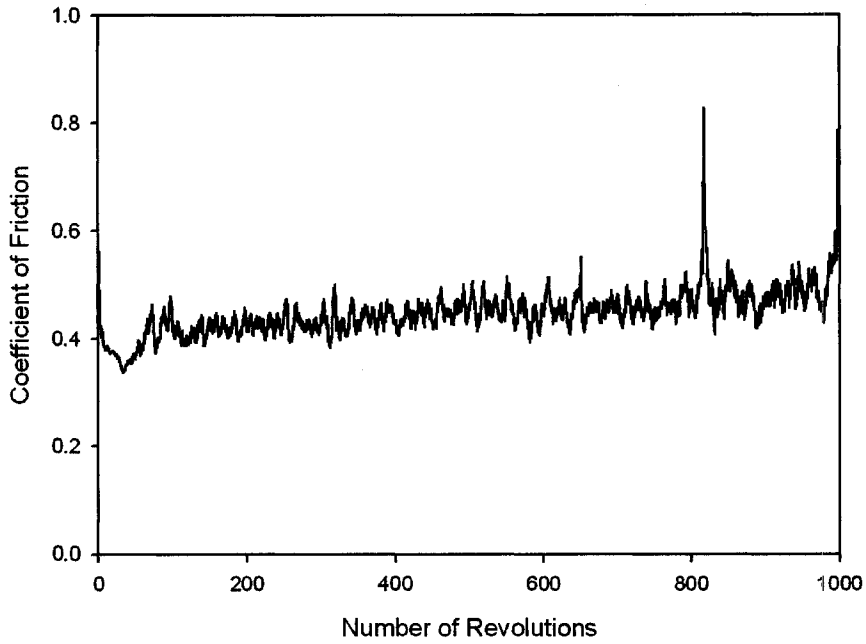

Figure A 1. 4 The COF curve between the B_4C coating and a 319 Al alloy during sliding at 25 °C under 14% RH.

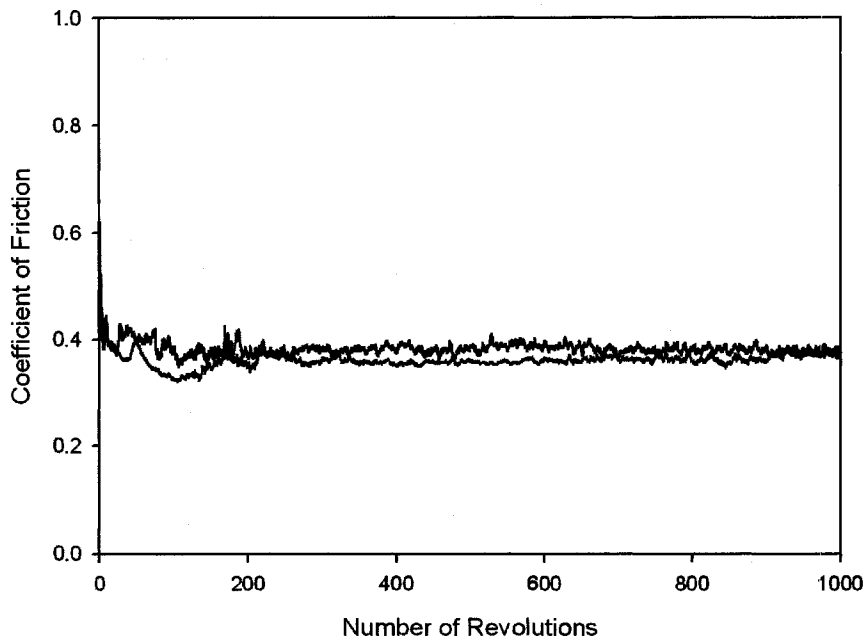

Figure A 1. 5 The COF curves between the B_4C coating and a 319 Al alloy during sliding in N_2.

A 1.2 52100 steel dry sliding against B_4C coatings

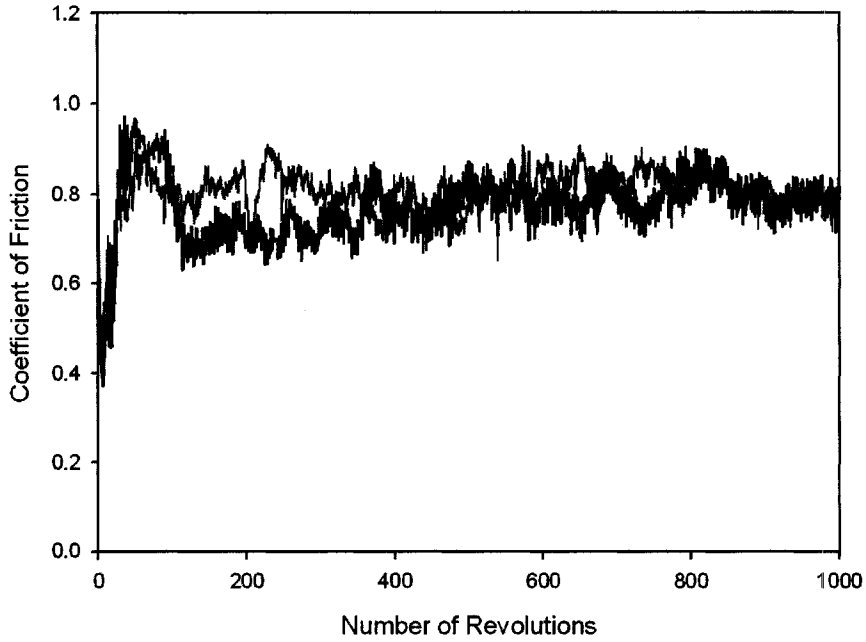

Figure A 1. 6 The COF curves between the B_4C coating and 52100 steel during sliding in ambient laboratory air (25 °C, 51% RH).

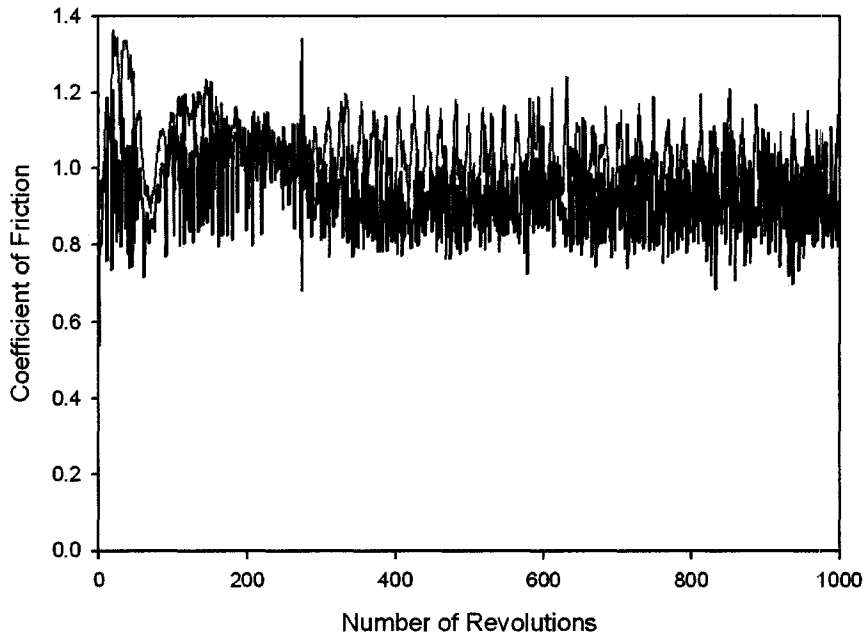

Figure A 1. 7 The COF curves between the B_4C coating and a 319 Al alloy during sliding at 120 °C

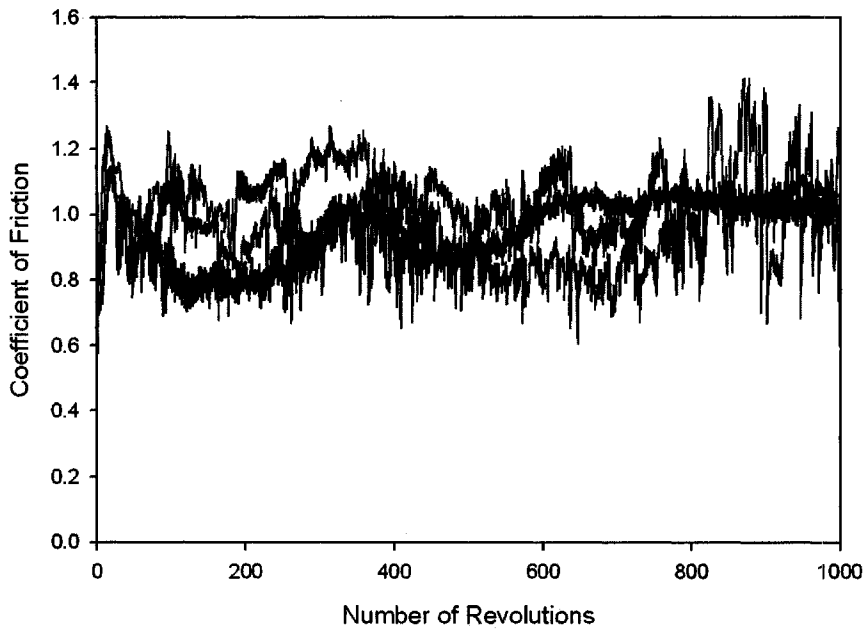

Figure A 1. 8 The COF curves between the B_4C coating and a 319 Al alloy during sliding at 300 °C

A 1.3 319 Al alloy dry sliding against DLC coatings

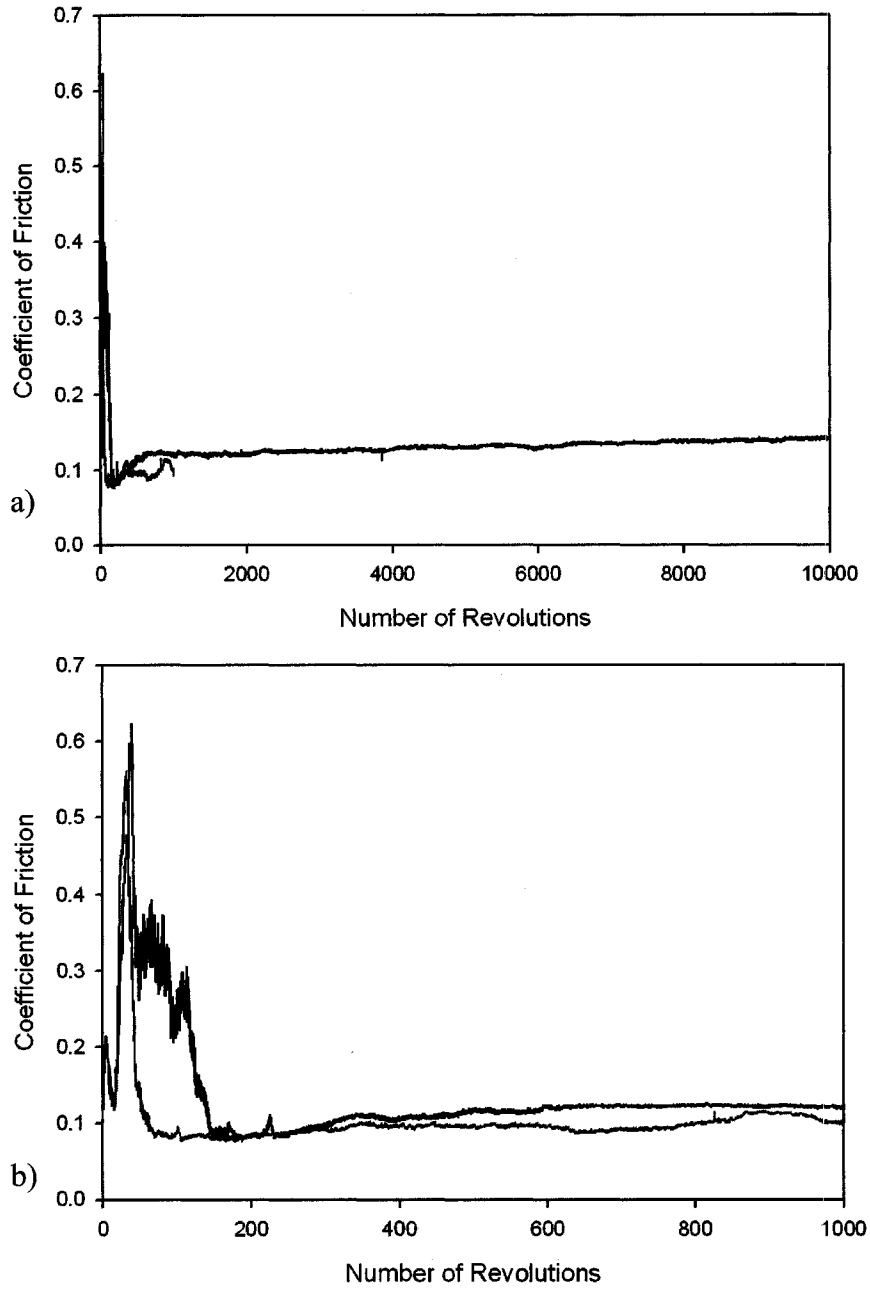

Figure A 1. 9 The COF curves between the WC-DLC coating and a 319 Al alloy during sliding in ambient laboratory air (25 °C, 51% RH). **a)** up to 10000 cycles of sliding; **b)** First 1000 cycles shown in **a)**.

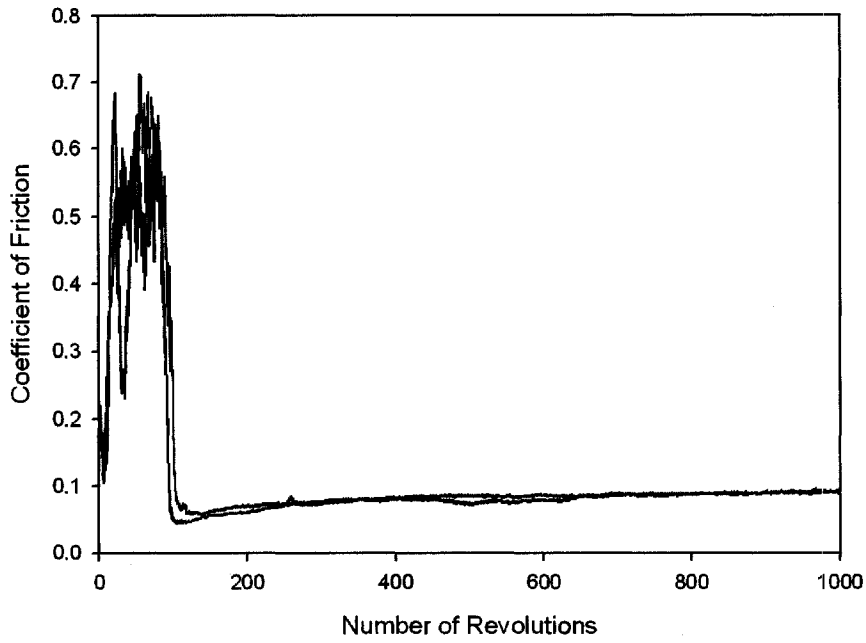

Figure A 1. 10 The COF curves between the WC-DLC coating and a 319 Al alloy during sliding at 120 °C

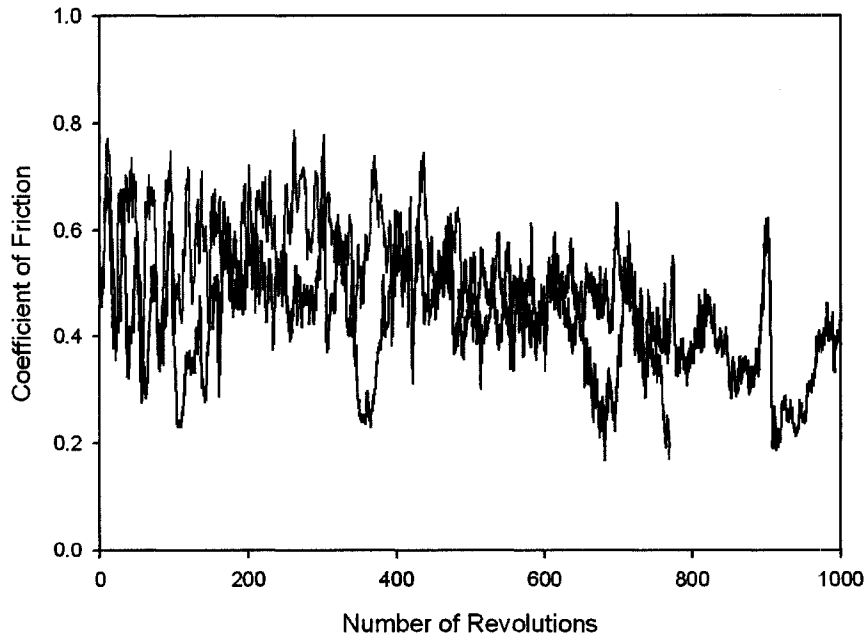

Figure A 1. 11 The COF curves between the WC-DLC coating and a 319 Al alloy during sliding at 300 °C

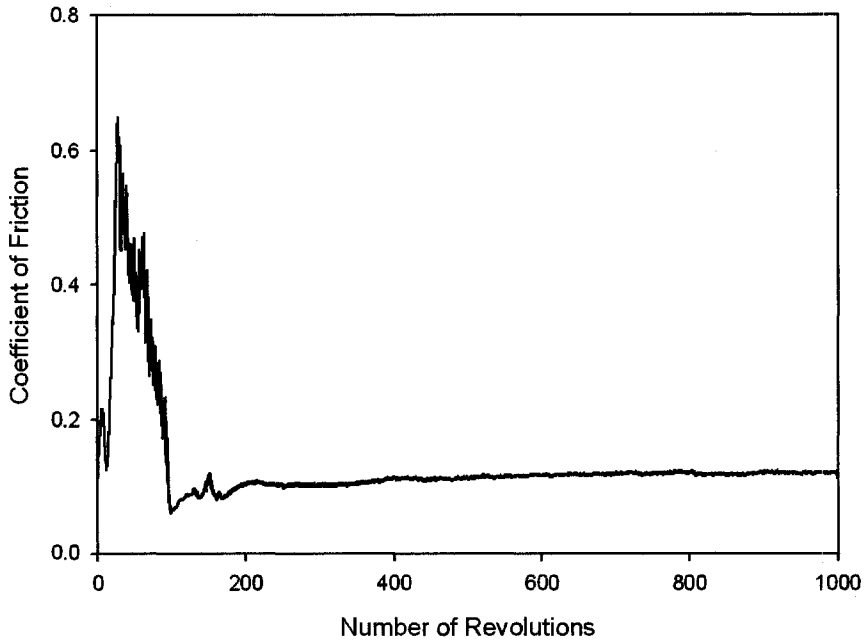

Figure A 1. 12 The COF curve between the WC-DLC coating and a 319 Al alloy during sliding under 14% RH.

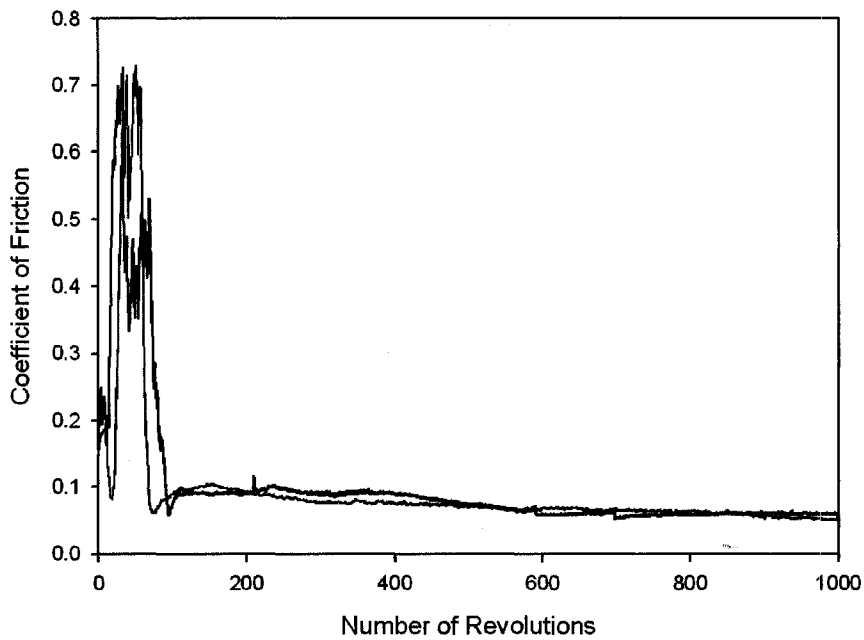

Figure A 1. 13 The COF curves between the WC-DLC coating and a 319 Al alloy during sliding in N_2.

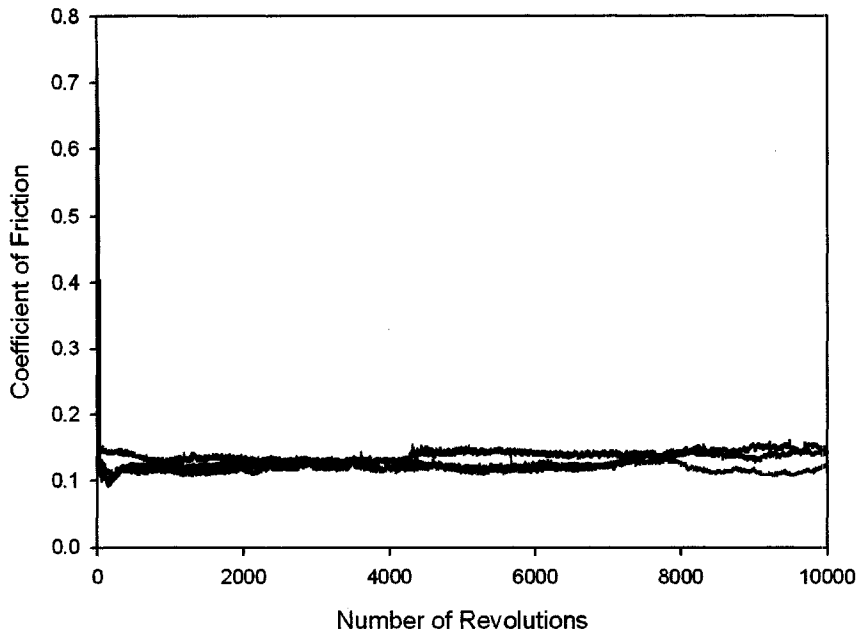

Figure A 1. 14 The COF curves between the DLC/WC-DLC coating and a 319 Al alloy during sliding in ambient laboratory air (25 °C, 51% RH)

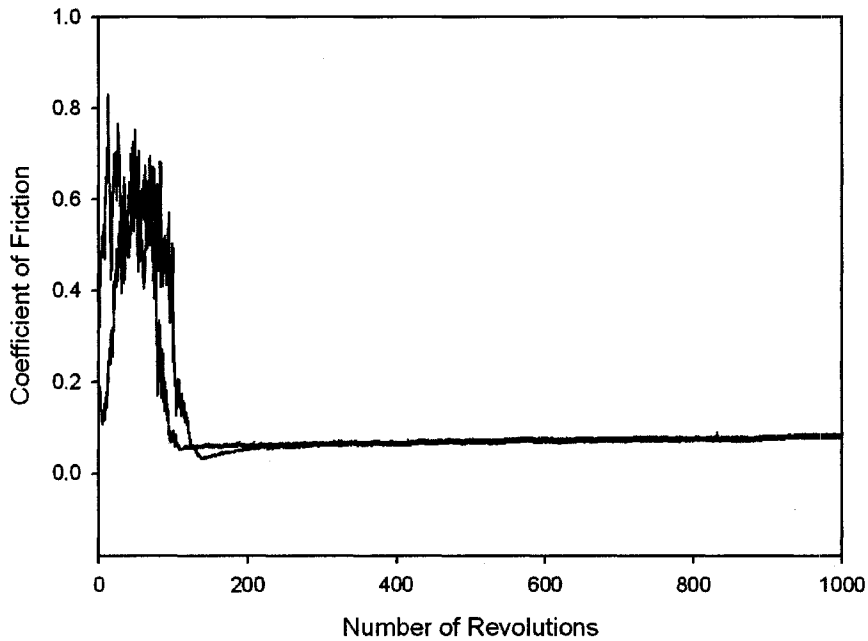

Figure A 1. 15 The COF curves between the DLC/WC-DLC coating and a 319 Al alloy during sliding at 120 °C

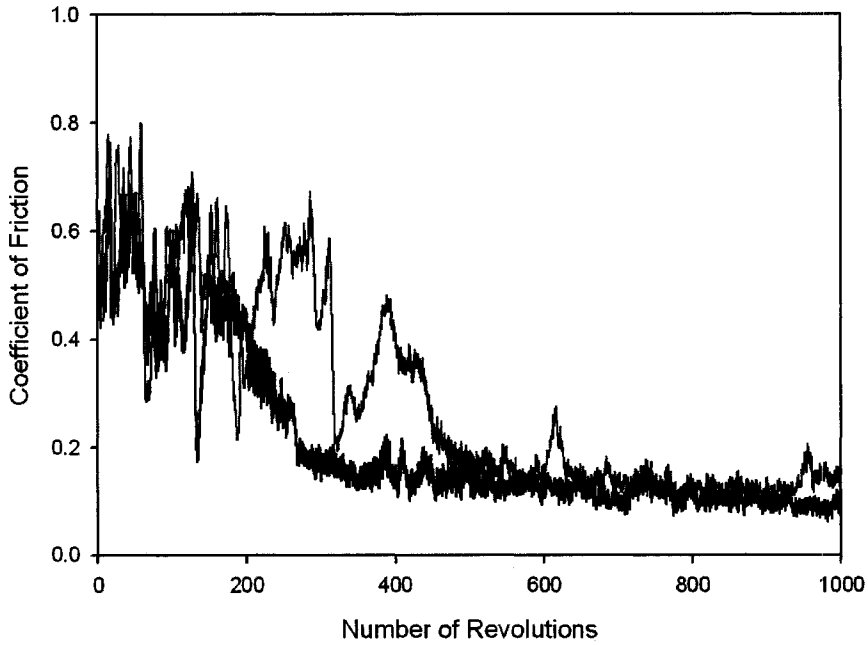

Figure A 1. 16 The COF curves between the DLC/WC-DLC coating and a 319 Al alloy during sliding at 300 °C

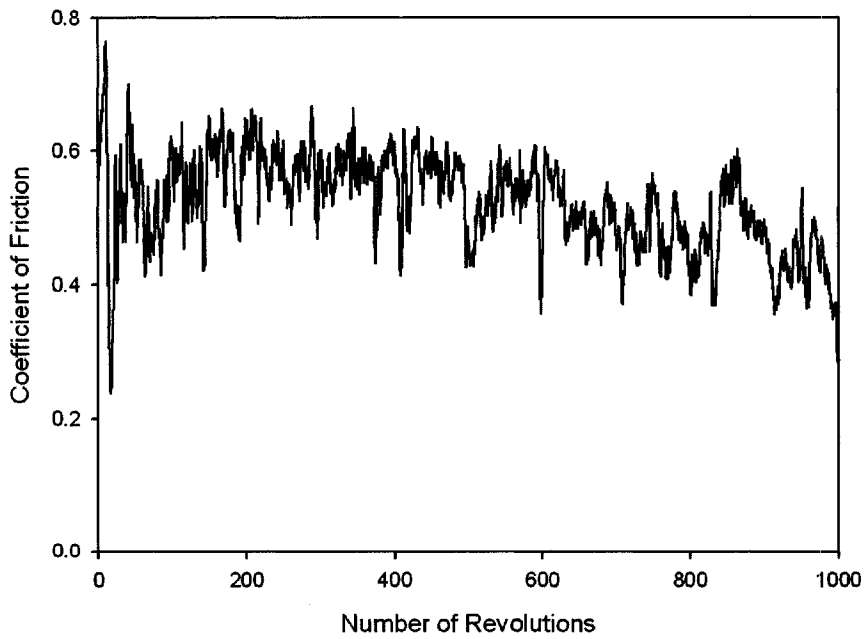

Figure A 1. 17 The COF curve between the DLC/WC-DLC coating and a 319 Al alloy during sliding at 350 °C

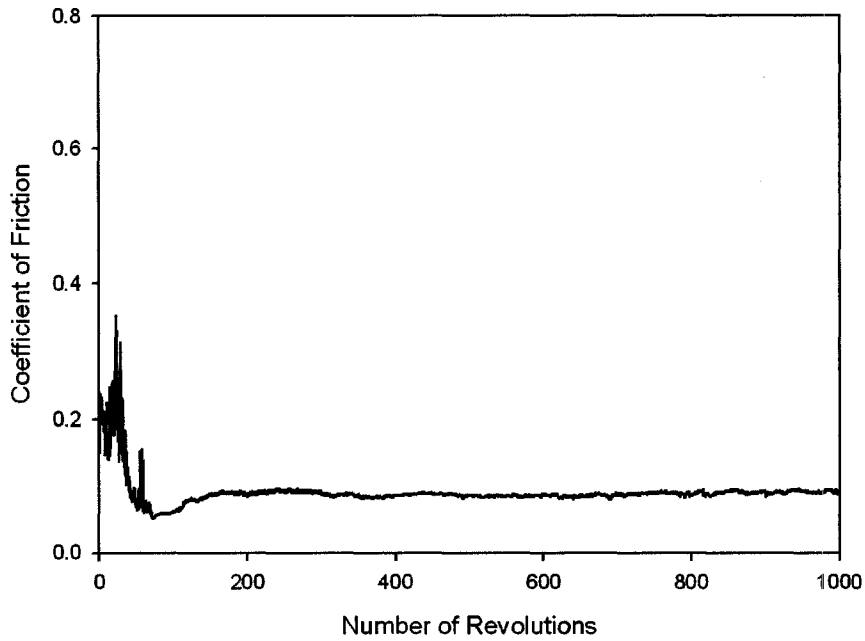

Figure A 1. 18 The COF curve between the DLC/WC-DLC coating and a 319 Al alloy during sliding under 14% RH.

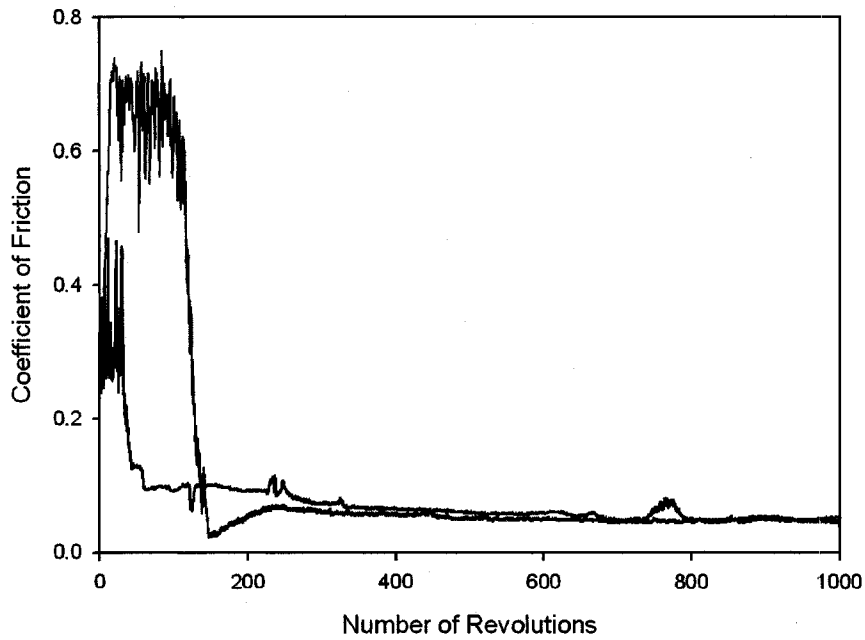

Figure A 1. 19 The COF curves between the DLC/WC-DLC coating and a 319 Al alloy during sliding in N_2.

A 2 Ashby's Method of Flash Temperature Calculation

The methodology developed by Ashby and his co-workers [146] were applied to calculate the temperature increase at the sliding interface due to the heat generated by friction between WC-DLC coating, DLC/WC-DLC coating and a 319 Al pin, respectively. This section presents a description of their model as well as the procedure that has been taken to calculate the values displayed in **Section 5.5.2**.

When two contacting solids slide on each other, heat is generated and then distributed between the sliding surfaces according to their geometry and thermalphysical properties. The rate of heat generation (q) due friction per unit nominal contact area (A_n) at the sliding surface is given by

$$q = \frac{\mu F v}{A_n}$$ **Equation A 2. 1**

where μ is the coefficient of friction (COF), F is the applied load, v is the sliding velocity. In the current study, the temperature calculation was done for a pin-on disc configuration as shown in **Figure A 2. 1**. Subscript 1 is used for the pin and subscript 2 is used for the disc.

Two important variables are defined: the mean or bulk temperature (T_b) and the flash temperature (T_f). The bulk temperature is defined as the surface temperature due to the

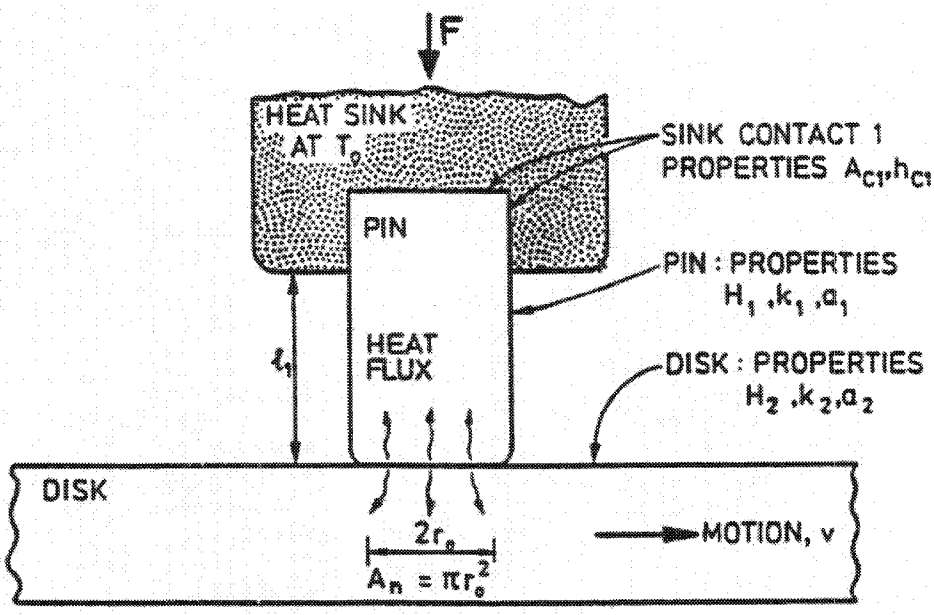

Figure A 2. 1 A typical pin-on-disc configuration [146].

uniformly injected frictional heat across the nominal contact area (A_n). The flash temperature is the local temperature of the asperities on the sliding surface and is almost always higher than the bulk temperature. T_b is given by

$$T_b - T_0 = \frac{\mu F v}{A_n}\left(\frac{1}{\frac{k_1}{l_{1b}} + \frac{k_2}{l_{2b}}}\right) \qquad \textbf{Equation A 2. 2}$$

where T_0 represents the temperature of the remote heat sink, k_1 and k_2 are the thermal conductivities of the materials in sliding contact, and l_{1b} and l_{2b} are the equivalent linear heat diffusion distances from the sliding surface to the heat sink for surfaces 1 and 2.

T_f is expressed as

$$T_f - T_b' = \frac{\mu F v}{A_r}\left(\frac{1}{\frac{k_1}{l_{1f}} + \frac{k_2}{l_{2f}}}\right) \qquad \textbf{Equation A 2. 3}$$

where A_r is the real contact area that consisting of contact asperities, l_{1f} and l_{2f} are the new equivalent linear heat diffusion distances and T_b' is the effective sink temperature that is given as

$$T_b' = T_b - \frac{A_r}{A_n}(T_b - T_0), \text{ where} \qquad \textbf{Equation A 2. 4}$$

$$\frac{A_r}{A_n} = \frac{F}{F_s} \qquad \textbf{Equation A 2. 5}$$

F_s is defined as the seizure load at which A_r becomes equal to A_n and is given by

$$F_s = \frac{A_n H_0}{\left(1 + 12\mu^2\right)^{1/2}} \qquad \textbf{Equation A 2. 6}$$

H_0 is the hardness of the softer of the two surfaces. Since the disc is coated with a layer of DLC coating with different thermal properties from the substrate M2 steel, an effective thermal conductivity, k_{2e} was used in place of k_2, which is expressed as

$$k_{2e} = \frac{k_{steel} k_{coat.}}{\left(1 - \frac{Z}{\beta r_a}\right) k_{coat.} + \frac{Z}{\beta r_a} k_{steel}} \qquad \text{where,} \qquad \textbf{Equation A 2. 7}$$

$\beta = \frac{l_{1b}}{r_0}$ and Z is a constant with a value of 10^{-6}.

The nomenclature and expressions for the equivalent linear heat diffusion distances l_{1b}, l_{2b}, l_{1f} and l_{2f} are listed in **Tables A 2.1 a)** and **b)**. The assumptions applied to calculate the variables are also presented. The material properties and the values of other parameters used to calculate the bulk and flash temperatures that were discussed in

Section 5.5.2 are listed in **Table A 2. 2** and **Table A 2. 3**. Properties of pure Al insteady of 319 Al alloy was used for calculation.

Table A 2. 1 a) Nomenclature, and **b)** expressions and assumptions for the equivalent heat diffusion distances.

a_1, a_2,	Thermal diffusivities of surfaces 1 and 2, (m^2/s)
H_0	Hardness of the softer material at 25 °C
n, n_1, n_2	A measure of the lifetime of a contacting asperity; which survives a sliding distance, $(\pi/2)nr_a$. n_1 was taken as 1 for Al asperities and n_2 was taken as 100 for DLC asperities
r_a	Radius of a single isolated asperity junction (m), assumed to be 1×10^{-4} m.
r_j	Radius of a contact junction that can be made up of many unit asperities ($r_a<r_j<r_0$) (m)
r_0	Radius of nominal contact area (m), measured from the SEM image of the pin tips after sliding against DLC coatings under conditions described in **Section 5.1**.

a)

Bulk Temperature	l_{1b}, set to be the physical length of the pin, 15 mm $l_{2b} = \frac{r_0}{\pi^{1/2}}\tan^{-1}\left(\frac{2\pi a_2}{r_0 v}\right)^{1/2}$
Flash Temperature	$l_{1f} = \frac{r_j}{\pi^{1/2}}\tan^{-1}\left(\frac{n_1 2\pi a_2}{r_j v}\right)^{1/2}$ $l_{2_f} = \frac{r_j}{\pi^{1/2}}\tan^{-1}\left(\frac{n_2 2\pi a_2}{r_j v}\right)^{1/2}$ $r_j = r_0\left\{\left(1-\frac{F}{F_s}\right)\left(\frac{r_0}{r_a}\right)^2+1\right\}^{-1/2}$

b)

Table A 2. 2 The material properties used to calculate the bulk and flash temperatures.

	Al [152]	DLC [153]	M2 [152]
Density (kg/m^3)	2700	1750	7900
Heat Capacity (J/kg·K)	904	711	450
Thermal Conductivity (W/m·K)	229	15	48
Thermal Diffusivity (m^2/s)	9.38×10^{-5}	9.17×10^{-6}	5×10^{-6}

Table A 2. 3 The measured steady-state COF and radius of nominal contact area values in ambient air (25 °C, 51% RH).

Coating	COF	r_0 (m)
WC-DLC	0.14	2.86×10^{-4}
DLC/WC-DLC	0.12	1.58×10^{-4}

REFERENCES

1. US National Institute for Occupational Safety and Health Publication No 98-102, Occupational exposure to metalworking fluids: A criteria for a recommended standard, January (1998), 1, 2, 44, 143.
2. M.Lahres, P. M. –Hummel and O. Doerfel, Applicability of different hard coatings in dry milling aluminum alloys, Surf. Coat. Technol. 91 (1997) 116-121.
3. M. Lahres and G. Jorgensen, Properties and dry cutting performance of diamond coated tools, Surf. Coat. Technol. 96 (1997) 198-204.
4. F. Klocke and T. Krieg, Coated tools for metal cutting - features and application, CIRP Ann. Manuf. Technol. 48 (1999) 515-525.
5. J. F. Kelly and M. G. Cotterell, Minimal lubrication machining of aluminum alloys, J. Mater. Process. Technol. 120 (2002) 327-334.
6. K. Enke, Dry machining and increase of endurance of machine parts with improved doped DLC coatings on steel, ceramics and aluminium, Surf. Coat. Technol.116-119 (1999) 488-491.
7. E. Konca, Adhesion and material transfer between aluminum and surfaces coated with diamond-like carbon and other coatings, Ph. D dissertation 2005, University of Windsor, Windsor, Ontario, Canada.
8. B. West, Boron carbide tool coatings make their entry, Modern Machine Shop 61 (1989) 76-80.
9. W. Cermignani and M. G. Robinson, T. Hu, L. Stiehl, W. Rafaniello, T. Fawcett, P. Marshall and S. Rozeveld, Processing, properties and performance of high volume sputter deposited boron-carbon coatings, Proc. Annu. Tech. Conf. Soc. Vac. Coaters (1998) 66-74.

10. R.P. Elliott, Contract No. AT (11-1), 578, Project Agreement No. 4, Armour Res. Found., Rep. ARF 220012, 1961.
11. C. Wood and D. Emin, Conduction mechanism in boron carbide, Phys. Rev. B 29 (1984) 4582-4587.
12. D. Emin, Structure and single-phase regime of boron carbides, Phys. Rev. B 38 (1988) 6041-6055.
13. I.A. Howard, C.L. Beckel, D. Emin, Bipolarons in boron-rich icosahedra: Effects of carbon substitution, Phys. Rev. B 35 (1987) 9265-9270.
14. K. Shirai, S. Emura, S. Gonda, Y. Kumashiro, Infrared study of amorphous $B_{1-x}C_x$ films, J. Appl. Phys. 78 (1995) 3392-3400.
15. A. O. Sezer, J. I. Brand, Chemical deposition of boron carbide, Mater. Sci. Eng. B79 (2001) 191-202.
16. H. Yang, H.-Y. Chen, J. Wang, H. Yang, W.-Z. Li and H.-D. Li, Synthesis of boron carbide films by ion beam sputtering, Surf. Coat. Technol. 128-129 (2000) 329-333.
17. T. Eckardt, K. Bewilogua, G. van der Kolk, T. Hurkmans, T. Trinh, W. Fleischer, Improving properties of sputtered boron carbide coatings by process modifications, Surf. Coat. Technol. 126 (2000) 69-75.
18. H.-S. Ahn, P.D. Cuong, K.-H. Shin, Ki-Seung Lee, Tribological behavior of sputtered boron carbide coatings and the influence of processing gas, Wear 259 (2005) 807-813.
19. O. R. Monteiro, M. –P. Delplancke-Ogletree and C. C. Klepper, Boron carbide coatings prepared by cathodic arc deposition, J. Mater. Sci. 38 (2003) 3117-3120.
20. H.R. Salimijazi, T. W. Coyle, J. Mostaghimi and L. Leblanc, Microstructure of vacuum plasma-sprayed boron carbide, J. Thermal Spray Technol. 14 (2005) 362-368
21. Z. Han, G. Li, J. Tian and M. Gu, Microstructure and mechanical properties of boron carbide thin films, Mater. Lett. 57 (2002) 899-903.
22. U.S. Patent #4,594,294, E. Eichen and J. Flasck (1984).
23. U.S. Patent #4,619,865, J. Keem and J. Flasck (1984).
24. U.S. Patent #4,645,715, S. Ovshinsky, J. Keem, J. Flasck, R. Bergeron and J. Tyler (1982).
25. U.S. Patent #4,590,031, E. Eichen and J. Flasck (1986).

26. U.S. Patent #4,643, 951, J. Keem and J. Flasck (1987).
27. U.S. Patent #4,716,083, E. Eichen and J. Flasck (1987).
28. S. Lee, J. Mazurowski, G. Ramseyer, P. A. Dowben, Characterization of boron carbide thin films fabricated by plasma enhanced chemical vapor deposition from boranes, J. Appl. Phys. 72 (1992) 4925-4933.
29. H. T. Tsou, W. Kowbel, Design of multilayer plasma-assisted CVD coatings for the oxidation protectionof composite materials, Surf. Coat.Technol. 79 (1996) 139-150.
30. K. Shirai, S. Emura, and S. Gonda, Y. Kumashiro, Infrared study of amorphous $B_{1-x}C_x$ films, J. Appl. Phys. 78 (1995) 3392-3400.
31. A. Erdemir, Tribological properties of boric acid and boric-acid-forming surfaces. Part I: crystal chemistry and mechanism of self-lubrication of boric acid, Lubr. Eng. 47 (1990) 168-173.
32. A. Erdemir, G. R. Fenske, R. A. Erck, F. A. Nichols and D. E. Busch, Tribological properties of boric acid and boric-acid-forming surfaces. Part II: Mechanisms of formation and self-lubrication of boric acid films on boron- and boric oxide-containing surfaces, Lubr. Eng. 47 (1990) 179-184.
33. A. Erdemir, G. R. Fenske and R. A. Erck, A study of the formation and self-lubrication mechanisms of boric acid films on boric oxide coatings, Surf. Coat. Technol. 43-44 (1990) 588-596.
34. S. D. Dvrak, K. J. Wahl and I. L. Singer, Friction hehavior of boric acid and annealed boron carbide coatings studied by in situ Raman tribometry, Lubr. Eng. 59 (2003) 14-22.
35. P. Larsson, N. Axen, S. Hogmark, Tribofilm formation on boron carbide in sliding wear, Wear 236 (1999) 73-80.
36. P. D. Cuong, H. -S Ahn, E. -S. Yoon and K. -H Shin, Effect of relative humidity on tribological properties of boron carbide coting against steel, Surf. Coat. Technol. 201 (2006) 4230-4235.
37. A. Erdemir, C. Bindal, Formation and self-lubrication mechanisms of boric acid on borided steel surfaces, Surf. Coat. Technol. 76-77 (1995) 443-449.
38. C. Bindal and A. Erdemir, Ultralow friction behavior of borided steel surfaces after flash annealing, Appl. Phys. Lett. 68 (1996) 923-925.

39. A. Erdemir, C. Bindal and G. R. Fenske, Formation of ultralow friction surface films on boron carbide, Appl. Phys. Lett. 68 (1996) 1637-1639.
40. A. Erdemir, Rolling-contact fatigue life and wear resistance of hard coatings on bearing-steel substrates, Surf. Coat. Technol. 54/55 (1992) 482-489.
41. S. J. Harris, G. Krauss, M. T. Siniawski, Q. Wang, S. Liu, Y. Ao, Surface feature variations observed in 52100 steel sliding against a thin boron carbide coating, Wear 249 (2002) 1004-1013.
42. S.J. Harris, G.G. Krauss, S.J. Simko, R.J. Baird, S.A. Gebremariam, G. Doll, Abrasion and chemical-mechanical polishing between steel and a sputtered boron carbide coating, Wear 252 (2002) 161-169.
43. F. M. Borodich, S. J. Harris, L. M. Keer, C. V. Cooper, Wear and abrasiveness of hard carbon-containing coatings under variation of the load, Surf. Coat. Technol. 179 (2004) 78-82.
44. M.T. Siniawski, S.J. Harris and Q. Wang, Effects of contact on the abrasiveness of a thin boron carbide coating, Tribol. Lett. 20 (2005) 21-30.
45. M.T. Siniawski, S.J. Harris, Q. Wang, Y.-W. Chung and C. Freyman, Effects of thickness and roughness variations on the abrasiveness, Tribo. Lett. 17 (2004) 931-937.
46. J.A. Greenwood and J.P. Williamson, Contact of nominally flat surfaces, Process. Roy. Soc. Lond. Ser. A 295 (1966) 300-319.
47. J. Robertson, Diamond-like amorphous carbon, Mat. Sci. Eng. R 37 (2002) 129-281
48. B. Bhushan, Chemical, mechanical and tribological characterization of ultra-thin and hard amorphous carbon coatings as thin as 3.5 nm: recent developments, Diamond Relat. Mater. 8 (1999) 1985-2015.
49. S. Aisenberg, R. Chabot, Ion beam deposition of thin films of diamond like carbon, J. Appl. Phys. 49 (1971) 2953-2958.
50. A. Grill, Diamond-like carbon: state of the art, Diam. Relat. Mater. 8 (1999) 428-434.
51. K. Bewilogua, R. Wittorf, H. Thomsen, M. Weber, DLC based coatings prepared by reactive d.c. magnetron sputtering, Thin Solid Films 447-448 (2004) 142-147.

52. S. Zhang, X. L. Bui, Y. Fu, D. L. Butler, H. Du, Bias-graded deposition of diamond-like carbon for tribological applications, Diam. Relat. Mater. 13 (2004) 867-871.

53. S. Zhang, H. Xie, Improving of amorphous carbon coatings on cemented carbide through plasma cleaning, Surf. Coat. Technol. 113 (1999) 120-125.

54. S. P. Bugaev, V. G. Podkovyrov, K. V. Oskomov, S. V. Smaykina, N.S. Sochugov, Ion-assisted pulsed magnetron sputtering deposition of ta-C films, Thin Solid Films 389 (2001) 16-26.

55. X. T. Zeng, S. Zhang, X. Z. Ding, D. G. Teer, Comparison of three types of carbon composite coatings with exceptional load-bearing capacity and high wear resistance, Thin Solid Films 420-421 (2002) 366-370.

56. K. J. Clay, S. P. Speakman, N. A. Morrison, N. Tomozeiu, W. I. Milne and A. Kapoor, Material properties and tribological performance of rf-PECVD deposited DLC coatings, Diam. Relat. Mater. 7 (1998) 1100-1107.

57. K. Iechika, Y. Kokaku, M. Ootake, K. Abe, H. Tani and H. Inaba, Performance of hard DLC protective film prepared by PECVD method for thin film magnetic disk, IEEE Trans.Megn. 30 (1994) 4134-4136.

58. R. F. Huang, C. Y. Chan, C. H. Lee, J. Gong, K. H. Lai, C. S. Lee, K. Y. Li, L. S. Wen and C. Sun, Wear-resistant multilayered diamond-like carbon coating prepared by pulse biased arc ion plating, Diam. Relat. Mater. 10 (2001) 1850-1854.

59. A.A. Voevodin, M.S. Donley and J.S. Zabinski, Pulsed laser deposition of diamond-like carbon wear protective coatings: a review, Surf. Coat. Technol. 92 (1997) 42-49.

60. J. M. Lackner, C. Stotter, W. Waldhauser, R. Ebner, W. Lenz and M. Beutl, Pulsed laser deposition of diamond-like carbon coatings for industrial tribological applications, Surf. Coat. Technol. 174-175 (2003) 402-407.

61. R. F. Bunshah (Edt.), Handbook of Deposition Technologies for Films and Coatings - Science, Technology and Applications (2nd Edition), William Andrew Publishing, Noyes, 1994.

62. Y. Catherine, Preparation techniques for diamond-like carbon, Diamond and Diamond-like Films and Coatings, Plenum, New York, 1991, pp. 193-227.

63. J.J. Cuomo, D.L. Pappas, J. Bruley, J.P. Doyle and K.L. Seagner, Vapor deposition processes for amorphous carbon films with sp^3 fractions approaching diamond, J. Appl. Phys. 70 (1991) 1706-1711.

64. C. Donnet, Recent progress on the tribology of doped diamond-like and carbon alloy coatings: a review, Surf. Coat. Technol. 100-101 (1998) 180-186.

65. K. Bewilogua and H. Dimigen, Preparation of W-C:H coatings by reactive magnetron sputtering, Surf. Coat. Technol. 61 (1993) 144-150.

66. W. van Duyn and B. van Lochem, Chemical and mechanical characterisation of WC:H amorphous layers, Thin Solid Films 181 (1989) 497-503.

67. J. Deng and M. Braun, DLC multilayer coatings for wear protection, Diam. Relat. Mater. 4 (1995) 936-943.

68. A. A. Voevodin, M. A. Capano, S. J. P. Laube, M. S. Donley and J. S. Zabinski, Design of a Ti/TiC/DLC functionally gradient coating based on studies of structural transitions in Ti-C thin films, Thin Solid Films 298 (1997) 107-115.

69. H. Ronkainen, J. Likonen, J. Koskinen and S. Varjus, Effect of tribofilm formation on the tribological performance of hydrogenated carbon coatings, Surf. Coat. Technol. 79 (1996) 87-94.

70. Y. Liu, E. Meletis and A. Erdemir, A study on the wear mechanism of diamond-like carbon films, Surf. Coat. Technol. 82 (1996) 48-56.

71. E. Meletis, A. Erdemir and G. Fenske, Tribological characteristics of DLC films and duplex plasma nitriding/DLC coating treatments, Surf. Coat. Technol. 73 (1996) 39-45.

72. A. Erdemir, C. Bindal, J. Pagan and P. Wilbur, Characterization of transfer layers on steel surfaces sliding against diamond-like hydrocarbon films in dry nitrogen, Surf. Coat. Technol. 76-77 (1996) 559-563.

73. Y. Liu and E. I. Meletis, Evidence of graphitization of diamond-like carbon films during sliding wear, J. Mater. Sci. 32 (1997) 3491-3495.

74. Y. Liu, A. Erdemir and E. I. Meletis, An investigation of the relationship between graphitization and frictional behaviour of DLC coatings, Surf. Coat. Technol. 86-87 (1996) 564-568.

75. T. W. Scharf and I.L. Singer, Monitoring transfer films and friction instabilities with in situ Raman tribometry, Tribol. Lett. 14 (2003) 3-8.
76. J. C. Sanchez-Lopez, A. Erdemir, C. Donnet and T. C. Rojas, Friction-induced structural transformation of diamondlike carbon coatings under various atmospheres, Surf. Coat. Technol. 163-164 (2003) 444-450.
77. E. Konca, Y.-T. Cheng, A.M. Weiner, J.M. Dasch and A.T. Alpas, Effect of test atmosphere on the tribological behaviour of the non-hydrogenated diamond-like carbon coatings against 319 aluminum alloy and tungsten carbide, Surf. Coat. Technol. 200 (2005) 1783-1791.
78. E. Konca, Y.-T. Cheng, A. M. Weiner, J.M. Dasch and A.T. Alpas, The role of hydrogen on the tribological behaviour of non-hydrogenated DLC coatings against aluminum, Tribol. Trans. 50 (2007) 178-186.
79. G. Irmer and A. Dorner-Reisel, Micro-Raman studies on DLC coatings, Adv. Eng. Mater. 7 (2005) 694-705.
80. E. Konca, Y. –T. Cheng, A. M. Weiner, J. M. Dasch, A. T. Alpas, Vacuum tribological behavior of the non-hydrogenated diamond-like carbon coatings against aluminum: Effect of running-in in ambient air, Wear 259 (2005) 795-799.
81. A. Erdemir, The role of hydrogen in tribological properties of diamond-like carbon films, Surf. Coat. Technol. 146-147 (2001) 292-297.
82. H. Ronkainen, S. Varjus, J. Koskinen and K. Holmberg, Differentiating the tribological performance of hydrogenated and hydrogen-free DLC coatings, Wear 249 (2001) 260-266.
83. C. Donnet, J. Fontaine, A. Grill and T. Le Mogne, The role of hydrogen on the friction mechanism of diamond-like carbon films, Tribol. Lett. 9 (2000) 137-142.
84. H. I. Kim, J.R. Lince, O.L. Eryilmaz and A. Erdemir, Environmental effects on the friction of hydrogenated DLC films, Tribol. Lett. 21 (2006) 53-58.
85. C. Donnet and A. Grill, Friction control of diamond-like carbon coatings, Surf. Coat. Technol. 94-95 (1997) 456-462.
86. J. Andersson, R. A. Erck and A. Erdemir, Friction of diamond-like carbon films in different atmospheres, Wear 254 (2003) 1070-1075.

87. A. Erdemir, Genesis of superlow friction and wear in diamondlike carbon films, Tribol. Int. 37 (2004) 1005-1012.
88. Erdemir, Design criteria for super lubricity in carbon films and related microstructures, Tribol. Int. 37 (2004) 577-583.
89. J. Fontaine, C. Donnet, A. Grill and T. Le Mogne, Tribochemistry between hydrogen and diamond-like carbon films, Surf. Coat. Technol. 146-147 (2001) 286-291.
90. Y. Qi and L. G. Hector, Jr., Hydrogen effect on adhesion and adhesive transfer at aluminum/diamond interfaces, Phys. Rev. B 68 (2003) 201403-1.
91. J. Jiang, S. Zhang and R. D. Arnell, The effect of relative humidity on wear of a diamond-like carbon coating, Surf. Coat. Technol. 167 (2003) 221-225.
92. J. Andersson, R.A. Erck and A. Erdemir, Frictional behavior of diamondlike carbon films in vacuum and under varying water vapor pressure, Surf. Coat. Technol. 163-164 (2003) 535-540.
93. M.N. Gardos, in: K.E. Spear, J.P. Dismuke (Eds.), Synthetic Diamond: Emerging CVD Science and Technology, Wiley, New York, 1994, p. 419
94. T. Le Huu, H. Zaidi, D. Paulmier, Lubricating properties of diamond-like coating, Wear 181-183 (1995) 766-770.
95. Y. Liu, A. Erdemir, E.I. Meletis, Influence of environmental parameters on the frictional behavior of DLC coatings, Surf. Coat. Technol. 94-95 (1997) 463-468.
96. K. Miyoshi, Studies of mechanochemical interactions in the tribological behaviour of materials, Surf. Coat. Technol. 44 (1990) 799-812.
97. K. Enke, H. Dimigen and H. Hubsch, Frictional Properties of diamondlike carbon layers, Appl. Phys. Lett. 36 (1980) 291-292.
98. C. Donnet, T. Le. Mogne, L. Ponsonnet, M. Melin, A. Grill, V. Paetl and C. Jahnes, The respective role of oxygen and water vapour on the tribology, Tribol. Lett. 4 (1998) 259-256.
99. Y. Qi, E. Konca and A. T. Alpas, Atmospheric effects on the adhesion and friction between non-hydrogenated diamond-like carbon (DLC) coating and aluminum – A first principles investigation, Surf. Sci. 600 (2006) 2955-2965.
100. A. Grill, B. Meyerson, Diamond: Emerging CVD Science and Technology, Wiley, New York, 1994, p. 91.

101. A. Grill, V. Patel, K.L. Saenger, C. Jahnes, S.A. Cohen, A.G. Schrott, D.C. Edelstein and J.R. Paraszczak, Diamondlike carbon materials as low-k dielectrics for multilevel interconnects in ULSI, Mater. Res. Soc. Symp. Proc. 443 (1997) 155-164.

102. A. Grill, V. Patel and C. Jahnes, Novel low k dielectrics based on diamondlike carbon materials, J. Electrochem. Soc. 145 (1998) 1649-1653.

103. S. Reinke and W. Kulisch, Mechanisms in ion-assisted deposition of superhard coatings: Cubic boron nitride-tetrahedral amorphous carbon, Surf. Coat. Technol. 97 (1997) 23-32.

104. R. K. Y. Fu, Y. F. Mei, M. Y. Fu, X. Y. Liu and P. K. Chu, Thermal stability of metal-doped diamond-like carbon fabricated by dual plasma deposition, Diam. and Relat. Mater. 14 (2005) 1489-1493.

105. W. J. Yang, Y. –H. Choa, T. Sekino, K. B. Skim, K. Niihara and K. H. Auh, Thermal stability evaluation of diamond-like nanocomposite coatings, Thin Solid Films 434 (2003) 49-54.

106. Z. Ziebert, M. Rinke, M. Stüber, S. Ulrich and H. Holleck, Interfaces and temperature stability of stepwise graded DLC films studied by nanoindentation and Raman spectroscopy, Surf. Coat. Technol. 200 (2005) 1127-1131.

107. A. Vannhulsel, B. Blanpain, J. P. Celis, J. Roos, E. Dekempeneer and J. Smeets, Study of the wear behaviour of diamond-like coatings at elevated temperatures, Surf. Coat. Technol. 98 (1998) 1047-1052.

108. Flavien Bremond, Pierre Fournier and Francis Platon, Test temperature effect on the tribological behavior of DLC-coated 100C6-steel couples in dry friction, Wear 254 (2003) 774-783.

109. E. Konca, Y.-T. Cheng, A. M. Weiner, J. M. Dasch and A. T. Alpas, Elevated temperature tribological behaviour of non-hydrogenated diamond-like carbon coatings against 319 aluminum alloy, Surf. Coat. Technol. 200 (2006) 3996-4005.

110. T. Krumpiegl, H. Meerkamm, W. Fruth, C. Schaufler, G. Erkens and H. Böhner, Amorphous carbon coatings and their tribological behaviour at high temperatures and in high vacuum, Surf. Coat. Technol. 120-121 (1999) 555-560.

111. W. Ni, Y.-T. Cheng, A. M. Weiner and T. A. Perry, Tribological behaviour of diamond-like-carbon (DLC) coatings against aluminum alloys at elevated temperatures, Surf. Coat. Technol. (2006) 3229-3234.

112. Guido Reisel, Siegfried Steinhäuser and Bernhard Wielage, The behaviour of DLC under high mechanical and thermal load, Diam. Relat. Mater. 13 (2004) 1516-1520.

113. R. Gilmore and R. Hauert, Control of the tribological moisture sensitivity of diamond-like carbon films by alloying with F, Ti or Si, Thin Solid Films, 398-399 (2001) 199-204.

114. R. Gilmore and R. Hauert, Comparative study of the tribological moisture sensitivity of Si-free and Si-containing diamond-like carbon films, Surf. Coat. Technol. 133-134 (2000) 437-442.

115. H. Dimigen and C.-P. Klages, Microstructure and wear behavior of metal-containing diamond-like coatings, Surf. Coat. Technol. 49 (1991) 543-547.

116. J.S. Wang, Y. Sugimura, A.G. Evans and W.K. Tredway, Mechanical performance of DLC films on steel substrates Thin Solid Films 325 (1998) 163-174.

117. K. Bewilogua and H. Dimigen, Preparation of W-C:H coatings by reactive magnetron sputtering, Surf. Coat. Technol. 61 (1993) 144-150.

118. Singh, J. C. Jiang and E. I. Meletis, Cr-diamond-like carbon nanocomposite films: Synthesis, characterization and properties, Thin Solid Films 489 (2005) 150-158.

119. K. Bewilogua, C. V. Cooper, C. Specht, J. Schröder, R. Wittorf and M. Grischke, Effect of target material on deposition and propertie of metal-containing DLC (Me-DLC) coatings, Surf. Coat. Technol. 127 (2000) 224-232.

120. C.Strondl, G. J. Van der Kolk, T. Hurkmans, W. Fleischer, N. M. Carvalho and J. T. M. De Hosson, Mechanical and tribological properties of metal containing diamond-like carbon coatings (Me-DLC) deposited under different plasma confinement conditions, Proc. Annu. Tech. Conf. Soc. Vac. Coaters (2001) 67-71.

121. A. Hieke, T. Hurkmans, G. J. Van Der Kolk, M. Tobler and R. Bonetti, Comparison between WCC/DLC, CrN/DLC and RF produced DLC coatings, Proc. Annu. Tech. Conf. Soc. Vac. Coaters (2005) 556-561.

122. W. C. Oliver and G. M. Pharr, An improved technique for determining hardness and elastic modulus using load and depth sensing indentation experiments, J. Mater. Res. 7 (1992) 1564-1583.

123. E. N. Kaufmann (Edt.), Characterization of materials, v. 2, , John Wiley & Sons, Inc., NJ, 2003, p.1807.

124. A. C. Ferari and J. Robertson, Interpretation of Raman spectra of disordered and amorphous carbon, Phys. Rev. B 61 (2000) 14095-14107.

125. J. E. E. Baglin, Elastic Recoil spectrometry, in Encyclopedia of materials characterization - Surfaces, Interfaces, Thin Films, Butterworth-Heinemann, MA, 1992.

126. J. H. Westbrook and H. Conrad (Eds.), Science of hardness testing and its research applications, ASM, Metals Park, OH, 1973.

127. A. M. Korsunsky, M. R. McGurk, S. J. Bull and T. F. Page, On the hardness of coated systems, Surf. Coat. Technol. 99 (1998) 171-183.

128. J. R. Tuck, A. M. Korsunsky, R. I. Davidson, S. J. Bull and D. M. Elliott, Modelling of the hardness of electroplated nickel coatings on copper substrates, Surf. Coat. Technol. 127 (2000) 1-8.

129. J. R. Tuck, A. M. Korsunsky, D. G. Bhat and S. J. Bull, Indentation hardness evaluation of cathodic arc deposited thin hard coatings, Surf. Coat. Technol. 139 (2001) 63-74.

130. J. R. Tuck, A. M. Korsunsky, S. J. Bull and R. I. Davidson, On the application of the work-of-indentation approach to depth sensing indentation experiments on coated systems, Surf. Coat. Technol. 137 (2001) 217-224.

131. J. Bulmer, Ionbond© US, private communication.

132. M. Chen, T. Perry and A.T. Alpas, Ultra-mild wear in eutectic Al–Si alloys, doi:10.1016/j.wear.2006.12.025.

133. W.R. Stott, Myths and miracles of gear coatings, Gear Technology, July/August (1999) 35-44.

134. M.T. Siniawski, A. Martini, S.J. Harris and Q. Wang, Effects of lubrication and humidity on the abrasiveness of a thin boron carbide coating, Tribol. Lett. 18 (2005) 185-195.

135. F. P. Bowden and D. Tabor, The friction and lubrication of solids, Clarendon Press, Oxford, 2001.

136. D. J. Siegel, L. G. Hector, Jr., and J. B. Adams, Adhesion, atomic structure, and bonding at the Al(111)/α-Al_2O_3(0001) interface: A first principles study, Phys. Rev. B 65 (2002) 085415-1.

137. D. J. Siegel, L. G. Hector, Jr., and J. B. Adams, Adhesion, stability, and bonding at metal/metal-carbide interfaces: Al/WC, Surf. Sci. 498 (2002) 321-336.

138. D. J. Siegel, L. G. Hector, Jr., and J. B. Adams, First-principles study of metal-carbide/nitride adhesion: Al/VC vs. Al/VN, Acta Mater. 50 (2002) 619-631.

139. D. J. Siegel, L. G. Hector, Jr. and J. B. Adams, *Ab initio* study of Al-ceramic interfacial adhesion, Phys. Rev. B 67 (2003) 092105-1.

140. G.M. Hamilton and L.E. Goodman, The stress field created by a circular sliding contact, J. Appl. Mech. 33 (1966) 371-376.

141. J. Zhang and A. T. Alpas, Delamination wear in ductile materials containing second phase particles, Mater. Sci. Eng. A 160 (1993) 25-35.

142. X. Meng-Burany and A. T. Alpas, FIB and TEM studies of damage mechanisms in DLC coatings sliding against aluminum, Thin Solid Films (2007) doi: 1.1016/j.tsf.2007.06.038.

143. J. A. Dean, ed., Lange's Handbook of Chemistry, 15th ed., McGraw Hill, New York, (1999) 6.81-6.123.

144. J. Larsen-Basse and S. S. Sokoloski, Influence of atmospheric humidity on abrasive wear - II. 2-body abrasion, Wear 32 (1975) 9-14.

145. F. Thevenot, Boron carbide-a comprehensive review, J. Europ. Cer. Soc. 6 (1990) 205-225.

146. H. S. Kong and M. F. Ashby, Friction-heating maps and their applications, MRS Bulletin, 10 (1991) 41-48.

147. T. Le Huu, H. Zaidi, D. Paulmier and P. Voumard, Transformation of sp^3 to sp^2 sites of diamond like carbon coatings during friction in vacuum and under water vapor environment Thin Solid Films 290-291 (1996) 126-130.

148. T. Mikami, H. Nakazawa, M. Kudo and M. Mashita, Effects of hydrogen on film properties of diamond-like carbon films prepared by reactive radio-frequency magnetron sputtering using hydrogen gas, Thin Solid Films 488 (2005) 87-92.

149. A. Erdemir and G. R. Fenske, Tribological performance of diamond and diamondlike carbon films at elevated temperatures, Tribol. Trans. 39 (1996) 787-794.

150. H. Liu, A. Tanaka and K. Umeda, The tribological characteristics of diamond-like carbon films at elevated temperatures, Thin Solid Films 346 (1999) 162-168.

151. A. Pertsin and M. Grunze, Water as a lubricant for graphite: A computer simulation study, J. Chem. Phys. 125 (2006) 114707-1.

152. A. Bejan and A. D. Kraus (Eds), Heat transfer handbook, John Wiley & Sons, Inc., Hoboken, NJ, 2003, pp 123, 132.

153. B. Bhushan and B. K. Gupta, Handbook of Tribology, McGraw-Hill, Inc., 1991, p 14.118.

VITA AUCTORIS

Ying Zhang was born in September 1981 in Lingyuan, China. He graduated from Lingyuan 1st High School in 2000. Then he headed south to Xiamen, where he obtained his B.Sc. degree in Materials Chemistry from the Xiamen University in 2004. Ying Zhang joined the Engineering Materials M.A.Sc. Program at the University of Windsor in September 2005 and hopes to graduate in September 2007.